# High Resolution Three-Dimensional Tracking of Motor Proteins with Optical Tweezers

**Dissertation**
der Mathematisch-Naturwissenschaftlichen Fakultät
der Eberhard Karls Universität Tübingen
zur Erlangung des Grades eines
Doktors der Naturwissenschaften
(Dr. rer. nat.)

vorgelegt von

Dipl. Phys. Michael Bugiel

aus Frankfurt an der Oder

Tübingen, 2017

Gedruckt mit Genehmigung der Mathematisch-Naturwissenschaftlichen
Fakultät der Eberhard Karls Universität Tübingen.

| | |
|---|---|
| Tag der mündlichen Qualifikation: | 01.06.2017 |
| Dekan: | Prof. Dr. Wolfgang Rosenstiel |
| 1. Berichterstatter: | Prof. Dr. Erik Schäffer |
| 2. Berichterstatter: | Prof. Dr. Tilman E. Schäffer |

"We are constantly searching, not just for answers to our questions, but for new questions."

Benjamin Lafayette Sisko.

**Kurzfassung**

Optische Pinzetten sind hochauflösende Orts- und Kraftsensoren, die sowohl in der Biologie wie auch der Physik verwendet werden. Ihre Fähigkeit, mikroskopische Objekte einzufangen und deren Auslenkung mit hoher Präzision im Nanometer-Bereich zu messen erlaubt es, einzelne Moleküle zu vermessen und Kräfte im Pikonewton-Bereich auszuüben. In dieser Arbeit habe ich eine optische Pinzette benutzt, um die dreidimensionale Bewegung zytoskelettaler molekularer Maschinen, sogenannter Kinesin-Motorproteine, zu untersuchen. Die exakte Art und Weise der Bewegung von Kinesinen auf ihrer Schiene, dem Mikrotubulus, ist entscheidend für ihre biologische Funktion. Ich habe eine Versuchsanordnung entwickelt, in dem die dreidimensionale Bewegung von Kinesin-Motoren mittels der optischen Pinzette mit hoher Auflösung verfolgt werden kann. Ich habe diesen Ansatz auf verschiedene Kinesine angewandt. Für das Mikrotubulus-verkürzende Kinesin-8 *Kip3* habe ich herausgefunden, dass es neben der Vorwärtsbewegung auch Seitwr̈tsbewegung sowohl nach links als auch nach rechts zeigte. Diese Seitwärtsbewegung konnte durch die mit der optischen Pinzette angelegten Seitwärtskräfte asymmetrisch verschoben werden. Die Seitwr̈tsbewegung von Kip3 könnte ein wichtiger Teil seines Bewegungsmechanismus sein, da sie eine einfache Möglichkeit bietet, Hindernisse auf dem Weg zu umgehen. Bei einem anderen Kinesin, Kinesin-1, habe ich keine Seitwärtsbewegung, sondern nur Vorwärtsbewegung beobachtet. Diese unidirektionale Fortbewegung konnte genutzt werden, um die Struktur der Mikrotubuli zu untersuchen. Die entwickelte dreidimensionale Versuchsanordnung kann in Zukunft auch benutzt werden, um die Bewegung anderer molekularer Motoren zu untersuchen.

**Abstract**

Optical tweezers are high resolution position and force transducers used in biology and physics. The instrument's ability to trap microscopic objects and measure their displacements with high precision on the nanometre scale allows to track single molecules and to exert forces in the piconewton range. In this work, I used optical tweezers to investigate the three-dimensional motion of cytoskeletal molecular machines, so-called kinesin motor proteins. The exact path of kinesin's motion on its track, the microtubule, is crucial for its biological function. I implemented an assay in which the three-dimensional motion of kinesin motors can be tracked using optical tweezers with high resolution. This approach, I applied to different kinesins. For the microtubule-depolymerising kinesin-8 *Kip3*, I found that it showed sideward motion to the left and right, in addition to its forward motion. This sideward motion could be asymmetrically biased by applying sideward forces with the optical tweezers. The sideward motion of Kip3 might be an important part of its motility mechanism as it provides a simple way to bypass obstacles on its track. For another kinesin, kinesin-1, I observed no sideward motion but only forward motion. This unidirectional motion could be used to investigate the structure of the microtubules. The developed three-dimensional experimental assay can be used to track the motion of other molecular motors with high resolution in the future.

# Contents

# List of Figures

# List of Tables

# List of Symbols and Abbreviations

| | |
|---|---|
| $\beta$ | displacement sensitivity |
| $\Delta\phi_{\mathrm{pf}}$ | angular step size |
| $\Delta y$ | sideward displacement |
| $\delta_f$ | focal shift |
| $\delta_x$ | forward step size |
| $\epsilon$ | measurement precision |
| $\eta$ | dynamic viscosity |
| $\gamma$ | drag coefficient |
| $\kappa$ | trap stiffness |
| $\lambda$ | wavelength |
| $\omega$ | angular speed |
| $\phi$ | angular position |
| $\rho$ | radial position |
| $\sigma^2$ | variance |
| $C$ | volts-to-nm converting factor |
| $D$ | diffusion constant |
| $F$ | force |
| $f$ | frequency |
| $f_c$ | corner frequency |
| $h$ | height |
| $k$ | rate |
| $K_c$ | critical gain |
| $k_{\mathrm{B}}$ | Boltzmann constant |
| $L$ | linker length |
| $N$ | number of data points |
| $P$ | pitch |
| $p$ | momentum |
| $QPD$ | QPD signal |
| $QPD^0$ | QPD offset |
| $R$, $r$ | radius |
| $rP$ | reciprocal pitch |
| $T$ | temperature |
| $U$ | voltage |
| $v$ | speed |
| 2D | two-dimensional |
| 3D | three-dimensional |
| aa | amino acid |
| AMPPNP | adenosine-5′-(β,γ-imido)-triphosphate |
| ATP | adenosine-5′-triphosphate |
| BB | borate buffer |
| BRB80 | Brinkley resuspension buffer 1980 |
| BSA | bovine serum albumin |
| CRTD | Center for Regenerative Therapies Dresden, Germany |
| deg | degree of arc |
| DIC | differential interference contrast |
| DMSO | dimethyl sulfoxide |
| DTT | dithiothreitol |

| | |
|---|---|
| EDC | 1-ethyl-3-(3-dimethyl-aminopropyl) carbod-iimide |
| eGFP | enhanced green fluores-cent protein |
| EGTA | ethylene glycol tet-raacetic acid |
| GDP | guanosine-5′-diphosphate |
| GFP | green fluorescent protein |
| GMPCPP | guanosine-5′-(α,β-methyleno)-triphosphate |
| GTP | guanosine-5′-triphosphate |
| his | histidine |
| IRM | interference reflection microscopy |
| LED | light emitting diode |
| MAP | microtubule-associated protein |
| MES | 2-(N-morpholino) eth-anesulfonic acid |
| MPI-CBG | Max Planck Institute of Cell Biology and Genet-ics, Dresden, Germany |
| MSAD | mean squared angular displacement |
| MSD | mean squared displace-ment |
| MT | microtubule |
| OT | optical tweezers |
| PBS | phosphate-buffered sa-line |
| PDMS | polydimethylsiloxane |
| PEG | polyethylene glycol |
| PFPE | perfluoropolyether |
| PID | proportional-integrative-differential |
| PIPES | piperazine-N,N′-bis-(2-ethanesulfonic acid) |
| PMMA | polymethyl methac-rylate |
| PS | polystyrene |
| PSD | power spectral density |
| QPD | quadrant photodiode |
| rms | root mean squared |
| SD | standard deviation |
| SE | standard error |
| SEM | standard error of the mean |
| sulfo-NHS | N-hydroxysulfosuccinimide sodium salt |
| TEM | transmission electron microscope |
| TIRF | total internal reflection fluorescence |
| UV | ultraviolet |

# 1. Introduction

Motor proteins are a special class of biomolecules that are involved in many biological processes. They convert chemical energy into force and motion and are thereby involved in muscle contraction, intracellular transport, cell motility, and cell division [1, 2]. Malfunctions of motor proteins are related to various diseases like Alzheimer's disease and different kinds of cancer [3–5]. Thus, understanding the functioning of motor proteins on the molecular level can provide important information about those diseases and eventually enable drug development.

The aim of this thesis was to investigate the molecular properties of members of the motor protein superfamily of *kinesins*. These kinesins generate force and motion by translocating on cytoskeletal microtubules. I focused on members of two subfamilies: kinesin-1 and kinesin-8. Both have different biological functions *in vivo*. The path of how kinesins translocate along the microtubules is an important aspect of their biological function. Hence, I investigated the molecular trajectories of both kinesins, using high-resolution tracking with optical tweezers. Optical tweezers are an ideal tool to investigate motor proteins, as their force and spatial sensitivity are in the same range of motor proteins [6, 7]. I used optical tweezers to detect the motion and to exert forces on the kinesins.

This thesis is divided into two parts. After a short introduction to motor proteins, microtubules, and optical tweezers in Chapter 2, the first part discusses the implementation of the three-dimensional optical tweezers force-clamp (Chapter 3), the basic kinesin stepping assay (Chapter 4), the functionalisation of microspheres that were used as probes for the optical tweezers (Chapter 5), and the topographic surface treatment that was needed for three-dimensional assays (Chapter 6). Part two describes the results of two-dimensional (Chapter 7) and three-dimensional (Chapter 8) experiments with kinesin-1 and kinesin-8, respectively. Additionally, I discovered a new optical trapping effect which is described in Chapter 9. A critical discussion of the results and an outlook are given in the last chapter.

# 2. Biological and Physical Background

This chapter contains a brief overview about the motor protein superfamily of kinesins, their track, the microtubule, and the optical tweezers apparatus.

## 2.1. Microtubules

The cytoskeleton is an important cellular organelle that helps the cell to maintain its shape by supporting the membrane from the inside. The cytoskeleton is also involved in important processes like cell division and provides tracks on which motor proteins move on [1, 2].

The cytoskeletal filaments, that were of interest in this work, were *microtubules* (MTs). Microtubules are macromolecular structures that are build of the protein *tubulin*. Tubulin itself is a heterodimer, built of α- and β-tubulin (Fig. 2.1A). It forms elongated chains that are called *protofilaments* (Fig. 2.1B). Those protofilaments bind laterally to each other with a small axial mismatch between each protofilament (indicated by a red asterisk in Fig. 2.1C). The protofilaments form a cylindrical tube, the microtubule, with a diameter of about 25 nm [1]. The axial mismatch between the protofilaments causes a helical structure of neighbouring tubulin subunits that is broken at the so-called *seam*, where the summed up axial mismatch corresponds to half the size of a tubulin dimer (Fig. 2.1D, [8]). Microtubules usually have 13 protofilaments *in vivo* [9]. In contrast, microtubules that were grown *in vitro* can have a broad range of protofilament numbers from 8–19 [1, 10]. The number of protofilaments can vary between different microtubules [1, 11] but also within one microtubule [12]. Protofilaments in a microtubule with 13 protofilaments are parallel to the overall MT axis. In microtubules with other protofilaments numbers, the protofilaments form a helix around the MT axis; the overall microtubule structure is called *supertwisted* [1]. According to the lattice rotation model, the periodicity length of this helix, called supertwist pitch $P$, depends on the protofilament number in the microtubule [13, 14]. The composition *in vitro* with respect to the protofilament numbers of microtubules highly depends on the preparation conditions [11].

Due to the dimeric nature of the tubulin, the microtubule has a polar structure. The MT ends have different properties concerning growth dynamics. The faster growing end is called plus end, the slower growing end is called minus end (Fig. 2.1D). Microtubules are rigid but highly dynamic structures. The bonds between the tubulin subunits are dependent on guanosine-5′-triphosphate (GTP)

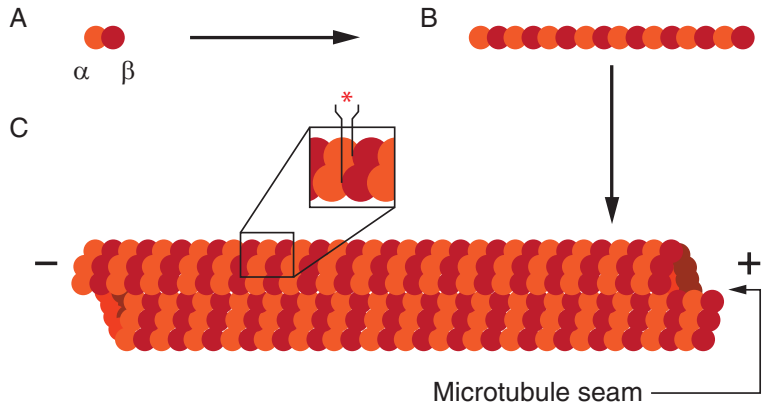


**Figure 2.1: Illustration of the microtubule structure.** (A) Tubulin subunits, made of the α- and β-tubulin dimer, form (B) protofilaments. (C) Protofilaments bind laterally to another with a small axial mismatch (* in inset) forming a hollow cylinder. Due to the mismatch (*), the tubulin subunits wind helically around the microtubule axis with this symmetry broken at the seam. The β-monomer is directed to the so-called plus end (+), the α-monomer to the minus end (−).

that is bound to β-tubulin [1]: After hydrolysis of the bound GTP to guanosine-5′-diphosphate (GDP), the inter-tubulin bonds get strained and the MT structure becomes unstable [2]. Thus, MT polymerisation is an energy-dependent process. Microtubules can only grow as long as the tubulins at the ends are in the GTP state; otherwise, rapid phases of depolymerisation, called catastrophes, occur. The equilibrium between these two phases of growth and shrinkage is called dynamic instability. There are many microtubule-associated proteins (MAPs) known that polymerise [15], stabilise [16, 17], or depolymerise microtubules [18–22]. Such proteins are thought to regulate the MT length in the living cell. For *in vitro* experiments, microtubules can be stabilised by using the slowly hydrolysable GTP analogue guanosine-5′-(α,β-methyleno)-triphosphate (GMPCPP) [23], or drugs like taxol [24–26] that inhibit the MT dynamics. The way of MT stabilisation defines the MT composition with respect to the protofilament number: MT polymerisation in presence of GTP with subsequent adding of taxol provides microtubules with a broad variety of the protofilament number that highly depends on the buffer conditions [11]. In contrast, MT polymerisation in the presence of GMPCPP gives microtubules that have almost exclusively 14 protofilaments [27, 28].

## 2.2. Motor Proteins

Microtubules serve as tracks for the motor protein superfamilies of kinesins and dyneins. Both move on microtubules, converting energy from adenosine-5′-triphosphate (ATP) hydrolysis into force and velocity [1, 2]. Kinesins form a broad superfamily of proteins having a common, highly conserved catalytic motor domain, called head, that binds to the MT lattice and generates force by hydrolysing ATP. Most kinesins like conventional kinesin-1 are homodimers.

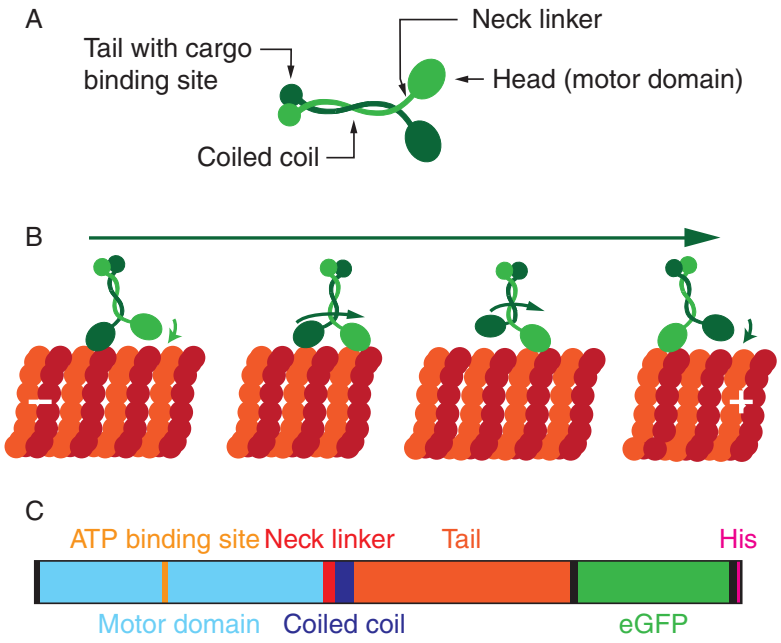


**Figure 2.2: Kinesin structure and motility.** (A) Basic structural features of conventional kinesin. (B) Simplified schematic of kinesin's motility on a microtubule. (C) Protein sequence of Kip3-eGFP-his$_6$ with respect to the number of amino acids (aa): Motor domain (blue, 435 aa), neck linker (red, 17 aa), coiled coil (blue, 28 aa), tail (orange, 325 aa), eGFP tag (green, 227 aa), and his tag (magenta, 6 aa).

The tails of two monomers form a coiled coil, holding the dimer together. At the end of the tail, "cargo transporters" like kinesin-1 have a cargo binding site. The coiled coil is connected with the motor domains via short, flexible neck linkers. The basic kinesin structure is illustrated in Fig. 2.2A. Most kinesins translocate along microtubules towards the plus end by a walking-like mechanism, where the two heads bind to the tubulin subunits sequentially (Fig. 2.2B). When one head binds to the microtubule, it hydrolyses ATP which causes a conformational change in the head and neck linker structure. This conformational change pulls the rear, unbound head forward to the next binding site on the MT lattice where it can bind [29]. The result is a hand-over-hand walk [30, 31]. Because, one of the two heads is always bound to the microtubule, the kinesin can make many steps before dissociating from the microtubule [32], i.e. it moves processively. For every forward step, one ATP molecule is hydrolysed [33–35]. The step size of about 8 nm coincides with the distance between the tubulins along the protofilament [6]. The kinesin stepping mechanism, e.g. the velocity, is highly dependent on the ATP concentration [33, 34]. Using the non-hydrolysable ATP analog adenosine-5'-(β,γ-imido)-triphosphate (AMPPNP) stalls the kinesin cycle in the MT-bound state and thus binds kinesins very tightly to microtubules [36]. The kinesins, I investigated in this thesis are members of two different kinesin families, kinesin-1 and kinesin-8.

Kinesin-1 is a cargo transporter and involved in anterograde intracellular transport. Thus, it is strong and can generate a force of about 5–6 pN. Compared to other kinesins it is also fast with 800 nm/s at saturated ATP concentration [7]. The run length, the mean distance kinesin walks without dissociating, is about 1 µm [37–39]. I used the kinesin construct *rkin430*, a mutant of rat kinesin-1 that is truncated at amino acid 430 and has an additional hexahistidine (his$_6$) and an

enhanced green fluorescent protein (eGFP) tags. The first tag is for purification purposes, the second a fluorescent label.

The second kinesin, I studied, is the kinesin-8 *Kip3* from budding yeast, which is very different from kinesin-1: It is relatively weak, generating a force of about 1.1 pN [40] and slow with 40–50 nm/s [19, 41]. These properties make a transporter function *in vivo* unlikely[1]. Also, with a mean run length of 10–12 µm [41], it is much more processive than kinesin-1 and every other known kinesin. Kip3 has been shown to depolymerise the microtubule plus ends in a collective, MT length-dependent manner [19, 41]. It is thought that this depolymerisation is part of a MT length control mechanism which plays a role during cell division and defines the biological function of Kip3 [42]. Consistent with this hypothesis, yeast mutants that lacked functional Kip3 showed unnaturally long microtubules during cell division which caused a mispositioning of the mitotic spindle [20, 43]. There are different Kip3 analogues in other organisms with similar properties [40, 44, 45]. The human kinesin-8 *Kif18A* is known to be linked to colorectal cancer [46]. Thus, a better understanding of Kip3 may be relevant for cancer research. It was shown that Kip3's high processivity rises from (i) an additional weakly bound state in its catalytic stepping cycle [40] and (ii) an additional MT binding site at Kip3's tail domain [47]. This MT binding site enables Kip3 to cross-link and slide microtubules against each other what is thought to be part of Kip3's role during cell division [48]. As the depolymerisation occurs at the microtubule plus end [41], it is crucial that Kip3 reaches it. Thus, Kip3 must be able to (i) walk long enough on the microtubules and (ii) bypass obstacles on the MT lattice. The high processivity of Kip3 fulfils the first condition. It was also shown that Kip3-driven microtubules rotated in a left-handed manner [49, 50] implying protofilament switching. This sideward motion would meet the second requirement. However, the exact details of Kip3's trajectory on the microtubule were unknown and it was the aim of this thesis to investigate the trajectory in more detail.

Previous left-handed rotation by Kip3 was detected under multiple-molecule conditions [50]. However, the characteristics of single Kip3 molecules are of interests. Thus, I performed assays under single-molecule conditions to investigate Kip3's path of motion on the microtubule. These assays are explained in detail in the following part of this thesis. I used Kip3 mutants with eGFP and his tags, similar to kinesin-1. The structure is depicted in Fig. 2.2C based on the structural data in the UniProtKB database (ID code: P53086) and predictions by Bormuth et al. [50]. I followed two different experimental approaches:

First, to detect Kip3 protofilament switching and to investigate its force dependence, I applied alternating sideward forces on single Kip3 that walked on immobilised microtubules. Second, I used microtubules that were suspended on topographic surface structures. On these microtubules, kinesins could move freely along and around them. The motion of Kip3 on such microtubules was tracked in three dimensions without applying any force. As kinesin-1 is generally accepted to follow the protofilament axis [11], I performed analogous experiments with rkin430 as control. However, there is a scientific debate

[1] So far, no transport activity of Kip3 has been observed *in vivo*.

about kinesin-1. It is known that the neck linker of Kip3 is longer than that of kinesin-1 [50] which is thought to be the reason that Kip3 can make sideward steps on the MT lattice in contrast to kinesin-1. A longer neck linker enables Kip3 to reach a binding site on a neighbouring protofilament which is impossible with a shorter neck linker. Consequently, prolonging the kinesin-1 neck linker by mutation significantly increased the probability of protofilament switches [51]. However, also for kinesin-1 with normal neck linger length, protofilament switches have been observed. As no asymmetry between left and right was measured [51], this was still consistent with kinesin-1 following the protofilament on average [11]. Other studies observed the possibility of kinesin-1 to bypass artificial, permanent "road blocks" on the microtubule, though it is less likely compared to detaching [52–55]. The obvious explanation for being able to bypass obstacles would be protofilament switching. Therefore, three-dimensional high resolution tracking experiments with kinesin-1 could contribute to a better understanding of kinesin-1, as well.

## 2.3. Optical Tweezers as Tool to Probe Motor Protein Mechanics

Since their discovery in 1986 by Ashkin et al. [56], optical tweezers have evolved into a versatile tool to investigate living cells as well as micro- and nanoscopic objects and even single molecules [57, 58]. With optical tweezers, dielectric objects of the size in the micrometre range down to the size of atoms can be trapped [57]. The objects' displacement inside the optical trap and the corresponding force can be measured. Common objects are microspheres that are called "beads". The so-called optical trap consists of a tightly focused laser beam. In the focus, objects are trapped.

For small objects (typical object size $\ll$ wavelength of light $\lambda$), the trapping is explained by electric dipoles that are induced in the object by the light's electric field. These dipoles are attracted towards the point of maximal electric field, which is the focus' centre. Because the resulting force is oriented along the electric field gradient, it is called "gradient force". This approach is valid for objects that are small enough to be considered as single dipoles [59].

For bigger objects (typical object size $\gg$ wavelength of light $\lambda$), the trapping effect is explained by geometric optics [59]. The incident light is refracted twice according to Snell's law by the object, here a microsphere. The Compton effect proved that an electromagnetic wave carries a momentum $\boldsymbol{p}$ [60]. Hence, the refraction of the light's path causes a change of the light's momentum $\Delta\boldsymbol{p}$ which results in a force that is transferred to the microsphere, following Newton's 3rd law as illustrated in Fig. 2.3. The intensity gradient of the focused light leads also to a gradient force that pulls the microsphere back to the focus centre when it is displaced relative to it. According to the microsphere material and the corresponding ratio of transmissivity and reflectivity, some part of the light is not refracted by the microsphere but reflected or scattered. The same effect of momentum transfer accounts for reflected light resulting in a "scattering force"

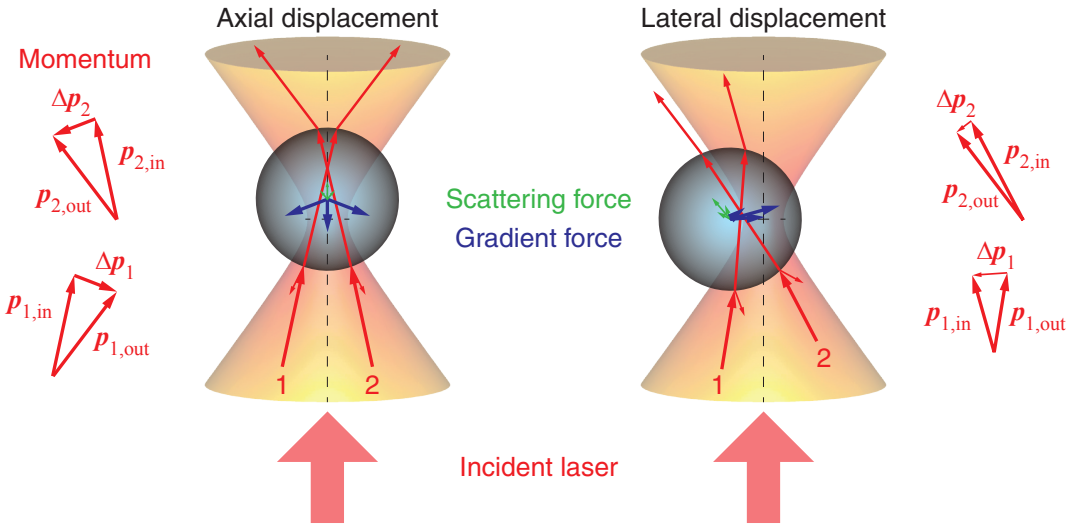


**Figure 2.3: Trapping of a microsphere in a focused laser beam.** An axial (left) or lateral (right) displacement cause refractions of incoming light, whose change of momentum $\Delta\boldsymbol{p}$ (red) leads to a summed up gradient force (blue) that drives the microsphere back to the focus centre. The reflected (scattered) light causes a summed up scattering force (green), that is opposite to the gradient force.

that points along the propagation direction of the laser (Fig. 2.3). Thus, optical trapping is a balance between refraction and reflection. It has been shown that minimising the share of reflection by the microspheres increases the reachable trapping force [61]. Due to the scattering force, the axial equilibrium position of the microsphere is above the focus centre in an inverted microscope geometry. Besides refraction and reflection, the microsphere also absorbs some of the laser light. This share does not result in any force but reduces the effective trapping force per laser power.

Trapping of objects of intermediate size (typical object size $\approx$ wavelength of light $\lambda$) is explained by the so-called Mie theory [59, 62].

All theories result in a gradient force that pulls trapped objects back to the trap centre when displaced. Over a certain range, this force is proportional to the displacement, i.e. the optical trap can be described as a Hookean spring. The spring constant $\kappa$ is called trap stiffness and defines the restoring force $F$ by $F_i = \kappa_i \cdot \Delta x_i$, where $\Delta x_i$ is the displacement and the index $i = x,y,z$ refers to the axes in a Cartesian coordinate system. The displacement $\Delta x$ is often measured by a quadrant photodiode (QPD) [63], also employed in the setup used here. A QPD is an array of 4 photodiodes. The three-dimensional displacements of a trapped microsphere in a laser focus can be measured by projecting the outgoing laser beam onto the QPD. Lateral displacements shift the projected laser spot on the QPD resulting in different voltages in the different photodiodes as illustrated in Fig. 2.4. The differences of the voltages in the quadrants, here called QPD signal $QPD$, can be used to calculate the corresponding displacement. Axial displacements of the microsphere inside the trap cause a change of the overall sum of the voltage, resulting in an analogous relation. Typically, the QPD signal has a non-zero offset $QPD_i^0$ for trapped microspheres in the absence of

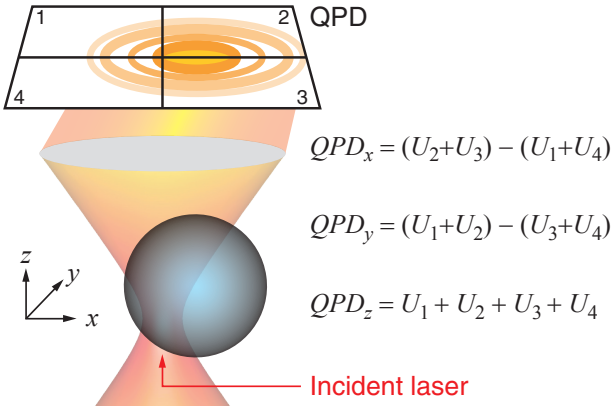


**Figure 2.4: Position detection with a quadrant photodiode.** The quadrant photodiode (QPD) signals $QPD_i$ ($i = x,y,z$) are calculated from the voltage signals $U_l$ ($l = 1 \ldots 4$) of the different sub-diodes.

an applied force. For the axial direction, an offset is always present. The corresponding voltage difference signal is then $\Delta U_i = QDP_i - QPD_i^0$, where $QPD_i$ is the QPD signal for direction $i$. The relation between displacement $\Delta x$ and $\Delta U$ is linear for small displacements, resulting in $\Delta x_i = \beta_i \cdot \Delta U_i$, where the factor $\beta$ is called displacement sensitivity. Both factors $\kappa$ and $\beta$ must be determined. To quantify force and displacement shall be measured, the optical trap needs to be calibrated. Usually, both parameters depend on laser power, the microsphere material, and diameter. There are different methods in use, with different advantages and disadvantages [64, 65]. The trap stiffness can be determined by measuring the position variance of the Brownian motion of a trapped microsphere. The displacement sensitivity can be measured by scanning with a microsphere through the optical trap. A very elegant way is to analyse the Brownian motion of a trapped microsphere by calculating the power spectral density (PSD) of the displacement $x_i(t)$. The PSD is the mean square of the Fourier transform of $x_i(t)$. For a trapped microsphere, there is a balance between trapping, drag, and thermal forces. Without inertia, the PSD that corresponds to the solved equation of motion, is then described by a Lorentzian function. A Lorentzian is characterised by two parameters: an amplitude and a characteristic frequency. To measure both calibration factors $\kappa$ and $\beta$, one has to know the drag coefficient $\gamma$. Thus, the problem is underdetermined. One can measure the third by oscillating the sample stage with a sinusoidal wave [67].

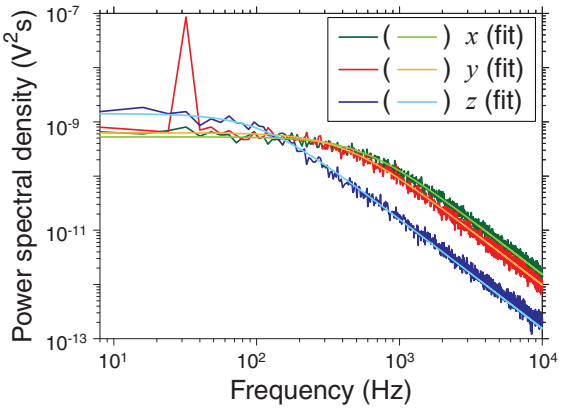


**Figure 2.5: Power spectral density of an optically trapped microsphere.** PSDs of a 590 nm polystyrene microsphere that was trapped above the surface. An oscillation was applied on the sample in the $x$-direction with a frequency of 32 Hz, visible as a discrete peak. The PSDs were fitted with Lorentzian functions resulting in trap stiffnesses of 0.023 pN/nm, 0.018 pN/nm and 0.006 pN/nm for $x$, $y$ and $z$, respectively. Modified from [66].

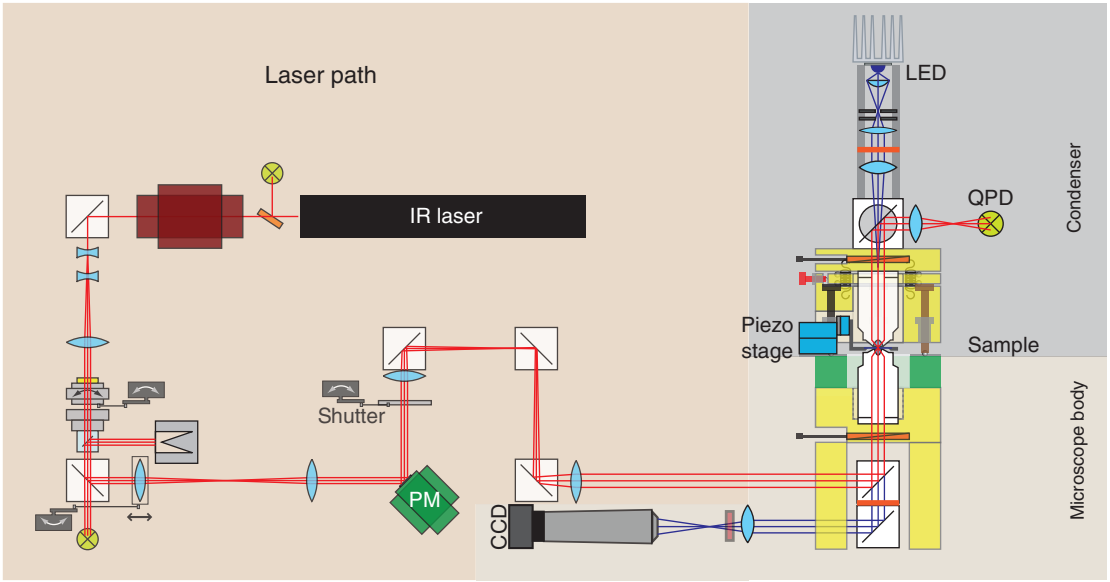


**Figure 2.6: Schematic of the used optical tweezers setup.** The laser light is focused and projected on the sample via a system of lenses and mirror, including a steering piezo-tilt mirror (PM) and a piezo-translation stage. The outgoing laser light is then reflected on the QPD. The sample is illuminated by a LED and imaged by a CCD camera. A shutter enables activation and deactivation of optical trapping. With permission from Mohammed Mahamdeh [69].

The oscillation causes a discrete peak in the PSD at the oscillation frequency. The peak power depends on the system parameters. Figure 2.5 shows exemplary PSDs for all three dimensions with the oscillation in the $x$-direction. As the drag coefficient depends on the distance between microsphere and sample surface, a distance-dependent calibration can account for this [68].

For optical trapping, I used a single-beam optical tweezers setup (Fig. 2.6) which is described in detail in [69–71]. Briefly, the setup was equipped with a 5 W infrared laser ($\lambda = 1064$ nm) and a millikelvin-precision temperature control system, which provides high stability and thus a high spatial resolution. All experiments were performed at a temperature of 29.2 °C [70]. The laser is focused by an objective with high numerical aperture (CFI S Fluor 100×/0.7–1.3 oil objective, Nikon, Japan). A piezo-tilt mirror can be used to deflect the laser beam and so move the optical trap laterally inside the sample. A piezo-translation stage can move the whole sample in all three dimensions. Visualisation of the sample is provided by illumination with a blue light emitting diode (LED) using differential interference contrast (DIC) [72] in an inverted microscope. For light detection, a CCD camera (Lu135M, Lumenera, Ottawa, Canada) with a maximal frame rate of 26 Hz and a pixel size of 44.6 nm was used.

Optical tweezers are a perfect tool to investigate motor proteins like kinesins in *in vitro* experiments [6, 37]. The ability to measure forces in the pN range and displacements in the nm range makes it possible to determine mechanical parameters like the stall force of motor proteins, i.e. the maximal force, a mo-

tor protein can hold, or the discrete 8 nm step size of kinesin [6, 7]. However, velocities at a constant force cannot be determined in a static trap, as the force increases with every step. The velocity of motor proteins typically depends on the force, applied to the protein. In this context, this force is often called load [7]. An opposing load slows down the motor protein, whereas an assisting load might speed it up. Hence, the motor protein gets slower inside a static trap until the motor stalls or detaches. Methods to measure the velocity are optical tracking of freely walking, microsphere-coupled or fluorescently labelled kinesins [37, 38]. However, an optical trap can be used in an active mode, where focus and sample are moved against each other to keep the displacement of the microsphere inside the trap constant. The relative motion between sample and focus corresponds to the motion of the kinesin. This active mode is called *force clamp* and requires suitable feedback hardware and software which are introduced in the next chapter. Optical tweezers force-clamps have been widely used to investigate the mechanical properties of kinesins [73, 74] and other motor proteins like myosins [75, 76] and dyneins [77].

The kinesin Kip3 has already been subjected to forces using a two-dimensional (2D) force clamp with and against its walking directions [40]. This measurements observed a speed-up and slow-down due to hindering and assisting loads, respectively and revealed the weakly bound slip state. I used the two-dimensional force clamp to apply alternating sideward loads on walking kinesins and measure sideward motion on the microtubule and its force-dependence. Subsequently, I extended the force clamp to three dimensions (3D) and used it to track the three-dimensional motion of kinesins on microtubules freely accessible from all sides.

For different control measurements, I also performed stepping assays, using total internal reflection fluorescence (TIRF) microscopy as described in [19, 41]. In TIRF, fluorophores close to the sample surface are excited exclusively by the evanescent field of total internal reflection. The light emitted by the fluorophores, situated in the evanescent field can be then detected. TIRF assays can be performed as gliding assay, in which a floating microtubule is driven by multiple immobilised kinesins [11], or as stepping assay, in which free single kinesin motors can walk on immobilised microtubules [38]. In TIRF assays, one can measure basic motility parameters like velocity and processivity.

# Part I.

# Implementation of 3D Optical Tweezers Assays with Kinesins

# 3. Implementation of a 3D Force Clamp

An optical tweezers force-clamp keeps the displacement of a microsphere relative to the trap centre and the applied force constant. The force clamp is able to track the motion of microsphere-coupled motor proteins under zero and non-zero loads and thus to measure the load-dependence of parameters like velocity and run length. Keeping the displacement constant requires a feedback system that measures and compensates for deviation from a constant displacement.

In this chapter, a brief introduction into feedback and control is given and the implementation of 3D-force-clamp assays is explained. The following sections on feedback control and the expansion of an optical tweezers force-clamp from 2D to 3D have been published as book chapter in *Optical Tweezers: Methods and Protocols* [66] and are quoted here.

## 3.1. Practical Principle of 3D Feedback

### 3.1.1. Basic Principle of PID Control

Feedback measures the difference between a process variable, here the microsphere displacement inside the trap or the corresponding force $F$, respectively, and a desired setpoint, here a load $F_{\text{set}}$ that is applied to the microsphere. This difference is defined as the error $e$:

$$e = F - F_{\text{set}}. \tag{3.1}$$

The feedback system calculates a response to this error that should minimise it. A very commonly used feedback loop control mechanism is the proportional-integrative-differential (PID) controller. There are many articles, reviews and books on the topic (see e.g. [78–82]). Once the process variable is known, the PID controller response is calculated as a sum of three components:

**Proportional** The proportional response $r^P(t)$ is proportional to the error

$$r^P(t) = K^P \cdot e(t), \tag{3.2}$$

where $K^P$ is the coefficient for the proportional gain. If $K^P$ is too small, the error is only slowly compensated. If $K^P$ is too large, the error is overcompensated. In the subsequent feedback cycle, the error will have changed its sign and the controller will overcompensate the error in the opposite direction and so on.

In this manner, the system will start to oscillate. Using solely a proportional controller, even with an optimal value of $K^P$, the desired setpoint is never reached because otherwise the controller response would result in a zero force $F(e = 0) = 0 \neq F_{\text{set}}$. Thus, the measured force can never reach the desired non-zero setpoint force. The remaining error is called the steady-state error—here it would be $1/(1 + K^P)$—and can be eliminated by adding an integral gain.

**Integral** For the integral response $r^I(t)$, all errors are summed up from the beginning until the time $t$

$$r^I(t) = K^I \cdot \int_{t_0}^{t} e(t')\mathrm{d}t', \tag{3.3}$$

where $K^I$ is the coefficient for the integral gain. For a positive error, this error sum response increases with time unless the error becomes zero. Therefore, this response is able to eliminate the steady-state error. If $K^I$ is too small, the elimination is slow, reducing the overall response time of the feedback loop. If $K^I$ is too large, an overshoot and/or oscillations develop. Large overshoots and/or output limitations of the controller can cause a long relaxation time before the setpoint is reached. In particular for situations that cause a large error, for example a large setpoint change or a large and fast movement of the microsphere, the integral error may wind up to such a large integral response value that even when the error has switched sign it will take a long time until the overshoot is compensated by the controller. This phenomenon is called integral windup. It can be avoided by anti-windup filters [81].

**Derivative** For the derivative response $r^D(t)$, the time derivative of the error is calculated according to

$$r^D(t) = K^D \cdot \frac{\mathrm{d}e(t)}{\mathrm{d}t}, \tag{3.4}$$

where $K^D$ is the coefficient for the derivative gain. The derivative response gives information on how fast the error changes and can therefore be used for an extrapolation of how the error will change. Because this extrapolation predicts the state of the system for the next cycles of the feedback loop, a correctly tuned $K^D$ value can speed up the response of the controller by reducing the amplitude of both the overshoot and subsequent oscillations that occur after a step response. However, since derivatives are susceptible to noise, a large $K^D$ value can amplify the system noise or even destabilise the controller. Thus, in particular for single-molecule assays, for which Brownian motion is a dominant noise source, derivative control needs to be carefully used. Moreover, it may not be useful for every feedback system.

The working principle of a force-clamp experiment with microsphere-coupled kinesin is illustrated in Fig. 3.1. The overall response of a PID controller is cal-

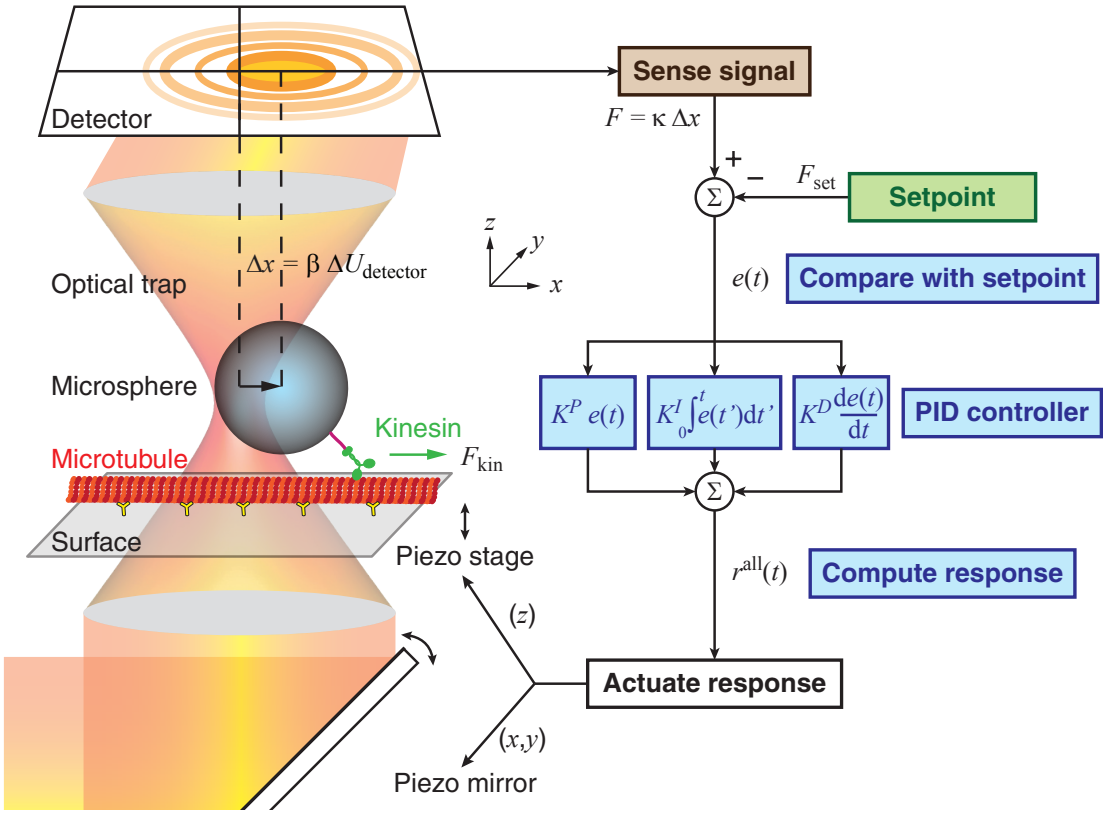


**Figure 3.1: Schematic of a force-clamp feedback loop for a kinesin experiment.** The kinesin motor generates a force $F_{kin}$, which displaces the microsphere from the trap centre. This displacement $\Delta x$ causes the detector to generate a voltage $\Delta U_{detector}$, proportional to the displacement with a displacement sensitivity $\beta$. In this manner, the trapping force $F = \kappa\Delta x$ is sensed, where $\kappa$ is the trap stiffness. Based on the error $e$, the feedback response $r^{all}$ is calculated by a PID controller (see text for details). Finally, any change in the desired force or displacement is compensated by moving the trap and microsphere relative to each other according to $r^{all}$ by actuating a piezo-tilt mirror in $x$ and $y$, and by a piezo-translation stage in $z$. Modified from [66].

culated by summing up:

$$\begin{aligned} r^{all}(t) &= r^P(t) + r^I(t) + r^D(t) \\ &= K^P \cdot e(t) + K^I \cdot \int_{t_0}^{t} e(t')\mathrm{d}t' + K^D \cdot \frac{\mathrm{d}e(t)}{\mathrm{d}t}. \end{aligned} \tag{3.5}$$

For a good feedback performance, all three feedback coefficients $K^P$, $K^I$, and $K^D$ must be optimised according to the system's properties. How to set "good" values for them is explained in Sec. 3.2. Prior to this, the implementation of the controller and the choice of the optimal feedback rate are discussed.

### 3.1.2. Hardware Requirements

An optical tweezers force-clamp requires, besides a suitable optical trap, system hardware that can move the sample and/or the trap focus. In the setup I used, relative movement is provided by a piezo-tilt mirror that deflects the laser laterally (i.e. $x$ and $y$ in Fig. 3.1) and a piezo-translation stage that moves the sample in all three dimensions ($x$,$y$,$z$). These pieces of hardware act as actuators, that accomplish the response $r^{\text{all}}$ (Eq. 3.5). Both options have advantages and disadvantages: Piezo mirrors usually react faster. However, compared to stages, their working range is usually smaller and the optical trap's properties depend on the tilt angle. Nonetheless, as the disadvantages are negligible here as discussed below, the piezo mirror was used as actuator in $x$ and $y$. The piezo stage was used to tune the force clamp in $x$- and $y$-direction, as discussed in Section 3.2.3. For axial feedback, either a 3D piezo-translation stage, a piezo-driven objective mount, or a deformable mirror [83] can be used as an actuator. Since our setup was only equipped with a piezo stage, this stage was used as the actuator for the $z$-direction.

## 3.2. Implementation

### 3.2.1. Programming

A digital PID controller can be implemented in a software that can communicate with the required hardware. We used the software LabVIEW (National Instruments, Austin, Texas, USA). Figure 3.2 illustrates the basic flow chart for a force clamp.

There are several system parameters that need to be provided such as the sampling and feedback rates and the volts-to-nm converting factors $C$ for the actuators. Other parameters that are specific to the trapped particle and experiment, are necessary too: the trap stiffness $\kappa_i$, the displacement sensitivity $\beta_i$, the PID parameters $K_i^j$, the setpoint force $F_i$, and the offsets $QPD_i^0$ of the position detector, here a QPD. By choosing different values for $F_x$, $F_y$, and $F_z$ one can apply loads in the three-dimensional space with arbitrary angles. Once all parameters are given, the force clamp can be activated. During one cycle of the closed-loop operation, first, the process variable—here the QPD signal $QPD_i$—is read in. Whether the error is calculated in units of voltage, displacement, or force is arbitrary. In contrast to the former notation (Eq. 3.1), I chose to calculate it in displacement units of nm, because the interesting information is the displacement that the kinesin generates under a constant force. To this end, the QPD offset voltage is subtracted from the current QPD value and this difference multiplied by the respective displacement sensitivity to convert the voltage to a displacement. The force setpoint is converted to a displacement setpoint by dividing it by the trap stiffness. The difference between the displacement setpoint and the current QPD displacement reading is the error in nanometres. In addition to the current error, the cumulative error is calculated by an addition to the previous sum of errors that was passed on from the previous feedback

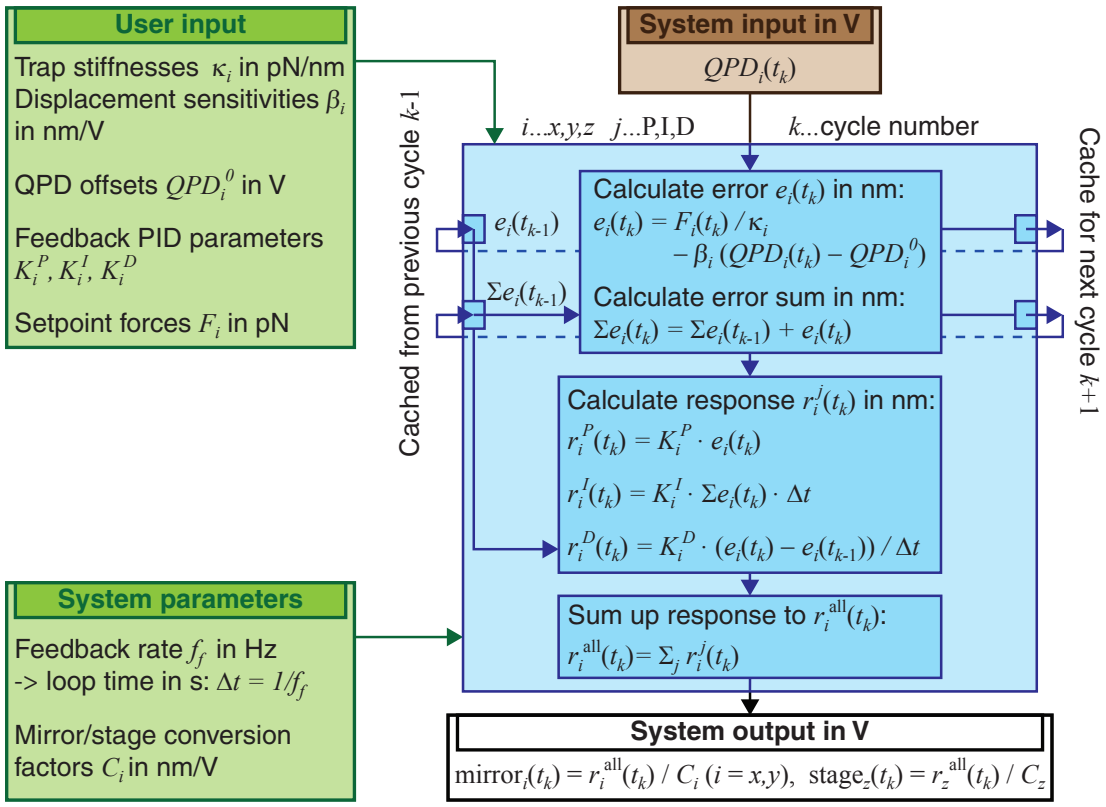


**Figure 3.2: Program flow chart for one feedback cycle.** The chart includes input parameters and calculations for a digital controller. The colour coding is the same as in Fig. 3.1. Here, a piezo-tilt mirror was used as actuator for the $x$- and $y$-direction and a quadrant photodiode (QPD) as a position detector. For the $z$-direction, a piezo stage was used. The index $i$ stands for the directions ($x$,$y$,$z$), the index $j$ for the partial response (P,I,D). Modified from [66].

cycle. Similarly, the current error is cached for the next cycle. The response of the PID controller is calculated as outlined in Section 3.1. Finally, the response is converted to a voltage which is sent as output to control the actuator, here to adjust the mirror and stage positions. The loop usually repeats until the motor protein, the kinesin, detaches, the actuator reaches its maximal range, or the user terminates the clamp. After termination, trap and/or stage automatically return to their starting position by a user-defined speed that is small enough that the drag force does not cause a loss of the trapped particle.

For the subsequent data analysis, the actual microsphere positions for all directions in nm must be known. For $x$ and $y$, where a piezo mirror is used as actuator, it is calculated by:

$$\begin{aligned} \text{microsphere position}_i &= \text{mirror position}_i - \text{displacement}_i \qquad i = x,y \\ &= C_i \cdot \text{mirror}_i^{\text{sensor}} - \beta_i \cdot (QPD_i - QPD_i^0)), \end{aligned} \tag{3.6}$$

where $\text{mirror}_i^{\text{sensor}}$ is the mirror position in volts provided by a sensor, $C_i$ the mirror's volts-to-nm conversion factor, and $QPD_i^0$ the offsets on the QPD. The displacement term should on average be a constant. When large deviations

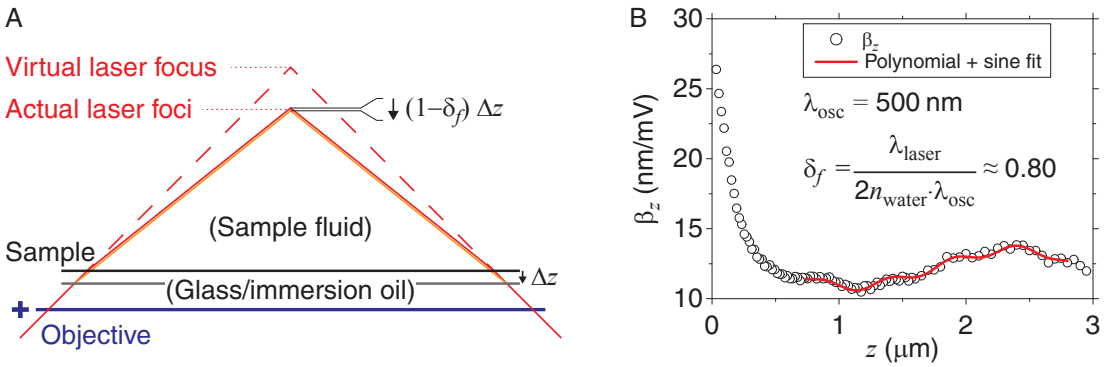


**Figure 3.3: Illustration of the focal shift.** (A) An axial displacement $\Delta z$ of the sample causes a displacement $(1 - \delta_f)\Delta z$ of the focus, resulting in relative trap–surface displacement $\delta_f \Delta z$. Drawn to scale. (B) Determination of the focal shift $\delta_f$ by measuring the height-dependent axial displacement sensitivity $\beta_z$.

occur, such as a large step, the applied force is not constant. During these times, care must be taken as motor displacements may be attenuated if length changes of the compliant motor-microsphere linkage occur. However, the microsphere position is always accurately known according to the above equation and sharp steps and transitions can be observed even for slow feedback loops. For the axial direction $z$, this calculation is very similar, though the stage position instead of the mirror position must be used. Yet, there is a crucial difference: When using oil immersion objectives as in our setup, the focal shift $\delta_f$ caused by spherical aberrations [84] needs to be accounted for. If the sample surface is moved relative to the trapping objective by an amount $\Delta z$, the microsphere centre-surface distance changes only by $\delta_f \Delta z$ as illustrated in Fig. 3.3A. The focal shift can be determined by measuring the height dependence of the axial displacement sensitivity $\beta_z(z)$ as described in [68, 85]. Between the microsphere and sample surface, a standing wave forms whose intensity is height dependent and oscillating. This dependence is visible in the $\beta_z$ data [86]. The periodicity can be used to determine $\delta_f$, when the refractive index of the sample fluid, usually that of water, and the wavelength of the used laser are known. An example is given in Fig. 3.3B. I measured $\delta_f$ with the used microspheres (590 nm diameter, polystyrene) at different laser powers and found that the focal shift of this setup was constant at $0.78 \pm 0.06$ (SEM, $N = 23$). I used a value of 0.8 for all further calculations. The axial microsphere position was calculated by

$$\begin{aligned} \text{microsphere position}_z &= \text{focal shift} \cdot \text{stage position}_z - \text{displacement}_z \\ &= \delta_f \cdot C_i \cdot \text{stage}_z^{\text{sensor}} - \beta_z \cdot (QPD_z - QPD_z^0)), \end{aligned} \tag{3.7}$$

where $\text{stage}_z^{\text{sensor}}$ is the axial stage position in volts provided by a sensor.

As the three-dimensional motion of kinesin takes place along and presumably around the microtubule, it is useful to define three coordinates to describe the motion: the $x$-position along the microtubule (with positive $x$ towards the plus end), the angular position $\phi$ on a circle with the microtubule as a centre, and the radial position $\rho$ of the microsphere centre with respect to the microtubule

centre. The $x$-position can be read out directly from the force-clamp position data (Eq. 3.6). This geometry is illustrated in Fig. 3.4. Often, the microtubule was not perfectly aligned with the setup's $x$-axis. In this case, the $x$- and $y$-position of the microsphere were rotated in a coordinate transformation such that the MT axis was aligned parallel to the new $x$-axis. If necessary, I performed the same transformation for the MT axis in the $xz$-plane.

The angle $\phi$ was determined by fitting the data in the $yz$-plane with a circle. The angle was then calculated from the centre of that circle by

$$\phi = \operatorname{atan}\left(\frac{z - z_c}{y - y_c}\right), \tag{3.8}$$

where ($y_c$,$z_c$) are the circle's centre coordinates. This calculation assumes that the microtubule is not bent. Therefore, bent microtubules were not used for experiments or analysis. Finally, the angle $\phi$ was adjusted such that positive angle changes refer to a left-handed rotation around the MT axis. The zero $\phi$-position were defined to be at the microtubule's side. For convenience, all angles are given in units of degrees (deg). The measured radius of the circle should be the sum of the microsphere radius, the MT radius, and the length of kinesin and the linker between the motor and the microsphere. Angular traces might not cover an angular range that was large enough for a reasonable circular fit. In those cases, an expected or mean value for the circle radius from successful fits were used to determine the centre position manually.

The radial position $\rho$ with respect to this centre position can be calculated according to

$$\rho = \sqrt{(z - z_c)^2 + (y - y_c)^2} \tag{3.9}$$

as given in Fig. 3.4. The mean of this position should be approximately equal to the corresponding circle radius. The position signals $\phi$ and $\rho$ from force-clamp assays which were recorded with 4 kHz where smoothed with a running median filter over 500 data points. The smoothed data was used for all further analysis.

Apart from the position calculation, there are several additional issues con-

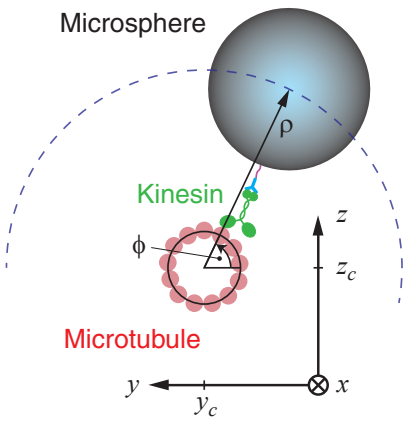


**Figure 3.4: Definition of the 3D assay's geometry.** Schematic (not to scale) of a 3D stepping assay with microsphere-coupled kinesins (green) on freely accessible microtubules (red). The angular and radial position $\phi$ and $\rho$ of the microsphere centre are calculated from the microtubule centre coordinates ($y_c$,$z_c$) that are gained from a circular fit to the curved path of the microsphere centre around the microtubule (blue dashed). Note that this definition does not account for 2D assays on immobilised microtubules.

cerning axial feedback that must be considered. Since optical tweezers are three-dimensional position and force transducers, force clamps can also be extended to three dimensions [87]. As already noted, the axial information, here the $z$-direction (Fig. 3.1), is extracted from the sum signal of the QPD after subtracting the offset voltage [63, 68]. After this subtraction, the $z$-position is linearly proportional to the power on the QPD. Since the offset for the $z$-direction is large compared to the signal, it is essential that the laser power has low power fluctuations [68]. Fluctuations of the laser intensity cause additional noise in the QPD sum signal and thus apparent displacements in $z$ that are not related to actual displacements. Our setup was equipped with a laser stabilisation system that was able to keep fluctuations of the laser intensity below 0.003 % over long times [70]. For a typical experiment, the sum signal was 126 mV with an axial displacement sensitivity of 23 nm/mV at the surface. A laser fluctuation of 0.003 % would then result in an apparent axial displacement of $\Delta z = 0.09$ nm. This value was very small and negligible. The temperature control of the setup keeps the temperature constant within 1 mK [70]. Changes in the temperature of 1 mK correspond to an axial displacement of 1 nm. Thus, the temperature stability was the limiting source of noise.

For 3D experiments close to the surface, the input parameters (trap stiffness, displacement sensitivity, and QPD offset) might depend on the microsphere-surface distance, in particular when using an oil immersion objective for trapping [68]. This dependence may have to be measured prior to and corrected for during a 3D-force-clamp experiment. This issue is discussed in Section 3.3.

### 3.2.2. Setting the Feedback Rate

For an optimal feedback performance, the choice of the feedback rate $f_f$ or the loop time $\Delta t = 1/f_f$ at which the actuator is updated is important. If the feedback rate is too low, the force clamp may be too slow to follow the motion of the motor protein, leading to a deviation from the force setpoint. If the feedback rate is too fast, the force clamp tracks the Brownian motion of the microsphere. Even though the force fluctuations are still reduced if the Brownian motion is tracked, the reduction occurs at the cost of larger positional fluctuations of the actuator [88], resulting in an overall higher noise on the experimental readout (Eqs. 3.6 and 3.7). Thus, there must be an optimal feedback rate.

The optimal rate is primarily determined by the response time of the microsphere. If the molecular motor performs a step, the drag on the microsphere prevents an instantaneous response. The response of the microsphere and, therefore, of the feedback is limited by the auto-correlation time constant $\tau_c = \gamma/\kappa = 1/(2\pi f_c)$ of the trapped and filament-tethered microsphere, where $\gamma$ is the drag coefficient of the microsphere, $f_c$ the corner frequency of the microsphere's Lorentzian-like power spectral density [67], and $\kappa$ the effective spring constant—approximately the sum of the trap stiffness and inverse linker-motor compliance [89, 90]. If the motor takes a step, the microsphere has reached $1 - 1/e \approx 63\,\%$ of its new equilibrium position after one auto-correlation time. The user needs to decide how aggressive the feedback should run. Generally, a

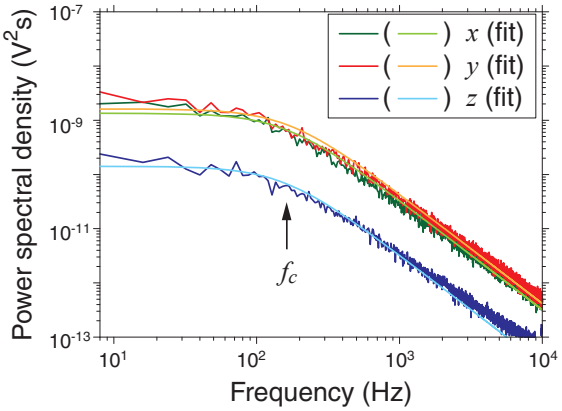


**Figure 3.5: Power spectral density of an AMPPNP-bound microsphere.** Here, a kinesin-8–decorated, 590 nm-diameter microsphere, bound to a surface-immobilised microtubule with AMPPNP was used. The trap stiffness was 0.023 pN/nm, 0.018 pN/nm and 0.006 pN/nm for $x$, $y$ and $z$, respectively. For the respective directions, the Lorentzian fits resulted in corner frequencies $f_c$ of 159 Hz, 165 Hz and 153 Hz. Modified from [66].

conservative feedback loop is operated with $\Delta t \approx 10\tau_c$, a moderate with $\Delta t \approx \tau_c$, and an aggressive one with $\Delta t \approx 0.1\tau_c$ [91]. For single-molecule assays, feedback is usually desired to track the molecules as fast as possible with the lowest amount of noise. For lowest-noise performance, the feedback should be operated with a rate about equal to the corner frequency $f_f \approx f_c$ [88] which is between moderate and conservative feedback tuning. For the kinesin-microsphere linkage used here, microsphere size, and trap stiffness (details on the assay and microsphere preparation are given in Chapters 4 and 5), I measured the corner frequency $f_c$ by analysing the PSD of the position of a trapped kinesin-coated microsphere that was bound to a microtubule using AMPPNP as described before [92]. Figure 3.5 shows a representative measurement. The PSDs were fitted with Lorentzian functions to extract the corner frequencies, here around 160 Hz. The corresponding auto-correlation time was 1 ms and the corresponding feedback rate $f_f$ was 1 kHz. This rate was about six-fold higher than the corner frequency and thus represented rather aggressive running. However, using this tuning enabled the force clamp to also follow faster motion. Hence, I performed all force-clamp experiments with a feedback rate of 1 kHz. The sampling rate of the used setup was 4 kHz. After the optimal feedback rate is determined, one can proceed with the tuning of the PID parameters.

### 3.2.3. PID Parameter Tuning

There are many ways to tune and choose PID parameters and the best choice usually depends on the application. For most single-molecule assays, a fast response is often desired. However, a fast response typically implies a larger overshoot and less stability against disturbances or nonlinearities that may be caused by changes in the setpoint. Initial tuning and testing of the force clamp can be done by tracking the motion of surface-immobilised microspheres. Fine tuning should be done under conditions that mimic the experiment by using, for example, kinesin-coated microspheres that were immobilised to the microtubule. The linker that connects the motor to the microsphere adds compliance to the system and increases the overall response time. The motion of the bound kinesin can then be mimicked by computer-controlled movements of the sample

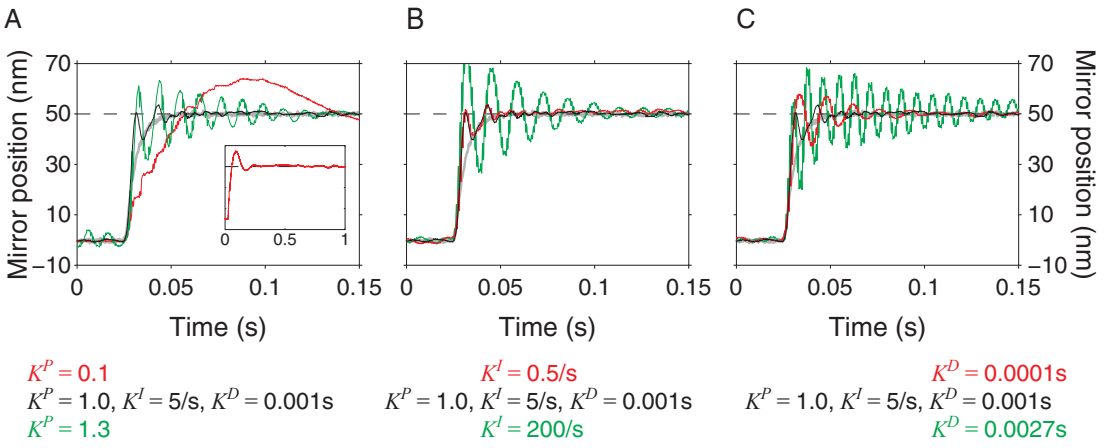


**Figure 3.6: Tuning of PID parameters.** The feedback response to 50 nm steps of a 590 nm-diameter microspheres is plotted for different PID parameters. The steps (grey lines) with a rise time of 15 ms (time between 10–90 % of the step amplitude) were generated by the sample stage. Relative to the optimal parameters (response in black), parameters were decreased (red lines) or increased (green lines). Parameter values are indicated below the graphs. (A) $K^P$, (B) $K^I$, and (C) $K^D$. The optimal parameters are depicted in black. Inset in (A): Response for a too small $K^P$ value on a longer time scale.

using, for example, a piezo-translation stage with nanometre precision. If such a stage is unavailable or used as actuator, the feedback loop can be tested by stepwise changes of the setpoint. The latter case applied for the axial feedback in our setup.

For the tuning of the PID loop, I used the Ziegler-Nichols tuning method [93] which is a heuristic method and one of the most frequently used methods of tuning PID controllers, supplemented by trial-and-error fine-tuning. Because the response times of optical tweezers force-clamps are typically on the millisecond time scale, this fine-tuning is a fast way to achieve the desired feedback behaviour. In the Ziegler-Nichols method, the parameters $K^I$ and $K^D$ are set to zero and $K^P$ is increased until a critical value $K_c$ is reached for which the system maintains an oscillation with a constant amplitude after a step response. Subsequently, optimal PID parameter values are calculated from the critical proportional gain and the period of the oscillation. In the literature, different improvements and expansions of the Ziegler-Nichols method can be found [80, 94]. For systems that have relatively large dead times, i.e. the time a control system needs to react on changes in the process variable, other methods like the Cohen-Coon method [91, 95] are in use.

In an initial approach [66, 92], polystyrene microspheres with a diameter of 590 nm were immobilised unspecifically to the surface in a high-molarity buffer (100 mM KCl). Before immobilisation, the calibration factors and offsets were measured using the optical trap. Lateral steps of 50 nm were applied by moving the sample stage. The PID parameters were tuned to resolve this stepwise motion of the microsphere following the Ziegler-Nichols method. Figure 3.6 illustrates the effect of fine-tuning the parameters. When the proportional

gain $K^P$ was too high, the system oscillated. When the value was too small, the response was very slow (Fig. 3.6A). The oscillation period was comparable to the oscillation period with the critical gain. For the data shown, the critical gain was $K_c \approx 1.5$ with an oscillation period of $t_c \approx 0.01\,\mathrm{s}$. With these values, the optimal parameters according to the Ziegler-Nichols method were: $K^P \approx 1$, $K^I \approx 150\,\mathrm{s}^{-1}$, and $K^D \approx 0.001\,\mathrm{s}$. The integral control eliminated the steady-state error. The optimal $K^I$ value according to the Ziegler-Nichols method caused an overshoot (Fig. 3.6B). Because the feedback performance was stable over a broad range of $K^I$ values with only a small compromise with respect to the response time, I typically reduced the integral gain significantly until the overshoot disappears. As pointed out in Section 3.1.1, the derivative gain reduces an oscillatory response (Fig. 3.6C). If the derivative gain was too high, noise and oscillations were amplified.

The choice of the optimal parameters depended on the experiment. Like the optimal feedback rate, the PID parameters depend on the linkage between microsphere and motor and its compliance. A stiffer linkage facilitates the motion between microsphere and motor faster, i.e. the response time is smaller. Such a system requires a faster response of the feedback system with different PID parameters. Thus, the found PID values for surface-immobilised microspheres were not optimal for microspheres that were bound to microtubules by a motor. Nevertheless, the general step response resembles the one for surface-immobilised microspheres if parameters were to small or large.

To adjust the force clamp for motor experiments, the PID parameters were tuned using kinesin-coated microspheres. The microspheres were bound to microtubules with AMPPNP as noted above and the force clamp was tuned as described in [66, 92]. The expected motion of the kinesin was simulated by moving the sample stage laterally in steps of 8 nm with a stepping rate of 5 Hz which corresponds to Kip3's step size and velocity [19, 40]. The values for $K^I$ and $K^D$ were set to zero and gradually $K^P$ increased until the system became unstable. While increasing $K^P$, the overdamped response to the step first became faster. Then, an overshoot developed until the response eventually started to oscillate. The corresponding $K^P$ value is called the critical gain $K_c$. The oscillation period for $K^P = K_c$ was determined and the optimal parameters according to the Ziegler-Nichols method were calculated. However, all parameter were finally adjusted for the actual requirements of the system:

For example, in some experiments, alternating sideward loads were applied on walking kinesins. To change the direction of a sideward load, the load needs to be changed quickly over a large distance compared to the molecular stepping distance. The large movement was necessary because the microsphere and the linker between it and the kinesin act as a lever amplifying the motion. Large sudden changes in the setpoint require different PID parameters compared to a concatenation of small steps. For a fast response, a higher proportional gain is necessary. Thus, the proportional gain was increased from 0.1 to 0.3 while still avoiding oscillations as shown in Fig. 3.7. The increased proportional gain resulted in small overshoots to responses on small steps. Nevertheless, the steps were still resolvable. The optimal $K^I$ value caused an overshoot. Because

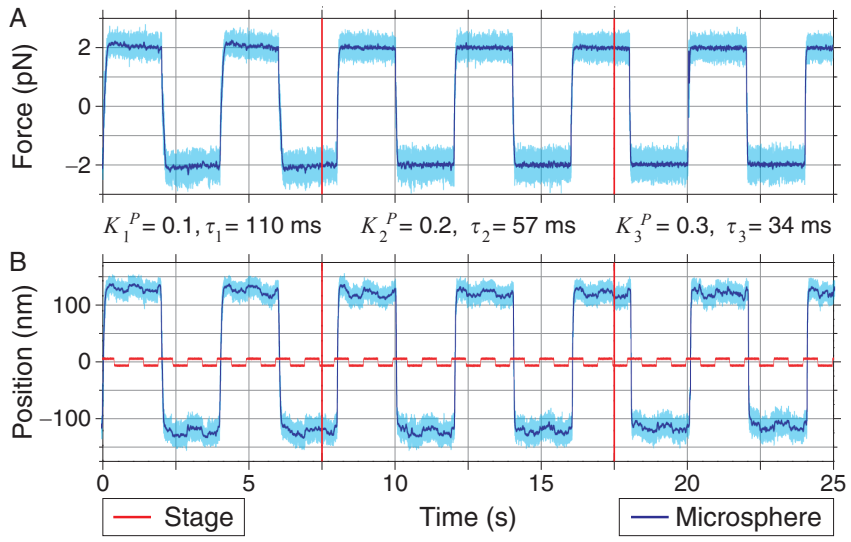


**Figure 3.7: Alternating sideward load tuning experiment mimicking experimental conditions.** (A) Force and (B) position versus time of a kinesin-bound microsphere in the presence of AMPPNP. A square wave of 10 nm amplitude and 1 Hz was applied to the stage. The sideward load of ±2 pN switched the direction every 2 s. The proportional gain $K^P$ was increased at 7.5 s and 17.5 s. Its value and the rise time $\tau$ (time for 10–90 % rise) are given. $K^I = 0.1\,\mathrm{s}^{-1}$ and $K^D = 0$. Modified from [66, 92].

the feedback performance was stable over a broad range of $K^I$ values with only a small compromise with respect to the response time, I reduced the integral gain significantly until the overshoot disappeared. For the described system, I found that any non-zero value for the derivative part $K^D$ only increased the noise or even destabilised the feedback. Thus, $K^D$ was consequently put to zero. All axes of the force clamp were tuned separately.

The values for the integral and derivative gain depend on the feedback rate. Thus, if, for example, a different microsphere size was used or a different amount of tension was applied such that the corner frequency and optimal feedback rate changed, $K^I$ and $K^D$ were adapted. In the discrete calculation of Fig. 3.2, the integral and derivative gain are proportional and inverse proportional, respectively, to the loop time $\Delta t$. If $K_1^I$ and $K_1^D$ were optimised for the feedback rate $f_{f,1}$ as described in Section 3.2.2, new values $K_2^I$ and $K_2^D$ can be calculated for a new rate $f_{f,2}$ according to

$$K_2^I = K_1^I \frac{f_{f,2}}{f_{f,1}} \qquad \text{and} \qquad K_2^D = K_1^D \frac{f_{f,1}}{f_{f,2}}. \tag{3.10}$$

For example, if the feedback rate is increased two-fold, the parameters $K^I$ and $K^D$ should be increased and decreased two-fold, respectively, to have a well tuned force clamp.

I found that steps applied with the stage were only resolved clearly with non-zero loads on the microsphere. For a better resolution, the applied force can be increased to decrease the compliance, i.e. increase the stiffness, of the linker. The

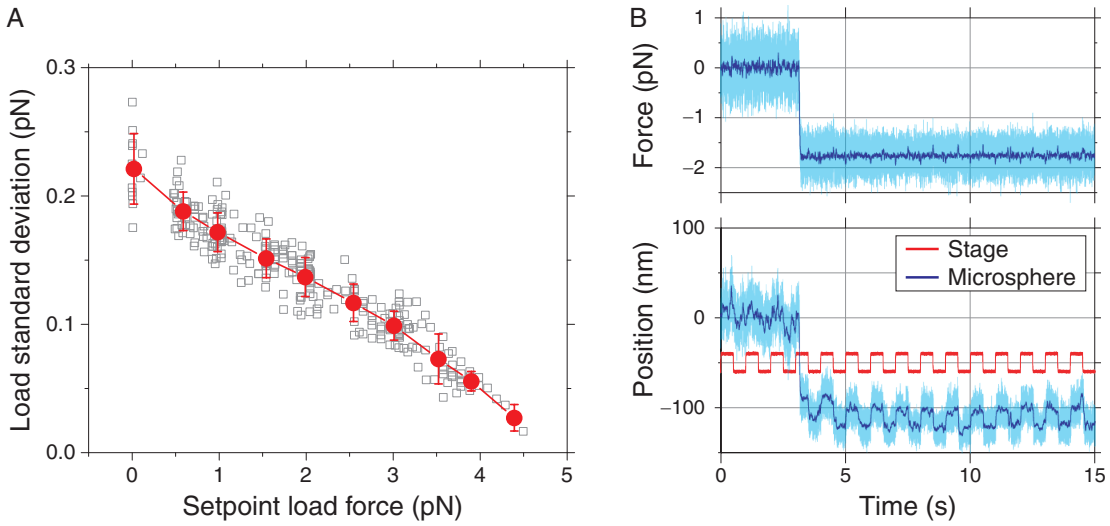


**Figure 3.8: Spatial resolution improvement with loads.** (A) Standard deviation of the applied load (□) as a function of the force setpoint with binned data (●). Data were obtained by applying constant loads on kinesin-bound microspheres ($N = 277$ from 34 data sets, trap stiffness was 0.02–0.03 pN/nm) in the presence of ATP. The line connecting the binned data is a guide to the eye. Error bars are standard deviations. (B) Force and position of a kinesin-bound microsphere as a function of time. A square wave of 20 nm amplitude and 1 Hz was applied to the stage. Steps could only be resolved with an applied load, here about 1.85 pN (light-blue: 4 kHz, dark-blue: median-filtered to 8 Hz, red: steps of the stage (the signal was offset for clarity), $\kappa = 0.024$ pN/nm). Data were acquired in the presence of AMPPNP. Modified from [66].

compliant linker between the microtubule-bound kinesin motor heads and the microsphere increases the auto-correlation time and, thus, the response time of the trapped microsphere. Therefore, compliance reduces the overall feedback rate. However, since the linker is an entropic spring, the compliance decreases with load which in turn reduces the response time and fluctuations both on force and position. Thus, the resolution of the force clamp improves with load. This behaviour is demonstrated in Fig. 3.8. As the setpoint force was increased, the fluctuations of the force setpoint decreased (Fig. 3.8A). With loads up to 4.5 pN, the standard deviation of the fluctuations was reduced by more than 10-fold compared to the zero-force value. The reduction in the force fluctuations is correlated with a reduction in positional fluctuations such that steps—invisible at low force—are resolved at a higher force (Fig. 3.8B). The higher positional resolution is due to the increased linker stiffness.

The above described protocol only accounts for a 2D force clamp. Tuning the axial feedback in the $z$-direction requires a different method, because the setup was not equipped with hardware to move an immobilised microsphere and the laser independently in the axial direction. Also, no loads were applied in the 3D force-clamp experiments which required different PID parameters compared to the 2D experiments with alternating loads. Thus, for 3D force clamping, the axial feedback was tuned by adjusting the PID parameters to sudden manual changes in the setpoint $F_z$, following a simplified Ziegler-Nichols

**Table 3.1: PID parameters of the force clamp.** Respective values for $K^P$, $K^I$, and $K^D$ for 2D and 3D-force-clamp experiments are given. Both experimental approaches used different program.

| Force-clamp mode | direction | $K^P$ | $K^I$ ($s^{-1}$) | $K^D$ (s) |
|---|---|---|---|---|
| 2D | $x$,$y$ | 0.25 | 0.1 | 0 |
| 3D | $x$,$y$ | 1 | 667 | 0 |
| | $z$ | 0.09 | 667 | 0 |

method, where I set good values for $K^P$, $K^I$, and $K^D$ manually.

The final PID parameter values are given in Table 3.1. Note that—besides the different requirements and approaches—for each the 2D and 3D-force-clamp experiments, two different LabVIEW feedback programs were used. The program for the 3D force clamp was a newer version, performing faster and more efficiently. Therefore, the optimal PID parameters differed a lot. For both programs, there was a broad range of stable feedback performance for the parameter $K^I$ as shown in Fig. 3.6 and [66].

## 3.3. Testing of Optical Tweezers Force-Clamping and Tracking

To test the feedback performance, the 2D force clamp was finally tested by simulating the Kip3 stepping motion. Figure 3.9 shows an example, in which the force clamp followed simulated steps of 8 nm and a random direction at a stepping rate of 5 Hz as described in [66, 92]. The steps could be resolved under a load of 1.1 pN using an unbiased step detector [96]. The average detected step size was 8.2 ± 0.3 nm (SEM, $N = 47$). The standard deviation (SD) of the applied load was 0.1 pN, providing sub-piconewton resolution for applied loads. The $K^P$ value was increased to the value in Tab. 3.1, providing faster transitions between alternating loads [66, 92].

The 3D feedback was tested without any loads, as this is not intended in the experiments. Also, any off-axis load, i.e. a load that is not parallel to the MT axis, would require the feedback to account for the cylindrical geometry of the motion. Similar to the 2D experiment, a kinesin-coated microsphere was immobilised on a microtubule. Here, AMPPNP was not used to bind kinesin-coated microspheres to the microtubules. Instead, I used phases of kinesin pausing between phases of motility in the presence of ATP. The microtubule itself was not immobilised on a plane surface but suspended on a topographic structure that enabled complete access of the microsphere to the microtubule. Appropriate structures are described in Chapter 6. Figure 3.10 illustrates the spatial and force resolution of a 3D force clamp with zero-loads. The 3D trajectory of the microsphere centre resulting from the Brownian motion was curved around the MT axis consistent with similar measurements by Jeney et al. in a static trap [97]. The average root mean squared (rms) noise of 12 such measurements in $x$, $y$, and $z$ were 13 nm, 18 nm, and 18 nm, respectively, too high to resolve any forward steps of 8 nm (Fig. 3.10A). These values were similar to the

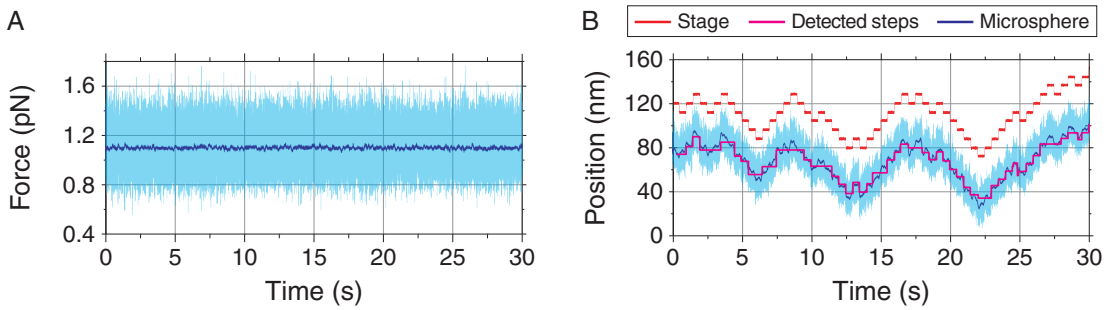


**Figure 3.9: Force-clamp test experiment mimicking experimental conditions.** The force clamp successfully followed a microsphere—anchored to a surface-bound microtubule via a kinesin motor in the presence of AMPPNP—that was moved in 8 nm steps in a random direction by the sample stage with a stepping rate of 5 Hz. (A) Force as a function of time (light-blue: 4 kHz, filtered by a running median filter to 8 Hz). The setpoint was 1.1 pN. (B) Applied motion of the stage (red, top trace) and actuator response of the mirror added to the positional signal from the QPD (Eq. 3.6, blue, bottom trace) overlayed with the detected steps (magenta line). The traces are depicted with an offset for clarity and displayed with a 4 kHz and 8 Hz bandwidth. PID values were $K^P = 0.1, K^I = 0.1\,\mathrm{s}^{-1}$, and $K^D = 0$. Modified from [92].

corresponding rms noise $\sigma_{rms} = \sqrt{k_\mathrm{B}T/\kappa}$ of an unbound microsphere in a static trap. The experimental values describe the measurement precision and *not* the localisation precision. In the here described test measurement, the microsphere swivelled freely around the microtubule. This motion was tracked by the force clamp whose localisation precision of a few nanometres or even less was much better as shown in [66, 70, 92]. However, this tethered Brownian motion of the microsphere was not related to kinesin-initiated motion and limited the spatial resolution which is called measurement precision.

In 3D assays, we planned to resolve angular steps between neighbouring protofilaments. The angular step size $\Delta\phi_\mathrm{pf}$ equals the full circle angle divided by the number of protofilaments in the microtubule, i.e. $360\,\mathrm{deg}/13 \approx 28\,\mathrm{deg}$. The average rms noise of the angle $\phi$ was 3.4 deg (Fig. 3.10B). With this resolution, angular steps of $\Delta\phi_\mathrm{pf}$ that correspond to protofilaments switching could be resolved with a signal-to-noise ratio of ≈9, well above the Rose criterion of 5 for visibility of steps [98]. The average rms noise of the radial position $\rho$ was 16 nm. The average rms noise of the forces were about 0.27 pN ($x$, $y$) and 0.13 pN ($z$, Fig. 3.10C) providing sub-piconewton resolution even for zero-loads. The values for the $x$- and $y$-direction were consistent with those in Fig. 3.8A.

During the feedback operation, mirror and/or stage positions were changed over a range of several micrometres. It is important to ensure that parameters like the calibration factors do not change significantly over that range. Consequently, I measured the displacement sensitivity $\beta$ and trap stiffness $\kappa$ for varying (i) lateral and (ii) axial trap positions. The former was varied by steering the laser focus with the piezo mirror, the latter one by moving the sample with the piezo stage. This control measurement was done in a sample with topographic structures around a height $z$, where the 3D experiments have been performed. The dependence on the lateral trap position was relevant for both

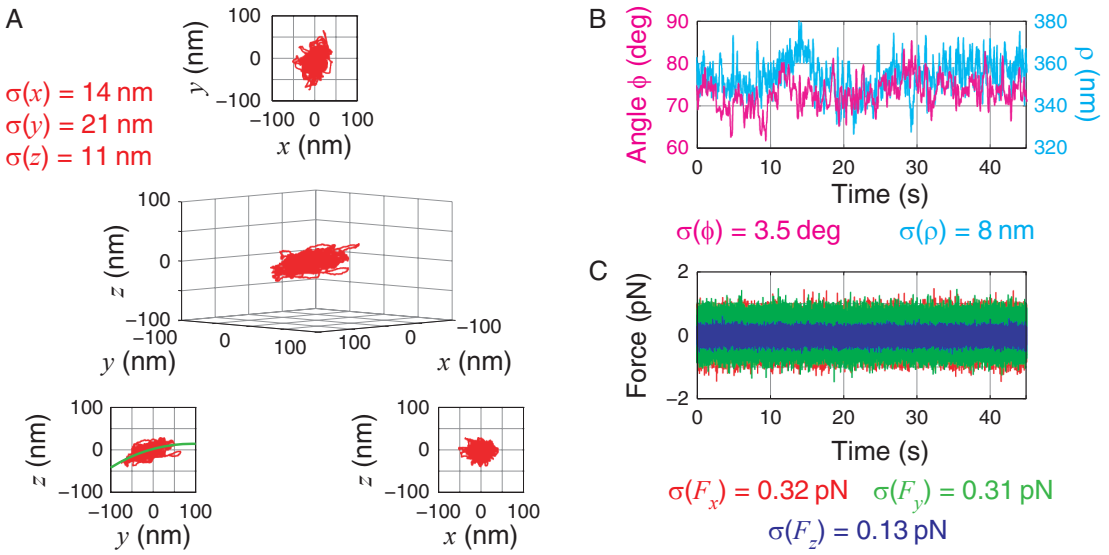


**Figure 3.10: Spatial resolution of a 3D kinesin assay with optical tweezers.** (A) Three-dimensional plot of $x$,$y$, and $z$-position, with $xy$, $yz$, and $xz$-projections of a kinesin-bound 590 nm polystyrene microsphere that was pausing on a microtubule. Standard deviations $\sigma(x,y,z)$ are given. The sampling rate was 4 kHz, median-filtered down to 8 Hz, the feedback rate 1 kHz. The data in the $yz$-projection were fitted with a circle (green line) to extract the angular position $\phi$. (B) Angle (left axis) and radial position (right axis) $\phi$ and $\rho$ as function of time with given standard deviation $\sigma(\phi)$ and $\sigma(\rho)$, respectively. (C) Force as a function of time (not filtered) with given standard deviations $\sigma(F_i)$. The trap stiffnesses were: $\kappa_x = \kappa_y = 0.036$ pN/nm, $\kappa_z = 0.006$ pN/nm.

2D and 3D assays, whereas the dependence on the axial trap position was relevant for 3D assays, only.

The dependence of the calibration factors on the lateral trap position is shown in Fig. 3.11. Interestingly, the displacement sensitivity and trap stiffness in the lateral directions $x$ and $y$ had a minimum and maximum approximately at the non-steered zero position, respectively. The extrema were determined by parabolic fits. For the $z$-direction, the extremum of $\beta_z$ deviated from the zero position. These extrema could be used to align the piezo mirrors with high precision. The corresponding relative deviations in units of %/µm are given in Fig. 3.11. They were calculated as deviations of the boundary values from the extremal values at the zero position. The absolute values were $\lesssim$1 %/µm. Thus, even if the laser focus was moved over a range of 5 µm, the overall deviations were $\lesssim$5 %.

The dependence of the calibration factors on the axial trap position is shown in Fig. 3.12. As expected and already described by Schäffer et al. [68], the calibration factors depend sensitively on the height of the microsphere above the surface, especially very close to the surface. However, the 3D experiments were performed further away from the surface. The relevant range was about 700 nm, two-fold the expected radius of the microsphere position around the microtubule. The MT height was defined as the zero position. Here, it was 1.5 µm above the surface. The relative deviations were calculated from linear

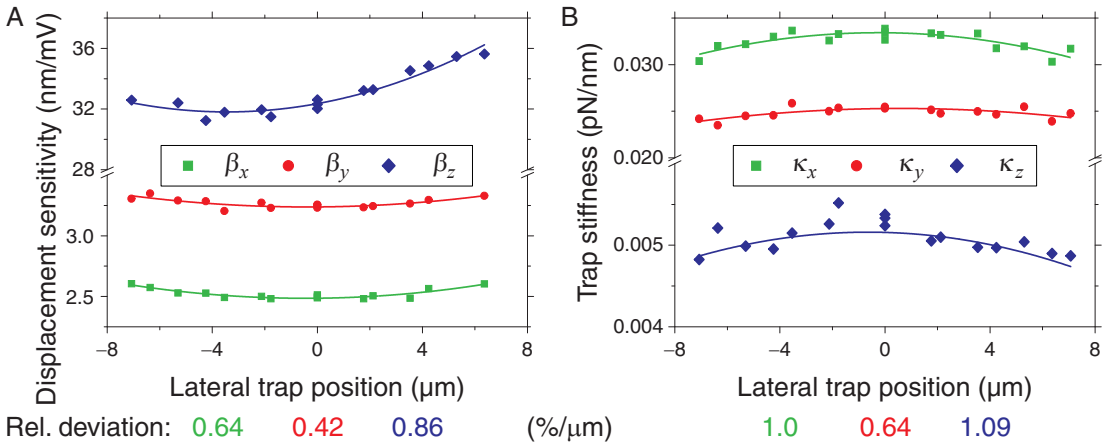


**Figure 3.11: Dependence of the calibration factors on the lateral trap position.** (A) Displacement sensitivity and (B) trap stiffness for a 590 nm polystyrene microsphere as a function of the lateral trap position for the $x$ (■), $y$ (●), and $z$ (◆) direction. The lateral trap position was controlled by changing the beam steering angle using a tilt mirror. The solid lines are parabolic fits. The relative deviations for $x, y$, and $z$ (based on the fits) in percent per μm in absolute values are given below the graphs.

fits as explained before. The variation of parameters was larger than for the lateral trap positions. For the lateral directions, the deviations were $\lesssim$4 %/μm and for the axial direction $\lesssim$13 %/μm. I did not correct for this variation.

Another parameter that depended on the lateral and axial trap position was the QPD offset $QPD_i^0$. Measurements of the position dependence were hard to reproduce, especially with respect to the QPD alignment. The reason was that a well aligned QPD should have lateral offsets of close to zero. Deviations from zero would produce large relative deviations explaining the irreproducibility. I measured relative deviations of the QPD offsets of $\lesssim$6 %/μm for the lateral trap position dependence and relative deviation of <1 %/μm for the axial trap position. These values were small enough that I did not correct for their variation.

An important limitation of an optical tweezers force-clamp is the linear range of the optical trap for which the basic calculations of displacement and force are valid. The limitation of the displacement calculation $\Delta x = \beta \cdot \Delta U$ arises from the limited linear detection range of the QPD, i.e. for higher displacements from the trap centre, the detected voltage signal deviates from a linear response. The limitation of the force calculation $F = \kappa \cdot \Delta x$ comes from the fundamental non-harmonic nature of an optical trap [99] that also starts to affect large displacements. The linear range for the optical trap is usually larger compared to the one of the position sensor [100]. Thus, the linear range of the QPD detection is the limiting factor. For the lateral directions, the linear range was symmetric relative to the focus centre. This was not the case for the axial direction because the equilibrium position of the microsphere was shifted vertically relative to the laser focus by the scattering force. Thus, maximum upward and downward loads differed. To calculate upper and lower boundaries correctly, the equilibrium height inside the trap must be determined. Moving a trapped

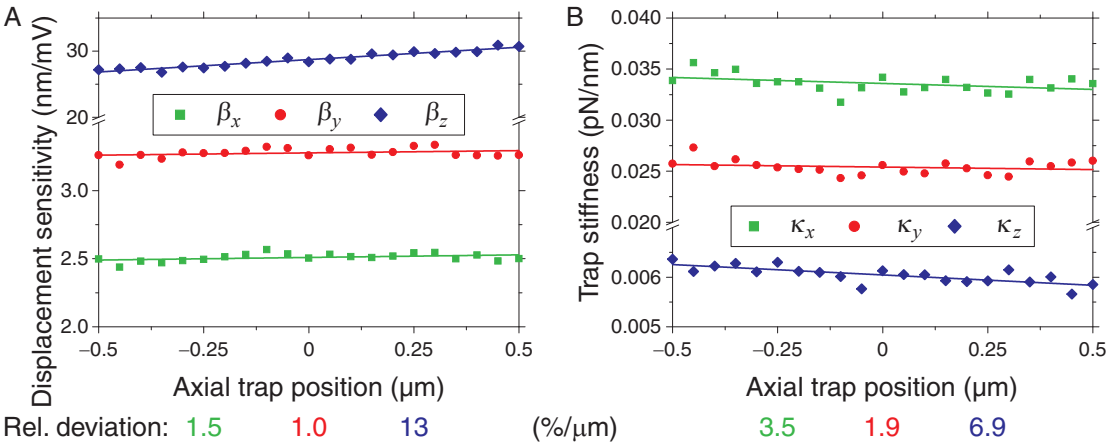


**Figure 3.12: Dependence of the calibration factors on the axial trap position.** (A) Displacement sensitivity and (B) trap stiffness for a 590 nm polystyrene microsphere as a function of the axial trap position for the $x$ (■), $y$ (●) and $z$ (◆) direction. The axial trap position was controlled by changing the sample height using a piezo stage. The solid lines are linear fits. The relative deviations for $x, y$, and $z$ (based on the fits) in percent per µm in absolute values are given below the graphs.

microsphere towards the sample surface using the piezo stage resulted in an immobilised microsphere if repulsive electrostatic interactions were screened using a high salt concentration buffer, here 100 mM KCl. From the QPD sum signal, one can read off the contact position of the microsphere with the surface. The linear range was estimated by a linear fit to the QPD signal versus the stage position. The range for which the QPD signal changed proportional to the stage position was the linear range; the inverse of the proportionality factor was the displacement sensitivity. I defined that range linear, in which the fitted data deviated less than 5 % from the linear fit. The linear range of the lateral directions was measured similarly by laterally scanning through the immobilised microsphere. Figure 3.13A shows the lateral QPD signal as a function of the stage position. The QPD signal changed proportional with the position for a relatively small range of about 150 nm, corresponding to a maximum force of ≈7 pN. The displacement sensitivity 1.83 nm/mV that corresponds to the inverse slope of the linear fit agreed well with the one from a calibration of 1.73 nm/mV. The overall change in the QPD signal was symmetric. The axial scanning with a free and then immobilised microsphere revealed that the equilibrium position of the microsphere inside the optical trap was significantly shifted to a higher value. The measured contact point was much closer to the lower boundary of the estimated linear range than to the upper one. Thus, the range of applicable upward loads was higher than for downward loads. Here, I measured an upward range of 480 nm (corresponding to a force of ≈3 pN) and a downward range of 70 nm (≈0.4 pN). The asymmetry in the linear range also affects the maximal force, the clamp can apply to the microsphere. Therefore, I measured maximal achievable upward loads of 3–4 pN and downward loads of <1 pN. Beyond these values, the force clamp failed. The forces could be increased by choosing a higher trap stiffness. Still, the asymmetry remained. This axial

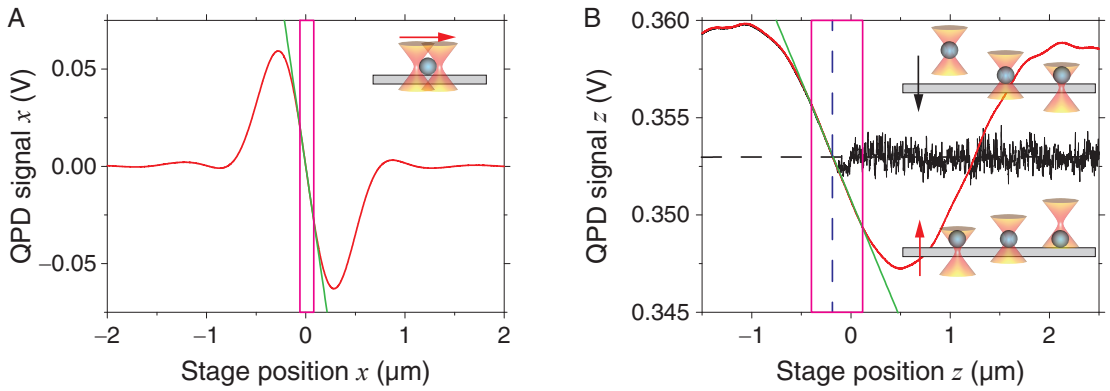


**Figure 3.13: Linear range of the optical trap.** (A) The ranges for the lateral directions, here $x$, were determined by scanning with the laser focus through an immobilised microsphere (polystyrene, 590 nm diameter) and detecting the QPD signal (red line) in $x$. The estimated linear range was fitted (green line) and indicated by a purple box. The trap stiffness was 0.048 pN/nm. (B) The range for the axial direction $z$ was determined by trapping a microsphere and bringing it closer to the surface until it was immobilised. The QPD sum signal is plotted as red line. Afterwards, the focus was scanned through the immobilised microsphere (black line). The estimated linear range was fitted (green line) and indicated by a purple box. The estimated contact point of the microsphere with the surface (vertical blue dashed line) was where red and black QPD signal split up and could be calculated as a crossing point of the linear fit line and a linear fit to the QPD signal prior to sticking (thick red line). The trap stiffness was 0.006 pN/nm.

asymmetry must be considered, when axial loads are applied to microspheres.

## 3.4. Three-Dimensional Video Tracking of Microspheres

In my project, I wanted to observe the three-dimensional motion of kinesin motors. In respective motility assays, kinesin-coated microspheres moved in all three dimensions and must be tracked to analyse this motion. In the optical tweezers assay, I obtained the trajectory using the 3D force clamp. As a control, I used 3D video tracking with the trap turned off. There exist many routines to track the lateral motion of objects in videos, e.g. different plugins for ImageJ (MTrack2, Manual Tracking, Mosaic Particle Tracker). Also, different methods exist to optically track the axial position of microspheres [101, 102]. Here, I developed a simple method to determine the axial position of a microsphere using defocussing microscopy. When a microsphere moves in the axial direction, i.e. above or below the focal plane of the microscope, its image defocuses and the intensity distribution of the image changes. These changes can be used to determine the axial displacement as it was done by Can et al. [103]. As a test, I used microspheres (590 nm, polystyrene) that were immobilised on the surface and recorded an image sequence of them while the sample stage was moving up and down with a constant speed (Fig. 3.14A). I used a triangular

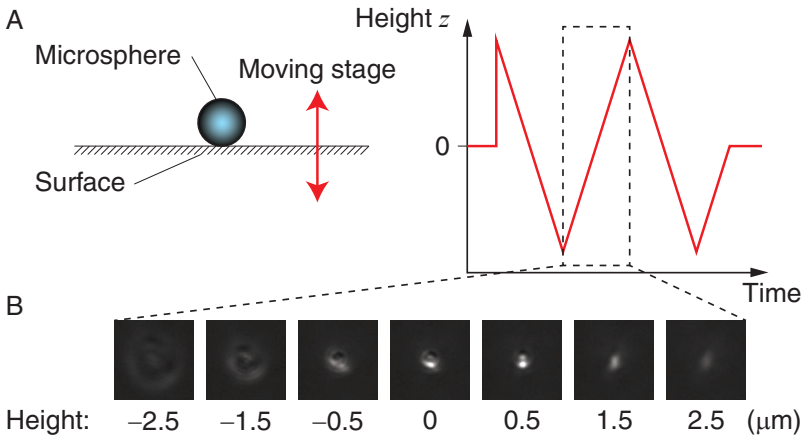


**Figure 3.14: Axial scanning through an immobilised microsphere to analyse its height-dependent images.** (A) The axial tracking is calibrated by scanning vertically through an immobilised microsphere of 590 nm size, using the sample stage. The height $z = 0$ is defined as height, where microsphere and surface are focused. For negative heights, the sample is below the focal plane of the microscope. (B) Different images of a microsphere as a function of height. The size of the region of interest was 95 pixels, the pixel size was 44.6 nm.

wave with an amplitude (peak-to-peak) of 5 µm, a frequency of 0.1 Hz, and an imaging rate of 13 frames per second. The zero height position was defined as height for which the microsphere and surface were in focus. I analysed an area of 95×95 pixel$^2$ around the microsphere centre. Exemplary images are shown in Fig. 3.14B. Images of the microspheres were recorded with the setup's camera. I analysed the images in ImageJ and found that the mean intensity depended on the sample height as shown in Fig. 3.15A. This dependence was not monotonous. The mean intensity had a maximum. Still, there was a certain, asymmetric linear range around the zero height. This range could be fitted with a linear function and the slope and intercept used to calculate the position from the mean intensity. I found that the linear range depended on the used area of the region of interest: For smaller areas, the maximum was shifted to higher $z$ values, decreasing the linear range. However, a smaller area also resulted in higher mean intensities and larger gradients. Thus, the contrast was better for smaller areas. I chose a compromise that provides a large enough range as well as a good sensitivity.

The calibration procedure was improved by a background subtraction, e.g. when other objects, e.g. dirt on the surface, appeared in the region of interest and compromised the intensity measurement. The height-dependent mean intensity of the background was subtracted from the mean intensity of the microsphere to get a corrected intensity signal (Fig. 3.15A). I tested this axial tracking after a calibration by applying an axial square wave with amplitude sizes of 20, 50, 100, and 200 nm. Figure 3.15B shows an example with an amplitude of 200 nm. The background subtraction resulted in more noise on the height signal but was crucial to obtain the correct step size. The smallest step size that could be resolved was 100 nm. Thus, the resolution of video tracking

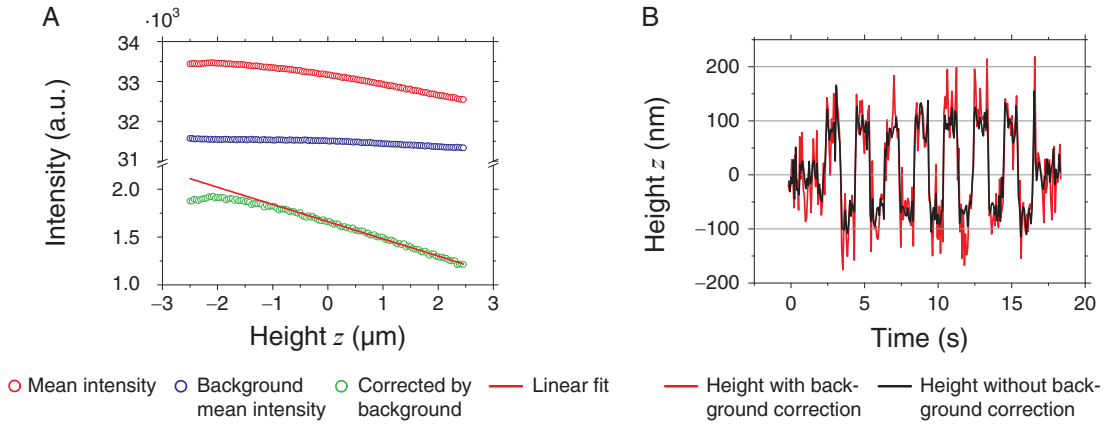


**Figure 3.15: Axial calibration by analysing the height-dependent intensity.** (A) Mean intensity in a region of interest around an immobilised microsphere (red circles) and mean intensity without the microsphere (background, blue circles) for different heights. The background intensity was subtracted from the microsphere intensity (green circles) to get a calibration (linear fit, red line). The size of the region of interest was 70 pixels. (B) Calculated height of the same microsphere that was moved axially by a 200 nm square wave by a calibration with (red line) and without (black line) background subtraction.

was much worse compared to optical tweezers.

Tracking of actual motile microspheres was performed by image analysis in ImageJ. A self-written algorithm used the lateral position data that was obtained by the Mosaic Particle Tracker [104] to draw a square with user-defined size around it. The mean intensity in this square, the region of interest, was than measured for every frame. The same measurement was performed on the surface without the microsphere as a background measurement. The mean intensity data of the motility measurement and background were then analysed further as described. The used frame rate was 5.2 frames per second.

# 4. Kinesin Assay

In this chapter, the details of the kinesin stepping assay, microtubule and sample preparation are given. The original Kip3 optical tweezers assay was developed by Volker Bormuth [49]. The Kip3 TIRF stepping assay based on standard protocols by Varga et al. [19]. Both protocols are reliable and provide reproducible results. The protocols could be easily adapted to other kinesins like kinesin-1.

## 4.1. Purification of Kinesins

The motor proteins budding yeast Kip3 ($his_6$-Kip3-eGFP) and rat kinesin-1 ($his_6$-rkin430-eGFP, abbreviated as rkin430) were expressed and purified according to a standard protocol described in [40, 105]. Briefly, after two intermediate purification steps, including a cation and a buffer exchange, the his-tagged protein was specifically bound to a nickel column and eluted with a high-molarity imidazole buffer. Both constructs had the his tag at the N-terminus of the protein chain, i.e. the motor domain, and the eGFP tag at the C-terminus, i.e. the tail domain. The kinesin-1 rkin430 is a truncated construct with only the first 430 amino acids of the wild type plus the tags. Protein concentrations were measured in Bradford assays. The yield of the Kip3 purification, performed by Aniruddha Mitra, Frederic Schiemann, and me in the lab of Stefan Diez, MPI-CBG, Dresden, Germany, was tested with a SDS-PAGE gel showing high purity (Fig. 4.1). This Kip3 construct was used for 2D Kip3 optical tweezers assays and TIRF assays.

For the 3D optical tweezers assays, I used different Kip3 constructs. In the first 3D assays, I used Kip3 with his tag and an additional SNAP tag at the tail (Kip3-eGFP-$his_6$-SNAP, denoted as Kip3-S). SNAP is a multifunctional tag that can be used to bind tagged proteins to various targets [106]. I did not use this

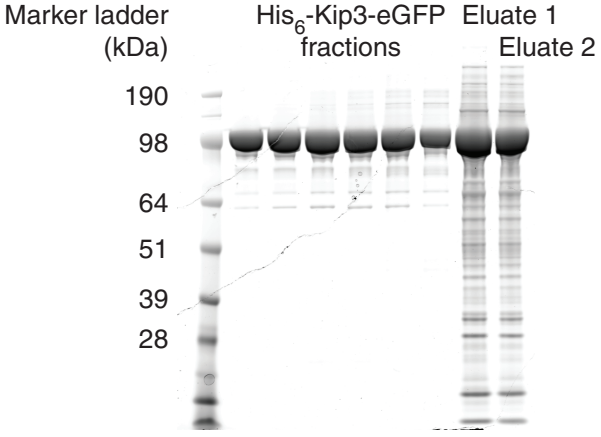


**Figure 4.1: Purification of $his_6$-Kip3-eGFP.** SDS-PAGE gel of a marker ladder with known molecular weights in kDa (left), different final Kip3 fractions (middle), and two different intermediate elution steps (right, eluate 1: after cation exchange, eluate 2: after buffer exchange).

tag in my assays. To avoid potential non-specific interactions of the his tag with the microtubules as shown for the microtubule-associated protein EB1 [107], I subsequently used a Kip3 construct with the his tag at the tail (Kip3-eGFP-$his_6$, denoted as Kip3-H). These three constructs have been tested in standard TIRF and optical tweezers stepping assays with respect to velocity, stall force and MT depolymerisation. The results did not depend on the constructs. Previous studies also found no differences in the motility of Kip3 with respect to the location of the his tag [40]. Also, in my experiments I observed no qualitative nor quantitative difference between both constructs used for 3D assays. Thus, 3D data of Kip3-S and Kip3-H have been analysed together. These constructs were expressed and purified in our lab by the same protocol with the help and under the supervision of Naghmeh Azadfar.

## 4.2. Microtubule Preparation

Porcine tubulin was polymerised in BRB80 (Brinkley resuspension buffer 1980, containing 80 mM piperazine-N,N′-bis-(2-ethanesulfonic acid (PIPES), 1 mM ethylene glycol tetraacetic acid (EGTA), 1 mM $MgCl_2$, pH = 6.9 adjusted with KOH) with 5 % dimethyl sulfoxide (DMSO), 4 mM $MgCl_2$ and 1 mM GTP for 1 h at 37 °C. Afterwards, microtubules were diluted with BRB80 containing 10 µM taxol (BRB80T), spun down in a Beckmann airfuge and resuspended in BRB80T. Microtubules were visualised with differential interference contrast employing a light emitting diode (LED-DIC) [72]. Tubulin was purified from porcine brains following the protocol in [108]. I decided to use taxol-stabilised microtubules instead of GMPCPP-stabilised ones because the microtubules grew faster, longer, and the protocol turned out to be more reliable. If not noted otherwise, all chemicals were from Sigma Aldrich, St. Louis, MO, USA.

For 3D assays, microtubules were grown for 1.5–2 h to get longer microtubules. This was advantageous for suspending them on surface structures.

## 4.3. Motility Assays with Kinesins

**Optical Tweezers Assays** The motility buffer for Kip3 stepping assays was BRB80 with 1 mM ATP, 0.16 mg/ml casein, 10 µM taxol, 112.5 mM KCl, and an anti-fading mix (20 mM glucose, 20 µg/ml glucose oxidase, 8 µg/ml, 1 vol% β-mercaptoethaol) to prevent photo-oxidation[40]. Motility buffer for assays with non-motile Kip3 contained 1 mM AMPPNP (Jena Bioscience, Jena, Germany) instead of ATP; motility buffers for rkin430 assays had 1–2 µM ATP and no KCl. The ATP concentration was decreased in kinesin-1 assays such that kinesin-1 speeds were comparable to the ones of Kip3.

The motility buffer for 3D Kip3 stepping assays were the same as for 2D assays but contained 10 mM dithiothreitol (DTT) instead of β-mercaptoethanol and additionally 0.1 vol% Tween-20. The detergent Tween-20 was added to inhibit unspecific binding of microspheres to the surface structures. Motility

buffers for 3D assays with rkin430 were identical to Kip3 assays except for the lack of KCl and the reduced ATP concentrations of 5 and 10 µM.

For all optical tweezers assays, 2 µl of functionalised microspheres (20× diluted in motility buffer, prepared as described in Chapter 5) were mixed with 2 µl of kinesins that were diluted in motility buffer. The mix was gently mixed 40 times by pipetting, incubated for 7 min at room temperature, and finally diluted 20–25× with motility buffer.

Single-molecule conditions were achieved when at most one out of three tested microspheres showed motility. In addition to the microsphere statistics, I performed a test for single-molecule conditions using the known stall forces of the used kinesins [7, 40]. Microspheres that reached significantly higher forces compared to the stall force (>1.8 pN for Kip3, >6 pN for rkin430) were not used for experiments nor data analysis. The statistics about single-molecule conditions are discussed in Chapter 5.

**TIRF Assays** Measurements were performed in the TIRF setup in the former lab of Stefan Diez and Jonathon Howard (MPI-CBG, Dresden, Germany) [41] at a temperature of 29 °C using frame rates of 0.2 Hz for Kip3 and 0.25–9 Hz for rkin430. The speeds of single kinesins walking along immobilised microtubules were determined from analysing the kymographs along the microtubules using the image analysis software ImageJ (NIH, Bethesda, MD, USA). A kymograph is a concatenation of intensity profiles over all frames. A motor, translocating with constant speed, is then depicted as a line with an angle $\alpha$ as exemplarily shown in Fig.4.2. The speed $v$ of the motor can then be calculated from that angle which is obtained from a manually drawn line by

$$v = \left| \frac{\text{pixel size}}{\text{frame time} \cdot \tan \alpha} \right| . \tag{4.1}$$

The motility solution contained ATP with concentrations of 0.5–2000 µM and 10 mM DTT. As microtubules, GMPCPP-stabilised ones were used (0.5 mg/ml tubulin, 1 mM GMPCPP (Jena Bioscience), 1 mM $MgCl_2$ in BRB80, incubated for 2 h at 37 °C). The pixel size was 100 nm.

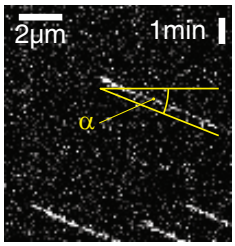


**Figure 4.2: Determination of kinesin speeds using TIRF microscopy.** Exemplary kymograph of Kip3 at 100 µM ATP with drawn line (yellow, with vertical offset for clarity) to determine the angle $\alpha$ and speed $v$ by Eq. 4.1.

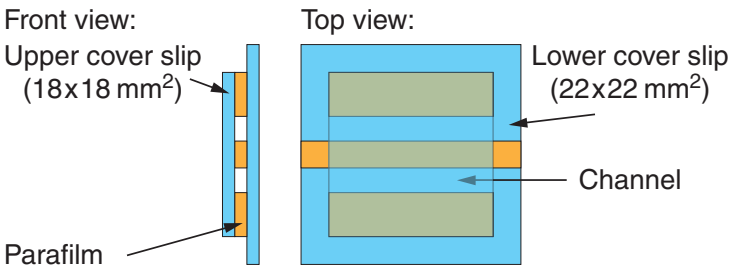


**Figure 4.3: Schematic of a flow cell.** The flow cell was built of two cover slips of different sizes and parafilm. Modified from [92].

## 4.4. Sample Preparation

Kinesin motility assays were performed in flow cells that were constructed as described in [40, 92, 109]. Briefly, they were built of glass cover slips (18×18 mm$^2$ from Menzel-Gläser, Braunschweig, Germany and 22×22 mm$^2$ from Corning Inc., Corning, NY, USA) and stripes of parafilm (PM-996, Bemis Company, Neenah, Wisconsin, USA) as illustrated in Fig. 4.3. The glass cover slips were made hydrophobic before by silanisation. For this purpose, slips were washed in aceton, ethanol, piranha solution and KOH, and silanised in trichlorethylene containing dichlorodimethylsilane as described before [92]. Alternatively, silanisation was performed by placing glass slides with 100 µl of perfluorodecyltrichlorosilane (FDTS from abcr, Karlsruhe, Germany) in a desiccator at a pressure of about 25 mbar for about 10 min. The channels, formed with parafilm, were filled with the sample solutions using a small vacuum pump and stripes of filter paper.

Microtubules were immobilised on the hydrophobic sample surface by β-tubulin antibodies (monoclonal from mice, Sigma-Aldrich, order number T7816). The rest of the surface was blocked by Pluronic F-127. F-127 is a triblock copolymer with both hydrophobic and hydrophilic domains. It binds to and blocks hydrophobic surfaces very efficiently from further attachment [68]. Thus, the channels were thoroughly washed with BRB80 and filled and incubated with anti-tubulin for 20 min. After another washing steps the channels were filled and incubated with F-127 (1 wt% in BRB80) for 20 min and washed again with BRB80. Afterwards, microtubules were flushed in and incubated for several minutes. Finally, kinesin-coated microspheres or diluted kinesins were flushed into the channel, respectively. In optical tweezers assays, a trapped microsphere was placed on top of a microtubule to await kinesin-initiated motility. For motile microspheres, the force clamp was activated and the measurement started.

# 5. Functionalisation of Microspheres

In optical tweezers assays with motor proteins, the protein must be coupled to a microsphere. Corresponding protocols must fulfil several conditions: (i) The protocol should be simple and reproducible. (ii) The motor-to-microsphere ratio must be tunable to reach single-molecule conditions. (iii) The coupling procedure must not influence the functionality of the protein.

The first motor protein-coated surface protocols with kinesin-1 were based on non-specific adsorption of kinesin on casein-coated glass slides or microspheres [37, 110]. While the C-terminal tail domain of kinesin-1 naturally binds glass surfaces and the stalk is thought to be in a compact form not bound to the surface [111], casein helps to reduce non-specific interactions. Since truncated kinesin-1 or other kinesins have different C-termini, the non-specific casein assay may not work. To achieve specific binding, microspheres are often coated with antibodies which then bind to the complementary epitope of the motor protein. Those protocols differ with respect to the coupling of the antibody to the microspheres (e.g. biotinylated his antibodies bound to streptavidin-coated microspheres [30]; flag antibodies bound to amino microspheres with glutaraldehyde and protein G [112]; myc antibodies covalently [113] or GFP antibodies unspecifically [114] bound to carboxylated polystyrene microspheres). Another option is to couple kinesins tagged with biotinylated DNA to streptavidin-coated microspheres [115, 116]. Common problems of coupling protocols are microsphere clustering or adhesion to the sample surface. Furthermore, some coupling protocols are time-consuming and may require more attempts for successful coupling [117].

Here, co-workers and me developed, optimised, and extended a versatile and reproducible protocol that can be used for many kinesins and other proteins. The protocol has been published in the *Journal of Biological Methods* [118] and is quoted in this chapter. I used the protocol in all my optical tweezers assays with kinesins.

## 5.1. Functionalisation Protocol

### 5.1.1. Principle of Coupling

The protocol uses a polyethylene glycol (PEG) linker to covalently bind an antibody to the microspheres. The coupling uses the well-established NHS/EDC activation of carboxyl groups. In addition, to prevent microsphere aggregation, the microspheres were simultaneously covered with a dense monolayer of covalently attached PEG molecules which do not have any further reactive

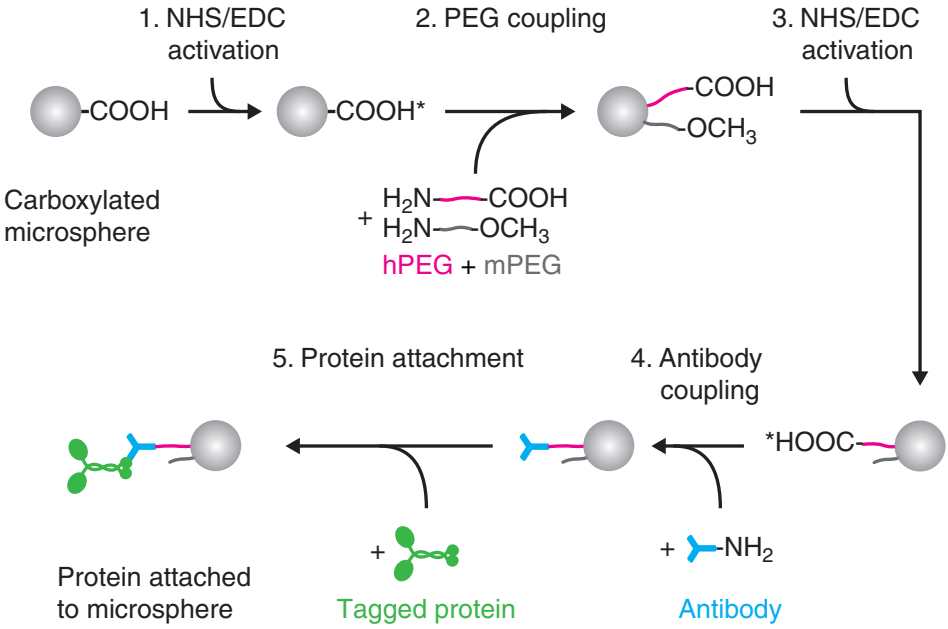


**Figure 5.1: Schematic of the PEG-mediated, protein-coupling procedure.** The monofunctional mPEG and heterobifunctional hPEG (ratio = 9:1) are covalently bound to the activated (indicated by an asterisk), carboxylated microsphere. The mPEG forms a non-reactive polymer brush on the microsphere's surface suppressing non-specific interactions. The antibodies (e.g. against GFP) are covalently bound in a random orientation to the activated carboxyl groups of the hPEG. Finally, the GFP-tagged protein binds to the GFP antibody. Not drawn to scale. Modified from [118].

groups at the free end. PEGylation, i.e. covalent covering with a PEG layer, is widely used to efficiently passivate microspheres for *in vivo* [119–122] and *in vitro* [123–126] experiments and for different kinds of surfaces [127–129]. Also, there are other protocols that use PEG for functionalisation [130, 131]. Our combined approach uses PEG both as a blocking agent and linker. We used GFP antibodies to couple GFP-tagged proteins to the microsphere. Figure 5.1 illustrates the principle. The protocol consists of different substeps that are described in the following.

### 5.1.2. Microsphere Preparation

Below, a standard protocol for 590 nm-diameter polystyrene microspheres, coated with a monofunctional, 2 kDa $\alpha$-methoxy-$\omega$-amino PEG (called mPEG) and a heterobifunctional, 3 kDa $\alpha$-amino-$\omega$-carboxyl PEG (called hPEG) in a 9:1 ratio, bound to GFP antibodies, is described.

**Activation of carboxylated polystyrene microspheres** Carboxyl-functionalised polystyrene (PS) microspheres (25 µl) of the stock solution (Bangs Laboratories, order number PC03N/6487, diameter = 590 nm, 10 % solids, surface charge 28.5 µeq/g) were washed twice in 1000 µl 2-(N-morpholino) ethanesulfonic acid buffer (MES, 50 mM, pH = 6.0 adjusted with NaOH, filtered). To

wash the microspheres, the aliquot was centrifuged 3 min at 14,000 g and the supernatant was removed. Fresh buffer was added and the pellet was resuspended. To ensure that the pellet was resuspended well, the solution was vortexed for 10 s and sonicated in a bath sonicater (Isonic CD-7810A) for 90 s. Finally, the microsphere pellet was resuspended in 250 µl MES buffer. Immediately before usage, 6.8 mg of 1-ethyl-3-(3-dimethylaminopropyl) carbodiimide (EDC, molecular weight 191.7 g/mol) and 7.7 mg of N-hydroxysulfosuccinimide sodium salt (sulfo-NHS, molecular weight 217.1 g/mol) were each dissolved in 100 µl MES buffer. Usually, different masses of EDC and sulfo-NHS were weighted and dissolved in 100 µl MES. In this case, the added volume was adapted for these values. The same accounts for the next step. The final EDC and sulfo-NHS concentrations were a hundred-fold higher than the total concentration of carboxyl groups on the microspheres (71 nmol). First, 20 µl of the sulfo-NHS solution, then 20 µl of the EDC solution were added to the washed microspheres and mixed well. The suspension was incubated for 15 min at 37 °C and mixed at 600 rpm in an Eppendorf ThermoMixer C. It is critical for the activation step that EDC and sulfo-NHS are freshly dissolved in MES buffer and added within 2 min to the microspheres. The protocol also worked for ten to thousand-fold higher concentrations of EDC and sulfo-NHS compared to the effective COOH concentration from the microspheres. After incubation with EDC and sulfo-NHS, the activated microspheres were washed twice in 500 µl MES. Finally, the microsphere pellet was resuspended in 250 µl borate buffer (BB, 130 mM boric acid, 18 mM sodium tetraborate, pH = 8.5, filtered). EDC reacts with the carboxyl group and forms an amino-reactive O-acylisourea intermediate. This intermediate is susceptible to hydrolysis and short-lived in aqueous solutions. The addition of sulfo-NHS stabilises the amino-reactive intermediate by converting it to an amino-reactive sulfo-NHS ester. The sulfo-NHS ester increases the efficiency of EDC-mediated coupling reactions [132]. The amino-reactive sulfo-NHS ester intermediate is only semi-stable. Washing and adding the PEGs should not take longer than 20 min.

**PEG Coupling** 7.8 mg of the heterobifunctional hPEG ($NH_2$-PEG-O-$C_3H_6$-COOH × HCl, 3 kDa, Rapp Polymere, Tübingen, Germany, order number 133000-20-32) were dissolved in 100 µl BB. 9.4 mg of the monofunctional mPEG ($CH_3O$-PEG-$NH_2$, 2 kDa, Rapp Polymere, order number 122000-2) were dissolved in 20 µl BB. 20 µl of the hPEG-borate solution were mixed with the 20 µl mPEG-borate solution. The mixed PEG-borate solution was then added to the activated microspheres in 250 µl BB and mixed well (vortexed for 5–10 s). The total amount of the functional group R-$NH_2$ should be ten to a hundred-fold higher than the amount of carboxyl groups on the microspheres. The coupling reaction was allowed to proceed for 90 min at 37 °C and mixed at 600 rpm in the thermomixer. To remove remaining PEG after the incubation, coated microspheres were washed five times in 500 µl BB by spinning them down and resuspending them. Finally, the microsphere pellet was resuspended in 250 µl MES buffer.

**Antibody Coupling** The PEGylated microspheres were activated in a procedure identical to the first activation. The same amount of EDC and sulfo-NHS were used here. In the second activation step, only 1 out of 10 PEGs should have a carboxyl group. All carboxyl groups on the microspheres should have either reacted or be inaccessible for further reactions. Therefore, the amount of EDC and sulfo-NHS should be a thousand-fold higher than the carboxyl group concentration of the activated hPEGs. After the activation, the microspheres were washed and then resuspended in 250 µl phosphate-buffered saline (PBS, pH = 7.0, filtered) containing 10 µl GFP antibody (monoclonal from mice, antibody facility of MPI-CBG, Dresden, Germany, 3 mg/ml in PBS). The suspension was incubated for 90 min at 37 °C and mixed with 600 rpm in the thermomixer. Because of the large size of the antibodies (≈150 kDa), many amino groups are exposed on their surface. Therefore, a random orientation of the covalently coupled antibodies can be expected. Finally, the microspheres were washed 3 times in PBS, resuspended in 250 µl PBS and stored at 4 °C. The microspheres were functional for up to three weeks.

**Determination of the Microsphere Concentration** The microsphere concentration was needed to correctly calculate the motor-to-microsphere ratio. Because of buffer exchanges and surface adsorption, usually an unknown number of microspheres was lost during the preparation. Therefore, I determined the final microsphere concentration by measuring the extinction of visible and near-ultraviolet light (220–750 nm) by the functionalised polystyrene-PEG-anti-GFP microspheres at a specific wavelength (Fig. 5.2A) in a Nanodrop 1000 spectrophotometer. As a reference, the extinction at the same wavelength by uncoated microspheres of known concentration was measured. Extinction includes both absorption and scattering of the light by the microspheres. The extinction peak height scaled linearly with the microsphere concentration (Fig. 5.2B) and was used as a calibration. According to my measurements, a loss of 50–60 % of the microspheres was typical during a preparation. The wavelength of the extinction peak depended on the microsphere diameter which is consistent with the literature [59, 133]. Figures 5.2C and D show extinction spectra and peak wavelengths for different microsphere diameters. The peak wavelength increased with increasing diameters and could be used to determine the size of unknown microspheres.

**Sample Preparation and Kinesin Assay** Samples with immobilised microtubules were built and prepared as described in the previous Chapter 4. Accordingly, kinesins were bound to the microspheres, to measure motility with optical tweezers.

The protocol is described for the kinesin-8 Kip3 [40, 49] but can be easily adapted for other GFP-tagged kinesins.

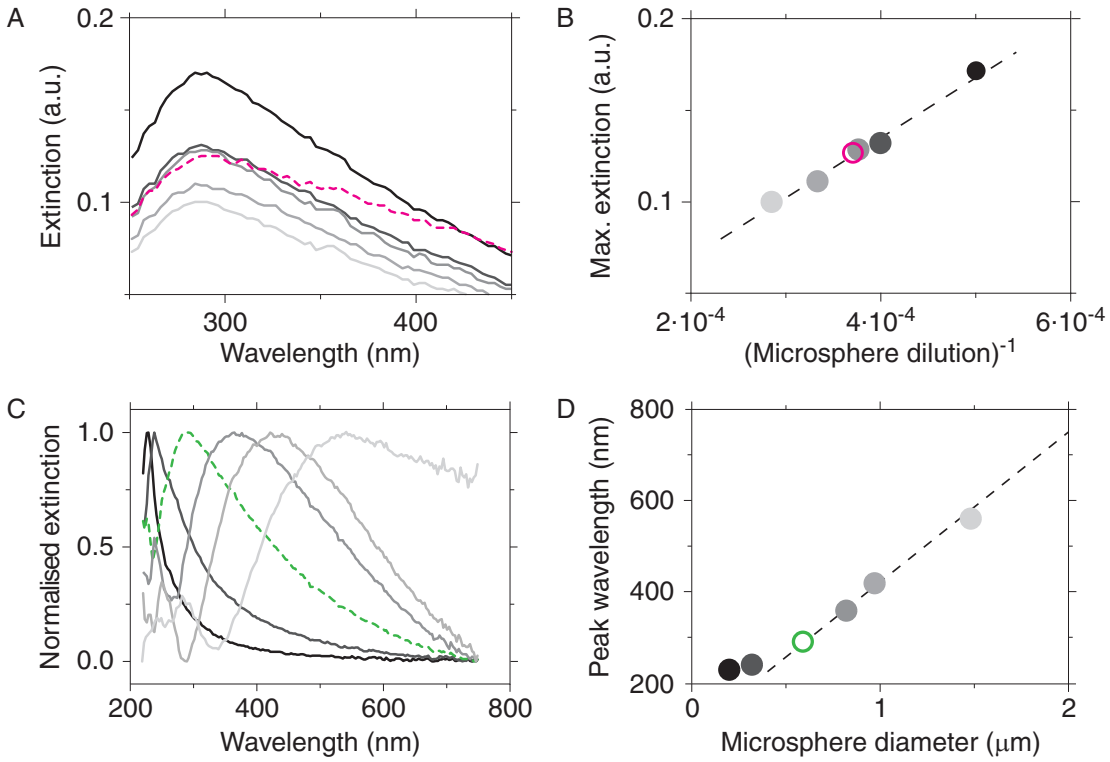


**Figure 5.2: Determination of the Microsphere Concentration.** (A) Extinction spectra for different stock microsphere (590 nm PS-COOH) dilutions (2000, 2500, 2700, 3000, 3500×: lines from black to light grey) and one batch of diluted anti-GFP-PEG-coated PS microspheres (magenta dashed line, 1000). (B) Maximum extinction for 590 nm-diameter microspheres at 290 nm as function of (microsphere dilutions)$^{-1}$. Symbol colours correspond to (A) with a linear fit (black dashed line). The peak height was inversely proportional to the microsphere dilution. (C) Normalised extinction spectra for different microsphere diameters (200 nm, 320 nm, 820 nm, 970 nm, 1480 nm: lines from black to light grey; 590 nm: green dashed line). (D) Peak wavelength of the extinction spectra as function of the microsphere diameter with a linear fit (dashed line) for diameters ≥590 nm. Symbol colours refer to (C). Modified from [118].

### 5.1.3. Tests and Results

**The protocol was efficient** The protocol turned out to be reproducible, as nearly all preparations gave functional microspheres. Also, clusters of microspheres appeared seldom for fresh preparations. The efficient passivation of the microspheres can be tested by incubating them with fluorescent bovine serum albumin (BSA) as described in [118]. I tested the functionality with both the kinesin-1 rkin430 and the kinesin-8 Kip3, which all had eGFP tags. During this project, I used many different Kip3-eGFP constructs. All of them turned out to be functionally coupled to the microspheres. Figure 5.3A shows the measured forces of rkin430 and Kip3. The respective stall forces of 5–6 pN and 1.1–1.5 pN[1] were consistent with previously reported values [7, 96] and supported the no-

[1]Note that the stall force of Kip3 of 1.1,pN measured in a force-clamp assay is different from the stall force measured in a static trap of 1.5 pN as discussed before [92].

**Table 5.1: Speeds of free and microsphere-coupled kinesins.** $v$, mean speed; SEM, standard error of the mean; $N$, number of data points. The speeds of motors coupled to microspheres were not significantly different to speeds of free motors, based on two-tailed t-tests.

| Kinesin | ATP concentration (mM) | Free kinesins $v \pm$ SEM (nm/s) | Microsphere-coupled kinesins $v \pm$ SEM (nm/s) |
|---|---|---|---|
| rkin430 | 0.1 | 603 ± 26 ($N$ = 98) | 546 ± 84 ($N$ = 10) |
| Kip3 | 1 | 41.0 ± 0.6 ($N$ = 167) | 40.0 ± 1.6 ($N$ = 52) |

tion that the functionality of the coupled proteins was preserved. To further test if the coupling procedure affected the functionality of the kinesin motors, we compared the average speed of free motors to the speed of motors coupled to microspheres. The speeds of free motors were measured by tracking single fluorescently labelled kinesins moving along immobilised microtubules in a TIRF microscope (Section 7.2). The speeds of the motor-coated microspheres were determined by video-tracking them in DIC time-lapse images. The results for the two different kinesins are shown in Tab. 5.1. Within error margins, the speeds were consistent with the TIRF measurements and literature values [7, 19], confirming the functionality of the kinesins when coupled to a microsphere. The functionality was also tested successfully with other proteins by Anita Jannasch and Anastasiya Trushko [118].

**Single kinesin steps were resolved** Single-molecule conditions, i.e. the interaction of only one motor protein per microsphere with the microtubule, can be reached by controlling the density of motors on the microsphere surface via the fraction of microspheres that show motility. A statistical analysis of the interaction probability of motor-coated microspheres with immobilised microtubules [7, 37] shows that this fraction is a function of the motor-to-microsphere ratio and follows Poisson statistics.

Assuming that at least one motor shows always interaction with the microtubule, this probability can be described by

$$P_{\geq 1}(n) = 1 - \mathrm{e}^{-\Gamma n}, \tag{5.1}$$

where $n$ is the motor-to-microsphere ratio in the solution and $\Gamma$ is a scaling factor that relates the motor-to-microsphere ratio *on* the microsphere to the ratio in the solution. In case that all motors that were pipetted have bound to microspheres and no losses occurred, an ideal $\Gamma$ of 1 is expected.

When assuming that at least two motors interact with the microtubule, the probability is described by

$$P_{\geq 2}(n) = 1 - \mathrm{e}^{-\Gamma n} - \Gamma n \mathrm{e}^{-\Gamma n}. \tag{5.2}$$

If the assay can achieve single-molecule conditions, Eq. 5.1 described the data better than Eq. 5.2. Single-molecule conditions with at least 95 % confidence are then achieved for a low motor-to-microsphere ratio if only one out of three microspheres shows motility. In Figure 5.3B, the fraction of motile microspheres

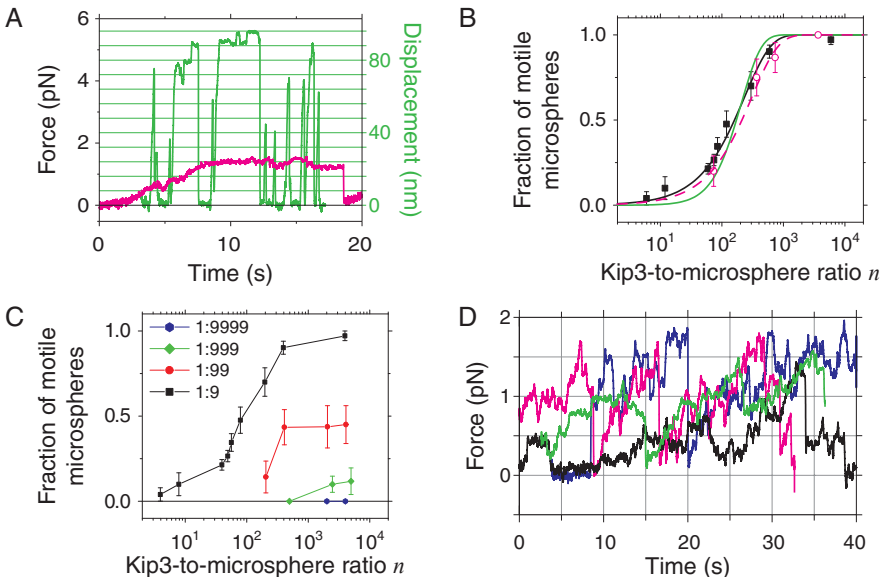


**Figure 5.3: Motility measurements with preserved functionality.** (A) Force measurements of single Kip3-eGFP (magenta) and rkin430-eGFP (green) motor proteins. Sampling rate: 10 kHz, box car filtered to 50 Hz (except rkin430: 4 kHz, median filtered to 8 Hz). Microsphere displacement for rkin430, only (right axis, green scale and grid). (B) Fraction of motile microspheres $P$ as a function of Kip3-to-microsphere ratio $n$. Plotted are data from 590 nm-diameter polystyrene microspheres, coated with 2 kDa mPEG and 3 kDa hPEG (■: anti-GFP, mPEG:hPEG = 9:1, ○: anti-GFP antigen-binding fragments (Fab), mPEG:hPEG = 1:1). The data points (number of tested microspheres each ≥21) are fitted with Eq. 5.1 for at least one functional molecule per microsphere (black line for the anti-GFP microspheres, magenta dashed line for Fab) and Eq. 5.2 for two or more molecules per microsphere (green line for anti-GFP microspheres). (C) Fraction of motile microspheres as a function of Kip3-to-microsphere ratio for preparations with different mPEG:hPEG ratios. Lines are guides to the eye. (D) Force measurements of single Kip3-eGFP, using microspheres with anti-GFP and without hPEG (magenta), antigen-binding fragments of anti-GFP (black), antigen-binding fragments and without hPEG (blue), and NeutrAvidin and biotinylated anti-GFP (green). Sampling rate: 4 kHz, median filtered to 8 Hz. Modified from [118].

decreased with lower motor-to-microsphere ratios and could be fitted very well with Eq. 5.1, amounting to $\Gamma = (4.4 \pm 0.3) \cdot 10^{-3}$ and $\chi^2_{\text{red}} = 0.6$. Equation 5.2 did not fit the data well ($\Gamma = (13 \pm 1) \cdot 10^{-3}$ and $\chi^2_{\text{red}} = 2.7$). Therefore, single-molecule conditions could be achieved with this protocol.

For single-molecule trajectories and subsequent analysis of kinesin experiments, it is desirable to resolve the 8 nm steps that are typical for kinesins [6]. I could observe clear steps for rkin430 (Fig. 5.3A, green scale and grid) for higher loads. For Kip3, it had been shown that steps can be resolved when a load of about 1 pN is applied [40]. This report is consistent with my observations (Fig. 3.8).

## 5.2. Variation of the Protocol

We varied the parameters of the described standard protocol to prove its versatility and general use for the optical tweezers and kinesin community.

### 5.2.1. Varying the PEG Ratio

To reach single-molecule conditions, either the kinesin-to-microsphere ratio or the density of antibodies on the microspheres can be tuned. To achieve the latter, I varied the mPEG (2 kDa)-to-hPEG (3 kDa) ratio from 9:1 to 9999:1 in the preparation. Subsequently, I tested the microspheres with Kip3. I observed motility at ratios of 9:1 (ratio of motile to total number of tested microspheres, 34/35 = 97 %), 99:1 (9/20 = 45 %) and 999:1 (2/17 = 12 %) at saturating Kip3 concentrations during the final coupling step. At 9999:1, there was no motility (0/20 = 0 %). Thus, with a 999:1 ratio, single-molecule conditions were given. I also measured the fraction of motile microspheres as function of the kinesin-to-microsphere ratio. The results are shown in Fig. 5.3C. The motility of microspheres decreased with increasing mPEG:hPEG ratio. These experiments showed that the protocol worked with various mPEG:hPEG ratios, but a minimal hPEG fraction was required for motility. The advantage of a reduced antibody surface density is that, irrespective of the motor concentration used for coupling, single-molecule conditions are always achieved.

### 5.2.2. Functionalisation without hPEG

The spatial signal-to-noise ratio of a trapped microsphere in an optical trap and thus the accessible spatial resolution is, among other factors, influenced by the linker stiffness and the probe size, i.e. the microsphere diameter [89]. A small microsphere and a short linker are desirable for highest resolution. However, if the linker is too short or the protein is directly coupled to a surface, the functionality of the proteins may be influenced. Anita Jannasch tested different combinations of PEG lengths (1–10 kDa for hPEG, 0.5–5 kDa for mPEG) and microsphere diameters (320–820 nm) in Kip3 assays. She showed that the protocol worked for a broad range of PEG lengths and microsphere sizes with low clustering [118]. To reduce the linker length as much as possible, I tested 590 nm microspheres without any hPEG. The antibodies, together with mPEG, were coupled directly to the carboxyl groups on the microsphere surface requiring only one activation step. In a Kip3 assay, I found that an antibody-to-mPEG ratio of about 1:23,000 yielded functional microspheres (Fig. 5.3D, magenta line). For this ratio, I also observed a low number of clusters. Using less mPEG led to increased cluster formation. Clustering may be caused by multiple amine groups on the antibodies that could lead to cross-linking of several microspheres if the repulsive effect of the PEG brush is compromised. The fraction of motile microspheres and thus single-molecule conditions could be further tuned by varying the kinesin-to-microsphere number (see above). For the direct-antibody-coated microspheres, this fraction was generally smaller at

comparable kinesin concentrations than for microspheres with the spacer hPEG. The smaller fraction indicates that using hPEG as a linker between the antibody and the microsphere helped to preserve the kinesin's functionality.

### 5.2.3. Preparations with Antigen-Binding Fragments, NeutrAvidin, and Anti-Tubulin

To test the versatility of the protocol, I coupled proteins via different binding proteins and tags to the microspheres. Because antibodies have more than one antigen binding site, one or more motor proteins could bind to the same antibody (disregarding steric constraints), potentially compromising single-molecule conditions. As shown above, using the protocol with GFP antibodies, single-molecule conditions were achievable (Fig. 5.3B). Thus, binding of two motors to a single antibody appears to be unlikely. Nevertheless, to rule out the possibility completely, I tested the protocol with purified antigen-binding fragments (Fab) of GFP antibodies that have only one GFP-binding site per molecule. Fab were purified from the above-mentioned GFP antibodies using the Fab generation kit from Thermo Scientific (order number 44885) in the antibody facility of MPI-CBG, Dresden, Germany. Such microspheres showed motility with Kip3, followed Poisson statistics, and could be tuned to single-molecule conditions (Figs. 5.3B, purple circles and D, black line). The fraction of motile Fab-based microspheres for a mPEG:hPEG ratio of 1:1 was within error bars comparable to the antibody-coated microspheres. It could be fitted well with Eq. 5.1 and $\Gamma = (3.3 \pm 0.3) \cdot 10^{-3}$ ($\chi^2_{\mathrm{red}} = 0.2$). For Fab-based microspheres with the same mPEG:hPEG ratio as the standard GFP antibody preparation, the fraction of motile microspheres was generally smaller. This smaller fraction may originate from carboxyl groups binding to the antigen binding site of the Fab fragment blocking motor coupling. In case of an antibody, another free binding site would still be left increasing the total number of motor binding sites per microsphere. Additionally, I tested microspheres with antigen-binding fragments directly bound to the microspheres, i.e. without hPEG, together with 2 kDa mPEG in a 1:2300 ratio, higher than the previously used ratio for the direct antibody coupling. These microspheres were also functional (Fig. 5.3D, blue line).

Besides the coupling of GFP-tagged proteins to the corresponding antibodies or antigen-binding fragments, I tested other tags. NeutrAvidin is a protein that binds the molecule biotin very tightly and is often used as coupling agent. I bound NeutrAvidin together with mPEG to the microsphere surface in a 1:10,000 ratio. Less mPEG led to cluster formation. These microspheres were subsequently incubated with biotinylated GFP antibodies and tested successfully with Kip3 (Fig. 5.3D, green line). The NeutrAvidin-coated microspheres could also be bound to biotinylated giant unilamellar vesicles for membrane-tether-pulling experiments, performed by Gero Hermsdorf, Biotec, TU Dresden, Germany [134].

Furthermore, I coupled tubulin antibodies instead of GFP antibodies to microspheres. The tubulin antibody was the same antibody that was used for

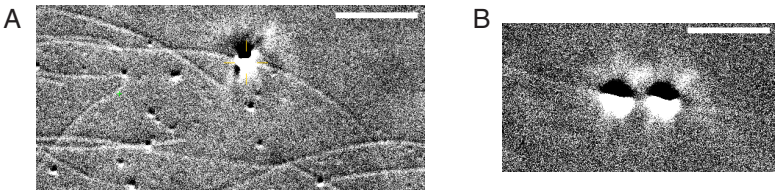


**Figure 5.4: Specific binding of polystyrene-PEG-anti-tubulin microspheres to microtubules.** Binding was shown on (A) completely and (B) incompletely immobilised microtubules. Images were recorded in differential interference contrast and averaged 10×. Scale bars are 5 μm.

microtubule immobilisation on the surface. I trapped such coated microspheres with optical tweezers, put them on immobilised microtubules, and observed a strong, specific interaction as shown in Fig. 5.4. All 24 tested microspheres immediately bound to the microtubule after they had been put on it. Some microtubules were only partly bound to the surface. Fortunately, this incomplete immobilisation enabled to check whether the binding of the microspheres to the microtubules was really specific. As the microspheres also bound to parts of microtubules that were partially free in solution (Fig. 5.4B), any unspecific surface interaction of the microspheres could be excluded.

Thus, our microsphere preparation potentially allows for specific interactions using various tags while preserving the functionality of the coupled proteins. As many kinesins and other proteins have a his tag for purification purposes, a his antibody would be a promising candidate.

As alternative to antibodies and Fab fragments, so-called nanobodies might be of use in the future. Nanobodies are the smallest domain of antibodies that can still recognise and bind their epitope [135, 136]. Recently, nanobodies for GFP have been developed [137] and could replace the GFP antibodies in our protocol.

# 6. Topographic Surface Treatment to Suspend Microtubules

For three-dimensional experiments with kinesins, the microtubules must be arranged in a suitable manner such that the kinesin can freely walk around the whole microtubule. In *in vitro* assays, immobilisation of microtubules on surfaces makes the lower half inaccessible. Free access can be provided by either placing the microtubule upright with one end bound to the surface or suspending the microtubule on a three-dimensional structure like a bridge over a canyon. A variant of the second option is to hold microtubules via bound microspheres using multiple optical traps [112, 113]. The first option, though having some principle advantages, e.g. for the height calibration of the evanescent field in TIRF [111, 138], seems impracticable for many reasons. A stable immobilisation of the microtubules was difficult and in a motility assay, the axial position would vary significantly and cause non-negligible changes of the calibration factors. Thus, I did not investigated this idea further. Holding microtubules with multiple traps was also not possible, as our setup only had a single trap. Consequently, I tested different experimental approaches to place microtubules on topographic structures. Such microtubules are denoted as suspended microtubules in the following text, whereas microtubules on a planar surface are denoted as immobilised ones.

In optical tweezers motor assays, the motors are attached to microspheres. Thus, the height of the topographic structures must be large enough to accommodate the microspheres' movement. The microspheres had a diameter of 590 nm. Therefore, a suitable depth under the suspended microtubule including a reasonable safety margin would be 1–2 μm. The height should not be too large, as stable optical trapping was only possible close to the surface. Further away, spherical aberrations increase. In our setup, optical trapping was possible up to a height of about 10 μm.

The following chapter explains the details and results of the different approaches I tested. I found that topographic surface structures that were made by lithography to be best suited to suspend microtubules.

## 6.1. Suspending Microtubules on Immobilised Microspheres

In this approach, I used the microsphere functionalisation protocol, described in Chapter 5. As anti-tubulin-coated microspheres bound well to microtubules, I functionalised larger microspheres, immobilised them on the surface, and let

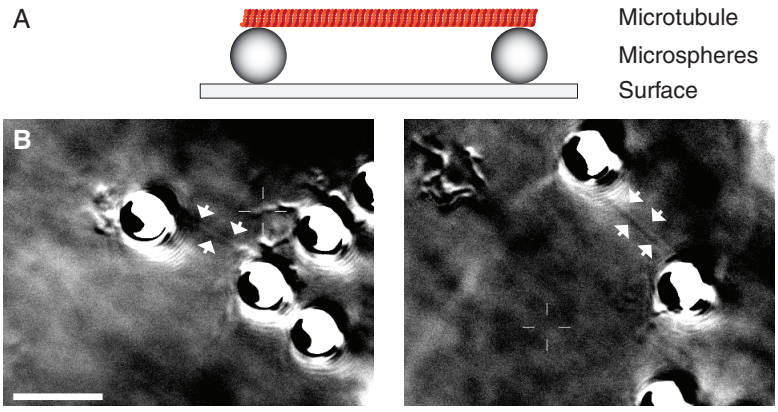


**Figure 6.1: Suspending microtubules with antibody-coated microspheres.** (A) Principle of suspending microtubules using anti-tubulin-coated microspheres. Not to scale. (B) Two examples of microtubules, suspended on microspheres (diameter = 2 μm, polystyrene), imaged by differential interference contrast. White arrows point to suspended microtubules. Scale bar is 5 μm.

microtubules bind to them. A similar approach was used by Can et al. [103] and Oguchi et al. [113]. I coated 2 μm carboxylated polystyrene microspheres with tubulin antibody, but without any PEG. The prepared microspheres were diluted in PBS buffer and incubated in a hydrophobic flow cell for 10 min. The microspheres stick to the surface unspecifically due to attractive van der Waals interactions [139]. Afterwards, I incubated 1 wt% F-127 for 10 min to prevent the microtubules from binding of the surface. After a washing step, microtubules were flushed in and incubated for 10 min, followed by another washing step, and a final incubation for 10 min. The channels were sealed with nail polish and the sample imaged using DIC. I found many microtubules bound with one end to a microsphere, but only few microtubules were bound with both ends to different microspheres (Fig. 6.1). The suspended length was about 7–9 μm. Suspending microtubules in this manner was possible, though the yield was very small. Furthermore, this approach had a fundamental disadvantage: There was no control over the orientation of the suspended microtubule. Microtubules were randomly tilted relative to the bottom surface, making experiments more difficult. For these reasons, I did not continue with this approach.

## 6.2. Suspending Microtubules on Carbon Grids

In another approach, that was originally suggested by Ernst-Ludwig Florin (Center for Nonlinear Dynamics, University of Austin, Texas, USA, personal communication), microtubules were suspended on transmission electron microscopy (TEM) grids. I used TEM copper grids, coated with amorphous carbon (Quantifoil S7/2, S117-1 via Plano GmbH, Wetzlar, Germany). The copper grids were about 12–15 μm thick and had quadratic holes with a width of 90 μm. They were coated with a 20 nm thin carbon film with quadratic holes. These holes had a width of 7 μm; the carbon bars between the holes had a width of 2 μm. I

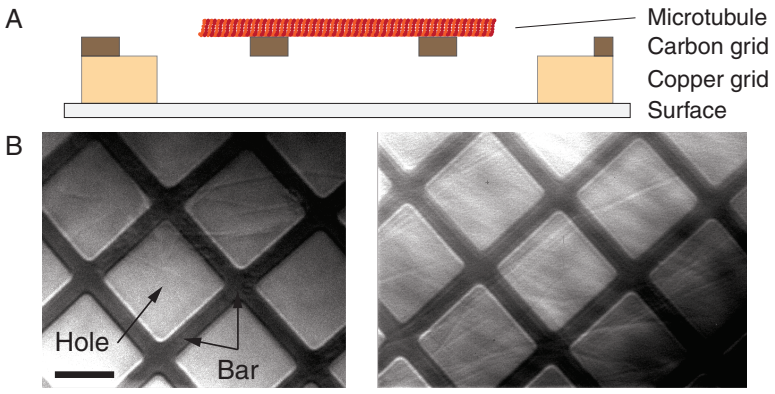


**Figure 6.2: Suspending microtubules with carbon grids.** (A) Principle of suspending microtubules using a carbon film with holes. Not to scale. (B) Two exemplary images of suspended microtubules, imaged by differential interference contrast. The right image is an average of 10 single images for better contrast. The scale bar is 5 μm.

glued those grids on a glass slide using vacuum grease from Beckman Coulter and built a flow chamber around it using parafilm. First, I filled the sample with 1 wt% F-127 in BRB80, as it improved the wetting of the grid. Subsequently, I incubated the sample with anti-tubulin in BRB80 and again with F-127 for 20 min each. Finally, I flushed in microtubules and incubated them for 10 min before a final washing step. I found microtubules suspended over the grid (Fig. 6.2) but not very well fixed, i.e. microtubules fluctuated a lot. Apparently, the immobilisation by anti-tubulin did not work well on the carbon.

Furthermore, this approach had other crucial disadvantages: The height of the suspended microtubule above the surface was significantly higher than the axial trapping range, i.e. a microsphere assay with optical tweezers was impossible. I shifted the optimal trapping height above the surface to higher values by using an immersion oil with a higher refractive index of 1.53 instead of the standard 1.518 as described by Reihani et al. [140]. However, trapping did not work well with these small microspheres. I tried to invert the assay by placing the grid upside down on top of 3 μm silica microspheres that were immobilised on the surface before. Unfortunately, the grid was not suspended by the microspheres. Besides these problems, there were often air bubbles in the corners of the grid and between the grid and the glass slides. The air bubbles made reproducible assays practically impossible. These issues could be reduced by adding F-127 as detergent to the buffer as described above. Because of these problems and the complicated sample design, I decided against the use of those grids for further experiments.

Interestingly, I discovered a novel trapping effect: With the laser shutter open, microspheres were attracted by the carbon grid. Once the laser shutter was closed, microspheres were released again. I investigated this trapping effect in more detail. The results are described in Chapter 9.

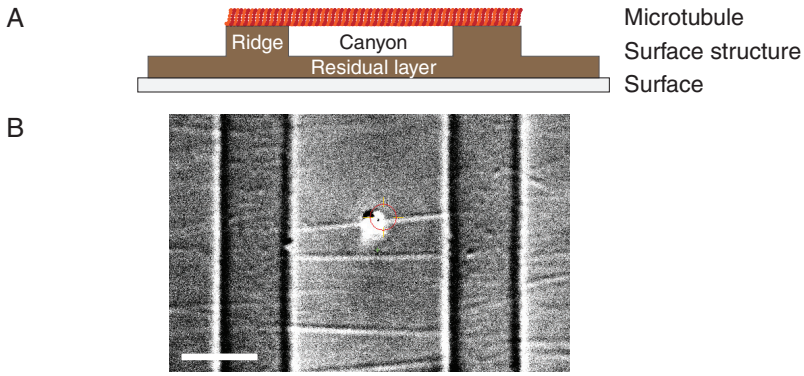


**Figure 6.3: Suspending microtubules with topographic structures.** (A) Principle of suspending microtubules on topographic surface structures. The structures consist of successive ridges and canyons on a residual layer of material. Not to scale. (B) Example of suspended microtubules, imaged by differential interference contrast. The image is an average of 10 single images. The scale bar is 5 μm.

## 6.3. Suspending Microtubules on Topographic Structures Made by Lithography

Topographic surface structuring with lithographic methods is an elaborate but reliable approach to suspend cytoskeletal filaments for motor protein assays. Different variants were successfully used, e.g. using pits in a silica layer on top of the sample slide [141] or elevated structures made of silica [111], polydimethylsiloxane (PDMS) [142], or polymethyl methacrylate (PMMA) [143]. Here, I used structures made of perfluoropolyether (PFPE) that were fabricated using ultraviolet nanoimprint lithography (UV-NIL) [144, 145]. PFPE is a polymer that is liquid at room temperature but photochemically cross-links and solidifies under UV light [146]. Its chemical and physical properties make it ideal for 3D assays: It is hydrophobic that antibodies against tubulin can be immobilised on to it to bind microtubules. PFPE is transparent, also for the trapping laser. Its refractive index is 1.341 [147], close to that of water (1.333). The small difference was important for the optical tweezers performance, because spherical aberrations were minimised. On the other hand, the difference of the refractive index turned out to be large enough to visualise the structures in the refractive index-sensitive imaging of DIC. Those structures were manufactured and provided by Salvatore Girardo in the BIOTEC/CRTD Microstructure Facility, TU Dresden, Dresden, Germany, using UV-NIL. A micro-patterned cover slip was fabricated by spin-coating a standard glass cover slip (22×22 $mm^2$) with KBM primer to improve the adhesion of the PFPE layer on its surface. A droplet of liquid PFPE was placed on the so-called master, a silicon wafer that carried the negative of the desired structure. The master template were also made of PFPE by photolithography and coated with an anti-sticking layer. The cover slip was then pressed into the droplet on the master with a pressure of 1 bar and exposed to UV light. The pressure determined the thickness of the surface pattern. After the cross-linking of the PFPE, the master was removed

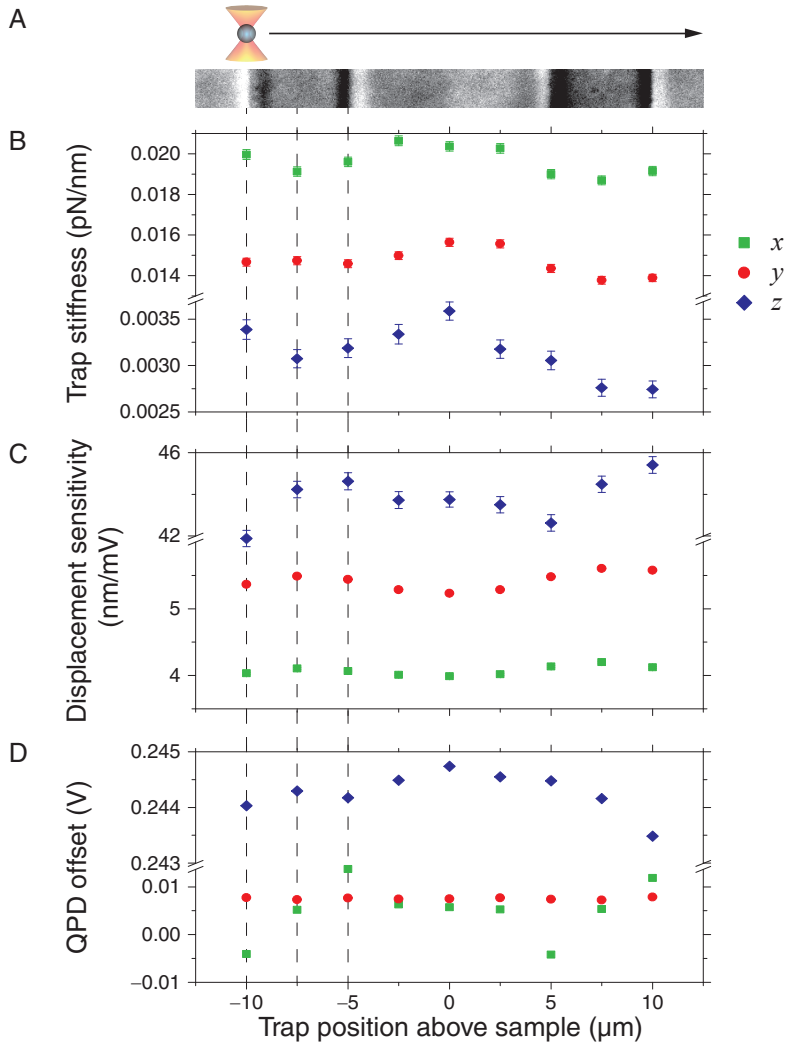


**Figure 6.4: Dependence of optical tweezers parameters on the lateral position above the topographic structure.** (A) A trapped 590 nm PS microsphere was moved with the sample stage to different positions, 1 μm above the topographic structure. The middle of the canyon was defined as the zero position. (B) Trap stiffness, (C) Displacement sensitivity, and (D) QPD offsets for $x$, $y$, and $z$.

and the patterned cover slip finished. I washed micro-patterned cover slips in an ultrasonic bath (USC-THD, VWR, Darmstadt, Germany) in desalted water and ethanol for each 10 min.

The final structures consisted of a repetitive pattern of linear ridges and canyons as illustrated in Fig. 6.3A. The width of the canyons was 10 μm, the widths of the ridges was 5 μm in one half of the slide and 2 μm in the other. The canyons were approximately 1.4 μm deep. Ridges and canyons lay on a residual layer with a thickness of 3.4 μm. Such structured slides were built into a flow cell similar to the standard design (Fig. 4.3). Microtubules were suspended after successive incubation at room temperature with tubulin antibodies (20 min), F-127 (45 min), and microtubules (5 min). Between and afterwards, the channels were washed with BRB80 buffer. Figure 6.3B shows that the binding of

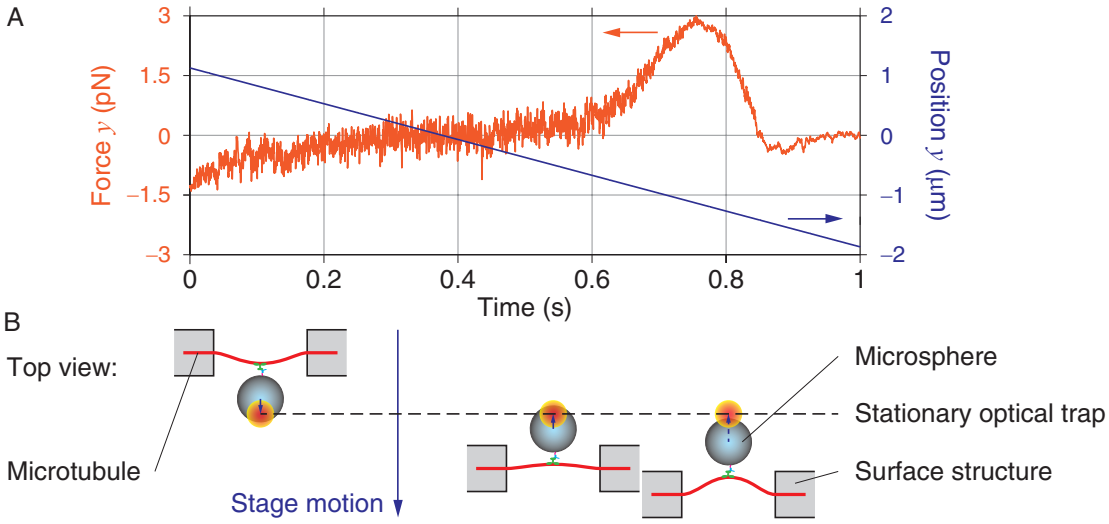


**Figure 6.5: Bending of suspended microtubules by increasing sideward loads.** (A) Applied force in the $y$-direction on the microtubule-bound microsphere (left) and stage position in the $y$-direction relative to the static optical trap (right). The zero position was defined as the position of the unbent microtubule. The trap stiffness was 0.026 pN/nm. (B) Schematic (not to scale) of bending the microtubule by applying loads on microtubule-bound microspheres.

microtubules to ridges suspending the canyons was successful. Furthermore, the assay was very efficient, as many microtubules were suspended over the multiple ridges. Also, it was reproducible. The microtubules were initially immobilised rigidly but started to detach from the structure after a few hours. For motility assays, I only used areas with 5 µm wide ridges, as the immobilisation of microtubules was better.

To test how the structures actually effected the optical tweezers performance, I measured the calibration factors and the QPD offsets 1 µm above the ridge surface on different positions of the structure, including the edges, the ridge, and the canyon (Fig. 6.4A). Note that the microsphere-surface distance was larger above the canyon. I found that all parameters changed significantly at the edges of the structure (Figs. 6.4B–D). Apparently, the structure's additional refraction did have an effect on the optical trap. As long as optical tweezers experiments were performed in the canyon or on the ridge, this effect should not disturb the experiments.

To test how rigid the microtubules were bound to the surface, I bound a microsphere-attached kinesin to a suspended microtubule and laterally moved the sample stage with a constant speed relative to the static optical trap as shown in Fig. 6.5A. Loads increased from negative to positive values. The microtubules were not to remove from the structures but were bent by the increasing load as illustrated in Fig. 6.5B. This bending was visible by eye in the microscope and could also be seen in the QPD force signal that showed increasing values until the microsphere was pull beyond the linear range of the trap (at ≈0.65 s in Fig. 6.5A, also compare with Fig. 3.13A). Bending was not a problem, as no loads were applied in the 3D assays.

# Part II.

# Results of 2D & 3D Optical Tweezers Assays with Kinesins

# 7. 2D Optical Tweezers Tracking of Kinesin-1 and Kinesin-8

The kinesin-8 Kip3 has been shown to shorten the microtubule at its plus end [19, 41]. To reach the end, Kip3 must walk far enough and be able to bypass obstacles on the MT track. The high processivity of Kip3 has been shown in TIRF stepping assays [41]. Gliding assays suggested an on average left-handed protofilament switching of Kip3. However, the exact manner of how Kip3 switches between protofilaments was unclear. Here, I tracked the motion of Kip3 with high precision under alternating sideward loads, similar to previous 2D force-clamping assays with forward and backward loads [40]. I found that Kip3 switched between protofilaments in both directions. This switching was asymmetrically biased by force. A simulation of the Kip3 stepping accounting for the assay's geometry suggested a diffusive sideward motion that was symmetric in the absence of force. A diffusive sideward stepping provides an effective mechanism to bypass obstacles. Control measurements with the kinesin-1 rkin430 revealed no effective sideward motion.

In the following chapter, the details and results of 2D-force-clamp assays with alternating sideward loads on Kip3 and rkin430 are explained. These results have been published in the *Biophysical Journal* [148] and are quoted in this chapter.

## 7.1. 2D-Force-Clamp Assays with Kinesins

Kinesin-coated microspheres were trapped and calibrated by analysis of the height-dependent power spectrum density as described in [67, 68]. The microsphere was then put on an immobilised microtubule to await motility as illustrated in Fig. 7.1A. On motile microspheres, sideward loads of 0.5 pN were applied with a trap stiffness of 0.02–0.03 pN/nm and alternated every 1.75–20 s. No load was applied along the microtubule axis. Additionally, sideward loads of 0.25, 1, and 2.1 pN were applied for an alternating time of 5 s (Fig. 7.1B). To distinguish this kind of experiment from stepping assays without applied loads, it is denoted as "side-stepping assay" in the following. The range of the force feedback was 3.5 µm in every direction, limiting the ability to determine the run length of the motor as a function of sideward load force. Data for forces and microsphere positions were smoothed with a running median filter for visualisation. No data points from transients between the alternating loads were used for the analysis. As a measure for the overall sideward motion during alternating times, the $y$-position was fitted by a line; the difference between

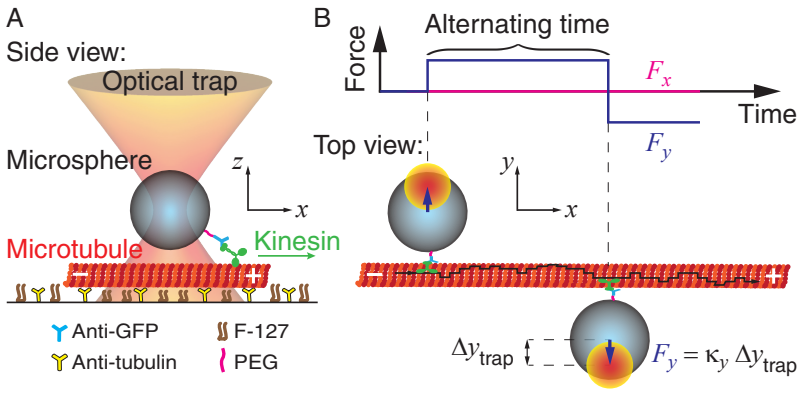


**Figure 7.1: Schematic of the 2D-force-clamp assay.** (A) Side view: A Kip3-coated microsphere is trapped with optical tweezers and placed on an immobilised microtubule. (B) Top view of a motor translocating toward the microtubule plus end ($x$-axis, black path) with no force applied in the direction of the microtubule axis. The motor is subjected to alternating, constant sideward loads of $F_y = \kappa_y \Delta y_{\text{trap}}$ perpendicular to the microtubule axis (in the $y$-direction), where $\Delta y_{\text{trap}}$ is the microsphere displacement from the trap centre and $\kappa_y$ is the trap stiffness in the $y$-direction. Schematics are not to scale. Modified from [148].

end and starting point of this fit has been taken as "sideward displacement" $\Delta y$. Sideward motion in the $y$-axis to the left is defined as positive change and vice versa. Means and variances were calculated; variances were averaged between different experiments. I preferentially used microtubules that were parallel to the flow cell channel coinciding with the $x$-axis of the detector and DIC camera image. The mean angle relative to this axis of all microtubules used in this work was $-2 \pm 7$ deg (SD, $N = 808$). The microtubule angle was determined via image analysis with a precision of better than 1 deg. Note that the force feedback automatically tracked the microtubule axis. The recorded data were rotated by this measured angle. Occasionally, this rotation angle was fine-adjusted in the MATLAB (MathWorks, Natick, Massachusetts, USA) analysis to minimise any overall trend in the $y$-position signal. I determined the zero-position of the $y$-axis with a precision of ≈10 nm corresponding approximately to the rms noise on the position traces. For a typical 50 s long trace, this precision resulted in a systematic deviation of $(10/50 = 0.2)$ nm/s. For an alternating time of 20 s, the systematic deviation would be about $20\,\text{s} \cdot 0.2\,\text{nm/s} = 4\,\text{nm}$. Because I averaged data obtained from many different microtubules, the mean of the systematic deviations should be zero. The error on the rotation angle increased the variance of $\Delta y$—for the 20 s example it would be 16 nm$^2$, which is approximately equal to the measurement precision. For shorter alternating times, the effect was even smaller. The measurement precision was estimated by determining $\Delta y$ of non-motile Kip3-coated microspheres in the presence of AMPPNP for alternating times of 5 s and various sideward loads of 0.3–2.2 pN.

To ensure the functionality of the motors, I measured the speed of Kip3-coated microspheres by video tracking [72] with the optical trap turned off. I determined the speed by linear fits to the tracked $x$-position.

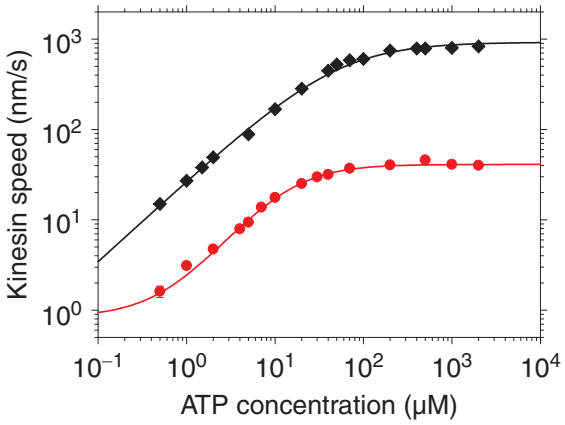


**Figure 7.2: ATP dependence of kinesin speeds.** Logarithmic plot of the speed of Kip3 (●) and rkin430 (◆) as a function of ATP concentration. At saturating ATP concentrations (>200 μM), the speeds were about 40 nm/s (Kip3) and 800 nm/s (rkin430). Data sets were fitted with Michaelis-Menten equations (Eq. 7.1, red line: Kip3, black line: rkin430).

## 7.2. TIRF Measurements Revealed ATP Dependence of Kinesin Speeds

In addition to the basic control measurements of kinesin speeds using TIRF microscopy described in Chapter 5, I measured the speeds of the kinesins Kip3 and rkin430 for a broad range of ATP concentrations. The results are plotted in Fig. 7.2. Both the speeds of Kip3 and rkin430 depended sensitively on the ATP concentration. The speeds at saturating ATP concentrations (>200 μM) were about 40 nm/s for Kip3 and 800 nm/s for rkin430. These data were already used as control in Chapter 5. The results for rkin430 were consistent with previous studies on other kinesin-1s [33, 34, 74, 110]. I fitted both data sets with a generalised Michaelis-Menten equation:

$$v = v_{\max}[\mathrm{ATP}]^{\zeta}/(K_{\mathrm{M}} + [\mathrm{ATP}]^{\zeta}). \tag{7.1}$$

Here, $v_{\max}$ is the maximal speed at saturating ATP concentration, $K_{\mathrm{M}}$ the so-called Michaelis-Menten constant, and $\zeta$ the Hill coefficient. The fitting parameters are given in Table 7.1.

## 7.3. Kip3 Slowed Down Under Off-Axis Loads

The speed of free Kip3-coated microspheres was 40 ± 2 nm/s ($N$ = 52, SEM if not noted otherwise), consistent with previous reports [19, 40, 96] and my own control measurements. This results has already been given in Table 5.1. With the trap turned on and no load applied in any direction (zero-force feedback), the speed was 39 ± 2 nm/s ($N$ = 90, zero-force data point in Fig. 7.3B), ensuring

**Table 7.1: Fitting results of kinesin speed, dependent on ATP concentration.** $v_{\max}$, maximal speed at saturating ATP concentrations; $K_{\mathrm{M}}$, Michaelis-Menten constant; $\zeta$, Hill coefficient for Kip3 and rkin430 with standard errors.

| Kinesin | $v_{\max}$ (nm/s) | $K_{\mathrm{M}}$ (μM$^{\zeta}$) | $\zeta$ |
|---|---|---|---|
| Kip3 | 40.2 ± 0.5 | 24 ± 2 | 1.21 ± 0.04 |
| rkin430 | 923 ± 40 | 34 ± 2 | 0.89 ± 0.02 |

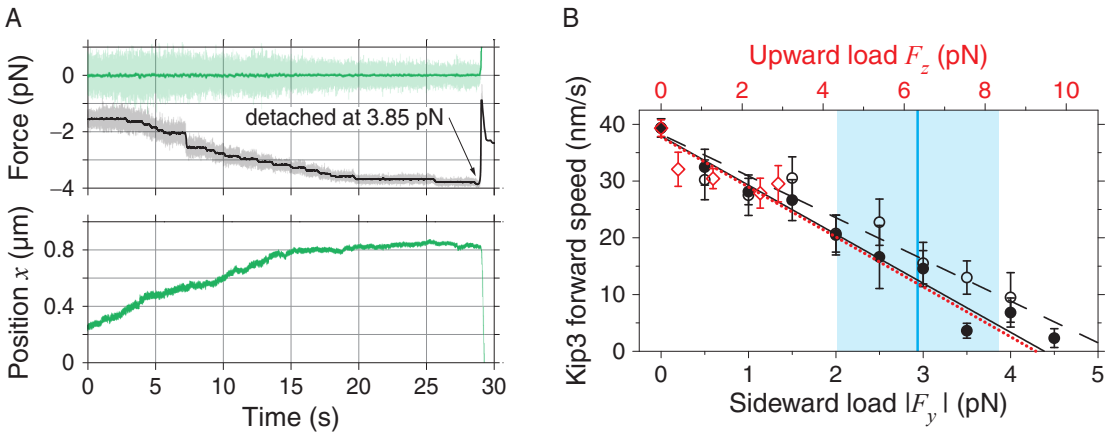


**Figure 7.3: Off-axis loads slowed down Kip3 motors.** (A) Upper Plot: Loads on a Kip3-coated microsphere, applied with a 2D force clamp in the forward direction $x$ (green line) and to the right side (black line). Lower plot: Forward position $x$ over time. The microsphere detached at around 29 s. (B) Forward speed as a function of the absolute value of sideward (○ and ● for left and right, bottom axis) and upward (◇, top axis) load. Linear fits to the data are indicated by the lines. Dashed and solid black lines: sideward loads with slopes of $-8.6 \pm 0.6\,\mathrm{nm\,s^{-1}\,pN^{-1}}$ (SE, $N = 10$) and $-7.3 \pm 0.6\,\mathrm{nm\,s^{-1}\,pN^{-1}}$ ($N = 9$) for leftward and rightward loads, respectively; red dotted line: upward loads with a slope of $-4.1 \pm 1.2\,\mathrm{nm\,s^{-1}\,pN^{-1}}$ ($N = 5$). The vertical blue line indicates the mean detachment force and the blue shaded region a range of two standard deviations around the mean. Modified from [148].

that the trap and feedback did not affect the motor. This speed was in agreement with the measurements using TIRF microscopy as already stated in Chapter 5. In single Kip3 runs with alternating sideward loads, the forward speed was only $31.5 \pm 0.6\,\mathrm{nm/s}$ ($N = 400$), corresponding to a forward stepping rate of $k_f \approx 4\,\mathrm{s^{-1}}$ for 8 nm steps [40]. To test whether the forward speed decreased with the sideward load, I applied a sideward load only to one side and increased it stepwise. I did not apply a load along the microtubule axis (Fig. 7.3A). This experiment has been already used to measure the standard deviation of the load as a function of the load (Fig. 3.8A). I found that the motor slowed down and eventually detached at a mean force of $2.9 \pm 0.2\,\mathrm{pN}$ ($N = 31$), averaged over left and right (Fig. 7.3B). Detachment forces and slopes did not significantly depend on the pulling direction. Based on the extrapolated fits, motors stalled at a sideward load of about 4.5–5 pN. Due to the geometry, the sideward load ($F_y$) also causes an upward load ($F_z$) on the motor. I will address the issue of the geometry in Section 7.6. The above results show that sideward loads moderately slowed down Kip3 compared to its ≈1.1 pN stall force on backward loads [40]. However, in contrast to kinesin-1 [74], no significant asymmetry was observed with respect to the sideward pulling direction.

I also applied upward loads of 0.5–3 pN on motile microsphere-bound Kip3, using the 3D force clamp. Measurements were done within the linear range of the optical trap (discussed in Section 3.3). I observed a decrease of the forward velocity as plotted in Fig. 7.3B.

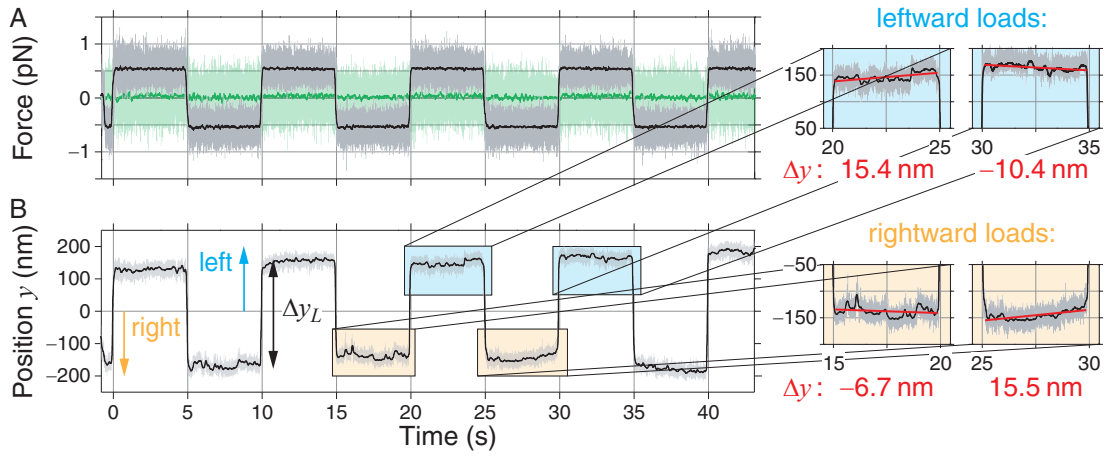


**Figure 7.4: Kip3-coated microspheres moved sidewards with and against loads.** (A) Sideward load force as a function of time (grey line: raw data with 4 kHz, black line: median filtered to 8 Hz). Zero-load was applied along the microtubule axis (light green line: raw data with 4 kHz, dark green line: median filtered to 8 Hz). (B) Sideward position $y$ perpendicular to the microtubule axis as a function of time. $\Delta y_L$ indicates the mean distance between the leftward- and rightward-pulled microsphere. Insets: Linear fits (red lines) to the sideward motion resulted in the sideward displacement $\Delta y$ indicated below the insets. Modified from [148].

## 7.4. Single Kip3 Motors Switched Protofilaments in Both Directions

To precisely measure the sideward motion of Kip3, I applied sideward loads of 0.5 pN perpendicular to the microtubule axis in the $y$-direction with no load along the microtubule axis (Fig. 7.1B, Fig. 7.4A). I regularly changed the direction of the load from left to right with different alternating times and recorded the $x$ and $y$-position of the trapped microsphere as a function of time. In the sideward direction, there were large transient displacements $\Delta y_L$ upon changing the load direction (Fig. 7.4B), which I attribute to the lever of the microsphere, motor and linker length. After the transient, small sideward displacements occurred during the constant-load time. I observed discrete sideward steps (Fig. 7.5A). The used step finder [96] detected a broad distribution of steps with and against load down to ≈3 nm and as large as 30 nm (see histogram in Fig. 7.5B) with a mean dwell time of ≈1 s (Fig. 7.5C). I observed a significant over-shoot of steps that followed the load. To check for an asymmetry in the mean dwell times in analogy to "limping" [30], I calculated the dwell times before steps with or against load for left and right, respectively. I did not find a significant difference between the means and the overall mean of ≈1 s in Fig. 7.5C. Surprisingly, the largest detected step sizes are larger than the largest projected distance between protofilaments of ≈6 nm and even larger than the ≈25 nm diameter of a microtubule. I attribute those large microsphere steps to (i) the geometry (Section 7.6), (ii) the possibility of two fast subsequent steps, and (iii) the intrinsic rms noise on the traces.

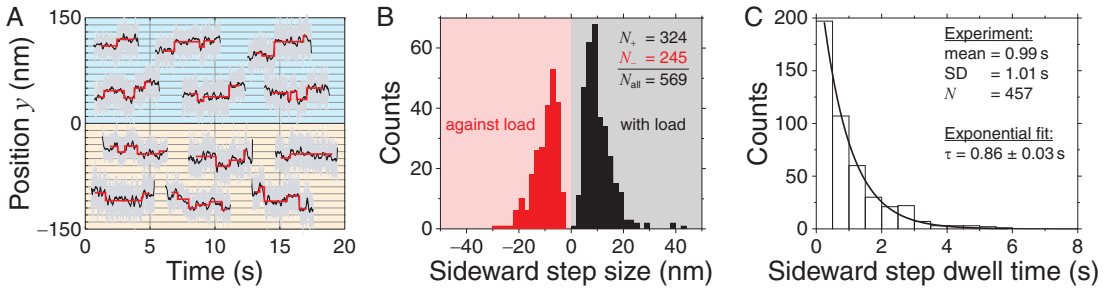


**Figure 7.5: Discrete sideward steps of Kip3.** (A) Representative traces for leftward (positive $y$) and rightward (negative $y$) loads, plotted together with detected steps (red lines). Traces are offset for clarity. (B) Histogram of detected step sizes from 95 plateaus of 28 traces for steps in the direction of or against the applied sideward load. (C) Histogram of experimental sideward step dwell times. An exponential (black line) was fitted to the experimental data. The mean, standard deviation (SD), and fitting result are given. Modified from [148].

Because it was impossible to detect all steps and the ones I could detect had a large, continuous variation in step sizes, I further analysed the sideward displacement $\Delta y$ during the alternating time *between* the transients (insets in Fig. 7.4). For this fit-based sideward displacement, I also measured a broad distribution of both positive and negative sideward displacements independent of the loading direction with displacements again exceeding the microtubule diameter (red distributions in Fig. 7.6). Interestingly, the mean values of the distribution significantly differed from zero: with a leftward and rightward load, there was a small mean displacement to the left and right, respectively, whereby the absolute value of the rightward displacement was larger. Together, these results suggest that Kip3 switched protofilaments in both directions and that the switching was asymmetrically biased by the loading force.

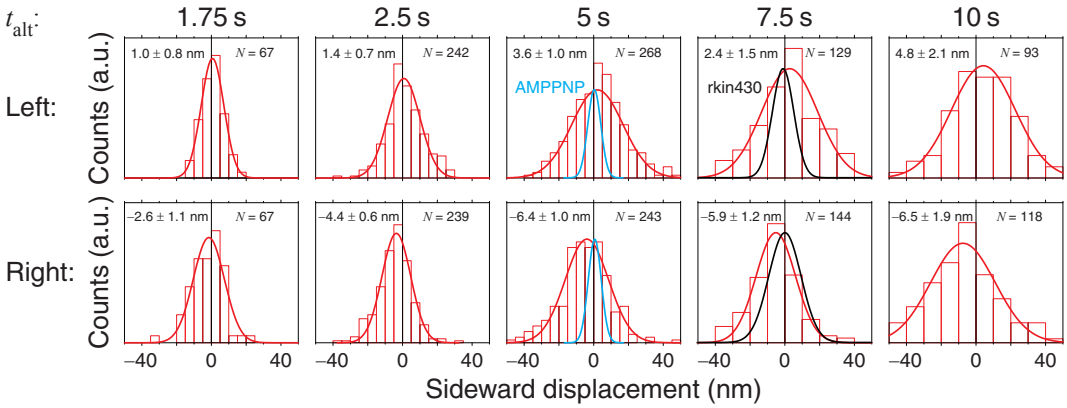


**Figure 7.6: Histograms of sideward displacements of Kip3.** Histograms and Gaussian fits (red lines) of sideward displacements $\Delta y$ of motile Kip3 for a sideward load of 0.5 pN and alternating times $t_{alt}$ of 1.75–10 s. The number $N$ of measured $\Delta y$'s and the mean ± SEM are given. For comparison, Gaussian fits of AMPPNP-bound Kip3 (blue line) for 5 s and rkin430 (black line) for 7.5 s, normalised to the same amplitude are plotted (see Figs. 7.9 and 7.10 for the corresponding data). Modified from [148].

### 7.4.1. The Mean and Variance of the Sideward Displacement of Kip3 Increased with Time

To determine whether protofilament switching was due to a directed or a random process, I varied the alternating time $t_{alt}$ (Fig. 7.6) and determined the mean and variance of the sideward displacement distribution. The absolute mean sideward displacements for left and right (open and closed red circles in Fig. 7.7A, respectively) first increased for alternating times less than about 10 s and then, within error bars, levelled off or slightly decreased.

Thus for Kip3, the increase in the mean sideward displacement supports the notion that the applied force biased the sideward stepping motion in the direction of the applied load. The variances of the distributions increased with time while also levelling off for longer times (Fig. 7.7B). The initial linear increase of the variance is reminiscent of a diffusive process. A linear fit of $2Dt_{alt} + 2\epsilon^2$ (dashed grey line in Fig. 7.7B) resulted in a sideward diffusion coefficient of $D = 20 \pm 1\,\mathrm{nm^2/s}$ and $\epsilon = 3.2 \pm 0.6\,\mathrm{nm}$. One can use this diffusion coefficient to estimate the average sideward stepping rate. To this end, I estimated the average projected distance between protofilaments on the top half of the microtubule to be $\langle \Delta y_p \rangle \approx 3.8\,\mathrm{nm}$ (Fig. 7.8). The underlying values of the projected distances were calculated from the geometry of a tridecagon, the arc length $\Delta s$ between two protofilaments, and the MT radius $r$. With this estimate, the sideward stepping rate was $k_{\Delta y_p} = 2D/\langle \Delta y_p \rangle^2 \approx 2.8\,\mathrm{s^{-1}}$. Taken together, the variance data for short alternating times is consistent with a random sideward walk. Yet, this simple analysis cannot account for the data at long alternating times and does not explain the broad distribution in sideward displacements and step sizes.

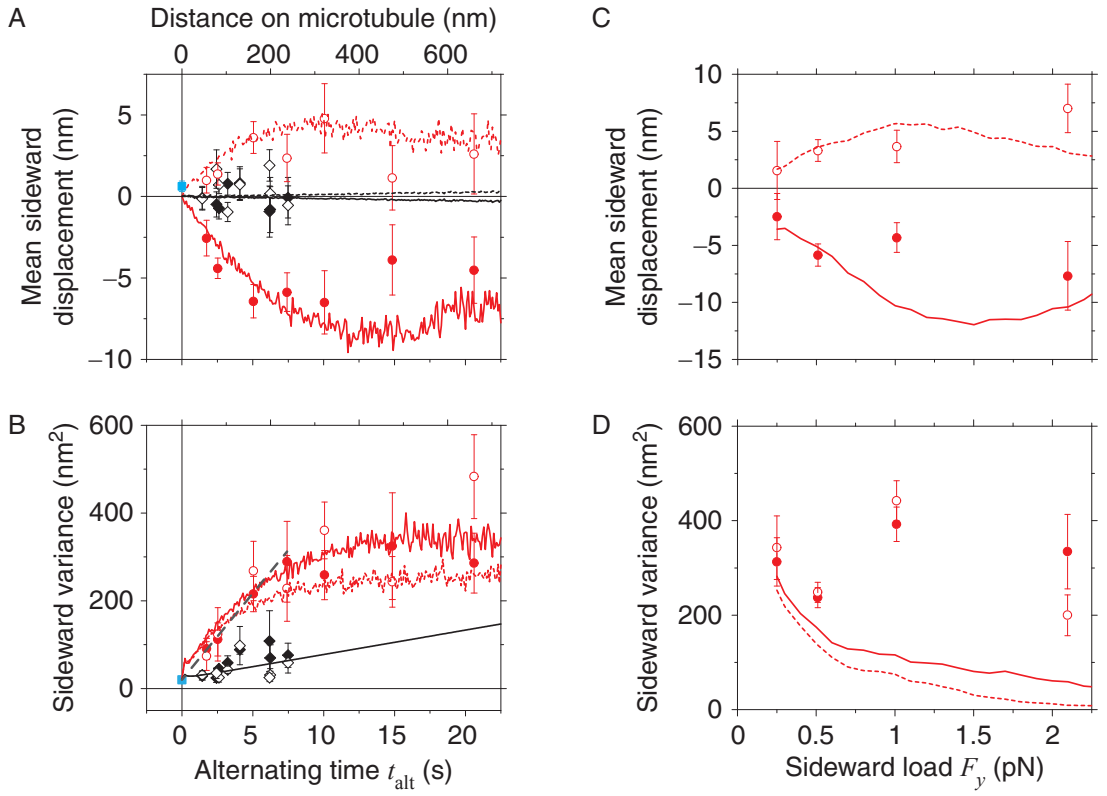


**Figure 7.7: Mean sideward displacements and variances for different alternating times and sideward loads.** (A) Mean sideward displacement and (B) variance as a function of alternating time with a sideward load of 0.5 pN for Kip3 (○ left and ● right), AMPPNP-bound Kip3 (■) and rkin430 (◇ left and ◆ right). Dashed and solid lines are the best-fit simulations for left and right, respectively (red: Kip3, black: rkin430). A linear fit (grey dashed) to the first four variance data points including both directions for Kip3. (C) Mean sideward displacement and (D) sideward variance as a function of the applied sideward load for Kip3 (○ left and ● right) and a constant alternating time of 5 s. Dashed and solid lines are the best-fit simulations for and left and right, respectively. Error bars are SEMs. Modified from [148].

### 7.4.2. The Mean Sideward Displacement of Kip3 Increased with Sideward Loads

In addition to the alternating time, I varied the sideward load for an alternating time of 5 s. The measurement revealed an increasing absolute mean sideward displacement with higher loads in both directions (Fig. 7.7C). The sideward variance showed no significant change as shown in Fig. 7.7D with an overall mean and SEM of $314 \pm 29\,\mathrm{nm}^2$. Based on video images, I attribute this large variance to insufficiently immobilised microtubules. In extreme cases, which were not used for data analysis, microtubules were visibly displaced in the lateral direction for forces exceeding 0.5 pN.

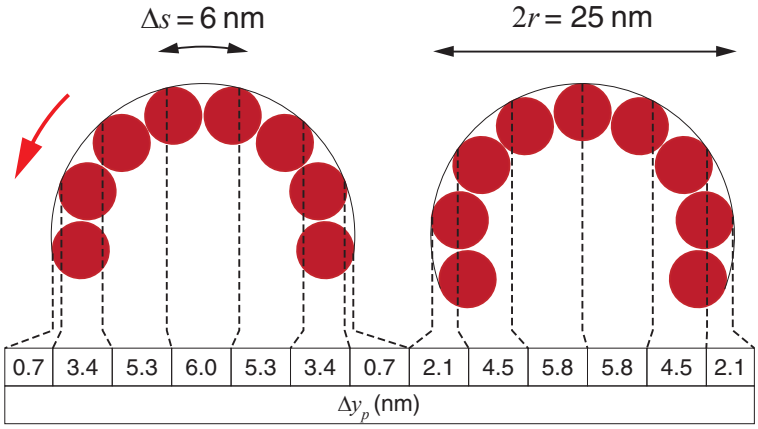


**Figure 7.8: Projected protofilament distances.** Upper half of a microtubule with a total of 13 protofilaments (red) in two angular orientations (left and right) with projected distances $\Delta y_p$ between protofilaments per sideward step to the left (red arrow). The average value is $\langle \Delta y_p \rangle = 3.8\,\text{nm}$. Modified from [148].

### 7.4.3. Immotile Kip3 Showed no Effective Sideward Motion

To determine the measurement precision, I applied sideward loads on immotile Kip3 either in assay buffer containing AMPPNP (Fig. 7.9A) or to pausing kinesins in the presence of ATP (Fig. 7.9B). Histograms of the sidewards displacements are plotted in Figs. 7.9C–H.

For AMPPNP assays, loads were applied both parallel and perpendicular to the microtubule axis. Sideward displacements $\Delta y$ were taken from 4 different microspheres (≥6 data points for several different forces in both directions). Since the lateral direction with respect to the MT plus end was unknown, I defined $\Delta y$ to be positive in the direction of load. T-tests ensured that the means for every force and direction were not significantly different from zero on the 95 % confidence level and thus consistent with each other[1]. Therefore, all sideward displacements were plotted in one histogram for each direction (Figs. 7.9C and D, corresponding Gaussian fit in Fig. 7.6). The mean values were less than 1 nm and not significantly different from zero. The weighted mean and SEM for both directions were $0.2 \pm 0.2\,\text{nm}$. If not noted otherwise, weighted means were weighted by the reciprocal squared standard error. Because motors were not moving, I plotted the mean and variance of Fig. 7.9C in Figs. 7.7A and B, respectively at an effective alternating time of zero. The variances of the distributions of $\Delta y$ were significantly smaller than in measurements using Kip3 in the presence of ATP.

Also, for pausing kinesin motors the means were not significantly different from zero (Figs. 7.9E–H). The rare pausing events seemed to be related to the tubulin batch. They occurred in Kip3 as well as in rkin430 assays but less often with other tubulin preparations. The variances for AMPPNP-bound Kip3 and pausing kinesins were all of similar sizes (Fig. 7.9). The average was $17\,\text{nm}^2$ which was in reasonable agreement with the offset $2\epsilon^2 = 20\,\text{nm}^2$ for the Kip3 variance data in Fig. 7.7B.

[1]For one perpendicular force, the individual mean was significantly different from zero but did not hold a Bonferroni correction.

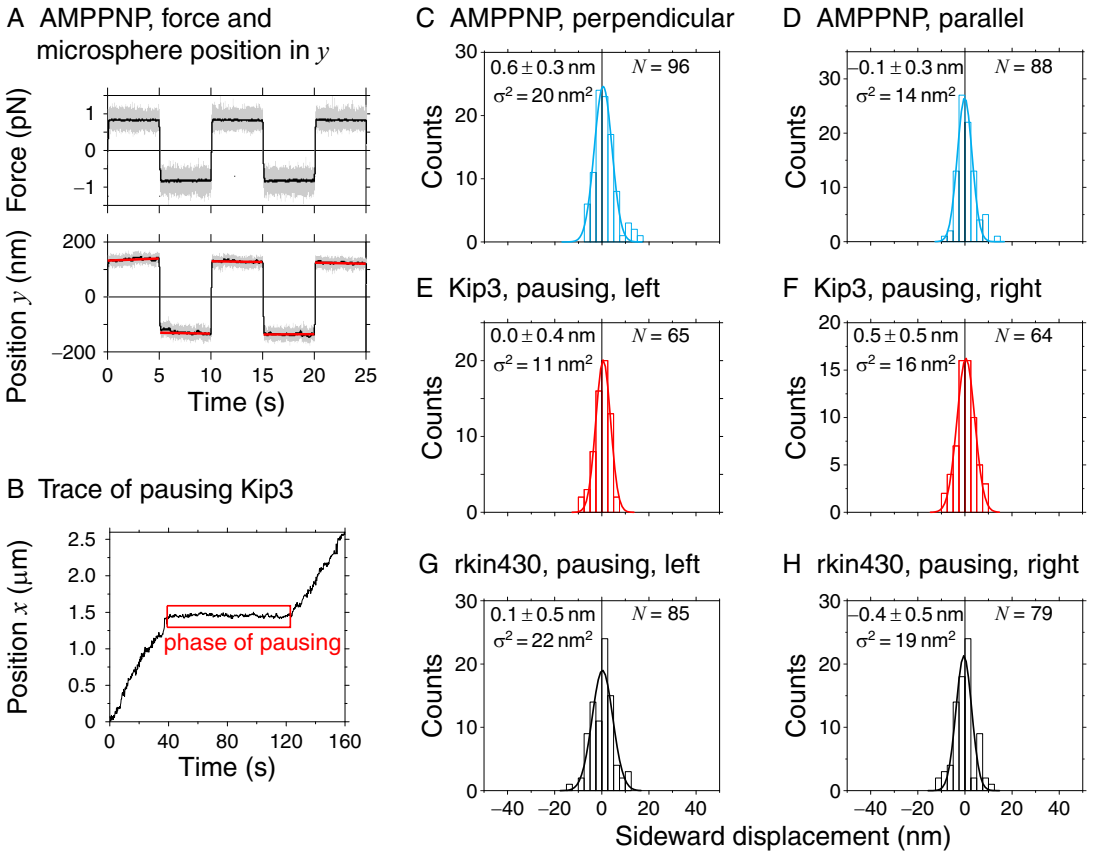


**Figure 7.9: Histograms of sideward displacements of immotile kinesins.** (A) Force (top) and microsphere position (bottom) as a function of time of stationary Kip3 in the presence of AMPPNP under loads of ≈0.8 pN and an alternating time of 5 s including linear fits (red lines). (B) Phase of pausing for a non-trapped microsphere pulled by Kip3 and tracked via video microscopy. (C–H) Histograms with Gaussian fits of sideward displacements for (C) AMPPNP-bound Kip3, perpendicular to the microtubule axis and (D) parallel to the microtubule axis, (E) pausing Kip3 with left and (F) right sideward loads of 0.5 pN, pooled for various alternating times (1.75–20 s), (G) pausing rkin430 with left and (H) right sideward loads of 0.5 pN. Sample numbers $N$, means ± SEMs, and variances $\sigma^2$ are given. Modified from [148].

## 7.5. rkin430 Showed no Effective Sideward Motion

To slow down rkin430 to speeds comparable to Kip3, I reduced the ATP concentration in the buffer to 1–2 µM. With the reduced ATP concentrations in four different experiments, the mean speeds were 21 ± 1 nm/s ($N$ = 45), 28 ± 2 nm/s ($N$ = 58), 37 ± 1 nm/s ($N$ = 36), and 51 ± 2 nm/s ($N$ = 106). The sideward load of 0.5 pN was alternated every 1.5–6 s. Longer alternating times were not feasible, as rkin430-coated microspheres detached on average before the end of the alternating time, consistent with kinesin-1's lower processivity compared to Kip3. I measured no decrease in the velocity due to the sideward loads. To compare the measured sideward displacements with those of Kip3, the alternating time $t_{\mathrm{alt}}$ was converted into an effective alternating time $t^{\mathrm{eff}}_{\mathrm{rkin430}}$, based on an equal number of forward steps on the microtubule lattice, i.e. equal distance:

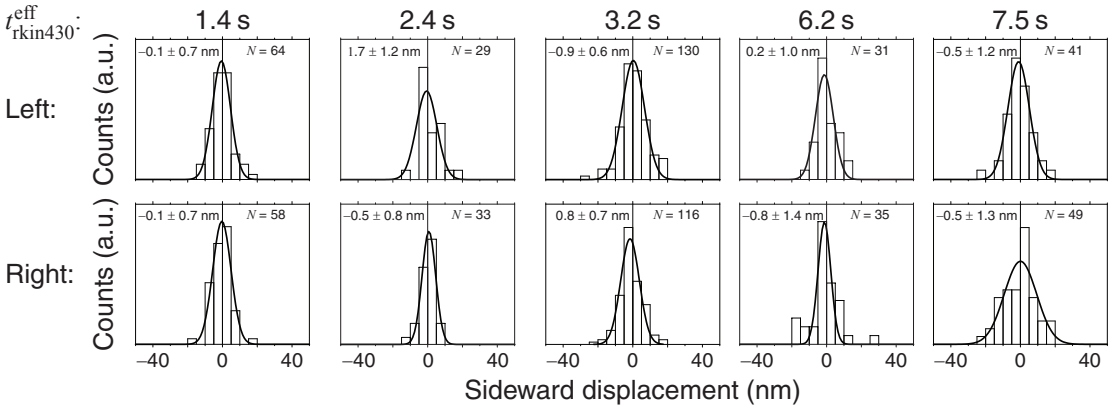


**Figure 7.10: Histograms of sideward displacements of rkin430.** Histograms and Gaussian fits (black lines) of sideward displacements $\Delta y$ of motile rkin430 for a sideward load of 0.5 pN and different effective alternating times $t^{\text{eff}}_{\text{rkin430}}$. Sample numbers $N$ and means ± SEMs are given. Modified from [148].

$t^{\text{eff}}_{\text{rkin430}} = t_{\text{alt}} \cdot v_{\text{rkin430}}/v_{\text{Kip3}}$. The effective alternating time of 0 s for AMPPNP-bound Kip3 in the previous section and Fig. 7.7 was calculated the same way.

For rkin430, the mean sideward displacements showed no significant increase over time for left nor right (Fig. 7.7A, Gaussian fits in Fig. 7.6, histograms shown in Fig. 7.10). This was additionally confirmed by Pearson correlation tests: The correlation coefficients were 0.04 for left and 0.22 for right.

All means were statistically consistent with zero, confirmed by a $\chi^2$ (chi-square) test. The weighted mean and standard error of all alternating times and pulling directions were $-0.1 \pm 0.2$ nm, indicating that kinesin-1 did not show any net sideward motion. The sideward variances of rkin430 increased less over time, compared to the increase of the variance of Kip3 (Fig. 7.7B). If rkin430 switched between protofilaments with a low probability and without being biased in the direction by the load, a diffusion constant for rkin430's sideward motion can be calculated from the variance data, similarly to Kip3. A linear fit (not shown) resulted in a diffusion constant of $D = 4.4 \pm 0.8\,\text{nm}^2/s$ which was an order of magnitude smaller than the estimated value for Kip3. The offset $2\epsilon^2$ was $19 \pm 4\,\text{nm}^2$ and consistent with the fitted value for the Kip3 data. The corresponding sideward stepping rate, based on the same average projected distance between protofilaments, was $k_{\Delta p} \approx 0.6\,\text{s}^{-1}$. At an effective forward stepping rate of $\approx 4\,\text{s}^{-1}$, every 8th step or 12.5 % of all steps would to the side. Stepping assays with quantum-dot-labelled kinesin-1 by Yildiz et al. revealed a probability for sideward steps of 13 % at similar ATP concentrations and speeds [51]. These values would be in good agreement to the results of my side-stepping assays. However, as already noted above, this simple model of projected sideward steps cannot account for the underlying geometry in this assay. Furthermore, it is not clear how the applied sideward loads influence the stepping behaviour. The absence of an asymmetry between left and right seems contradictory to other studies with kinesin-1 by Block et al. [74], who observed an asymmetric slow down of the forward speed due to high sideward loads of up to 8 pN.

Assuming that rkin430 did not switch between protofilaments at all, its time-dependent variance data can be used as a measurement of the time-dependent measurement precision. This precision was limited by experimental noise, e.g. microtubule fluctuations and the diffusion of the microsphere in the optical trap. This time dependence was an important complement to the precision measurement with immotile kinesins which only accounted for an effective alternating time of zero. This "background measurement" of the sideward variance was used for the quantitative analysis in the next section.

## 7.6. A Simulation Accounting for the Geometry Supported Asymmetrically Biased Diffusion of Kip3

### 7.6.1. Geometry of the 2D Side-Stepping Assay

To gain a deeper understanding of the observed data, I considered the experimental geometry. In the above estimate for the sideward stepping rate, it was tacitly assumed that the projected distance between protofilaments corresponds to the microsphere displacements that was measured. This assumption does not hold on close inspection of the geometry drawn to scale in Fig. 7.11A. The microsphere with radius $R$ was held by the optical trap which pulled the linker of length $L$ between the microtubule of radius $r$ and the microsphere taut.

I assume that the microsphere did not change its distance $h$ to the surface during the stepping motion of the motors but was kept on a constant height by the force clamp and the repulsive surface potential. This assumption is supported by surface force measurements [68] and the vertical displacements during the alternating time which on average did not significantly differ from zero (lower inset in Fig. 7.11A). With this geometry, the lateral microsphere centre position $y$ can be calculated from the angular motor position $\phi$ on the microtubule by

$$y(\phi) = \sqrt{(L+R)^2 - (R+h-r(1+\sin\phi))^2} + r\cos\phi. \tag{7.2}$$

Equation 7.2 has a maximum at $\phi_{\max} = \arcsin[(R+h-r)/(R+L+r)]$. If a motor moves sideward beyond two critical angles $\phi_1^*$ and $\phi_2^*$, the linker between the microtubule and microsphere starts to coil around the microtubule. In this case, the microsphere position was calculated based on a reduced linker length: $L(\phi) = L - r\cdot\left|\phi - \phi_{1,2}^*\right|$ for $\left|\phi\right| > \left|\phi_{1,2}^*\right|$. Note that the exact angular position of $\phi_{1,2}^*$ during coiling is not constant. However, the deviation from the initial value is negligible. The critical angles are given by:

$$\phi_{1,2}^* = \arcsin\left\{\frac{A(R+L) \pm r\sqrt{B^2 - A^2}}{B^2}\right\} \mp \frac{\pi}{2}, \tag{7.3}$$

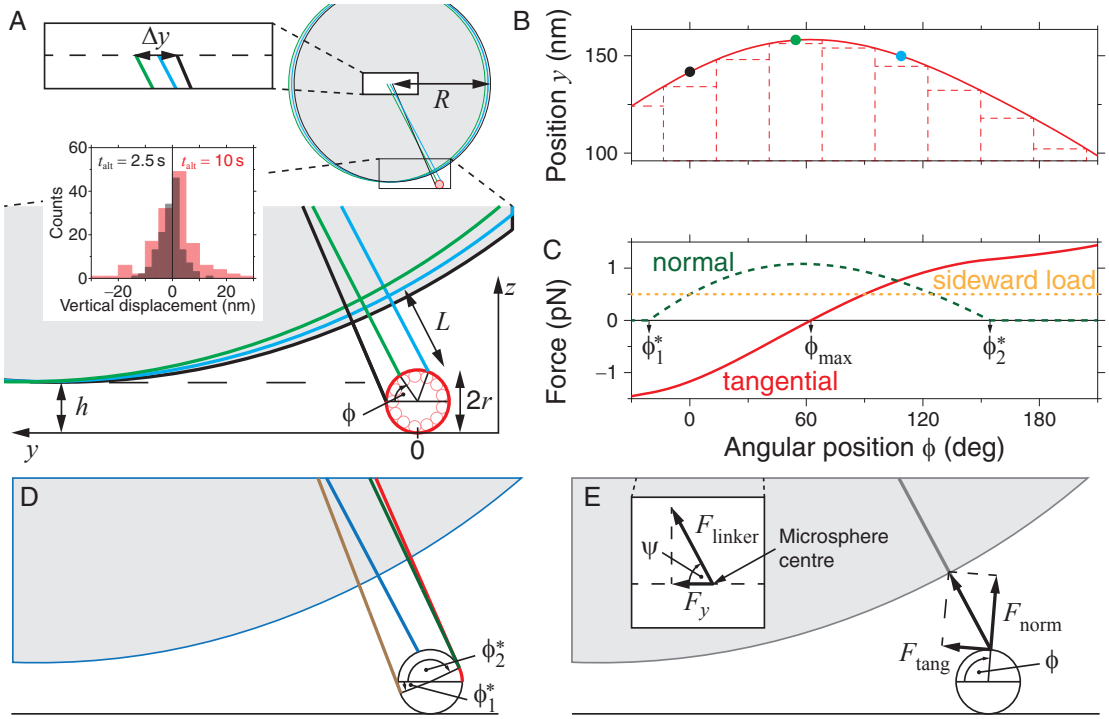


**Figure 7.11: Geometry of the 2D side-stepping assay.** (A) Geometry of microsphere (grey), linker and microtubule (red) drawn to scale. The different colours (black, green, blue) correspond to different angular motor positions. Upper inset: Magnification of microsphere centre position. Lower inset: Histogram of vertical displacements $\Delta z$ for alternating times of 2.5 s (black) and 10 s (red). Means ± SEMs were $0.2 \pm 0.4$ nm ($N = 146$) and $0.1 \pm 0.8$ nm ($N = 138$), respectively. (B) Microsphere position $y$ as a function of angular motor position $\phi$ with a 28 deg-grid to illustrate the various sideward step sizes between protofilaments. Coloured points (black, green, blue) indicate the angular positions sketched in (A). (C) Plot of the tangential (red) and normal force (green dashed) acting on Kip3 as a function of angular position $\phi$ relative to the applied sideward load (ocher dotted). (D) Schematic drawn to scale, illustrating the critical angles and coiling of the linker if the motor moved sideward beyond the critical angles (brown: $\phi = \phi_1^*$, green and red, respectively: $\phi \geq \phi_2^*$). (E) Schematic of the tangential, linker, normal, and sideward load forces. Modified from [148].

where $A = R + h - r$ and $B^2 = (R + L)^2 + r^2$. The microsphere radius was $R = 295$ nm, the linker length $L = 34$ nm. The height was $h = 20$ nm, based on surface potential measurements with optical tweezers, described in [68], and the MT radius was $r = 12.5$ nm. The critical angles are: $\phi_1^* = -21.0$ deg and $\phi_2^* = 154.6$ deg with the maximum angle being $\phi_{max} = 62.4$ deg.

Accounting for coiling, the microsphere centre position $y(\phi)$ as a function of the angular motor position $\phi$ is given by

$$y(\phi) = \begin{cases} \sqrt{C_1^2 - D_1^2} + r\cos\phi_1^* & \text{for } \phi < \phi_1^* \\ \sqrt{(L+R)^2 - E^2} + r\cos\phi & \text{for } \phi \in [\phi_1^*, \phi_2^*] \\ \sqrt{C_2^2 - D_2^2} + r\cos\phi_2^* & \text{for } \phi > \phi_2^*, \end{cases} \tag{7.4}$$

where

$$\begin{aligned} C_i &= R + L - r\left|\phi - \phi_i^*\right| \\ D_i &= R + h - r(1 + \sin\phi_i^*) \\ E &= R + h - r(1 + \sin\phi) \end{aligned} \tag{7.5}$$

with $i$ = 1,2. The coiling correction is a small correction for the microsphere displacements. Figure 7.11B shows this non-linear relation. Based on the geometry and the orientation of the microtubule protofilaments in Fig. 7.8, one can use Eq. 7.4 to estimate the mean sideward step size $\Delta y_s$ as measured by the microsphere. For the assumed MT orientations in Fig. 7.8, the mean sideward stepping distance of the microsphere centre is $\langle \Delta y_s \rangle \approx 8.9\,\text{nm}$. Using this value, one can re-estimate the sideward stepping rate. Based on the mean sideward stepping distance of the microsphere centre, the rate is $k_{\Delta y} = 2D/\langle \Delta y_s \rangle^2 = 0.5\,\text{s}^{-1}$ for Kip3 and $0.11\,\text{s}^{-1}$ for rkin430 which is each about 5× lower compared to the estimated values based on the projected filament distance. Thus, the geometry leads to counter-intuitive movement of the microsphere and does not allow for an analytical solution to describe the data. In addition to the estimated mean sideward stepping distance of the microsphere, Fig. 7.12 shows $\Delta y_s$ as a continuous function of angle $\phi$ for discrete sideward steps $\Delta\phi_{\text{pf}}$. Here, the microsphere sideward step size was calculated by $\Delta y_s = y(\phi) - y(\phi + \Delta\phi_{\text{pf}})$, using Eq. 7.4 for $y(\phi)$.

Overall, Eq. 7.4 and the corresponding microsphere displacements upon sideward stepping are consistent with the large sideward displacements seen in the experiment (Figs. 7.5 and 7.6). For the angular range shown in Fig. 7.11B, the difference between the maximum and minimum position is $\Delta y \approx 60\,\text{nm}$. Thus, sideward *microsphere* displacements of up to 60 nm are possible even though the motor has only moved roughly the projected distance corresponding to the microtubule diameter of 25 nm. The geometry results in an amplified microsphere displacement compared to the motor displacement. For single steps, the microsphere displacements can continuously vary between −30 nm and +40 nm (Fig. 7.12), consistent with the measured broad step size distribution (Fig. 7.5C).

As already noted, Eq. 7.4 is non-monotonic but has a maximum. This maximum results in a counterintuitive phenomenon: If in a gedanken experiment the motor starts at an angular position close to the maximum (green lines and

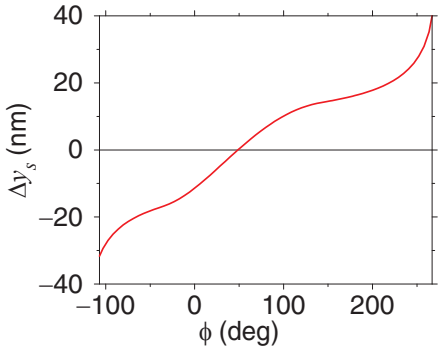


**Figure 7.12: Microsphere displacement between neighbouring protofilaments.** Plot of $\Delta y_s$ over a wide range of angular positions $\phi$, calculated by $\Delta y_s = y(\phi) - y(\phi + \Delta\phi_{\text{pf}})$, using Eq. 7.4 for $y(\phi)$ and $\Delta\phi_{\text{pf}} = 27.7\,\text{deg}$.

position in Figs. 7.11A and B, respectively) and takes two clockwise angular steps to the right (blue lines and position in Figs. 7.11A and B), the microsphere centre position also moves to the right (upper inset in Fig. 7.11A). However, if the motor takes two counter-clockwise angular steps to the left (black lines and position in Figs. 7.11A and B), the microsphere centre position does not move to the left but also to the right. Thus, the microsphere movement may not reflect the angular directionality of the motor nor the projected distance between protofilaments. For the same reason, the directionality and magnitude of the force acting on the motor may differ from the applied load (Fig. 7.11C). Based on the geometry, I defined the following forces: $F_{\text{tang}}$ was tangential to the MT cross section, $F_{\text{linker}}$ pointed from the motor to the microsphere centre, and $F_{\text{norm}}$ was normal to the MT cross section as illustrated in Fig. 7.11D. In the angular range without coiling of the linker, the tangential force on the motor is given by $F_{\text{tang}} = F_{\text{linker}} \sin(\phi - \psi)$. The force in the direction of the linker is $F_{\text{linker}} = F_y / \cos\psi$, where $F_y$ is the constant sideward load and $\psi$ is the angle between linker and surface calculated according to

$$\psi(\phi) = \arcsin \begin{cases} D_1/C_1 & \text{for } \phi < \phi_1^* \text{ in radians} \\ E/(R+L) & \text{for } \phi \in [\phi_1^*, \phi_2^*] \\ D_2/C_2 & \text{for } \phi > \phi_2^*. \end{cases} \tag{7.6}$$

For angles beyond the critical ones, the tangential force equals the linker force with reduced linker length. Thus, the tangential force is calculated by:

$$F_{\text{tang}}(\phi) = F_y \begin{cases} -1/\cos\psi(\phi) & \text{for } \phi < \phi_1^* \\ \sin(\phi - \psi(\phi))/\cos\psi(\phi) & \text{for } \phi \in [\phi_1^*, \phi_2^*] \\ +1/\cos\psi(\phi) & \text{for } \phi > \phi_2^*. \end{cases} \tag{7.7}$$

Without coiling, the normal force on Kip3 is calculated by $F_{\text{norm}} = F_{\text{linker}} \cos(\phi - \psi)$ and with coiling, the normal force is zero (see Fig. 7.11C):

$$F_{\text{norm}}(\phi) = F_y \begin{cases} 0 & \text{for } \phi < \phi_1^* \\ \cos(\phi - \psi(\phi))/\cos\psi(\phi) & \text{for } \phi \in [\phi_1^*, \phi_2^*] \\ 0 & \text{for } \phi > \phi_2^* \,. \end{cases} \tag{7.8}$$

Depending on the angular position of the motor, the tangential force, corresponding to the sideward force in the reference frame of the motor (red solid line in Fig. 7.11C), can be more than twice the sideward load applied with the optical tweezers (ocher dotted line in Fig. 7.11C) and of opposite direction. Note that at the maximal displacement of the microsphere, the tangential force is zero and the normal force (green dashed line in Fig. 7.11C) reaches a maximum. Thus, all forces that act on the motor in a side-stepping assay are not constant but change non-linearly with the motor position.

The geometry of the assay can also be used to estimate the mean linker length $L$. Based on the measured large, transient sideward displacements $\Delta y_L$ (Fig. 7.4) and using the angular-motor-position-to-microsphere-position con-

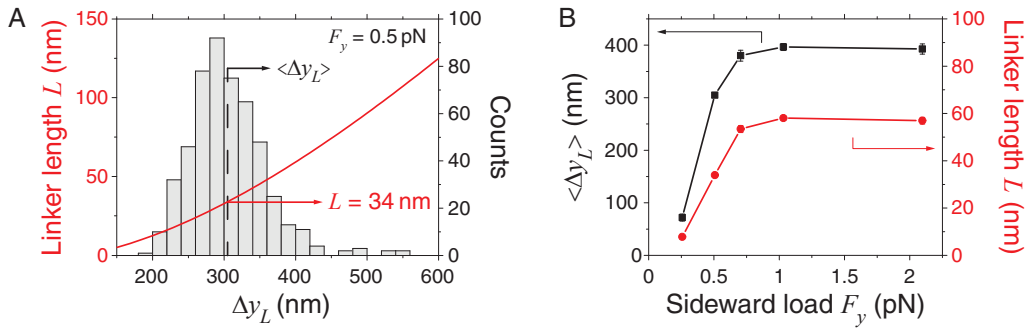


**Figure 7.13: Transient sideward displacements and linker lengths.** (A) Linker length $L$ (red line, left axis) as a function of large, transient sideward displacements $\Delta y_L$ for a sideward load of 0.5 pN. Plotted is the inverse of Eq. 7.9 using $\phi = \phi_{\text{max}}$. The mean (dashed line) of the $\Delta y_L$ histogram (right axis) intersects the red line at the linker length I used for all calculations. (B) Mean transient displacements $\langle \Delta y_L \rangle$ (■) and corresponding linker length $L$ as a function of the applied sideward load (●). Lines are guides to the eye. Modified from [148].

version (Eq. 7.2), one can determine the linker length $L$ under 0.5 pN load by

$$\Delta y_L = 2\sqrt{(L+R)^2 - (R+h-r(1+\sin\phi))^2}. \tag{7.9}$$

I assumed that after sideward pulling, the motor has reached on average the angular position $\phi_{\text{max}}$. For this angle, I plotted the linker length $L$ as a function of $\Delta y_L$ (red line in Fig. 7.13A). Also plotted in Fig. 7.13A is the histogram of the large, transient displacements with a mean of $\langle \Delta y_L \rangle = 305 \pm 2$ nm (SEM, $N = 509$). Graphically, the intersection of the mean with the red line resulted in the linker value of $L = 34 \pm 1$ nm at 0.5 pN which I used in all calculations. An estimation of the linker length can be made from the known structure of Kip3: The short coiled coil region of about 28 amino acids (Fig. 2.2C) is about 4 nm long when considered a regular coiled coil of two parallel $\alpha$-helices [149]. According to the crystal structure of the very similar human kinesin-8 Kif18A, the motor domain is about 4 nm thick (protein data bank code: 3LRE, [150]). As the tail region including the eGFP is of similar size as the motor domain, I estimated the size to be 4 nm as well. The length of the unstretched PEG linker is less than 1 nm, according to force-extension measurements by Kienberger et al. [151]. Summed up, the relaxed Kip3/PEG linker is about 12–14 nm. The measured linker length under loads was larger than this value and thus consistent. Only for very small loads (0.25 pN) the length of 8 nm was smaller than the contour length indicating that the linker may had additional folded regions. Analogously, the linker length for rkin430 for a sideward loads of 0.5 pN was $L = 52 \pm 1$ nm based on $\langle \Delta y_L \rangle = 376 \pm 4$ nm ($N = 466$). This indicated that rkin430 was significantly longer and/or less stiff than Kip3. The mean transient displacement $\langle \Delta y_L \rangle$ and linker length $L$ as a function of the sideward load are plotted in Fig. 7.13B. The increase of $\Delta y_L$ indicates a stretching of the protein/PEG linker. This stretching is in agreement with my previous measurement of Kip3 stretching in the presence of AMPPNP [92].

**Table 7.2: Microtubule composition.** Protofilament numbers, supertwist pitches, reciprocal pitches and abundances for microtubules, grown in BRB80, $MgCl_2$, GTP and DMSO. Left-handed supertwist pitches are denoted as positive and vice versa. The last line contains the average values, weighted according to the abundances.

| Protofilament number | Supertwist pitch $P$ (μm) [1, 14] | Reciprocal supertwist pitch $rP$ ($\mu m^{-1}$) | Abundance (%) [11] |
|---|---|---|---|
| 12 | −4.5 | −0.222 | 0 |
| 13 | ∞ | 0 | 14 |
| 14 | +5.8 | +0.172 | 72 |
| 15 | +3.3 | +0.303 | 11 |
| 16 | −5.5 | −0.181 | 3 |
| weighted mean | +6.58 | +0.152 | |

## 7.6.2. Simulation of Sideward Motion

To quantitatively describe all the data, we simulated the sideward motion of the kinesin motors accounting for the geometry. Therefore, we programmed a simulation routine in Java (Oracle Corporation, Redwood City, CA, USA) and analysed it in MATLAB. The simulation was based on the following model: Kip3 steps to the left, right, or forward with the zero-force stepping rates $k_l^0$, $k_r^0$, and $k_f$, respectively. The side-stepping rates are influenced by an applied tangential load in an Arrhenius-type, exponential manner [152]:

$$k_{l,r}(F_{\text{tang}}) = k_{l,r}^0 \exp(\pm F_{\text{tang}} \cdot x_{l,r}^\dagger / k_B T), \tag{7.10}$$

where $x_{l,r}^\dagger$ are the distances to the transition states for the respective directions, $F_{\text{tang}}$ is the tangential force acting on the motor, $k_B$ the Boltzmann constant, and $T$ the absolute temperature. A positive tangential force $F_{\text{tang}} > 0$ to the left increases the stepping rate to the left and decreases the rate to the right. To account for the dependence of the Kip3 velocity on the sideward load, we used a forward stepping rate of $31.5\,\text{nm}\,\text{s}^{-1} / 8\,\text{nm} = 3.9\,\text{s}^{-1}$ corresponding to the measured mean forward velocity. In the simulation, Kip3 performed a random walk on a cylinder with angular steps of $\Delta\phi_{\text{pf}} = \pm 27.7\,\text{deg}$, where $\Delta\phi_{\text{pf}}$ is the angle between neighbouring protofilaments in a 13 protofilament microtubule. Forward steps were $\delta_x = 8\,\text{nm}$ large—the distance between kinesin binding sites on a protofilament. The control experiment with rkin430 was simulated without sideward steps and a constant forward stepping rate. Additionally, we accounted for the microtubule supertwist.

Taxol-stabilised microtubules (grown in BRB80, $MgCl_2$, GTP and DMSO) are supposed to be built of 13–16 protofilaments with 14 occurring most often [11]. The distribution of the number of microtubule protofilaments is given in Table 7.2. We assumed the same distribution in our microtubules. The tubulin origin, porcine instead of bovine, was the only difference in the preparation of the microtubules compared to [11]. Based on this distribution, we calculated a mean reciprocal pitch by weighting the reciprocal pitches in Table 7.2 according to their abundances. Thus, the mean reciprocal pitch was $0.152\,\mu m^{-1}$ corresponding to a mean pitch of 6.58 μm. On a 13 protofilament microtubule, such a pitch

**Table 7.3: Numbers of used microtubules and load switches.** Average number of alternating times $N_{sw}$, i.e. switches of load direction, per trace and number of used microtubules ($N_{MT}$) for different alternating times $t_{alt}$ and different sideward loads $F_y$ for all kinesin side-stepping assays. The effective alternating times for rkin430 $t^{eff}_{rkin430}$ refer to different forward speeds. The total number of different microtubules used is indicated. The same microtubules have been used for multiple alternating times.

| Kip3 | | | | | | rkin430 | | | |
|---|---|---|---|---|---|---|---|---|---|
| $F_y = 0.5$ pN | | | $t_{alt} = 5$ s | | | $F_y = 0.5$ pN | | | |
| $t_{alt}$ (s) | $N_{sw}$ | $N_{MT}$ | $F_y$ (pN) | $N_{sw}$ | $N_{MT}$ | $t_{alt}$ (s) | $t^{eff}_{rkin430}$ (s) | $N_{sw}$ | $N_{MT}$ |
| 1.75 | 18 | 15 | 0.25 | 10 | 13 | 1.6 | 1.4 | 16 | 12 |
| 2.5 | 14 | 38 | 0.5 | 12 | 61 | 1.5 | 2.4 | 14 | 26 |
| 5 | 12 | 61 | 1 | 16 | 8 | 4.0 | 2.6 | 14 | 14 |
| 7.5 | 10 | 39 | 2.1 | 8 | 6 | 4.9 | 3.2 | 12 | 20 |
| 10 | 6 | 50 | | **Total:** | **88** | 2.5 | 4.1 | 12 | 22 |
| 15 | 4 | 53 | | | | 7.0 | 6.2 | 8 | 8 |
| 20 | 2 | 44 | | | | 5.3 | 6.2 | 6 | 2 |
| | **Total:** | **164** | | | | 4.7 | 7.5 | 6 | 10 |
| | | | | | | | | **Total:** | **57** |

would correspond to one sideward step to the left for 63 forward steps or a net leftward stepping rate of $0.06\,s^{-1}$, assuming a forward stepping rate of $4\,s^{-1}$ at $F_y = 0.5$ pN. Since the measured sideward stepping rate of about $1\,s^{-1}$, based on the mean sideward dwell time, was much higher, we do not expect that the supertwist had a significant influence on our measurements.

Nonetheless, we considered the supertwist by coupling a forward step with a small angular displacement of $\pm 2\pi\delta_x \cdot rP$, where $rP$ is the reciprocal pitch. Similarly, a sideward step was coupled to a small forward displacement of ±0.96 nm, corresponding to the geometry of a microtubule with a supertwist pitch $P$ [50] and forward step size $\delta_x = 8$ nm. Furthermore, because the distance to the directly adjacent tubulin dimers is shortest [1, 50], we assumed that a sideward step is to one of the neighbouring tubulin dimers and not diagonally to the front left or front right. Backward steps were not considered. Phases of pausing were also not included into the simulation, as the experimentally measured pausing events were not included into the side-stepping analysis. First, we simulated the forward stepping motion with an exponential distribution for the step duration with a mean of $k_f^{-1}$ [40] assuming that forward and sideward stepping are uncorrelated. Subsequently, we simulated and superimposed the sideward stepping motion. The probability of stepping to the left and right was calculated by the ratio of the corresponding rate to the sum of rates

$$P_{l,r} = \frac{k_{l,r}}{k_l + k_r}. \tag{7.11}$$

The duration of sideward steps were chosen to be also exponentially distributed with a mean dwell time of $(k_l + k_r)^{-1}$. An exponential distribution was consistent with my measurements (Fig. 7.5C). The angular starting position on the micro-

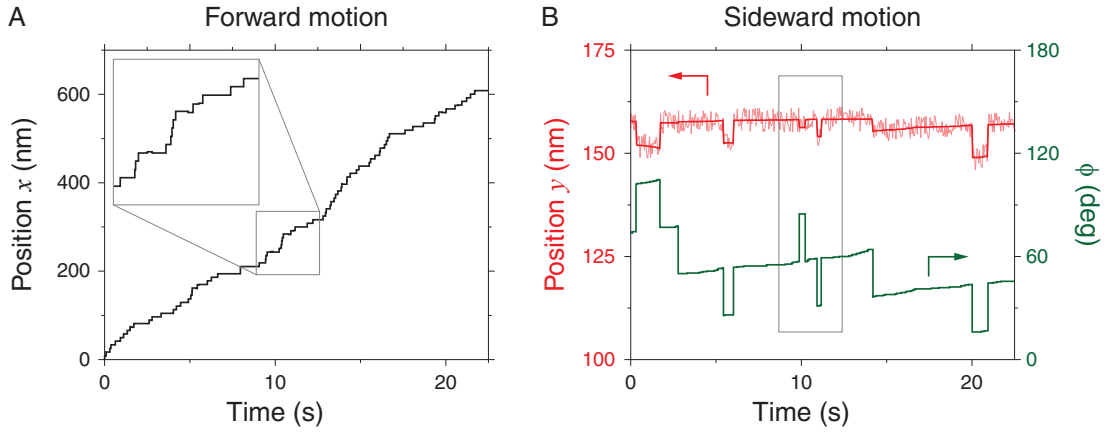


**Figure 7.14: Simulated forward and sideward traces.** (A) Simulated forward and (B) sideward (red line, left axis) motion of a Kip3-coupled microsphere along with the angular motor position (green line, right axis) and as a function of time. Inset: Magnification of forward steps showing small forward displacement at the times of sideward steps. Modified from [148].

tubule was chosen randomly between 0 and 180 deg. The number of alternating times per trace were chosen to be the same as in the experiments (Table 7.3). For alternating times between the experimental ones, interpolated even values were used. After a switch, i.e. a change in sideward loading direction, the last angular position was set as the new starting position. Since the angular position $\phi$ changed for every step, we calculated and updated the microsphere displacement $y(\phi)$, the tangential force $F_{\text{tang}}(\phi)$, the force dependent rates, the corresponding sideward stepping probabilities and step durations. Because the number of alternating times were equal to the experimental ones, the simulated traces also had the same overall durations accordingly. Additionally, we added normally distributed noise with a standard deviation of 3 nm corresponding to the experimental value of 12 nm, filtered down to the simulated sampling rate of 20 Hz. For each experimental alternating time, we simulated and analysed 200 traces. Sideward displacements $\Delta y$ and their means and variances were calculated from these traces in the same manner as for the experimental data. We accounted for additional experimental noise—e.g. due to remnant mobility of microtubules which showed up in the variance data—by a global linear fit to the difference between the experimental variance and the simulated variance using both Kip3 and rkin430 data. The best linear fit was added to the simulated variance data of both motor types.

Examples for simulated forward and angular traces are shown in Fig. 7.14. The simulated trace shows the counterintuitive effect that the sideward displacement $y$ may be positive, close to zero, or negative even though the angular position always changes in the same direction with the same magnitude (see angular steps at $\approx$2 s, 3 s, and 5 s in Fig. 7.14B). Without the linear fit parameters, the simulation had 5 free parameters: $k_l^0, k_r^0, x_l^\dagger, x_r^\dagger$, and the supertwist pitch $P$. For the simulations, we used the reciprocal of the pitch $rP$, which we limited to a reasonable range (Table 7.2) for different protofilament numbers.

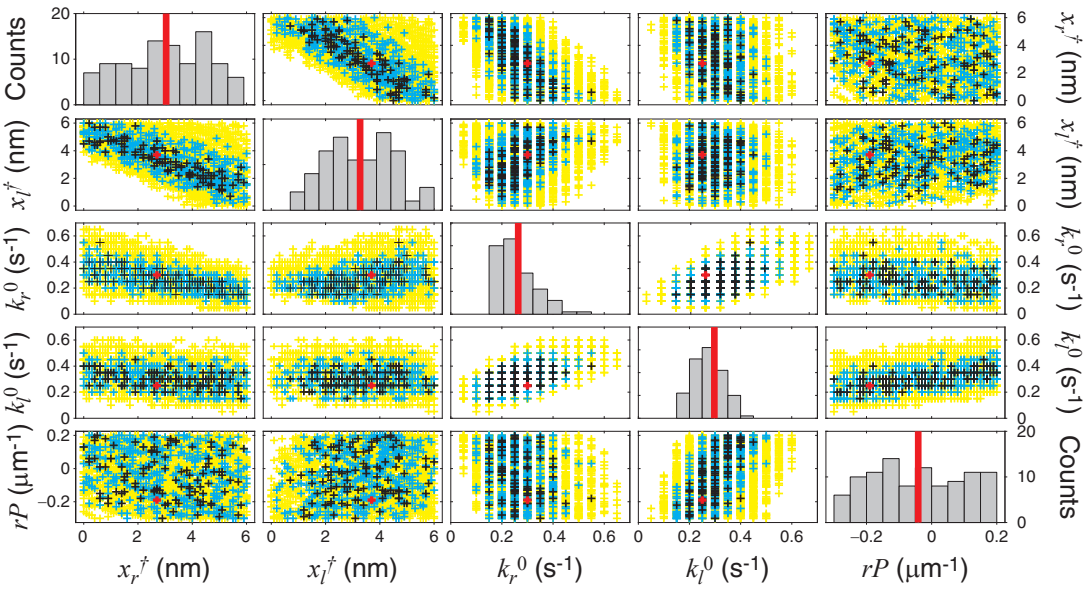


**Figure 7.15: Parameter sets for free supertwist pitch.** Plots of parameter sets for $k_l^0, k_r^0, x_l^\dagger, x_r^\dagger$ and $rP$ as a free parameter, plotted against each other. Red: best parameter set, black: best 100, blue: best 500, yellow: best 2500 parameter sets. Histograms with means (red bars) of the best 100 parameter sets are shown in the diagonal. Modified from [148].

The side-stepping rates were randomly chosen with increments of 0.05 s$^{-1}$, the distance to the transition states with 0.1 nm increments, and the reciprocal supertwist pitch with 0.01 µm$^{-1}$ increments. Each simulation set included more than 100,000 different parameters sets. To find the best-fitting set of parameters, we calculated for each parameter set the reduced $\chi^2$-value ($\chi^2_{\text{red}}$), based on the difference between experimental and simulated mean sideward displacements and sideward variances of Kip3, weighted by the experimental error bars. In the first set of simulations, we varied all 5 parameters randomly. For this set, we found that the value of $rP$ did not converge to a best-fit value of $\chi^2_{\text{red}}$, i.e. the value of the supertwist had little influence on the overall best-fit (Fig. 7.15). Also, the amplitude of the mean sideward displacement for the kinesin-1 simulation was always less than a nanometre for all values of the supertwist. These small values indicate that even for the protofilament tracker kinesin-1 the supertwist did not lead to any mean sideward displacements that should be detected by the experiment. Therefore, for the second set of simulations, we fixed the $rP$-value to the expected weighted mean value[2]. Using one weighted average $rP$-value for all simulated traces is justified as a sufficiently high number of microtubules have been used in the experiments (Table 7.3). The simulation results are shown in Fig. 7.16. We used the corresponding best parameter set to also simulate the force-dependent measurement. For this simulation, we used the load-dependent linker lengths $L$, given in Fig. 7.13B. For both sets, the

[2]Due to wrong values for some of the supertwist pitches, a weighted mean value of 0.126 µm$^{-1}$ instead of 0.152 µm$^{-1}$ has been used for the simulation. However, this small error had no influence on the outcome of the simulation.

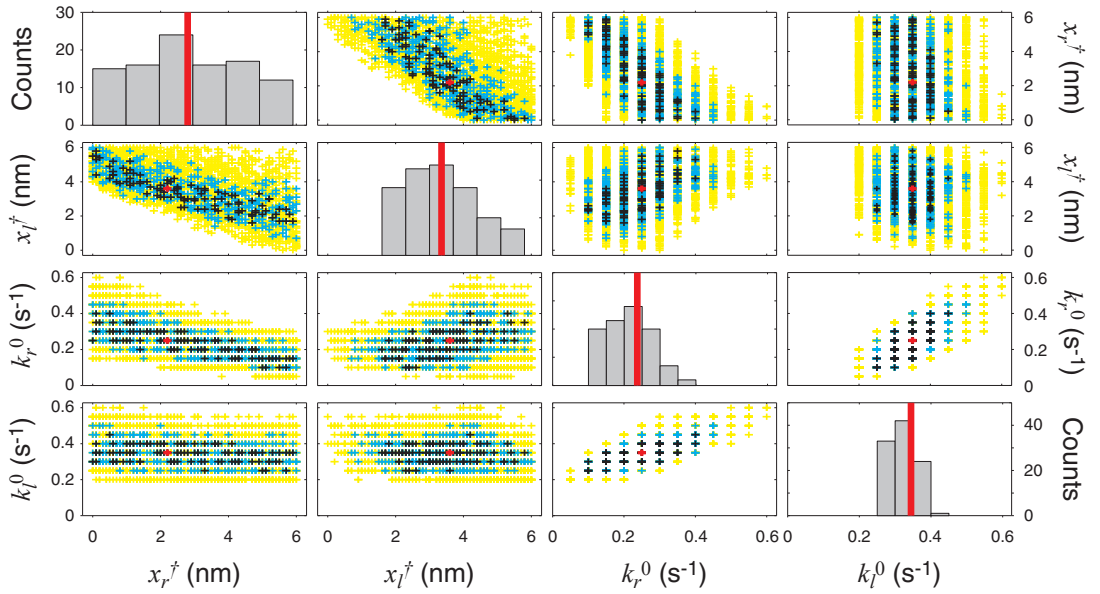


**Figure 7.16: Parameter sets for fixed supertwist pitch.** Plots of parameter sets for $k_l^0, k_r^0, x_l^\dagger, x_r^\dagger$, plotted against each other. $rP$ is fixed to a value of 0.126 µm$^{-1}$. Red: best parameter set, black: best 100, blue: best 500, yellow: best 2500 parameter sets. Histograms with means (red bars) of the best 100 parameter sets are shown in the diagonal. Modified from [148].

best-fit parameters are shown in Table 7.4. Because the simulations correspond to independent experiments, we calculated the weighted means and SDs of the parameters. Within error bars, the zero-force sideward stepping rates towards the left and right of $k^0 \approx 0.3\,\mathrm{s}^{-1}$ did not differ. The distance to the transition states of $3.6 \pm 0.8$ nm and $2.5 \pm 1.0$ nm (SD, $N = 95$) for left and right, respectively, depended on the direction. Thus, in the absence of force, the simulation results support a purely diffusive sideward motion with a sideward stepping time of $\tau = (2k^0)^{-1} \approx 1.7$ s. A directed process, i.e. with one of the rates being zero, does not describe the data well (Figs. 7.15 and 7.16). The mean and variance of the simulated sideward displacements as a function of alternating time using the best-fit parameters are plotted in Figs. 7.7A and B as dotted and solid lines. Mean and variance of simulated sideward displacements as a function of sideward load are plotted in Figs. 7.7C and D, using the same parameter set. Overall, the simulation fits the experimental data very well, supporting our diffusive, asymmetrically force-biased stepping model. The sideward variance as a function of sideward load, however, was not fitted well by the simulation. I measured roughly a constant value. The simulation predicted a monotonous decrease (Fig. 7.7D). This discrepancy may rise from the simulation: Also for the time-dependent sideward variance, the original simulated values were significantly lower than the experimental ones. Therefore, a linear function that accounted for the increasing experimental noise in the data, based on the "background measurement" with rkin430, was added to the variance to fit the data well. This could not be done for the force-dependent variance data, as no such a background measurement with rkin430 was performed. However, it can

**Table 7.4: Simulation results of Kip3 motion.** Best-fit results with standard deviations (SDs) of kinetic parameters and reduced $\chi^2$-values for simulations with fixed and free reciprocal supertwist pitch $rP$. The bottom line contains weighted means and SDs of the two parameters sets. $\chi^2_{\text{red}}$ includes only Kip3 data. The SD reflects the spread in parameters of simulations with a $\chi^2_{\text{red}}$-value range that contains 97 % of the probability distribution of the parameters. The number of simulations that were used for the SD calculations were 18 and 77 with 22 and 23 degrees of freedom, respectively.

| Parameter | $x_l^\dagger$ (nm) | $x_r^\dagger$ (nm) | $k_l^0$ ($s^{-1}$) | $k_r^0$ ($s^{-1}$) |
|---|---|---|---|---|
| Free | 3.7 ± 1.2 | 2.7 ± 1.4 | 0.25 ± 0.06 | 0.30 ± 0.05 |
| Fixed | 3.6 ± 1.0 | 2.2 ± 1.6 | 0.35 ± 0.04 | 0.25 ± 0.07 |
| Weighted | 3.6 ± 0.8 | 2.5 ± 1.0 | 0.31 ± 0.03 | 0.28 ± 0.04 |
| Parameter | Slope ($nm^2/s$) | Intercept ($nm^2$) | $\chi^2_{\text{red}}$ | |
| Free | 5.8 ± 0.2 | 21.6 ± 0.3 | 1.48 | |
| Fixed | 5.6 ± 0.3 | 21.9 ± 0.3 | 1.43 | |
| Weighted | 5.7 ± 0.2 | 21.7 ± 0.2 | | |

be expected that the noise also increase with higher loads and including this into a simulation would fit the data better. As discussed above, I attribute this increase to force-induced lateral fluctuations of the microtubule.

## 7.7. Discussion

My experiments have shown that (i) Kip3 motor-coated microspheres moved on average sidewards in the direction of load, (ii) the variance of the sideward displacement distribution increased with increasing sidewards pulling time, and (iii) detected individual sidewards steps had a broad distribution both in the direction of applied load and against it. While the latter two points are indicative of a diffusive process, the geometry may also be the cause for apparent bidirectional microsphere steps for a unidirectional, i.e. directed angular motion of the motors. However, such unidirectional motion is inconsistent with the load-induced sideward motion and steric hindrance. For a unidirectional angular motion, the motor would have to pass through underneath the microtubule, which is sterically impossible in this assay, due to the attached microsphere.

Why do the mean and variance of the sideward displacement distributions saturate or even decrease for long alternating times? The geometry of the experiment explained the broad distribution in sideward step sizes and sideward distances. Moreover, because of the geometry, in addition to the force-dependent sideward stepping rates, I expect that for long alternating times the motor should on average localise to the protofilament oriented at the angle $\phi_{\text{max}}$, for which the tangential force is zero (Fig. 7.3B). For deviations away from this angular position, the tangential force exponentially increases the counter-acting sideward stepping rate while exponentially decreasing the rate in the direction pointing away from $\phi_{\text{max}}$. Therefore, after a transient, the microsphere position should fluctuate around the position $y(\phi_{\text{max}})$. For long alternating times, the transient displacement to reach $\phi_{\text{max}}$ contributes little to the linear-fit based

sideward displacement (as defined in Fig. 7.4B) resulting in an overall mean sideward displacement $\Delta y$ approaching zero. Since the force dependence of the leftward rate is larger, we expect that the mean angular position $\phi_{\max}$ is reached faster compared to the right. Therefore, the transient is shorter and contributes less to the mean sideward displacement. The smaller contribution results in an overall smaller absolute mean sideward displacement to the left compared to the right. Thus, the dynamics of the system causes a larger mean displacement to the right, even though the leftward stepping rate is more sensitive to force. For long alternating times, we expect the variance to approach a constant value resulting from the fluctuations around the mean angular position. Taken together, our model is consistent with all of our experimental observations.

We assumed that the normal force did not affect the sideward stepping. Yet, I observed that the sideward load slowed down the forward motion. I attribute this slowdown to the normal force acting on the motor. To support this notion, I measured the forward speed while pulling upward on the motor (red open diamonds, top axis in Fig. 7.3B). I scaled the upward force axis relative to the sideward force axis by dividing the latter by $\cos\phi_{\max}$ (according to Eq.7.8 with $\psi(\phi_{\max}) = \phi_{\max}$), which corresponds to the normal load force expected according to the model under sideward pulling conditions after the transient. With such a scaling, the data overlap: within error bars, the decrease in forward speed upon upward loading suggests that the normal load is the key parameter that slows down the forward motion of the motor. While I could not measure any limping, one would expect the motor to limp with increasing sideward and normal loads.

For a single motor, our model suggest a purely diffusive sideward motion in the absence of loads with about every ninth step of the motor being a sideward step in a random direction, based on $[2k^0 + k_f]/(2k^0) = [0.6 + 5]/0.6 \approx 9$. However, microtubule rotations observed in gliding assays suggested a leftward bias of the steps [50]. According to our model, this leftward bias is due to the different force dependence of the sideward stepping rates (Table 7.4). The molecular origin of this difference may be due to the asymmetric structure of the kinesin head with respect to the neck linker [50]. In the gliding assays, multiple motors operate together. We developed a simple model according to which the asymmetric bias in the force dependence is sufficient to explain the observed rotation direction in gliding assays. The model is based on the mutual influence that multiple motors in a gliding assay geometry have on each other. For the gliding assays, in analogy to our loading experiments, we expect, after a transient phase, that all motors should on average be located at an angular position for which the tangential force for each individual motor should be zero (see Fig. 7.17A for an illustration). For simplicity, let us consider the case of two motors. If both motors are initially in a state without tangential forces and one of the motor takes one sideward step, this motor causes a tangential force. The microtubule should rotate to a new angular position that distributes the tangential loads equally on both motors in analogy to the fractional steps observed for cargo transport driven by multiple motors [153]. Since the motor can either step left or right with equal probability in the absence of a tangential

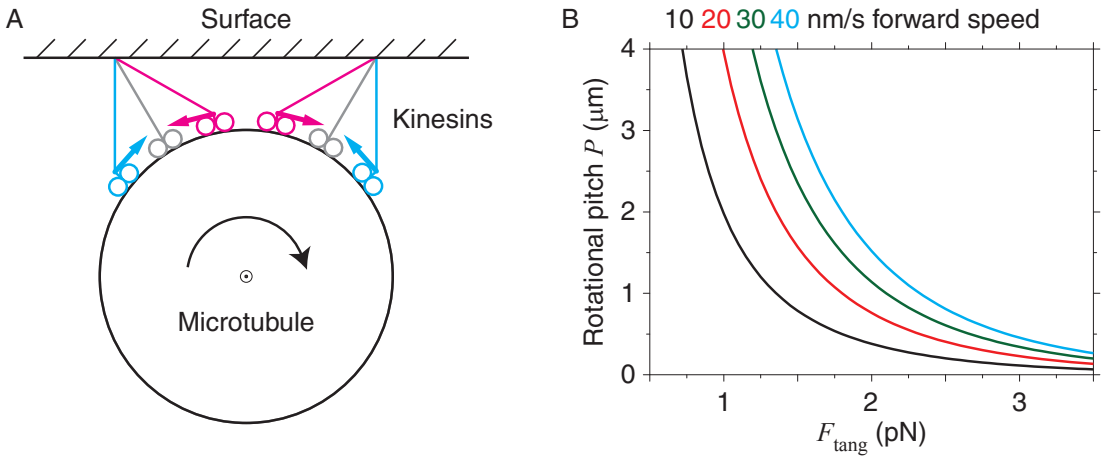


**Figure 7.17: Multiple-motor model.** (A) Schematic of multiple motors interacting with a gliding microtubule moving out of the image plane leading to a clockwise rotation, i.e. the motors step on average to the left. Two motors are drawn in three different states (magenta, cyan, grey). Magenta and cyan coloured motors symbolise the two different cases for which the tangential force (arrows) points in opposite directions. For grey motors, the tangential force is zero. Modified from [148]. (B) Rotational pitch $P$ (Eq. 7.14) as a function of tangential force for different forward speeds using $k^0 = 0.3\,\mathrm{s}^{-1}$ and $\Delta\phi_{\mathrm{pf}} = 27.7\,\mathrm{deg}$.

force, there are two cases of loading directions illustrated by the magenta and cyan motors in Fig. 7.17.

Because of symmetry, the magnitude of the tangential forces on both motors should be equal. However, because of the asymmetric force bias, the leftward stepping rate should be on average larger compared to the right one, i.e. the exponential with the largest positive exponent should dominate the system. The force-induced difference between the left and right stepping rates should result in a net motor movement to the left for both of the above-mentioned cases. In the magenta case, on average, the left motor is most likely to take a step to the left. This stepping rate is the highest compared to any other stepping rate that either the left or the right motor have. In the cyan case, the right motor is most likely to take a leftward step. Thus, in both cases in the geometry of Fig. 7.17A, which we expect to occur with equal probability, the net stepping rate toward the left should result on average in a clockwise rotation of the microtubule, which is the observed rotation direction in gliding assays [50]. For more than two motors acting together, the force balance is difficult because it will depend on the individual location of all the motors. However, motors should still exert tangential forces onto each other, on average half of the motors should be to the left and right of the centre, respectively, and the exponential with the largest positive exponent should dominate. Thus, also in this case we expect clockwise microtubule rotations and a net motor bias towards the left.

To calculate the rotational pitch with this model, let us first consider the cyan case in Fig. 7.17A. The respective contributions of the left motor 1 and right

motor 2 to the angular speed $\omega$ of the microtubule is

$$\omega_{1,2} = \Delta\phi_{\mathrm{pf}} \left[ k_l(\mp F_{\mathrm{tang}}) - k_r(\mp F_{\mathrm{tang}}) \right], \tag{7.12}$$

where $\Delta\phi_{\mathrm{pf}}$ is the angular displacement for a single sideward step of a single motor. For the magenta case, the direction of forces, i.e. the signs, are inverted in Eq. 7.12. For both cases, the net angular speed is $\omega_{\mathrm{net}} = \frac{1}{2}(\omega_1 + \omega_2)$. If we assume that the zero-force sideward stepping rates in Eq. 7.10 for left and right are equal, both cases result in the same net angular speed $\omega_{\mathrm{net}}$ and rotational pitch $P$:

$$\omega_{\mathrm{net}} = \Delta\phi_{\mathrm{pf}} k^0 \left[ \cosh\left( \frac{F_{\mathrm{tang}} x_l^\dagger}{k_{\mathrm{B}} T} \right) - \cosh\left( \frac{F_{\mathrm{tang}} x_r^\dagger}{k_{\mathrm{B}} T} \right) \right] \tag{7.13}$$

$$P = v_f(F_{\mathrm{norm}}) \cdot \frac{2\pi}{\omega_{\mathrm{net}}}, \tag{7.14}$$

where $k^0 \approx k_l^0 \approx k_r^0$ is the zero-load sideward stepping rate, and $v_f(F_{\mathrm{norm}})$ the forward speed which may depend on the normal load. This pitch equation (Eq. 7.14) does not account for any supertwist that would superpose with the motor-induced rotation. Because $x_l^\dagger > x_r^\dagger$, the net angular speed is positive ($\omega_{\mathrm{net}} > 0$), which means that on average motors would step to the left. Depending on how many motors interact with the microtubule, we expect that the average normal and tangential load per motor may vary. For example, for many motors, which do not step in synchrony, we expect that there should be a significant loading force caused by lagging motors in the direction of the microtubule axis. Because the microtubule is kept at a certain distance from the surface [111], this loading force has a component in the direction normal to the microtubule axis and a tangential component upon sideward stepping. The normal load should slow down the motors according to Fig. 7.3. Therefore, for many motors we expect the average normal force per motor to be larger compared to the few-motor case resulting in a slower gliding speed. Indeed, systematic MT gliding assays showed that the MT forward speed decreased with higher Kip3 surface density [49]. For our range of normal loads (Fig. 7.3), I plotted a family of curves of Eq. 7.14 (Fig. 7.17B) for different forward speeds. For the observed experimental pitch value of $\approx$ 1 µm for Kip3-rotated microtubules [50], the model would suggest that, depending on the normal load, on average about 1.4–2.4 pN of tangential load force is acting on the motors. The magnitude of the force range is comparable to the 1.3–1.5 pN stall force [40, 92] and falls within the range of forces tested in this work (Fig. 7.3). Thus, the force bias may account for the rotational pitch and left-handed bias in the gliding assays. A similar collective effect has been observed for dynein [103], suggesting that dynein may also have a difference in the force dependence of the sideward stepping rates.

Kip3 has a weakly bound slip state [40]. The motor switches to this short-lived state at a frequency comparable to the sideward stepping rate. Whether sideward stepping is related to this state is unclear at the moment. It can

be excluded that the discrete sideward steps of Kip3 were actually slipping events, as the steps with and against the load had the same distribution with respect to the range of the step size (Fig. 7.5). If Kip3 had slipped with the load, the measured step sizes in this direction had been bigger than in the other direction. A weakly bound state may enable the motor a longer reach to binding sites on neighbouring protofilaments [50]. Whether sideward stepping is coupled to ATP hydrolysis and how the sideward stepping rate depends on the ATP concentration is also unclear. I tested stepping assays at reduced ATP concentrations. However, a quantitative analysis of these assays turned out to be nearly impossible due to very low motor speeds and a reduced stall force. If sideward stepping is coupled to ATP hydrolysis, I would expect a small zero-force asymmetry in the sideward stepping rates which I could not determine within the error margins. Such an asymmetry should arise because of the helical microtubule geometry and the asymmetry of the motor [50].

What biological relevance does the diffusive sideward stepping mechanism have for Kip3? For axonemal dynein motors, off-axis movement—causing microtubule rotations and, thus, torque—may be important for the three-dimensional motion of the flagellar beat [154, 155]; for cytoplasmic dynein, sideward steps may be an essential biological requirement such that heads can pass each other, obstacles, or counterpropagating kinesin motors [103, 156–158]. For kinesin motors, the ability to bypass obstacles is also an essential property for cargo transport [53, 54, 159]. How torque generation [112, 154, 155, 160–162] on the cargo, i.e. a rotation of the cargo around the filament axis, induced by sideward stepping influences cargo transport remains to be seen.

Kip3 does not transport cargo but must reach the microtubule end for length regulation. Therefore, being able to bypass obstacles on both sides seems to be the most efficient way to do so. The asymmetric force bias may not have a biological function for Kip3.

# 8. 3D Optical Tweezers Tracking of Kinesin-1 and Kinesin-8

To verify the simulation results of the 2D-force-clamp assays, I performed 3D-force-clamp assays with kinesins on suspended microtubules. I tracked the motion of the kinesin-8 Kip3 with high precision in all three dimensions in the absence of any loads. I observed that Kip3 diffusively switched between protofilaments in discrete angular steps without an asymmetry between left and right. A quantitative analysis of the angular motion suggested distinct diffusional states of Kip3. The results of Kip3's diffusive sideward stepping were consistent with that of the 2D assays. Control measurements with the kinesin-1 rkin430 revealed protofilament tracking and no switching. This tracking was used to determine the supertwist pitches of the used microtubules.

In the following chapter, the details and results of 3D-force-clamp assays with zero loads on Kip3 and rkin430 are explained.

## 8.1. 3D-Force-Clamp Assays with Kinesins

Experiments were performed in flow cells that were constructed with topographically structured cover slips (Section 6.3), a smaller hydrophobic cover slip on top, and parafilm, analogously to the previously described flow cells (Fig. 8.1). The channels were washed with BRB80 and incubated with tubulin antibodies and F-127 as before, except that the F-127 incubation was prolonged to ≥45 min, as this improved the blocking of PFPE from unspecific binding. The

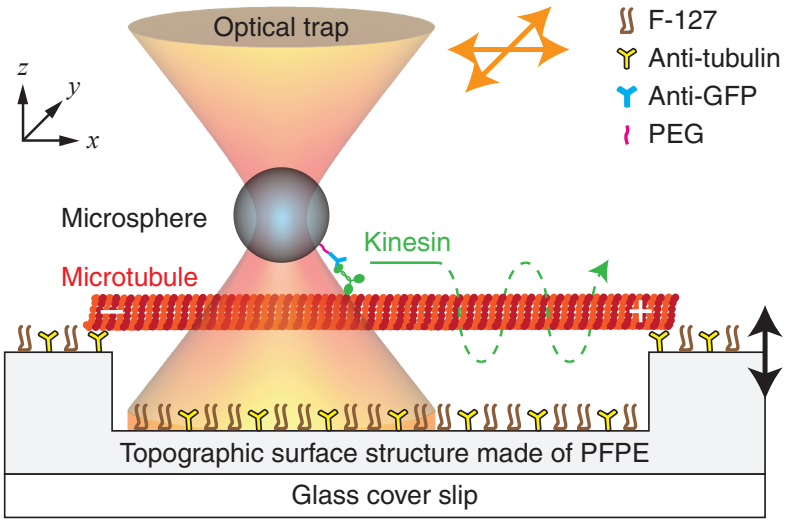


**Figure 8.1: Schematic of the 3D-force-clamp assay.** Topographic structures on the cover slip surface provide free access of kinesin-coated microspheres to suspended microtubules in an optical tweezers force-clamp assay. Schematics are not to scale.

rest of the assay preparation concerning kinesin and microsphere dilution and mixing followed the same protocol as for 2D assays (Chapter 4).

Positional and angular traces of the tracked microsphere were calculated as described in Section 3.2 according to the geometry in Fig. 3.4. The expected radius of the microsphere centre around the microtubule is about 340–360 nm, corresponding to the sum of the microsphere radius of 295 nm, the MT radius of 12.5 nm, and the kinesin/PEG linker length of 30–50 nm[1].

## 8.2. 3D Video Tracking of Kip3

In the beginning, I used the method of three-dimensional tracking of microspheres, based on defocussing microscopy as described in Section 3.4 to detect the motion of Kip3-coated microspheres on microtubules without using optical tweezers. Visually, I observed swivelling of the microspheres around the MT axis. When the microspheres reached the edge of the ridge structures, I observed both continuous translocation on the ridge and stalling of the microspheres when colliding with the ridge's wall. With this tracking method, I determined the three-dimensional position data of the microsphere and visualised the data in 3D plots (Fig. 8.2). I observed no significant angular motion of microspheres on immobilised microtubules on planar surfaces (Fig. 8.2A) but extended angular motion to the left and right around freely accessible microtubules (Fig. 8.2B). The spatial and temporal resolution was much worse than in an optical tweezers assay. Also, for measurements where a height calibration was not possible and calibration data from previous measurements had to be used, the axial position $z$ had been not calculated correctly which was visible by an elliptically distortion of the circular path in $yz$-projection of the trajectory. The average spatial resolution of non-motile phases of 3 traces (including Fig. 8.2A) was 32 nm ($x$), 46 nm ($y$), and 48 nm ($z$), the angular resolution 9 deg, and the radial resolution 44 nm. All values were larger than those that were achieved with the 3D force clamp. Thus, as this method had a worse resolution and the calibration was hard to reproduce, I did not follow it up any further.

[1] This value might be overestimated, as the unstretched kinesin/PEG linker is certainly shorter.

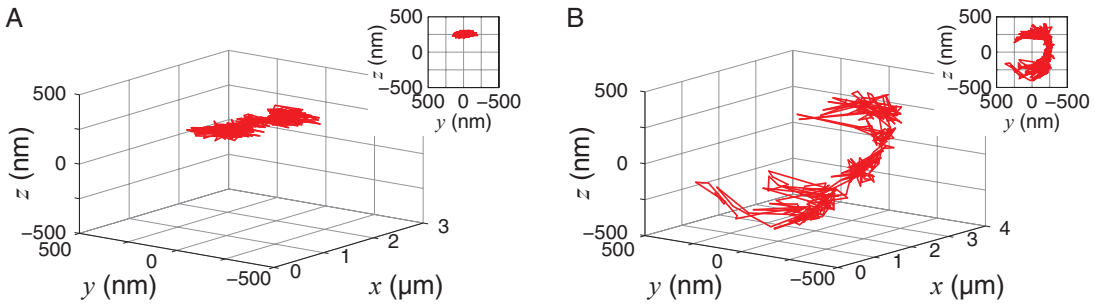


**Figure 8.2: 3D video tracking of kinesins.** Two 3D trajectories of Kip3-driven microspheres on suspended microtubules (A) on the ridge and (B) above the canyon. Insets: $yz$-projections. The microsphere in (A) stopped at the end of the microtubule.

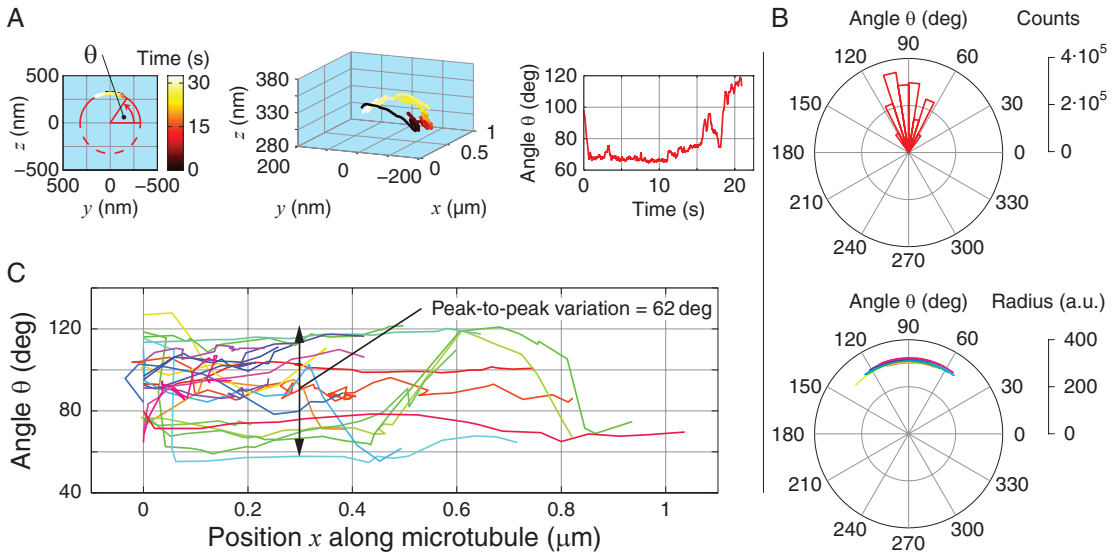


**Figure 8.3: 3D single Kip3 stepping assays on planar surfaces.** (A) An exemplary three-dimensional trace of a Kip3-coated microsphere on an immobilised microtubule, showing diffusional angular motion, represented by the $zy$-projection, the full 3D projection, and the angular trace over time. (B) Angular histogram, polar plot, and (C) angle plot as a function of $x$ of 22 measured traces on 15 different microtubules. An offset, equal to the mean of maximal and minimal values of each trace, was subtracted from the angular traces in the last plot.

## 8.3. 3D Stepping Assays with Kip3 on Planar Surfaces Revealed Confined Angular Motion

As a control for the three-dimensional assays, I calculated and analysed the traces of three-dimensionally tracked, Kip3-driven microspheres on microtubules that had been immobilised on planar sample surfaces. I plotted the angular traces as a function of the absolute forward position $x$ instead of time. In this manner, pausing artefacts are avoided and the motion of traces with different forward speeds can be compared.

The recorded traces, from which 22 were long enough to be used for further analysis, had a mean speed of $39 \pm 1$ nm/s ($N = 48$) that is consistent with the measurements in Chapter 7. The mean radius and SEM of the circular fit were $262 \pm 18$ nm ($N = 10$) which is smaller than the expected value of 340–360 nm. Most of the traces showed clear angular motion as shown in Fig. 8.3. However, all traces were restricted on a small angular range of ±30 deg on the upper half of the microtubule, i.e. around the 90 deg position (Figs. 8.3B and C). The angular motion occurred most often (15 out of 22 traces) in both directions and not unidirectionally which indicates angular motion in both directions. This angular motion could have been caused by protofilament switching or swivelling of the microsphere above the microtubule. To understand the angular range of ±30 deg around 90 deg, one has to analyse the complex geometry of stepping assays on a planar surface as done in the previous chapter. The measured angle

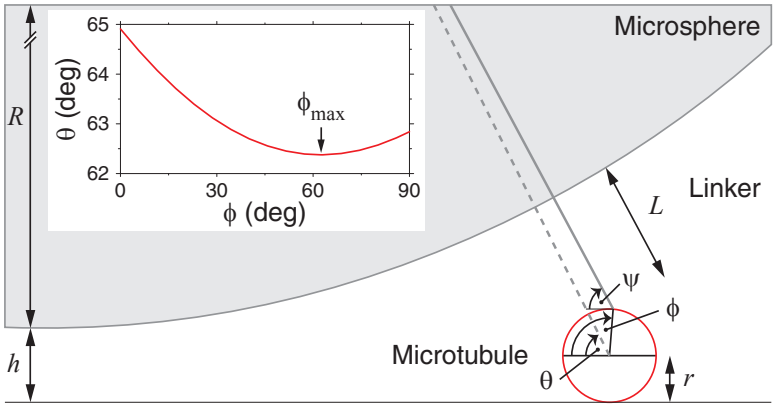


**Figure 8.4: Geometry of the 3D stepping assay on a planar surface.** Schematic (to scale) to illustrate angles $\phi$, $\psi$, and $\theta$. Inset: $\theta$ as a function of $\phi$, calculated using realistic values for $R, r, L$, and $h$ from Section 7.6.

in these assays, denoted as $\theta$ in Fig. 8.3A, is not equal to the angle $\phi$ at which the motor is positioned on the microtubule as defined in Fig. 3.4. This angle $\theta$ is the angle between the surface and the connection line of microsphere and microtubule centre, respectively (Fig. 8.4) and can be calculated for $\phi \in [0{,}90\,\text{deg}]$ by:

$$\theta(\phi) = \arctan\left\{\frac{\sin\phi + (R+L)/r \cdot \sin\psi}{\cos\phi + (R+L)/r \cdot \cos\psi}\right\}, \tag{8.1}$$

where the angle $\psi(\phi)$ is calculated by Eq. 7.6. However, this relation cannot be used to calculate the angular position $\phi$ as the original geometry model works only when a sideward load is applied and keeps the microsphere at a constant height with the linker stretched. Here, the force clamp worked in a zero-load mode. Thus, the microsphere could swivel freely above the microtubule, limited by the steric hindrance due to the surface. One cannot tell whether angular changes in the measured traces rose from actual protofilament switching. Still, Eq. 8.1 can be used to calculate the possible angular range of traces and compare it with the experimental value: The relation $\theta(\phi)$ has a minimum $\theta_{\text{min}} = \phi_{\text{max}}$ at the angle $\phi_{\text{max}}$ (Fig. 8.4, inset). The maximum angular range around the 90 deg position, the microsphere could swivel over is $180\,\text{deg} - 2\theta_{\text{min}} \approx 55\,\text{deg}$ which is in good agreement with the measured maximal peak-to-peak variation of the traces of 62 deg (Fig. 8.3D.

Thus, these experiments on planar surfaces were not suited to investigate three-dimensional motion of kinesins and therefore motivated the usage of 3D structures.

## 8.4. 3D Stepping Assays Confirmed Diffusive Protofilament Switching of Kip3

### 8.4.1. 3D Stepping Assays with Single Kip3 Motors

Three-dimensional stepping assays with single Kip3 on suspended microtubules using the topographic structures described in Section 6.3 revealed broad angular motion around the MT axis as shown in Fig. 8.5. The angular traces were

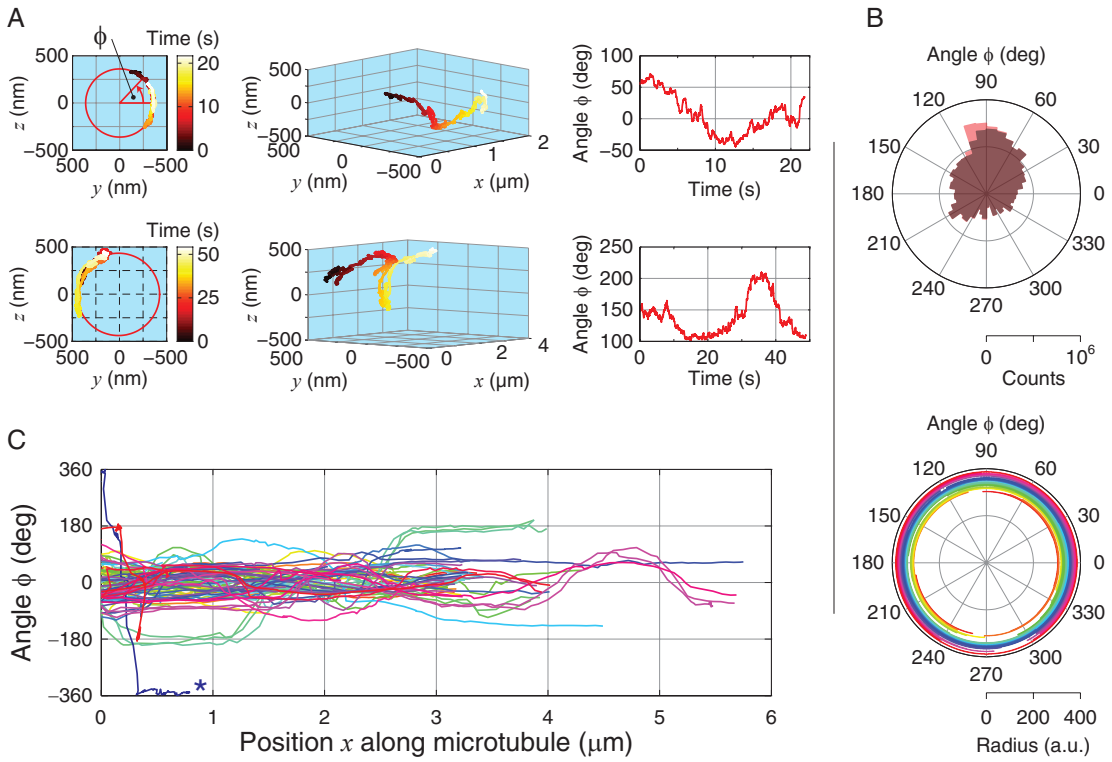


**Figure 8.5: 3D single Kip3 stepping assays on suspended microtubules.** (A) Two exemplary three-dimensional traces of Kip3-coated microspheres around suspended microtubules, showing diffusional angular motion. Each trace is represented by the $zy$-projection, the full 3D projection, and the angular trace over time. (B) Angular histogram, polar plot (with different, arbitrary but constant radii), and (C) angle plot as a function of $x$ of 84 measured traces on 58 different microtubules. An offset, equal to the mean of maximal and minimal values of each trace, was subtracted from the angular traces in the last plot. The angular histogram in (B) shows data for all recorded traces (red) and all traces except the outlier trace which is marked with a blue asterisk in (C).

located all around the microtubule with a preference for the upper half. This preference is not unexpected, as the experiment usually started with putting the microsphere on top of the suspended microtubule (Fig. 8.5B). The measured mean radius ± SEM of the circular fit was 375 ± 9 nm ($N$ = 181 including all 3D measurements with Kip3) which is in good agreement with the expected values of 340–360 nm. The angular traces showed unidirectional as well as bidirectional angular motion. Some traces did not show much or no angular motion at all. Interestingly, all 84 recorded traces (except one which is marked with a blue asterisk in Fig. 8.5C) were restricted to an angular range of about 360 deg, i.e. to one complete turn. With respect to all recorded traces, including those presented in the next sections, this particular trace is considered an outlier, also with respect to its very low forward speed and run length.

The average of all traces did not show a directional preference over time. The mean angular gradient, obtained by linear fits of angle over the forward position $x$, for all traces was −0.01 ± 0.02 deg/nm (0.0001 ± 0.0154 deg/nm excluding the outlier trace in Fig. 8.5C) and was not significantly different from

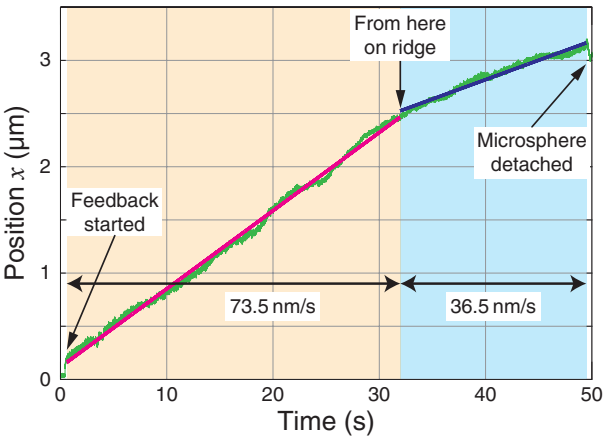


**Figure 8.6: Kip3 moved faster on suspended microtubules.** Exemplary trace (green) with $x$-position as a function of time of a Kip3-coated microsphere tracked with the force clamp. The microsphere first walked on the suspended part of a microtubule over the canyon, followed (from ≈32 s) by walking on the immobilised part on the ridge. Values of speeds from linear fits to $x$ (given as magenta and blue lines, respectively) for the different regions are given.

zero. This values imply that the microtubules were—at least on average—not supertwisted which is in contrast to Ray et al. [11] and the estimation for the average supertwist in the previous chapter (Table 7.2).

The measured forward speed of Kip3 in 3D assays was significantly higher, compared to 2D assays. On suspended microtubules, the mean speed and SEM of single Kip3-S were 58 ± 3 nm/s ($N$ = 52), of Kip3-H 66 ± 2 nm/s ($N$ = 70). Both values are consistent with each other and have an overall mean of 62 ± 1 nm/s. This speed was significantly higher, compared to the one, measured on microtubules that were immobilised on planar surfaces. Here, the speed was about 40 nm/s, tested with both constructs in TIRF stepping assays at the same conditions, consistent with previous results [19, 40, 148]. To test whether the force clamp unintentionally applied an effective load on the microsphere (and thus the Kip3), I measured the speed of Kip3-driven microspheres without the force clamp but via video tracking (Section 8.2). The mean speed was 56 ± 5 nm/s ($N$ = 11, Kip3-S only) which is consistent with the values that were measured with force clamping, excluding trap-induced artefacts. To make a direct comparison between Kip3 walking on suspended and immobilised microtubules, respectively, I measured the speed of microspheres ($N$ = 10, both Kip3 constructs) that first walked freely on suspended regions and then on the part that was immobilised on the topographic structure, i.e. ridge (Fig. 8.6). The corresponding means and SEMs were 55 ± 6 nm/s on freely accessible microtubules and 30 ± 5 nm/s on immobilised microtubules. A paired t-test showed the significant difference ($p = 3 \cdot 10^{-5}$) and that Kip3 was moving faster on freely accessible microtubules.

I went on analysing the recorded angular traces of Kip3 for steps, using the same step finding algorithm as in the previous chapter. Steps of about $\Delta\phi_{\mathrm{pf}} \approx$ 22–30 deg were expected for a protofilament switch. The variation is due to different protofilament numbers. Assuming the distribution of protofilament numbers in Table 7.2, the weighted mean angular step size is 25.7 deg. For a microtubule with 13 protofilaments, the expected angular step size is 27.7 deg. Many traces showed stepwise motion as shown in Fig. 8.7A. Very large steps of more than 50 deg have been detect as well; they likely arose from fast, successive

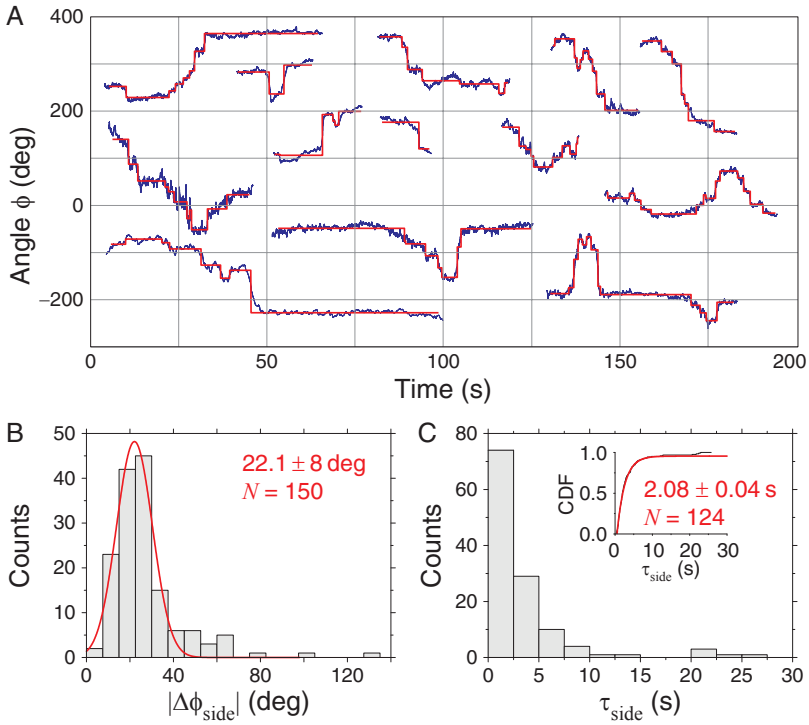


**Figure 8.7: Angular steps of Kip3 verified protofilament switching.** (A) Angular traces with detected steps (red lines). The offsets are chosen arbitrarily. Altogether, 150 steps in 30 traces were found. (B) Histogram of absolute angular step sizes with Gaussian fit, centre, standard deviation, and number of data points. (C) Histogram of angular step times. Inset: Cumulative distribution function (CDF) plot with exponential fit, decay time, standard error, and number of data points.

steps that could not be distinguished by the step finder. The histogram of measured absolute step sizes was fitted by a Gaussian (excluding data >50 deg, Fig. 8.7). The corresponding centre and thus mean angular step size $\Delta\phi_{\text{side}}$ was 22 deg with a standard deviation of 8 deg which is smaller than the expected value but still in acceptable agreement. The mean angular step dwell time $\tau_{\text{side}}$ was 2 s, based on an exponential fit to the cumulative distribution function of the experimental values, excluding data >8.5 s (Fig. 8.7C). The corresponding sideward stepping rate was $0.5 \pm 0.1\,\text{s}^{-1}$. This is consistent to the sideward stepping rate of $0.59 \pm 0.07\,\text{s}^{-1}$ from the simulation of the 2D side-stepping assays. From 150 steps, 88 were to the right and 62 to the left which did not prove a significant preference for one direction. Also, the overall mean ± SEM of $-5.0 \pm 2.6$ deg of the steps was not different from zero.

### 8.4.2. 3D Stepping Assays with Multiple Kip3 Motors

To test the model for the interaction of multiple Kip3 motors in e.g. gliding assays (Section 7.7), I performed three-dimensional Kip3 stepping assays under multiple-molecule conditions. Interaction of multiple Kip3 on one microsphere with the same microtubule was obtained by using 100–1000× higher Kip3-

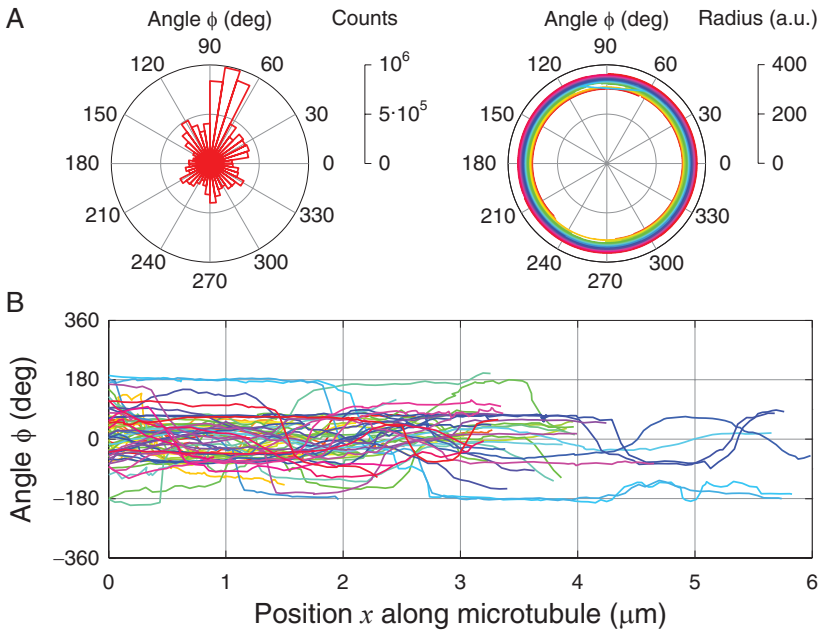


**Figure 8.8: 3D multiple Kip3 stepping assays on suspended microtubules.** (A) Angular histogram, polar plot (with different, arbitrary but constant radii), and (B) angle plot as a function of $x$ of 62 measured traces on 47 different microtubules. An offset, equal to the mean of maximal and minimal values of each trace, was subtracted from the angular traces in the last plot.

to-microsphere ratios compared to single-molecule conditions. At these Kip3 concentrations, nearly every microsphere showed motility with stall forces in the static trap of about 3.1 ± 0.2 pN ($N$ = 41) in contrast to forces of 1.50 ± 0.02 pN ($N$ = 77) under single-molecule conditions. To get more data for better statistics, I also analysed Kip3 traces with stall forces >2 pN that rarely occurred under single-molecule conditions, too. The forward speed without load was 57 ± 2 nm/s ($N$ = 67) for Kip3-H and 53 ± 3 nm/s ($N$ = 33) for Kip3-S with an overall mean of 56 ± 2 nm/s. This value is slightly but significantly lower than the mean for single-molecule conditions ($p$ = 0.004). On the other hand, the value was very similar to the speeds of single Kip3 measured with video tracking.

All measured 62 angular traces had angular positions that were distributed around the microtubules with a frequency peak close to the top position as in the single Kip3 assays (Fig. 8.8A). The traces were confined to an angular range of about 360 deg as the traces of single Kip3 were (compare Figs. 8.5A and 8.8B). Also, traces did not show a directional preference over time. This was confirmed by the mean angular gradient of −0.007 ± 0.009 deg/nm. The measured radii from the circular fit were not different and included in the mean data in the previous section. The traces revealed unidirectional and bidirectional as well as no angular motion as for single Kip3. The unidirectional traces were both left and right-handed. A qualitative difference to the traces of single Kip3 was not observed. Therefore, a collective interaction between multiple Kip3 that could lead to a preferential left-handed angular motion of the microsphere (Section

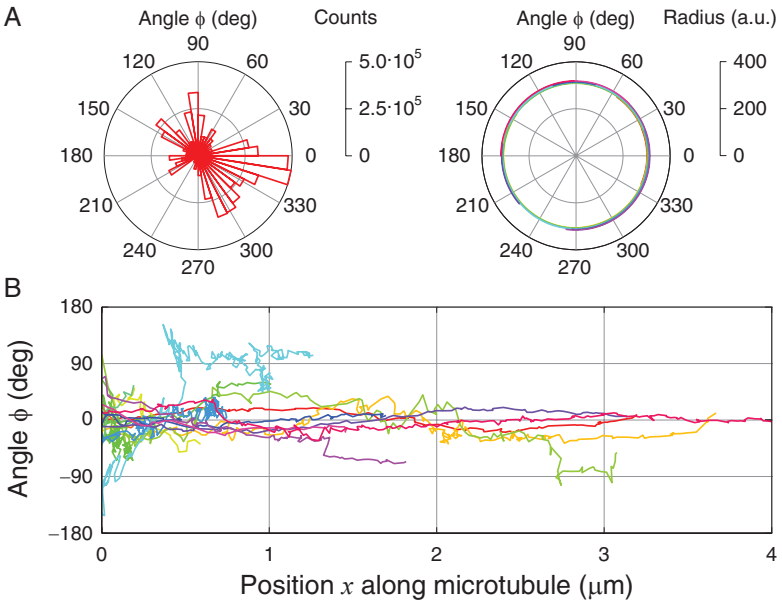


**Figure 8.9: 3D multiple Kip3 stepping assays on suspended microtubules at reduced ATP concentration.** (A) Angular histogram, polar plot (with different, arbitrary but constant radii), and (B) angle plot as a function of $x$ of 16 measured traces on 7 different microtubules. An offset, equal to the mean of maximal and minimal values of each trace, was subtracted from the angular traces in the last plot.

7.7) could not be observed with this experiment.

### 8.4.3. 3D Stepping Assays with Multiple Kip3 Motors at Reduced ATP Concentration

To investigate the ATP dependence of the protofilament switching of Kip3, I perform analogous experiments with a reduced ATP concentration of 10 μM. I found that the stall force of Kip3 dropped dramatically at this ATP concentration. Thus, all assays were done under multiple-molecule conditions, to be able to work with the force clamp in the first place. Using the same Kip3-to-microsphere ratio, the mean stall force in the static trap at 10 μM was 0.8 ± 0.1 pN ($N$ = 20), in contrast to about 3 pN at 1 mM ATP. The velocity dropped to 20 ± 2 nm/s ($N$ = 26) which is consistent with the value 17.6 ± 0.4 nm/s ($N$ = 89), measured in the TIRF stepping assay (Fig. 7.2). I observed much less angular motion than at 1 mM ATP (Fig. 8.9). The positions of the angular traces were also distributed around the used microtubules. Again, the traces showed no directional preference over time, implied by the mean angular gradient of 0.005 ± 0.04 deg/nm.

### 8.4.4. Angular Displacement Analysis Revealed Different Diffusive States of Kip3

To characterise the angular motion of Kip3, I performed a mean squared displacement (MSD) analysis. The terminus "displacement" refers to translational motion; for rotational motion like here, the terminus "mean squared angle displacement" (MSAD) is more suited. Using this type of analysis, different modes of motion can be identified and characterised, e.g. pure diffusion or diffusion combined with directed motion. I determined the MSAD by calculating the squared differences in the angle for overlapping time windows $\tau$ for all traces[2] and then calculating the mean of all these squared differences for each $\tau$. The original angular traces had a sampling rate of 4 kHz but have been averaged down to a rate of 1 Hz for Kip3. This was necessary, as the angular data for times $\tau \ll \tau_{\text{side}}$ are highly correlated and their fluctuations do not correspond to actual motion [163]. For rkin430, the data were averaged down to 10 Hz, as kinesin-1 is much less processive and the traces shorter. To calculate a MSAD for times $\tau$ as long as for Kip3, I combined the rkin430 traces to one long trace and calculated the MSAD from this trace. This was valid, as for short times $\tau$ the MSAD of all separate traces and the MSAD for one combined trace were identical. As the speeds differed between the different experiments, the times $\tau$ have to be adjusted if MSADs of the other experiments shall be compared quantitatively with the main experiment with single Kip3. This worked in complete analogy to the definition of the effective alternating time in Section 7.5. An effective time $\tau_{\text{eff}}$ for the different experiments $i$ were calculated based on an equal travelled distance on the microtubule lattice by $\tau_{\text{eff},i} = \tau_i \cdot v_i / v_{\text{Kip3}}$. Resulting MSADs of all experiments are shown in Fig. 8.10 in a semi-logarithmic plot. For example, the direct comparison between single Kip3 on suspended and immobilised microtubules shows the confinement of angular motion on the latter and how free accessibility enhances the possible angular motion. The MSADs for Kip3 at single and multiple-molecule conditions were equal and completely overlapped for not corrected $\tau$. No difference between the outcomes of both conditions could be observed here. However, the MSAD of the traces of Kip3 at lower ATP concentration were much smaller than the MSAD for Kip3 at full ATP.

The MSAD of Kip3 could be fitted by a parabola (not shown in Fig. 8.10 but discussed below). A quadratic contribution to the MSAD implies an additional directed component in the motion, in this system e.g. by a possible effective supertwist. However, the angular traces themselves did not confirm such a directed component (Fig. 8.5C). A closer look at the angular traces of Kip3 shows that there were different populations of traces that showed (i) basically no or only little angular motion, (ii) some intermediate angular diffusion, and (iii) large angular diffusion and rotation in both directions. An averaged MSAD like in Fig. 8.10 cannot reflect the distinctness of these populations. Therefore, I did not further analyse the MSAD but the distribution of the angular displacements

[2] Excluding the outlier trace in Fig. 8.5C did not give quantitatively or qualitatively different results and was thus not considered.

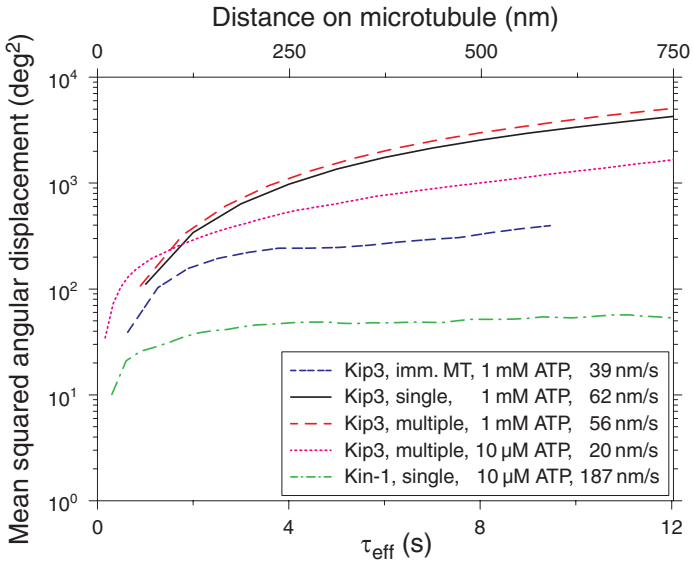


**Figure 8.10: Mean squared angular displacement analysis of angular motion of kinesins.** Plot of mean squared angular displacements as a function of $\tau_{\text{eff}}$ and distance on the microtubule with standard errors of angular motion of single Kip3 on microtubules, immobilised on planar surfaces at 1 mM ATP (blue), single Kip3 at 1 mM ATP (black), multiple Kip3 at 1 mM ATP (red), multiple Kip3 at 10 µM ATP (magenta), and single rkin430 at 10 µM ATP (green). The times $\tau$ have been adjusted for different experiments with different speeds (given in the legend) and transformed into an effective $\tau_{\text{eff}}$ (see main text).

for each $\tau$. The distribution's variance is then equal to the MSAD. I analysed the distributions by fitting multiple Gaussian functions to the histograms and analysed their parameters as done previously by Helenius et al. for different states in the diffusive motion of kinesin-13 [164]. I fitted sets of 1–4 Gaussian functions to the angle histograms of the traces of single Kip3 for $\tau = 1$–$20$ s. Multiple Gaussians were arranged and numbered by increasing variances. The fits were weighted by the number of counts in each bin. Several histograms with fits are shown in Fig. 8.11. Mean angular displacements and variances of the distributions are given in Figs. 8.12A and B. The histograms could be fitted much better with a sum of three Gaussians compared to two or only one Gaussian, as the $\chi^2_{\text{red}}$-values in Fig. 8.12C show. I also tried to fit a sum of four Gaussians, but either a converging fit was not possible or two of the peaks contained equal parameters. Thus, more than three Gaussians did not improve the fits. The subsequent analysis was performed with a fit of three Gaussians (Figs. 8.12D–F). The centres of all three fits (Fig. 8.12D) showed only a very small changes over time of each $\leq 0.3$ deg/s (obtained from linear fits, not shown in Fig. 8.12D), i.e. there was no effective directed motion in any of the populations which is consistent with the analysis of the traces. Also, the overall mean of the displacement distributions showed a small change over time of 0.2 deg/s to the left (linear fit in Fig. 8.12A). This small directional preference might be represented by the parabolic fit to the overall variance (Fig. 8.12B). At a forward speed of 62 nm/s, these small angular speeds correspond to rotational pitches

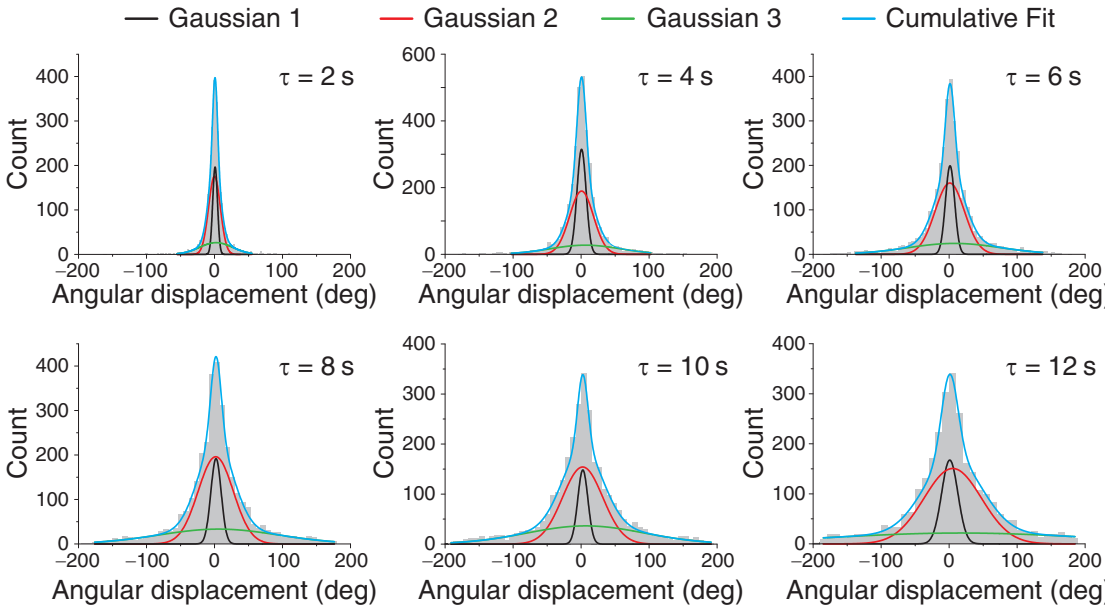


**Figure 8.11: Angular displacement distributions of single Kip3 traces.** Histograms of angular displacements of single Kip3 traces for different $\tau$. Each distribution was fitted with a set of 3 Gaussian functions, weighted by the number of data points. The different Gaussians are shown in different colours, together with the cumulative fit. More than 3000 data points were used in each histogram.

of about 100 µm. This large value does not fit to any experimental or predicted supertwist pitches for microtubules. Microtubules with that large pitches are considered to be not supertwisted. Thus, the observed changes of the mean angular displacements are not considered to represent effective angular motion due to supertwist.

The three Gaussians differed a lot in their widths and how fast the widths increased over time (Fig. 8.12E). I performed linear fits of the corresponding variances which were weighted by their standard errors, excluding $\tau < 2\,\mathrm{s}$, as these values were below the mean angular step time of Kip3, and $\tau > 10\,\mathrm{s}$ as the distributions were influenced by the angular confinement. For $\tau > 10\,\mathrm{s}$, the variances of the three populations saturated at values of $109 \pm 19\,\mathrm{deg}^2$, $1711 \pm 212\,\mathrm{deg}^2$, and $7435 \pm 568\,\mathrm{deg}^2$, respectively. The saturation of the variances suggests confined diffusion. For 1D diffusion which is restricted to a segment of length $S$, the mean squared displacement—in this case the variance of the angular displacements—converges to a value of $S^2/6$ for long $\tau$ [165]. Using this relation, the plateau value of the first population refers to an angular segment of $26 \pm 2\,\mathrm{deg}$ which is in agreement with the angular step size. For the second and third population, the corresponding angular segments were $101 \pm 6\,\mathrm{deg}$ and $211 \pm 8\,\mathrm{deg}$, respectively. The last value approximately refers to half a turn around the microtubule. Half the value of the slopes of the fits are the diffusion constants which are given in Table 8.1. The three populations had very different diffusion constants. I calculated the relative abundance of the populations based on the Gaussian's area divided by the sum of all three areas. The results are plotted in Fig. 8.12F. $\chi^2$-tests showed that all abundances were

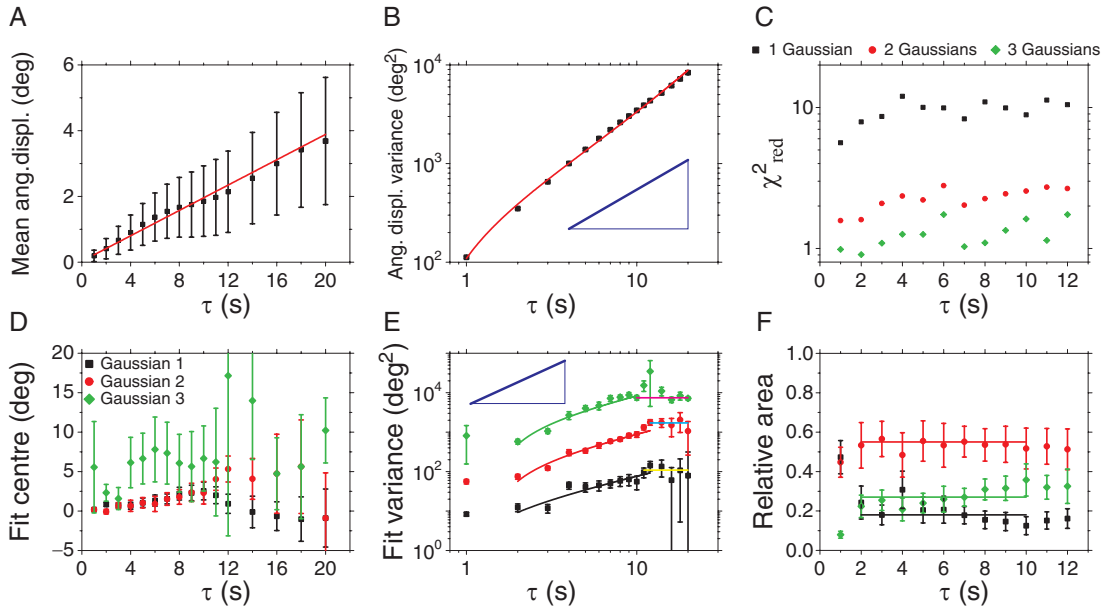


**Figure 8.12: Angular displacement of single Kip3 traces.** (A) Mean angular displacement and (B) angular displacement variance over tau, with linear and parabolic fit, respectively. (C) $\chi^2_{\text{red}}$ value for fitting the displacement histograms of Fig. 8.11 with a sum of 1, 2, and 3 Gaussian functions, respectively. (D) Centres, (E) variances with linear fits, and (F) relative areas with weighted means (horizontal lines) of the 3 Gaussians over $\tau$, using the same colour legend. Blue lines in (B) and (E) represent the slope of a linear function in a double-logarithmic plot. Error bars are SEs. Plateaus of the fit variances in (E) are given by magenta, cyan, and yellow lines, respectively.

constant over time. The weighted means and standard errors, normalised to a sum of the abundances of 100 %, are given in Table 8.1. With the final relative abundances, I calculated a weighted average of the diffusion constant of 162 ± 28 deg$^2$/s (Table 8.1). The diffusion constant $D$ can be used to calculate the mean sideward stepping rate $k$, using the equation $k = 2D/\Delta\phi^2_{\text{pf}}$, where $\Delta\phi_{\text{pf}}$ is the angular step size. I calculated mean sideward stepping rates for both the angular step size of 27.7 deg for a microtubule with 13 protofilaments and the measured mean angular step size of 22 deg (Fig. 8.7). For 13 protofilaments, the mean sideward stepping rate was $0.42 \pm 0.07\,\text{s}^{-1}$. At a forward speed of 62 nm/s, every 19th step would be to the side, then. For the measured mean angular step size, the corresponding sideward stepping rate was 0.66 ± 0.15 deg, i.e. every 13th step would be a side step.

In the following, I performed the same analysis for the angular traces of multiple Kip3 at high and reduced ATP concentration. Centres, variances and abundances of the Gaussian subdistributions are shown in Fig. 8.13. The results for multiple Kip3 at 1 mM ATP were not very different from the ones for single Kip3: The angular displacement distributions were fitted best with three Gaussians, for which the centres did not change over time $\tau$ which was confirmed by linear fits (not shown in Fig. 8.13A). The overall mean angular displacement (not shown) decreased linearly over time with a slope of −0.24 deg/s to the right. At the mean speed of multiple Kip3, this angular speed refers to a rotational

**Table 8.1: Diffusional states of Kip3.** Angular diffusion constants and offsets with standard errors referring to the linear fits to variances, relative abundances of the motion populations, based on multiple Gaussian fits, and the corresponding weighted average of the diffusion constants from Figs. 8.12 and 8.13 for different experimental conditions on Kip3. For comparison, a diffusion constant based on the sideward stepping rate that was obtained from the Kip3 stepping simulation (Section 7.6) is given. The diffusion constants for different experiments are given as effective ones that have been normalised on the speed of single Kip3 at 1 mM ATP, i.e. $D_{\text{eff}} = v_{\text{single}}/v \cdot D$.

| Single Kip3, 1 mM ATP, $v_{\text{single}} = 62$ nm/s | | | |
|---|---|---|---|
| Parameter | Fit 1 | Fit 2 | Fit 3 |
| Diffusion constant $D$ (deg$^2$/s) | 4.2 ± 0.7 | 52 ± 4 | 490 ± 54 |
| Offset (deg$^2$) | −7 ± 5 | −150 ± 27 | −1478 ± 280 |
| Relative abundance (%) | 18 ± 2 | 55 ± 3 | 27 ± 2 |
| Weighted diffusion constant (deg$^2$/s) | 162 ± 28 | | |
| 2D diffusion constant (deg$^2$/s) | 144 ± 25 | | |
| Multiple Kip3, 1 mM ATP, $v = 56$ nm/s | | | |
| Parameter | Fit 1 | Fit 2 | Fit 3 |
| Diffusion constant $D_{\text{eff}}$ (deg$^2$/s) | 5.6 ± 0.2 | 75 ± 6 | 514 ± 91 |
| Offset (deg$^2$) | −6.6 ± 0.8 | −107 ± 15 | −770 ± 170 |
| Relative abundance (%) | 33 ± 3 | 52 ± 4 | 15 ± 2 |
| Weighted diffusion constant (deg$^2$/s) | 116 ± 30 | | |
| Multiple Kip3, 10 μM ATP, $v = 20$ nm/s | | | |
| Parameter | Fit 1 | Fit 2 | |
| Diffusion constant $D_{\text{eff}}$ (deg$^2$/s) | 9.0 ± 0.5 | 95 ± 3 | |
| Offset (deg$^2$) | 0.8 ± 0.8 | 1 ± 5 | |
| Relative abundance (%) | 52 ± 3 | 48 ± 2 | |
| Weighted diffusion constant (deg$^2$/s) | 51 ± 4 | | |

pitch of 84 μm. As discussed before, these values are not thought to represent effective angular motion. The variances increased linearly over $\tau$ and saturated to constant values of 89 ± 12 deg$^2$, 986 ± 122 deg$^2$, and 6097 ± 256 deg$^2$ for the three populations (Fig. 8.13B). The corresponding angular segments were 23 ± 2 deg, 77 ± 5 deg, and 191 ± 4 deg, respectively. These values were consistent with those for single Kip3 results. The diffusion constants referring to the slopes of the angular displacement variances are given in Table 8.1. To compare the values to those of the original Kip3 measurement for single-molecule conditions with respect to the same travelled distance in $x$, the variances were fitted over the effective time $\tau_{\text{eff}} = v/v_{\text{single}} \cdot \tau$, with respect to the different speeds as described before. As result, the effective diffusion constants were scaled by $D_{\text{eff}} = v_{\text{single}}/v \cdot D$. The resulting diffusion constants for the three populations of single and multiple Kip3 were very similar. The abundances of the three populations were constant during the increase of the variance, only. The weighted means (given in Table 8.1) were different from single Kip3, as the abundances for populations 1 and 3 seemed to switched values. Consequently, the weighted average diffusion constant of 116 ± 30 deg$^2$/s was slightly but not significantly

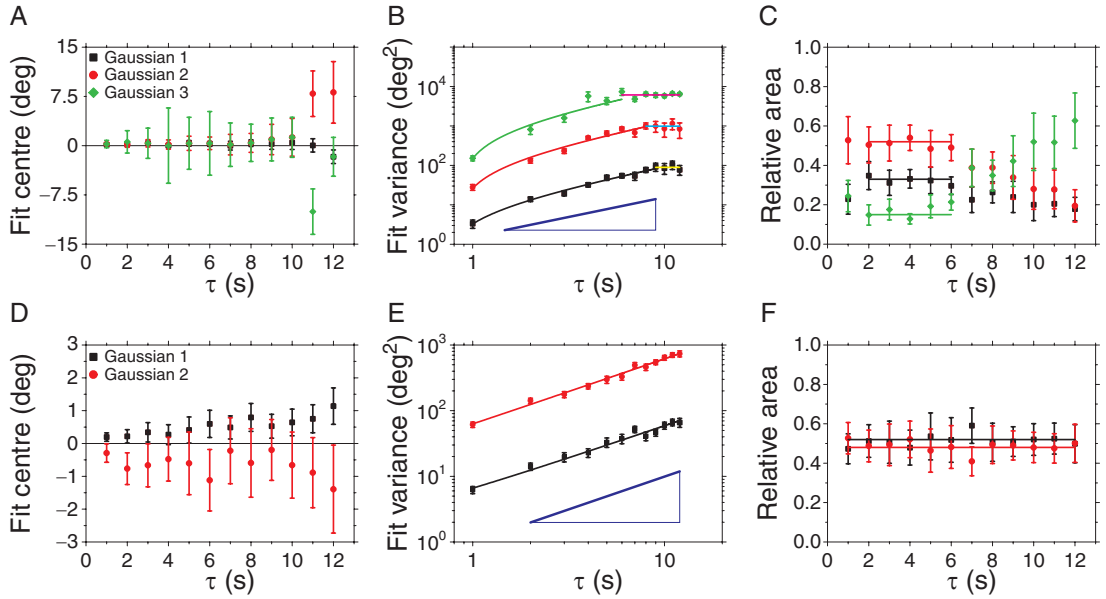


**Figure 8.13: Angular displacement analysis of multiple Kip3 traces.** Centres, variances with linear fits, and relative areas with weighted means, obtained from angle analysis for multiple Kip3 at 1 mM ATP (A–C), and at 10 µM ATP (D–F), respectively. Blue lines in (B) and (E) represent the slope of linear function in a double-logarithmic plot. Error bars are SEs. Plateaus of the fit variances in (B) are given by magenta, cyan, and yellow lines, respectively.

lower. Despite the differences, the results for single and multiple Kip3 were comparable: They both showed the existence of three distinct populations in the angular motion with distinct motion parameters and constant abundances.

However, the results for multiple Kip3 at low ATP concentrations (10 µM) differed from the other conditions. The angular displacement distributions could be fitted best with only two Gaussians. Using three Gaussians did not result in significantly lower $\chi^2_{\text{red}}$-values. Ockham's razor principle suggests to choose the model with less parameters in this case. Thus, the angular motion of Kip3 at low ATP concentration contained only two populations. Their centres were not significantly different from zero (Fig. 8.13D). The overall mean angular displacement (not shown) increased linearly with a slope of 0.04 deg/s that corresponds to a rotational pitch of almost 200 µm, representing no effective angular motion. The variances of the two Gaussians increased linearly over $\tau$ without saturation in the investigated range of $\tau$ (Fig. 8.13E). The corresponding diffusion constants, again calculated with the corrected $\tau_{\text{eff}}$, are given in Table 8.1. Both constants had similar values compared to the two smallest diffusion constants of the other Kip3 experiments. The abundances of both populations were each approximately 50 % within error margins (Table 8.1). The weighted average diffusion constant and SE were 51 ± 3 deg$^2$/s. The corresponding sideward stepping rate was 0.13 ± 0.01 s$^{-1}$ for the angular step size for 13 protofilaments. For the measured mean angular step size, the sideward stepping rate was 0.21 ± 0.03 s$^{-1}$. When using the actual time $\tau$ in Fig. 8.13E, the actual rate was 0.043 ± 0.004 s$^{-1}$ for 13 protofilaments and 0.07 ± 0.01 s$^{-1}$ for the

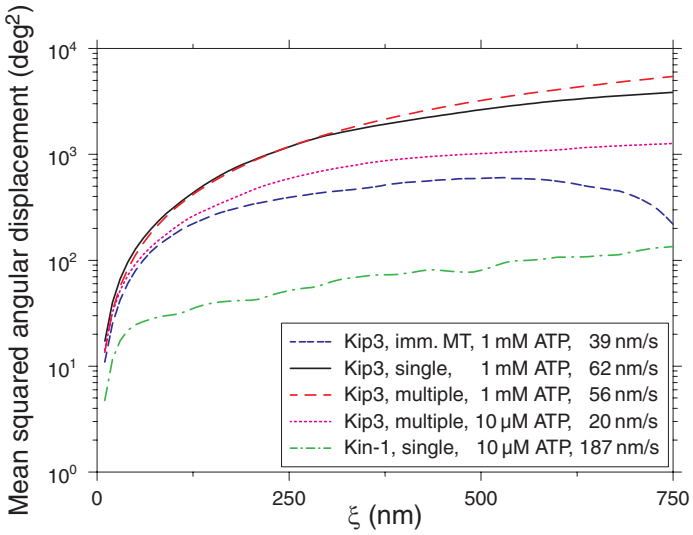


**Figure 8.14: Mean squared angular displacement analysis of angular motion as a function of the distance on the microtubule.** Plot of mean squared angular displacements as a function of the distance on the microtubule $\xi$ with standard errors of angular motion of single Kip3 on microtubules, immobilised on planar surfaces at 1 mM ATP (blue), single Kip3 at 1 mM ATP (black), multiple Kip3 at 1 mM ATP (red), multiple Kip3 at 10 µM ATP (magenta), and single rkin430 at 10 µM ATP (green).

measured mean angular step size. The forward speed at low ATP corresponds to a forward stepping rate of $2.5 \pm 0.3\,\mathrm{s}^{-1}$, meaning that every 60th or 39th step was a sideward step, respectively.

In addition to the described angular displacement and MSAD analysis, I followed a different approach: Instead of analysing the change of the distribution of angular displacements over the lag time $\tau$, I analysed this change as a function of the lag distance $\xi$ on the microtubule of the motor. This approach has the advantages that (i) the speed of the motor is not relevant for the analysis, i.e. a correction for an $\tau_{\mathrm{eff}}$ between different experiments is not necessary, and (ii) phases of motor pausing cannot be mistaken as phases of straight forward motion. To perform this analysis, a $\phi$-coordinate as a function of an equidistant $x$-values is needed. Thus, I defined bins of equal size in $x$ and assigned the median of all corresponding $\phi$-values in these bins to their bin centres. The bin sizes must be chosen big enough to have enough data in the bins for good statistics but also small enough to avoid binning over multiple angular steps. An upper bound for this bin size is the distance the motor travelled during the mean angular step dwell time. For the experimental condition with the lowest speed, i.e. multiple Kip3 at low ATP, this value is about $20\,\mathrm{nm/s} \cdot 2\,\mathrm{s} = 40\,\mathrm{nm}$. I finally chose a bin size of 10 nm, as there were still hundreds to thousands of data points in each bin. The following calculation of the MSAD as well as the angular displacement analysis were performed in the same manner as already described. The MSADs of the different experimental conditions of Kip3 and rkin430 are shown in Fig. 8.14. The MSADs for binned $x$ as a function of lag distance $\xi$ did not differ significantly from MSADs as a function of lag time $\tau$ (compare Fig. 8.10). Therefore, pauses did not have a large influence on the

analysis. Also, the analysis of the distributions of angular displacements (not shown) did not reveal qualitative differences from the previous analysis: For single and multiple Kip3 at high ATP, I found three populations with different diffusion constants. The results of single and multiple Kip3 did not differ significantly. For Kip3 at low ATP, I found again only two populations. The only difference were the values of the relative abundances, for which the weighted diffusion constants and sideward stepping rates differed.

## 8.5. 3D Stepping Assays with rkin430 Confirmed Protofilament Tracking

As a control for the measurements with Kip3, I performed 3D stepping assays using the non-protofilament switching rkin430 at reduced ATP concentrations of 5 and 10 μM to work at comparable speeds as Kip3. The measured velocities were 94 ± 5 nm/s ($N = 76$, 5 μM ATP) and 187 ± 5 nm/s ($N = 65$, 10 μM ATP). These values are consistent with results from TIRF stepping assays (Fig. 7.2): 88 ± 2 nm/s ($N = 278$, 5 μM ATP) and 168 ± 3 nm/s ($N = 280$, 10 μM ATP), showing that rkin430 did not speed up on suspended microtubules like Kip3. In a third series of experiments, I reduced the PIPES concentration in the motility solution to 20 mM, as lower salt concentrations increase the processivity i.e. the mean run length of kinesin-1 [38, 166]. This buffer is called BRB20. The used ATP concentration was 5 μM. The mean speed was reduced to 54 ± 2 nm/s ($N = 132$). The mean run length was 740 ± 68 nm ($N = 101$, BRB80, both ATP concentrations), confirming the low processivity of rkin430, compared to Kip3. In BRB20, the mean run length was 1100 ± 110 nm ($N = 65$), significantly higher than in BRB80 which was confirmed by a Mann-Whitney test. Both mean values correspond to lower bounds, especially for BRB20, as longer walking events could not be considered due to the limited lateral working range of the force clamp of 3.5 μm from the centre in each direction.

### 8.5.1. rkin430 Followed the Protofilament Axis

For 3D assays with kinesin-1, I calculated the angle $\phi$ by overlaying the $yz$-projection with a circle with mean radius that was given before. This was necessary, because fitting a circle was mostly impossible. For traces with possible circular fitting, I found a mean radius of 370 ± 18 μm ($N = 32$) which is consistent with the expected value of 340–360 nm and the results for Kip3.

For most traces, I found that rkin430 did not show any angular motion which is consistent with the outcomes of the 2D side-stepping assays with rkin430 described in Section 7.5. Exemplary traces are shown in Fig. 8.15A (top) and B. In addition, I recorded traces with significant rotations to the left or right around the microtubule (Figs. 8.15A (bottom) and C). I did not observe traces with angular diffusion nor discrete angular steps in the traces that would correspond to protofilament switching. I conclude that rkin430 followed the protofilament axis on microtubules having different supertwists.

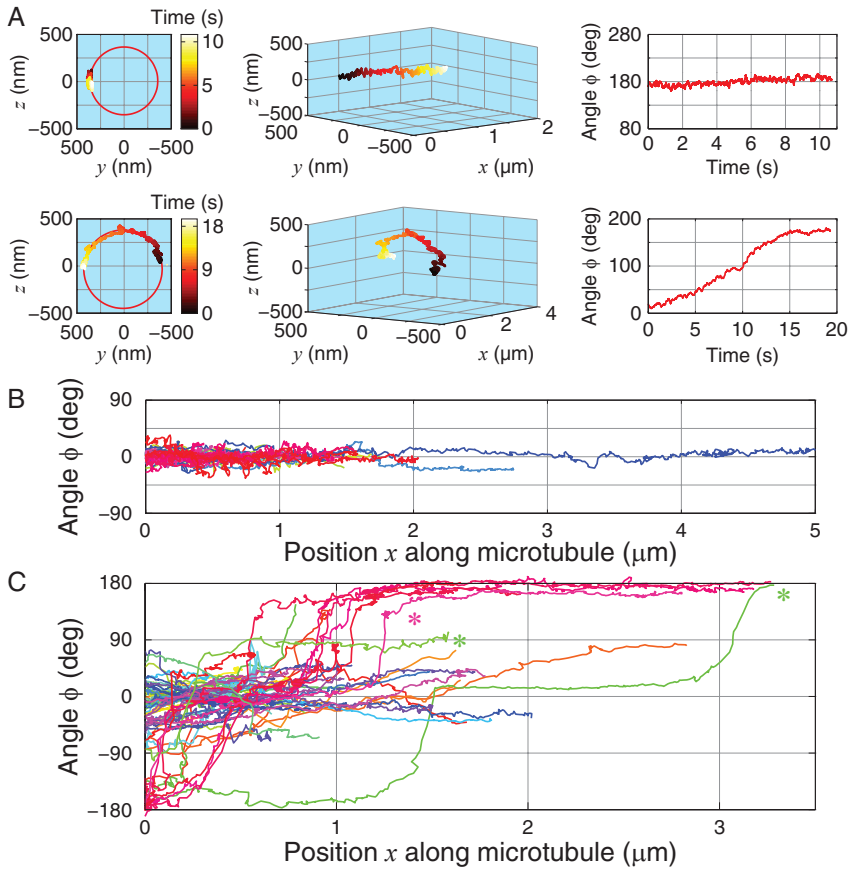


**Figure 8.15: 3D single rkin430 stepping assays on suspended microtubules.** (A) Two exemplary three-dimensional traces of rkin430-coated microspheres on suspended microtubules, showing basically no and directed angular motion, respectively. Each trace is represented by the $yz$-projection, the full 3D projection, and the angular trace over time. The bottom trace was already shown in [66]. Plots of 156 angular traces (all conditions) as a function of $x$ on 93 microtubules of rkin430, split into traces showing (B) no directed ($N = 93$) and (C) strong angular motion ($N = 63$). An offset, equal to the mean of maximal and minimal values of each trace, was subtracted from the angular traces. Some traces with sudden jumps are labelled with asterisks.

To use the rkin430 measurements as a control for the angular motion of Kip3, I calculated the MSAD in the same manner as for Kip3 using traces with no large-scale angular motions only. Traces with continuous rotations do not serve as a control as changes in the angle are due to the supertwist and not protofilament switching The MSADs were calculated for all three experimental conditions separately and the time $\tau$ was corrected as described before. Figure 8.10 shows only the result for rkin430 at 10 μM ATP and BRB80, as these conditions were closest to the main Kip3 experiment. The MSAD, after a short initial increase, settles down to a plateau value that is significantly lower than the MSAD values for all Kip3 experiments. The MSADs for the other rkin430 experiments behave similarly. This control showed that the measured angular motion of Kip3 was significant.

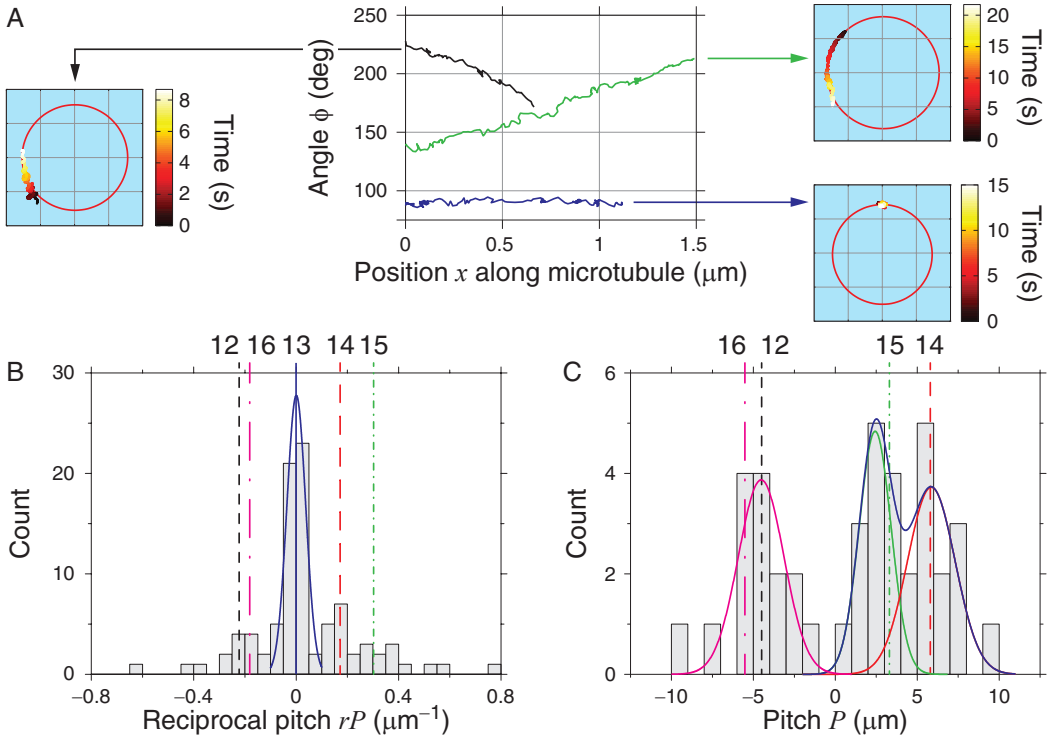


**Figure 8.16: 3D angular traces of rkin430 revealed microtubule supertwist.** (A) Three exemplary angular traces, plotted as a function of the $x$-position along the microtubule, showing left-handed (green), straight (blue), and right-handed angular motion (black), respectively. Corresponding insets show the $zy$-projection of the microsphere positions over a range of 1×1 $\mu m^2$, including circular fits that were used to calculate the angle $\phi$. (B) Histogram of reciprocal pitches, calculated for all microtubules with Gaussian fit (blue) to values $\in (-0.1, 0.1)\,\mu m^{-1}$. Vertical lines indicate values for supertwisted microtubules with 12–16 protofilaments. (C) Histogram of measured pitches, calculated from angular traces, excluding non-supertwisted ones with multiple Gaussian fits.

### 8.5.2. 3D Stepping Assays with rkin430 Revealed the Microtubule Supertwist

If rkin430 follows the protofilament, 3D traces can be used to measure the supertwist. The supertwist pitch should coincide with the values known from the literature. I calculated the pitch of rotational traces by analysing the angular position $\phi$ as a function of the forward position $x$ instead of time. In this manner, different speeds or pauses do not affect the analysis. I fitted $\phi(x)$ with a linear function and used the slope, i.e. the angular gradient $\partial\phi/\partial x$, to calculate the supertwist pitch $P$:

$$P = \frac{360\,\mathrm{deg}}{\partial\phi/\partial x}. \tag{8.2}$$

Since the pitches diverges for a 13 protofilament microtubules, the reciprocal pitch $rP$ was used to average values of different supertwists as in Section 7.6.

**Table 8.2: Expected and measured microtubule composition.** Literature and experimental values including standard errors for abundances and standard deviations for pitches. Mean pitches are weighted mean for the expected and overall mean for the measured composition, respectively. The experimental pitch for 13 protofilament microtubules bases on the Gaussian fit to the histogram of reciprocal pitches from $-0.1$ to $+0.1\,\mu m^{-1}$ (Fig. 8.16B).

| Protofilament number | 12 | 16 | 13 | 14 | 15 | Mean pitch (μm) |
|---|---|---|---|---|---|---|
| Expected pitch (μm) | −4.5 | −5.5 | ∞ | +5.8 | +3.3 | |
| Expected composition (%) | 0 | 3 | 14 | 72 | 11 | +6.6 |
| Measured pitch (μm) | −4.5 ± 1.4 | | $(+1.7 \pm 104) \cdot 10^3$ | +5.9 ± 1.5 | +2.4 ± 1.0 | |
| Measured composition (%) | 16 ± 3 | | 56 ± 5 | 15 ± 2 | 13 ± 2 | +18 ± 9 |

Some rkin430 traces did not show linear angular motion as a function of forward position but contained jumps, for example visible in Fig. 8.15C indicated by asterisks. These jumps are discussed in Section 8.5.3. I analysed all traces by excluding jumps and only fitted microtubule sections with a constant slope. Traces in BRB80 and BRB20 showed no qualitative nor quantitative differences with respect to the supertwist and were thus analysed together. Several rkin430 traces were recorded on the same microtubule. I recorded 77 traces on 44 microtubules in BRB80 and 79 traces on 49 microtubules in BRB20. In cases of multiple traces for the same microtubule, calculated reciprocal pitches were averaged to one pitch value for one microtubule. As before, three-dimensional traces of rkin430-coated microspheres moving along microtubules revealed left-handed, straight, and right-handed motion as shown in Fig. 8.16A. A histogram of the reciprocal pitches of all 156 measured traces corresponding to 93 distinct microtubules is shown in Fig. 8.16B. Zero values refer to straight 3D trajectories and thus non-supertwisted microtubules. According to previous measurements of microtubule supertwists, non-supertwisted microtubules have experimental pitches as long as several tens of micrometres [11]. Therefore, absolute pitches of more than 10 μm and absolute reciprocal pitches of less than $0.1\,\mu m^{-1}$ were denoted as non-supertwisted. The distribution of pitches of supertwisted microtubules is shown in Fig. 8.16C. It has peaks close to the expected values for microtubules with 12–16 protofilaments. The statistics and/or resolution of pitch determination did not allow to distinguish between pitches with protofilament numbers of 12 and 16. Previous studies found no microtubules with 12 protofilaments for this MT preparation [11]. Still, it can not be excluded entirely that both 12 and 16 protofilaments microtubules may be present. The overall composition of the used MT mix was estimated and given in Table 8.2 together with expected results from previous measurements and predictions [11, 14]. The abundances for 12 and 16 protofilaments are represented as one value. The distinct abundances for 14 and 15 protofilaments are based on the ratio

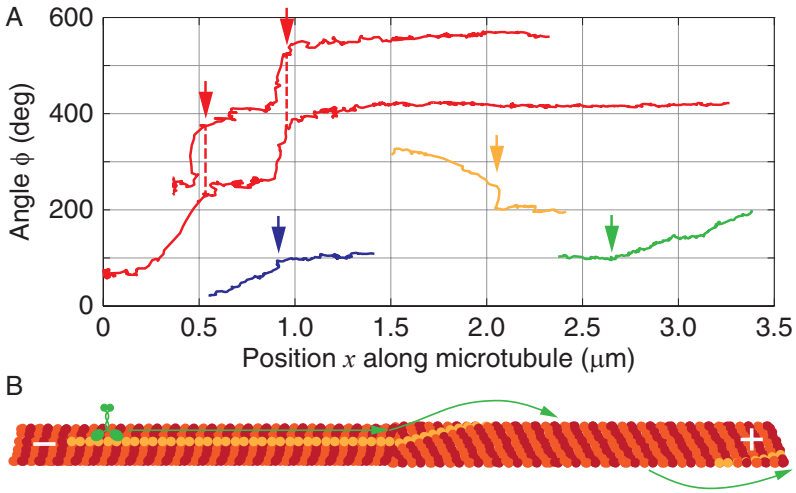


**Figure 8.17: Jumps in the angular slopes implied switches of the protofilament number.** (A) Four exemplary angular traces, plotted as a function of the $x$-position along the microtubule, showing sudden angular jumps in the angular slopes, indicated by arrows. The two traces in the left upper corner (red) were recorded on the same microtubule. (B) Schematic of a microtubule with a change in the protofilament number and supertwist, leading a moving kinesin from a straight to a helical path.

of areas of multiple Gaussian fits to the pitch distribution (Fig. 8.16C). These pitches based on the Gaussian fits are in good agreement with the expected values (Table 8.16). The measured microtubule composition differed significantly from the expected one. Non-supertwisted microtubules constituted the majority in my preparation, in obvious contrast to the composition, measured by Ray et al. [11]. The mean reciprocal pitch, weighted by the abundances, was $0.055 \pm 0.030\ \mu m^{-1}$ and not significantly different from zero. Therefore, the here used microtubules were not supertwisted on average. This is an important finding, because this protocol is often used for *in vitro* experiments.

### 8.5.3. Sudden Changes in Angular Traces of rkin430 Indicated Changes in the Protofilament Number

Some angular traces contained sudden jumps in the angular position accompanied by changes in the angular slope as shown in Fig. 8.17A. I interpret these events as possible switches in the protofilament number as illustrated in Fig. 8.17B. Those switches have been observed in microtubules *in vitro* and *in vivo* by Chrétien et al. [12]. The frequency of transitions per MT length was $0.25\ \mu m^{-1}$ for microtubules with mainly 13 protofilaments *in vitro*. I observed 21 switches on 17 out of 93 microtubules with an overall MT length of 90 μm, referring to a length frequency of $0.23 \pm 0.05\ \mu m^{-1}$. This is in excellent agreement with the literature value, supporting the hypothesis that jumps correspond to changes in the protofilament.

Furthermore, I observed these events those jumps on approximately the same positions for different traces recorded on the same microtubules (Fig. 8.17A).

This agreement showed that those events were related to particular positions on the microtubules and did not occur randomly.

## 8.6. Discussion

Using microtubules that were immobilised on planar surfaces enabled me to observe angular motion of Kip3 in a 2D assay. However, due to the arrangement of the microtubules they were not freely accessible and the angular motion was thus confined. This confinement, which was also visible in the mean squared angular displacement of all measured traces, could be explained by the geometry model, developed for the two-dimensional side-stepping assay. This consistency on the other hand confirms the validity of the suggested model. The angular position of the kinesin on the microtubule ($\phi$) was not measurable in the 2D assay. With no load applied, the microsphere can swivel freely above the microtubule and one cannot extrapolate from the measured angle to the actual trajectory.

Still, the data of this experiment can be used to estimate whether Kip3 performed angular motion: The spread of all angular traces in Fig. 8.3C, represented by the standard deviation of 12.5 deg, was much bigger than the measured angular resolution of 3.4 deg (Section 3.3). Also, the mean squared angular displacement was much bigger than for kinesin-1 on non-supertwisted microtubules (Fig. 8.10). In both control measurements, the microsphere could also swivel freely around the microtubule. Therefore, the angular motion measured on immobilised microtubules cannot be explained by microsphere fluctuations only. I conclude that sideward motion of Kip3 occurred in this experiment. Because the angular motion was confined by the geometry, 3D assays with suspended microtubules were necessary.

On suspended microtubules, angular motion of Kip3-coated microsphere was observable by video and 3D-force-clamp tracking. The video tracking had a lower resolution and suffered from practical issues. Using the 3D force clamp enabled to not only observe angular motion of Kip3 directly but also to detect discrete angular steps between neighbouring protofilaments. Since no load was applied in the 3D assays, the measured mean angular step dwell time was longer than the mean sideward step dwell time in the 2D side-stepping assays (Fig. 7.5C). The corresponding sideward stepping rate in the 3D assays of $0.5 \pm 0.1\,\mathrm{s}^{-1}$ was consistent with the zero-force rate of $k_l^0 + k_r^0 \approx 2k^0 = 0.59 \pm 0.07\,\mathrm{s}^{-1}$ predicted by the Kip3 stepping simulations in the previous chapter (Table 7.4). The mean squared angular displacement (MSAD) analysis of the angular motion of Kip3 was useful to compare different experiments with each other but gave no insight into the walking mechanism of Kip3 itself. Insight provided the analysis of the temporal behaviour of the angular displacement distributions revealing three different diffusional states of Kip3. These states were not observable in the 2D side-stepping assays and, thus, not simulated. Based on the average sideward stepping rate for the 2D assays, a diffusion constant $D$ can be calculated by $D = k^0 \Delta\phi_{\mathrm{pf}}^2$. Using the different angular step

sizes $\Delta\phi_{\mathrm{pf}}$ for protofilament numbers of 12–16 and $k_0 = 0.3\,\mathrm{s}^{-1}$, the expected diffusion constant varies from 150–265 $\mathrm{deg}^2/\mathrm{s}$. For 13 protofilaments with an angular step size of 27.7 deg, the expected value is $226 \pm 27\,\mathrm{deg}^2/\mathrm{s}$. For the measured angular step size of 22 deg (Fig. 8.7), the diffusion constant was $144 \pm 25\,\mathrm{deg}^2/\mathrm{s}$. This value is given in Table 8.1 for comparison. These values are consistent with the weighted average diffusion constant of $162 \pm 28\,\mathrm{deg}^2/\mathrm{s}$ in Table 8.1 showing that the 2D and 3D assays are consistent with each other. Also, the corresponding sideward stepping rate of $0.42 \pm 0.07\,\mathrm{s}^{-1}$ ($0.66 \pm 0.15\,\mathrm{s}^{-1}$) for am angular step size of 27.7 deg (22 deg) is consistent with the measured sideward stepping rate obtained from the detected angular steps. I assume that the 2D side-stepping assays measured a weighted average of these three states of motion. The origin of these three states is unclear.

The first state has a very small diffusion constant. During the mean angular step dwell time of 2 s, the motor diffuses over an angle of only 4 deg which is much lower than the angle between two protofilaments. The initial slope of the MSAD of kinesin-1 in Fig. 8.10 corresponds to a diffusion constant of $5.4 \pm 0.2\,\mathrm{deg}^2/\mathrm{s}$. During 2 s, the root mean squared angular displacement is 4.6 deg. This value is comparable to the one of the first state, suggesting that this state of motion represents noise instead of angular motion due to protofilament switching. Kip3 could track a protofilament because it was "trapped" between two microtubule seams. As already mentioned, kinesins are thought to be unable to switch protofilaments if a seam is between. It has been reported that microtubules can have multiple, i.e. an odd number of seams [8, 17]. However, even if every microtubule would have multiple seams with e.g. one protofilament between two seams, the probability of Kip3 landing on this protofilament would only be 8 % (1/13). This value is less than the abundance of 18 % of the first state. Thus, the confinement between two seams cannot explain this motion state alone. Kip3 might have an intrinsic motion state of not switching protofilaments or other structural confinements might inhibit protofilament switching. Kip3 has an additional microtubule binding site at its tail that is partially responsible for its high processivity [47]. If this tail domain was binding to a neighbouring protofilament, this binding might inhibit protofilament switching. Another cause for the first state might be Kip3 pauses between phases of processive motion (Fig. 7.9B). Those pauses also occurred in 3D assays, where Kip3 spent about 5 % of the recording time pausing (for both single and multiple-molecule conditions at full ATP). The angular displacement analysis cannot distinguish whether Kip3 paused completely or moved straight forward without angular motion and therefore, both cases contributed to the first state of motion.

The second and third states have much higher diffusion constants suggesting protofilament switching. The difference could be again Kip3's additional microtubule binding site which might influence the state of motion. This hypothesis could be tested by making the same experiments and analysis with truncated Kip3 lacking the MT binding site.

The negative offsets of the variance fits (Table 8.1) cannot be explained by additional filtering of the original data as described by Michalet [163]. Additional

filtering, like decimating or averaging, corresponds to a finite exposure time $t_{\mathrm{exp}}$ during which the molecule diffuses. In my assays, the sampling rate was high and therefore, I averaged of the data to avoid auto-correlation artefacts. This increased $t_{\mathrm{exp}}$ and causes an offset in the MSAD of $2\sigma^2 = 2\epsilon^2 - 2/3 \cdot Dt_{\mathrm{exp}}$ [163], where $\epsilon$ is the measurement precision of about 3.4 deg (Section 3.3), $D$ the diffusion constant, and $t_{\mathrm{exp}} = 1\,\mathrm{s}$. The negative offsets in Table 8.1 were much larger compared to the predictions from this equation. In contrast, the inverting of the equation yielded an approximate exposure time of about 5 s for the given offsets. This higher value for $t_{\mathrm{exp}}$ can be explained by the additional median-filtering of the 3D data which was not regarded in the given equation. The additional filtering results in an effectively higher exposure time which may explain the offset values.

I observed saturation of the angular displacement variances of all populations. The angular segment, to which the first diffusion state was confined, was equal to one protofilament switch $\Delta\phi_{\mathrm{pf}}$, i.e. the angular motion was confined to one protofilament. The angular confinement of the third diffusion state referred to half a turn around the MT axis which is in contradiction to the observed angular confinement of a complete turn. However, the limit of $S^2/6$ is only reached for times $\tau \gg S^2/(4D)$ which is ≈66 s for the fastest diffusing population and the expected maximal segment of 360 deg [165]. Because the experimental times were shorter, the angular displacement variance saturation plateau and thus, the values for the confined segments were underestimated. Therefore, the saturation of the third, fastest population might be still consistent with the angular motion's confinement to one turn around the microtubule. The origin of the confinement of the second population remains unclear.

Nevertheless, the analysis of the Kip3 angular diffusion at high ATP concentration revealed three distinct states of motion which are consistent with previous results and self-consistent.

I measured a significant increase of the single Kip3 forward speed in 3D assays of about 50 %, compared to the speed in 2D assays (60 nm/s vs. 40 nm/s, respectively). Obviously, making the microtubule freely accessible had an impact on the Kip3 stepping behaviour. A simple explanation might be the increase of the effective drag on the microsphere close to a surface, following Faxén's law [68]. The drag force on a microsphere with the here used values for diameter and water viscosity, a speed of 40 nm/s at a height of about 1.5 µm is about 0.2 fN and thus very small. The proximity to the surface, i.e. height of the microsphere centre ≈320 nm, only increases the drag by a factor of 2. Such forces are far too small to influence the Kip3 speed. Forces in the pN range would be necessary [40]. I suggest that in 2D assays the sideward stepping of Kip3 is inhibited when it meets the surface, leading to an overall reduced stepping rate because of futile steps. Because rkin430 follows the protofilament, no futile steps are expected. The surface would affect rkin430 stepping when a supertwisted protofilament guided kinesin-1 to the surface. Here, rkin430 would rather detach as it preferentially does so when meeting an obstacle on the microtubule [52, 53, 55]. This detachment would rather influence the mean run length of rkin430 but not the forward speed. Indeed, I measured no significant or only a small increase of the

rkin430 speed with respect to the control measurements (Section 8.5) supporting this interpretation. Unspecific interactions of the kinesin-coated microspheres with the sample surface also might reduce the forward speed which would affect both kinesins. Whether the mean run length of kinesin-1 changes on freely accessible microtubules could be tested in a TIRF stepping assay with thinner surface structures and without microspheres.

Nearly all recorded angular traces of Kip3 were confined to one turn around the microtubule. A possible explanation would be the MT seam (Section 2.1). It is suggested that kinesins cannot switch protofilaments with the seam between them [8]. At the seam, the axial mismatch between the neighbouring protofilaments is much bigger than usual which rules out protofilament switching of kinesins, even with longer neck linkers like that of Kip3 [50]. I observed traces, in which the Kip3 moved until a certain angle, stopped, and then moved in the opposite direction. For several traces, that were recorded after another with the same microsphere on the same microtubule with the same starting position, this angular point of return was at the same position, suggesting that it was related to the MT structure. This finding supports the hypothesis of the MT seam.

The radii of the angular traces I measured for kinesins in 3D assays were significantly higher than in 2D assays, i.e. on immobilised microtubules. One can explain this increase by the fluctuations of the microtubule that was much more pronounced for suspended than for immobilised microtubules. Additional fluctuations or possible bending of the microtubule would increase the radius of the trajectory around it.

The experiment with Kip3 under multiple-molecule conditions showed no difference to the single Kip3 experiment with respect to speed and the extent of the angular motion. The MSADs were identical within error margins and I did not observe a significant directional bias. Also, the angular displacement distribution analysis of the traces yielded results that were not different from those of single Kip3. Thus, the model based on a force-induced bias from Section 7.7 is not supported by the data. However, the effective number of motors per microsphere that can bind the same microtubule the same time is small. Even if e.g. five motors were bound to the same microsphere, they all had to be bound in a restricted area on the microsphere surface to be able to reach the microtubule simultaneously. This area divided by the surface area of the microsphere defines the probability for such a scenario and highly depends on the sizes of microsphere and motor/PEG linker. I calculated and discussed these geometric probabilities in detail previously [92] and found that for this system of microsphere, PEG linker, and Kip3, a multiple binding of more than three Kip3 motors is very unlikely. Thus, the postulated collective behaviour of tens to hundreds of Kip3 motors cannot be observed in an assay with only 2–3 motors. I conclude that such a multiple Kip3 microsphere stepping assay is neither suited to confirm nor rule out the model of collective motor interaction.

At a reduced ATP concentration of 10 μM, I measured a drop of the Kip3 stall force from about 3 pN to 0.8 pN under multiple-molecule conditions. The stall force for single Kip3 at this ATP concentration is expected to be even less. It could be interesting to measure the stall force of single Kip3 as a function of ATP

concentration directly. The MSAD was much lower than for high ATP (1 mM) and so was the general spread of the measured angular traces. The analysis of the angle distribution over time revealed two motion states, in contrast to the Kip3 measurements at high ATP. The diffusion constants were of similar values as the ones of the first two motion states at high ATP. This implies that the third and fastest motion state is somehow "shut down" at low ATP. The abundance of the of the first state increased, whereas the abundance of the second state stayed constant. This finding is consistent with the relative time, Kip3 spent pausing which increased to 13 %. The number of sideward steps per forward step decreased dramatically. Apparently, the protofilament switching of Kip3 is ATP dependent and occurs less frequently at low ATP concentrations with respect to forward stepping. Furthermore, at low ATP concentrations, the forward speed of Kip3 on suspended microtubules did not increase significantly compared to the control on microtubules immobilised on planar surfaces. This finding is consistent with the interpretation that more frequent sideward stepping is correlated to higher speeds as described above. The reason for this decrease of sideward stepping might be that at a generally lower stepping rate, the leading head of Kip3 has more time to "choose" the next binding site on the microtubule. As the closest one is the binding site in front, forward steps might be preferred under these conditions. In contrast to these results, gliding assays with Kip3 at 10 µM ATP showed a reduced rotational pitch, implying that sideward steps become more frequent with respect to forward steps under these conditions [49]. However, as discussed before, gliding assays do not provide single-molecule conditions and are thus hard to compare with single-molecule optical tweezers stepping assays.

Three-dimensional stepping assays with the kinesin-1 rkin430 confirmed protofilament tracking. Corresponding trajectories showed no angular motion or a linear angular increase of decrease consistent with microtubule supertwists. While the MSAD of traces without angular motion worked as a control for Kip3 assays, all rkin430 traces were used to determine the composition of the microtubules with respect to the supertwist and protofilament number. The calculated composition was different from the one reported in the literature [11]. Possible reasons for the difference might be: While we used an identical preparation protocol, we used porcine tubulin instead of bovine tubulin. It is known that microtubules from different species have different properties, see Widlund et al. for references [167]. However, it is unknown whether tubulin from different species polymerises differently under identical conditions. Another explanation for the deviation could be the selection of long microtubules by the assay itself. As the canyon is 10 µm wide, shorter microtubules cannot be used for measurements. Thus, the measured distribution of protofilament numbers corresponds to longer microtubules. The distribution for microtubule of all lengths might be different. However, there are no data whether microtubules with different protofilament numbers polymerise with different speeds. If MT growth is limited by diffusion, one would expect slower growth with increasing protofilament number i.e. microtubules with high protofilament numbers are shorter. The described 3D assay would preferentially use microtu-

bules with smaller protofilament numbers which would be consistent with the observed shift of higher abundances to smaller protofilament numbers (Table 8.2). The major difference between the here described MT preparation and the one in reference [11] is that my microtubules were stabilised with taxol. This stabilisation was not done in [11], where the microtubules were used for TEM preparation right after polymerisation. TEM imaging by Diáz et al. has shown that the binding of taxol to GTP-grown microtubules changes their structure and reduces their mean diameter [168]. Also, the binding of taxol to microtubules, grown in the presence of GTP and docetaxel (a taxol-related drug that stabilises microtubules) changes the MT structure and reduces the number of protofilaments. Moreover, microtubules grown in the presence of taxol have about one protofilament less than without taxol [169]. However, I did not grow microtubules in the presence of taxol. I added taxol after the growing phase. Yet, the reports imply that the stabilisation with taxol reduces the protofilament numbers in the microtubules. This reduction was in good agreement with the shift of the abundances to smaller protofilament numbers in my MT composition (Table 8.2).

Importantly, on average, my microtubules were not supertwisted. This finding is in agreement with the absence of any average angular gradient in the entirety of all measured angular traces of Kip3. For the simulation of the 2D side-stepping assays (Section 7.6), an on average left-handed supertwist, based on the literature values, was used. This value now turned out to be wrong. However, simulations with the supertwist as a free parameter showed that the actual value of the supertwist pitch had no influence on the simulation's outcome.

The observed jumps in the angular traces and the corresponding changes in the angular slopes can be interpreted as observation of switches in the protofilament number. Though the measured length density of those events was in very good agreement with results from electron microscopy measurements [12], direct evidence for this interpretation cannot be obtained by the optical tweezers approach. These events are expected to be also present in the Kip3 data but cannot be distinguished from fast protofilament switching.

# 9. Laser-Induced Trapping of Particles by Carbon Grids

Multiple optical trapping of microscopic objects is a powerful way of optical manipulation. Established approaches are e.g. holographic optical tweezers [170], time-shared optical traps [171], or optical trapping by surface plasmons [172]. Here, I found that laser illumination of a perforated carbon film supported by a TEM copper grid at a water-air interface induced reversible trapping of microscopic objects like microspheres and cells. The range of this trapping depended on the laser power and exceeded the grid size of several micrometres. Trapping forces exceeded 100 fN. This effect might have the potential for versatile applications such as manipulation of cells or sorting of microscopic objects.

In this chapter, the effect of laser-induced grid trapping and its properties are described.

## 9.1. Trapping of Various Objects by Different Carbon Grids

I built samples with quadratic carbon grids in a flow chamber as described in Section 6.2 and flushed in microspheres, diluted in nanopure water. When the laser was focused in the plane of the carbon and the shutter was opened, I observed an instantaneous attraction between the carbon grid and the microspheres around the laser (Fig. 9.1). When the laser shutter was closed again, the attraction was terminated and the microspheres diffused freely again. Trapping occurred only at the edges and preferentially in the corners of the carbon grid. Microspheres that were already held at the side of the grid moved preferentially into the corners afterwards. When the grid was positioned directly on the surface, there was no attraction. I observed the same reversible trapping effect for different polystyrene microsphere diameters (590, 1010, and 3000 nm) as well as for different materials (silica, 600 nm). I tested this effect with cells (E. coli bacteria in lysogeny broth buffer) and found trapping as well (Fig. 9.2A). In addition to the quadratic carbon grids, I also built samples with circular holes in the carbon film (Quantifoil R3.5/1) and observed the same trapping effect (Fig. 9.2B).

To estimate the trapping force, a flow was applied inside the sample channel of up to 10 µm/s for 590 nm PS microspheres (mean speed and SEM: 6.6 ± 0.4 µm/s, $N = 26$). Experiments with applied flow were performed in another optical tweezers setup, using interference reflection microscopy (IRM) for visualisation and a frame rate of 4 Hz at a temperature of 25 °C. The channels of the flow cells

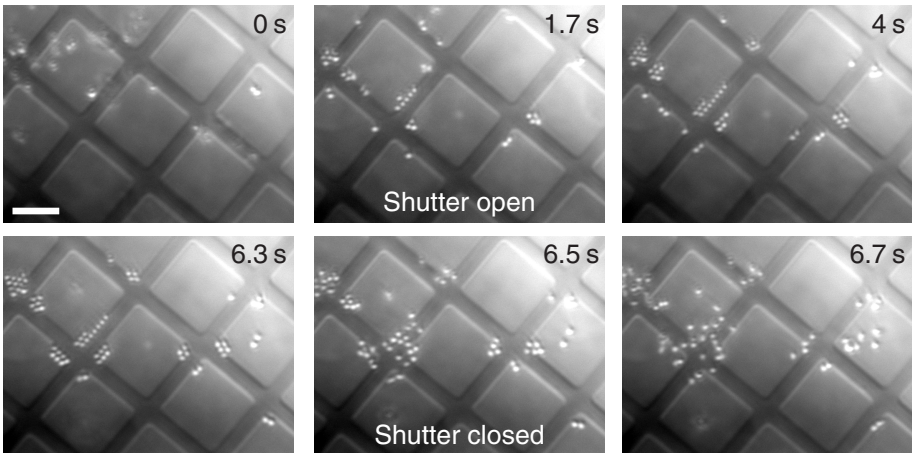


**Figure 9.1: Laser-induced trapping of microspheres by a carbon grid.** Image sequence with recording times. The first image was taken directly before the laser shutter was opened, the fifth directly after the shutter was closed again. Polystyrene microspheres with a diameter of 590 nm and a laser power of 25 mW in the focus were used. Scale bar is 5 μm.

were connected to thin microloader tips from Eppendorf. A flow inside the channel was generated by a height difference $\Delta h$ of 4–5 cm between the ends of both tips as illustrated in Fig. 9.3A. The flow speed $v$ was determined by video tracking of flowing microspheres. With opened laser shutter, the grid trapping was able to hold the microspheres against the flow (Fig. 9.3). The corresponding drag force was calculated by Stokes' law: $F_{\text{drag}} = \gamma \cdot v = 6\pi\eta R v$, where $\gamma$ is the drag coefficient, $\eta$ the fluid's viscosity (about 0.89 mPa·s for water at 25 °C and 0.81 mPa·s at 29 °C [173]), and $R$ the microsphere radius. The increase of the drag close to a planar surface, described by Faxén's law, was not considered here, as the microsphere were close to the lower surface. The maximum measured force of 50 fN (mean force and SEM: 33 ± 2 fN) is a lower estimate, because microspheres did not detach at that flow speed.

I tried to determine the maximum force by measuring the speed of microspheres that were attracted and trapped by the carbon grid. For a better temporal resolution, I used the maximum frame rate of 26 Hz and measured the

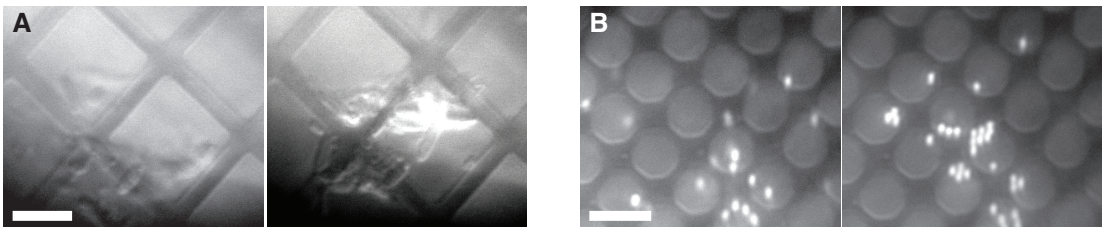


**Figure 9.2: Laser-induced trapping of cells and microspheres by different carbon grids.** Images of (A) quadratic carbon grid with bacteria and (B) a circular carbon grid with 590 nm polystyrene microspheres with closed (left) and opened (right) laser shutter, respectively. Scale bars are 5 μm.

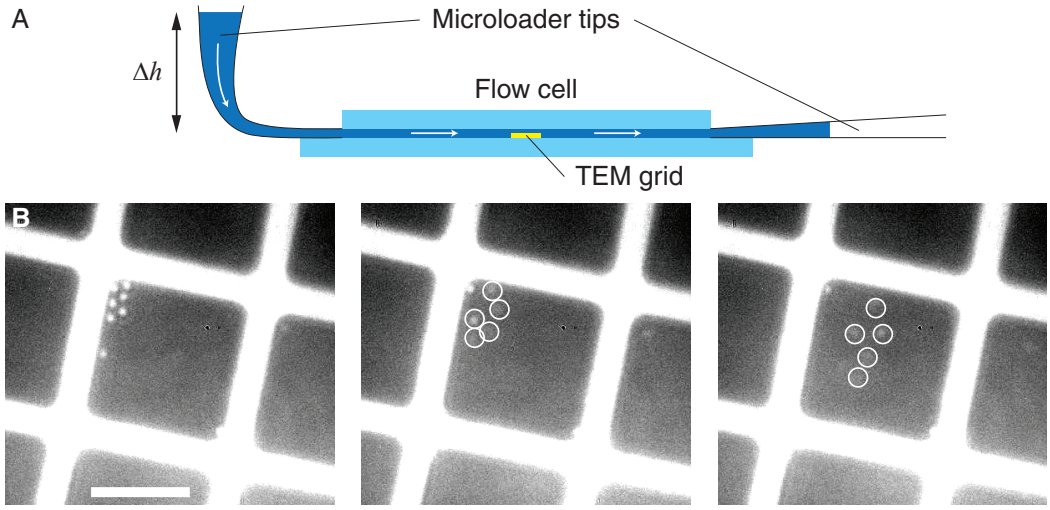


**Figure 9.3: Grid trapping held microspheres against a flow.** (A) Schematic (not to scale) of the flow cell with microloader tips. A flow (indicated by white arrows) was applied inside the channel with the TEM grid by maintaining a height difference $\Delta h$ between both tips. (B) Images of 590 nm polystyrene microspheres at 25 mW laser power in the focus, imaged in interference reflection microscopy. A flow of some μm/s was applied in the channel. When the laser shutter was opened, the induced trapping held the microspheres against the flow (left). When the laser shutter was closed, the microspheres moved with the flow (middle and right). Moving microspheres are marked with white circles. Scale bar is 5 μm.

speed by analysing the slopes of microsphere traces that were visualised by kymographs using Eq. 4.1 as shown in Fig. 9.4A. The speed towards the carbon grid I observed increased with time reaching a final constant speed as shown in Fig. 9.4A. We attribute this increase to an increase in the attractive trapping force. Depending on the laser power, the measured speeds for 590 nm PS microspheres reached up to several tens of μm/s as given in Fig. 9.4B. Forces were calculated from these speeds, using Stokes' law. Measurements showed a large variation, as (i) the speeds and forces were smaller further away from the laser focus, and (ii) the arrangement of the carbon grid did not provide a homogeneous force field which complicated the measurements a lot, (iii) the maximum frame rate was sometimes not large enough as some traces were only a few frames long. Thus, the measured speeds and forces can only be used to estimate the range of forces that can be exerted by this effect. The measured dependence of the speed on the laser power implies increasing forces with higher laser power. However, the discussed issues and the small number of data points do not allow for a more detailed interpretation.

The maximum forces were at least 100 fN for a laser power of 25 mW in the laser focus. This force is larger than the drag force applied by the flow but smaller than the maximum force, one could apply on a single microsphere using optical tweezers with the same laser power. The latter force would be several pN.

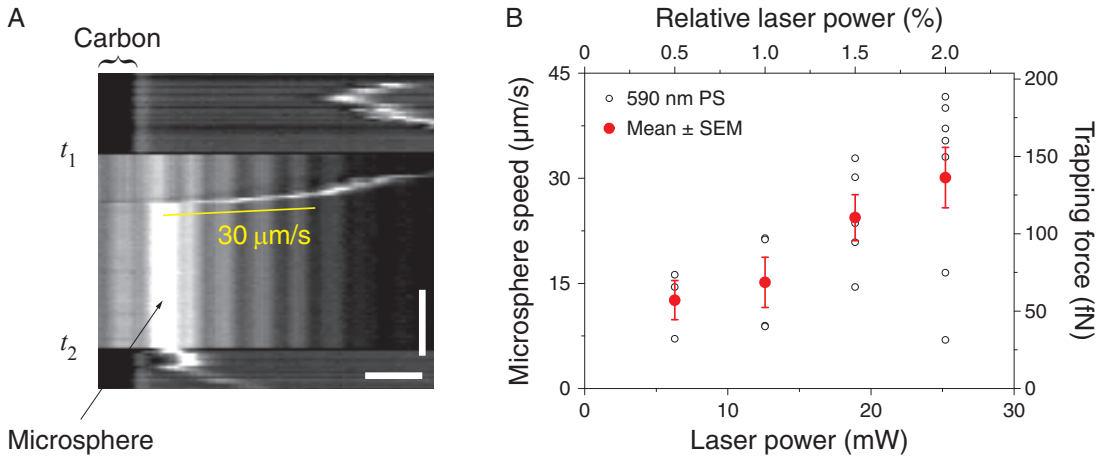


**Figure 9.4: Grid trapping exerted forces of more than 100 fN.** (A) Kymograph of a 590 nm PS microsphere that was attracted by the carbon grid. Before the laser shutter was opened at time $t_1$, the microsphere diffused freely but was attracted with an open shutter. The laser light is visible as bright fringes. A manually drawn line was used to calculate the given speed and is presented with a vertical offset (yellow). After the shutter was closed again at time $t_2$, the microsphere diffused away from the carbon. Vertical scale bar: 1 s; horizontal: 1 µm. (B) Dependence of the microsphere speed and corresponding force (all data points together with mean and SEM) on the laser power in the focus in the focus (in mW and % of the full laser power).

## 9.2. A Water-Air-Interface Was Crucial to Induce Trapping

Besides samples with grid trapping, I occasionally had samples where I did not observed any trapping. In some samples, there were even areas in the same sample where trapping was possible right next to areas where it was impossible. One difference between both areas was the bright laser spot which was only visible in trapping areas (Figs. 9.5A and B). Figures 9.5C and D show the interface between both areas in DIC and IRM imaging, respectively. What is the difference between both areas? To answer this question, I trapped bacteria with the laser focus and scanned upwards through a hole in the carbon grid, using the piezo stage. In trapping areas, the bacteria were pushed down and out of the centre of the trapping focus. Contrary, in non-trapping areas, the bacteria remained in the focus, also above the carbon grid. Thus, there was an interface at the carbon that prevented objects from moving upwards. This barrier most likely corresponds to an interface between an air layer on top of the carbon film and the sample fluid underneath. The images of the separation of both areas in Fig. 9.5C and D support that. This hypothesis is further supported by the following observations:

(i) Carbon is highly hydrophobic and hindered a complete wetting of the grid. I often observed only partial filling of the channel space around the grid after visual inspection. Wetting was improved by adding F-127 to the buffer which binds to hydrophobic surface, making them hydrophilic.

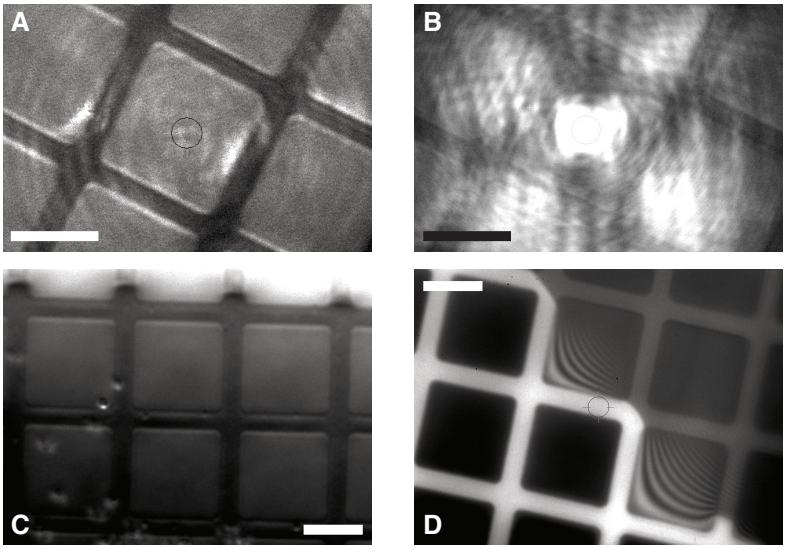


**Figure 9.5: Areas around carbon grids with and without trapping.** Laser spot, focused through the holes in the carbon film in a (A) non-trapping and (B) a trapping area, respectively. Interface between trapping and non-trapping area, visualised by (C) differential interference contrast and (D) interference reflective microscopy. The trapping areas are on the lower half and the left lower corner, respectively. Scale bars are 5 μm.

Sometimes, there were areas in the corners of the copper grid that had visible air bubbles on top. Trapping was possible here, too.

(ii) I never observed microspheres or cells above the grid in areas where trapping was possible.

(iii) When the laser was focused to unspecifically sticking microspheres on the carbon without in areas where trapping was not possible, it rarely produced cavitation bubbles. Beneath these bubbles, grid trapping worked.

(iv) The intensity fringes at the interface of areas where trapping was and was not possible (Fig. 9.5D) imply interference of LED light that was reflected at the glass-water interface and the suggested water-air interface, respectively.

Thus, I conclude that the water-air interface at the carbon film was crucial for the trapping effect.

## 9.3. The Trapping Range Was Limited

While trapping multiple microspheres, I observed that for lower laser powers only microspheres near the laser focus were trapped and microspheres close to the edge of the field of view were not. Thus, the trapping range was limited. I determined the trapping range quantitatively by measuring the distance between the laser focus and the furthest position of a microsphere that diffused

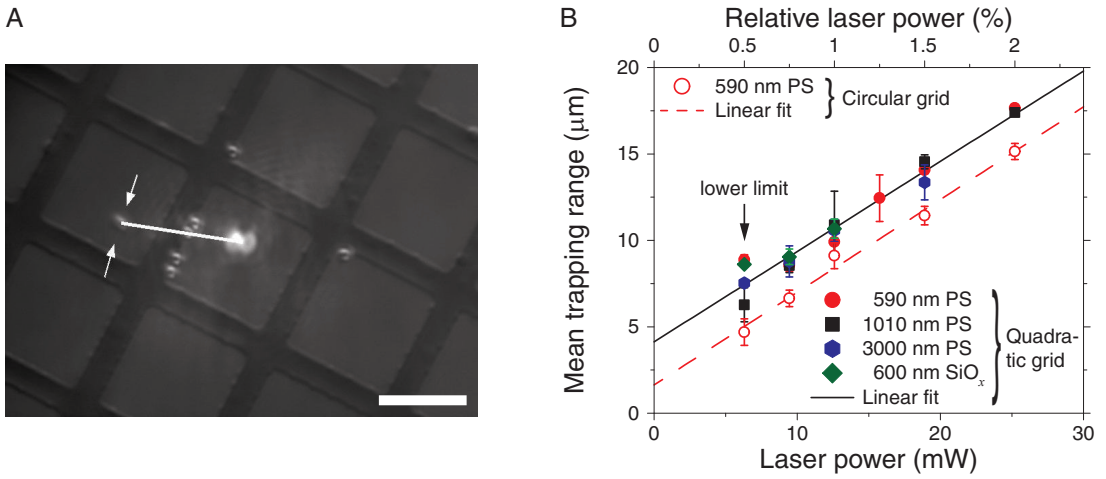


**Figure 9.6: The limited range of grid trapping.** (A) Image of laser-induced trapping of 590 nm polystyrene microspheres at 6 mW laser power. On the left, a freely diffusing microsphere is entering the trapping area around the laser focus. The distance between the position of the microsphere where it was attracted (indicated by white arrows) and the centre of the laser focus was defined as trapping range (white line). Scale bar is 5 µm. (B) Dependence of the trapping range (means with standard deviations as error bars) on the laser intensity (in mW and % of the full laser power in the focus) for polystyrene (PS) and silica ($SiO_x$) microspheres of different diameters with linear fits for quadratic and circular carbon grids, respectively.

into the trapping range and was attracted by a nearby section of the carbon grid (Fig. 9.6A.) This "trapping range" does not represent the distance between the particle and the trapping grid but the distance of the interaction in general from the laser focus. The trapping range between carbon grid and particle was not measurable here due to the limited geometry of the grid: The holes (size: 7 µm) in the carbon film were too small to measure trapping ranges of more than 10 µm for trapping between the carbon bars. I found that the trapping range scaled linearly with the laser power in a range of 6–25 mW in the laser focus (Fig. 9.6B). Note that I could not measure the trapping range for higher laser powers, as the range exceeded the field of view of the microscope. Interestingly, the data of the trapping range for different microsphere sizes and materials coincided when a quadratic carbon grid was used. For a circular grid, the trapping range scaled linearly with the same slope but a different intercept. The respective parameters of linear fits to the data are given in Tab. 9.1. For

**Table 9.1: Linear dependence of the grid-trapping range on the laser power.** Slopes and intercepts of linear fits to the grid-trapping range as a function of the laser power with standard errors (SEs) for different grids with typical hole sizes and bar widths.

| Grid geometry | Hole size (µm) | Bar width (µm) | Slope ± SE (µm/mW) | Intercept ± SE (µm) |
|---|---|---|---|---|
| Quadratic | 7 | 2 | 0.52 ± 0.03 | 4.1 ± 0.4 |
| Circular | 3.5 | 1 | 0.54 ± 0.03 | 1.6 ± 0.5 |

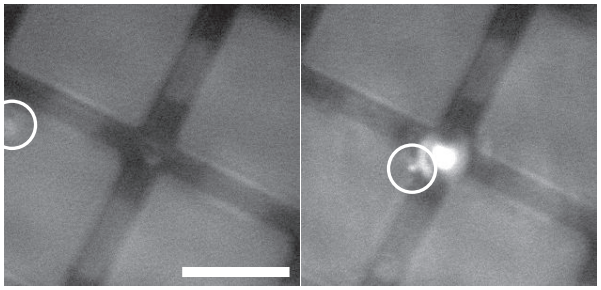

**Figure 9.7: Grid trapping was enhanced with the laser focused on the carbon.** Image of a 600 nm silica microsphere at 3 mW laser power with closed (left) and opened (right) laser shutter. When the laser was focused through the holes in the carbon film, no trapping was observed. When the laser was focused directly onto the film, the microsphere, indicated by a white circle, was attracted by the grid. Scale bar is 5 μm.

laser powers below 6 mW, I observed no or only weak trapping. When the laser was focused directly onto the carbon film with a low laser power, trapping was enhanced (Fig. 9.7). For laser powers above 12 mW, the carbon film was destroyed when the laser was directly focused on the film.

## 9.4. Focused Laser Light Was not Needed to Induce Trapping

To check whether focused laser light was necessary for the described trapping effect, I first put the laser focus 5 μm above and beneath the carbon film. In both cases, I observed trapping. Afterwards, I repeated the trapping experiment with wide-field illumination. To this end, I added another lens before the trapping objective to expand the laser beam. The laser light was not completely parallel but the focus was several millimetres above the sample which implies a nearly parallel laser light and a wide illumination of the sample. Also in this configuration, I observed trapping as shown in Fig. 9.8. Similar to measurements with focused laser light, there were areas were trapping did and did not work, respectively. I confirmed that laser light with both modes induced the trapping by checking the same area in one sample before and after adding the lens. I did not observe a limited trapping range; microspheres were trapped uniformly over the whole field of view. In contrast to the trapping by focused laser light, the trapping was not fully reversible, as some microspheres remained immobilised. The lower trapping limit of 6 mW in the laser power

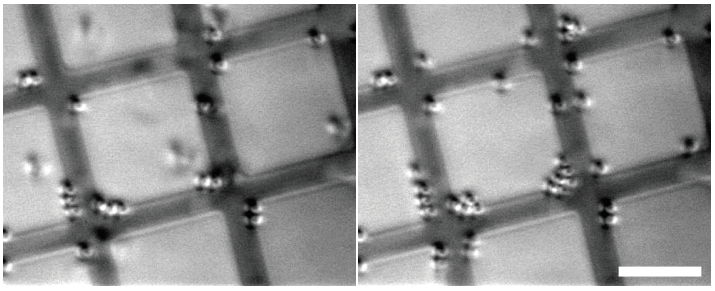

**Figure 9.8: Laser-induced trapping with wide-field illumination.** Images of 590 nm polystyrene microspheres with a laser power of 25 mW and closed (left) and opened (right) laser shutter. Scale bar is 5 μm.

was the same as for focused laser light.

## 9.5. Discussion

After the brief characterisation of this trapping effect, the question of its origin and theoretical description emerges.

The trapping with optical tweezers is due to the light intensity gradient in the tightly focused laser beam. Such intensity gradients can also be established on other ways. For example, evanescent fields that are created by total internal reflection, can be used to push dielectric particles along the field [174]. In so-called waveguides, three-dimensional micro-structures, in which the evanescent field is channelled, particles can be trapped by the evanescent field between the walls of the waveguide [175]. However, evanescent fields cannot explain my trapping effect, because no evanescent field should be present.

Trapping by surface plasmons might be another explanation. Surface plasmons are charge density oscillations that are confined to metallic structures. They can be excited with laser light and cause electromagnetic fields with strong gradients. Thin gold patterns have been used to trap dielectric particles in evanescent [172, 176, 177] or transient light [178]. However, it is not clear whether plasmons can be excited in the carbon. Also, the range of the optical forces created by plasmons are only very short ranged (<1 µm) which is not consistent with the observed trapping range of several micrometres between the carbon film and microspheres (Fig. 9.4A). The same limitation on the range accounts for the evanescent field interaction.

Another optical trapping effect on surface structures has been observed at the edge of gold structures in transient light [179]. The trapping is explained by the light intensity gradient at the metal edge arising from interference between the incident light and the light that is diffracted at the edge. This gradient attracted various dielectric particles. However, in my approach, the sample was not uniformly illuminated by the laser when using focused laser light. In contrast, the laser focus was projected through the holes in the film and not onto the bars of the carbon grid. It might be possible that the remaining laser light around the focus—still 17 % for an ideal Airy disk—was still sufficient to initiate the trapping effect. The observed trapping range in [179] was smaller than in my experiments. Nonetheless, this theory might explain my observations.

Besides trapping by an electromagnetic intensity gradient, other interactions might describe the observations better. One of these examples is thermophoresis. Thermophoresis is the movement of particles along a temperature gradient. This movement can be towards areas with lower or higher temperature [180]. The laser light, both focused or parallel, heats the carbon film up that then attracts the microspheres. The temperature profile of the sample could be checked in a suited setup with fluorescence imaging and a heating laser, using a temperature-sensitive fluorophore as described in [181]. However, thermophoresis measurements with a heating laser and PS microspheres of various sizes have shown repulsive interactions [182]. Also, the thermophoretic forces

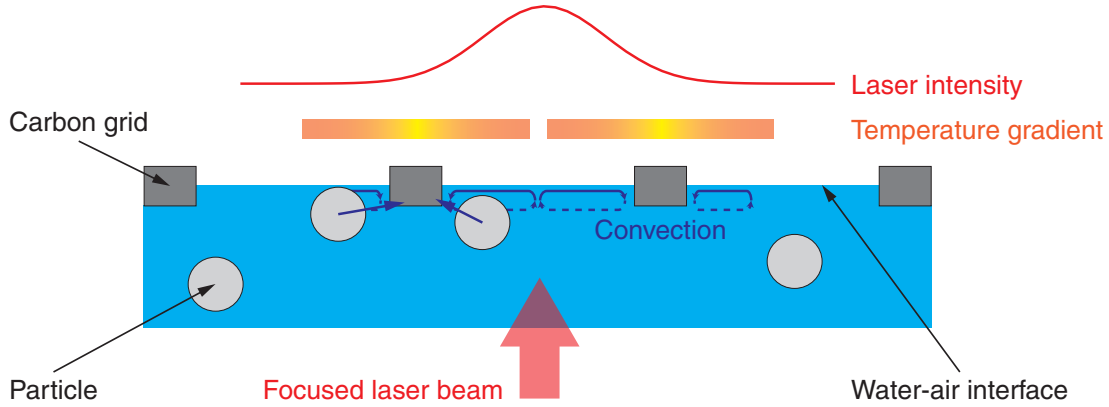


**Figure 9.9: Theory for grid trapping.** Illustration (not to scale) of a possible explanation of the grid trapping: The laser light around the focus heats up the carbon grid causing temperature gradients around the carbon bars. This temperature gradient causes thermal convection which is bringing suspended particles close to the grid, where there are hold by electrostatic interactions.

are expected to be only some tens of fN small [183], an order of magnitude smaller than the here measured forces. Therefore, thermophoretic forces are not a likely explanation for the trapping using perforated carbon films.

Heating is accompanied by thermal convection that is caused by temperature gradients at the holes in the carbon film. According to simulations by Duhr et al. [181], convection follows the direction of the heat source in the axial direction and then stream away from it. Here, a similar convection could form around the heated parts of the carbon film around the laser and push the particles against the film and water-air interface. However, I would expect the convective current to be directed away from the edges of the holes. In contrast, I observed trapped particles moving towards the laser focus (Fig. 9.6A). Therefore, convection seems also an unlikely explanation.

A different explanation for thermal convection is the Marangoni effect [184]. This effect describes convection that is driven by a surface tension gradient. In my grid sample, a surface tension gradient is obtained due to the temperature gradient, as the surface tension between water and air depends on the temperature. The temperature gradient was established around the carbon bars by the heating of the laser. The water streamed along the surface tension gradient to areas with higher surface tension, i.e. lower temperatures. This would mean that the water would, and with it the particles, stream away from the carbon grid. This is not consistent with my observations.

Thermal convection towards the carbon grid can be obtained by evaporation of liquid at the heated carbon. The evaporation causes a convection of liquid towards the carbon bars, taking the particles with it. This effect was similar to the so-called coffee ring effect [185], where increased evaporation of liquid at the edges of a fluid drop results in convection towards the edges. The effect explains (i) the limited trapping range, as only the part of the carbon grid close to the laser focus would be warm enough, (ii) the necessity of the air layer, and (iii) the motion of particles towards the carbon, regardless of the laser focus position.

Any convection takes suspended particles with it. Thus, there is no difference of the effect with respect to particle size and material which is consistent with the observed constant trapping range for all investigated microspheres (Fig. 9.6B).

However, even convection towards the grid does not explain the observed trapping alone. Convection could bring particles close enough to the grid, where a small, short-ranged interaction, that depended on the presence of the trapping laser light, could keep the particles trapped. The qualitative observations are most consistent with an electrostatic interaction. The particles clearly concentrated in the corners of the quadratic grid implying a concentration of electric field lines in the corners.

For example, a classic dipole-dipole interaction induced by the laser's electric field would be an explanation. Figure 9.9 illustrates the suggested model of convection and short-ranged electrostatic interaction of grid and particles.

# 10. Outlook

In summary, this work showed that the successful implementation of the three-dimensional optical tweezers force-clamp enabled new experiments on motor proteins. In this chapter, I conclude and give an outlook of possible future experiments.

**Implementation of 3D Optical Tweezers Assays with Kinesins** We successfully implemented the optical tweezers force-clamp first in two dimensions and extended it then to three dimensions. The force clamp was tuned and tested under conditions that mimicked the experimental. I used this clamp to track and apply loads on microsphere-coupled motor proteins in all directions. I found that the spatial resolution could be improved significantly to some nanometres by applying forces which is consistent with previous research [89, 90]. This spatial resolution was good enough to detect single kinesin forward steps [40, 118]. The precision of the applied force was always in the sub-piconewton range and could also be improved by applying loads. In 3D experiments with suspended microtubules, the precision of the angle around the microtubule axis was e few degrees. Overall, the spatial tracking precision was much better than in the simple video tracking assays. The angular resolution benefited from tracking the microsphere centre instead of the kinesin itself. Due to the microsphere diameter, the radius of the angular motion was amplified. Therefore, for a given spatial tracking precision, a better angular precision was possible.

The 3D tracking approach could be realised best with topographic surface structures manufactured using nanoimprint lithography techniques. Furthermore, we developed, varied, and extended a protocol to functionalise polystyrene microspheres to specifically bind GFP-tagged proteins. This protocol turned out to be very versatile and can be used to functionally bind a lot of different proteins apart from kinesins. In principle, the protocol can be also adapted for microspheres made of other materials than polystyrene, like silica or titania, or nanodiamonds as long as their surfaces are carboxylated.

The 3D force clamp could also be used to investigate other kinesins or motor proteins like myosins and dyneins. This is of special interest for motor proteins that have been already shown to switch protofilaments but were investigated with video tracking like kinesin-5 or single-headed kinesin-1 [162], cytoplasmatic and axonemal dynein [103, 186], or myosin-V [143]. With our approach, the spatial and angular resolution could be significantly improved. A different approach that would benefit from the 3D design was an assay with the kinesin-13 MCAK. In previous studies, the force-generating depolymerisation of the MT end by MCAK was shown on microtubules that were suspended using multiple traps [113]. However, the three-dimensional trajectory of MCAK

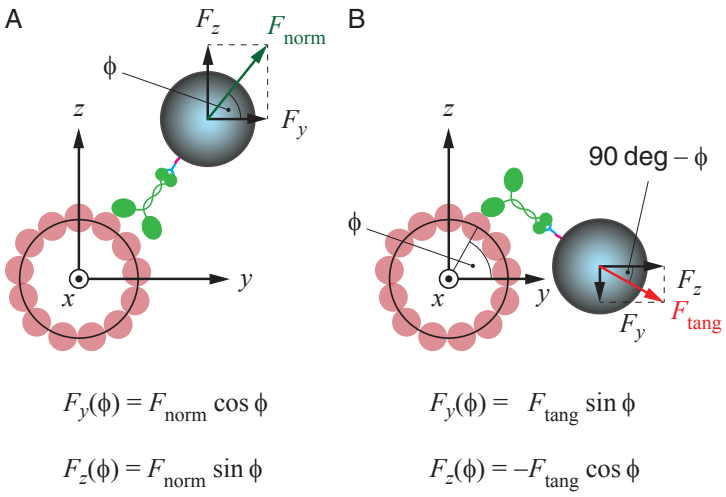


**Figure 10.1: Applying normal and tangential loads with a 3D force clamp.** Schematic (not to scale) of how to apply (A) normal loads $F_{norm}$ and (B) tangential loads $F_{tang}$ on kinesin-coated microspheres that move along freely accessible microtubules. Equations for corresponding axial and lateral loads ($F_z$ and $F_y$, respectively) as a function of the angular position $\phi$ are given.

when depolymerising the microtubule could not be tracked in these assays with high resolution. In our assay, the microtubules could be partly suspended on the ridges with one end hanging over the edge. These ends would be freely accessible and could be probed with MCAK-coated microspheres.

Besides motor proteins, an application on completely different biological systems *in vitro* and *in vivo*, e.g. tracking of cell organelles seems possible.

There is room for improvements on the force clamp. As already noted, the spatial and angular resolution can be improved by applying loads on the microsphere. In this work, I only applied unidirectional sideward and upward loads. However, applying a small load along the MT axis would enable to detect forward and angular sideward steps together and to investigate their correlation. For 3D cylindrical geometry of a kinesin stepping assay, one could also apply loads normal and tangential to the kinesin on the microtubule surface (illustrated in Figs. 10.1A and B, respectively). As the detection of the displacement via the QPD and the application of loads via mirrors and the stage were performed in a Cartesian coordinate system, tangential and normal loads could be realised by applying appropriate loads in $y$ and $z$ with the MT axis parallel to the $x$-axis. These partial loads depend on the angular position $\phi$ as given in Fig. 10.1. To apply a load requires the knowledge of the current value of $\phi$. This knowledge is non-trivial. When the centre coordinates of the MT axis are known, the angle $\phi$ could be calculated using Eq. 3.8. Another parameter that must be known is the angle where the force clamping started. This initial angle is even harder to determine, as one cannot control where with great accuracy to which protofilament the motor binds in the beginning. In a Kip3 assay, one could apply an upward load for some time, until it is very likely that the Kip3 steps on a protofilament close to the top of the microtubule. The experiment could be then initialised with a starting angle of 90 deg. Applying tangential and normal loads on Kip3 could be used to directly investigate the force-dependence of Kip3's sideward and forward stepping in the geometry of a 3D assay. Applying forward loads together with tangential loads could reveal subsequent forward and sideward steps and even show whether diagonal

steps exist. The possibility to apply loads with a 3D force clamp open up many possibilities. However, this approach has also practical limitations. Applying normal loads of more than a few piconewton would inevitably bend the microtubule as my own measurements showed (Fig. 6.5). This could lead to artefacts in the measurements. Tangential loads might also bend the microtubule and the kinesin linker could coil around the microtubule. This linker-microtubule wrapping would result in artefacts too, as the angle of the kinesin on the microtubule would be different from the angular position of the microsphere centre. This artefact might be avoided by (i) using small loads only, (ii) minimising the linker length by e.g. shorter PEGs or a different protocol, (iii) including the coiling and the known force-dependence of the linker length (Fig. 7.13) into the calculation of the partials loads in $y$ and $z$. Tangential loads might be even used to apply a torque on a microtubule itself for torsional experiments. For this purpose, the microsphere could be bound tightly to the microtubule via kinesin and AMPPNP or anti-tubulin as shown in Fig. 5.4.

**Results of 2D & 3D Optical Tweezers Assays with Kinesins** The force clamp was used to investigate the details of the motion of the kinesins Kip3 and rkin430. Two-dimensional assays with alternating sideward loads showed that the kinesin-8 Kip3 switched microtubule protofilaments in both directions. This switching was biased by a sideward load in the direction of the load. For loads up to 2 pN, sideward stepping still occurred with and against the load. Our simulation proposed a force-dependent switching mechanism with an asymmetry between the force dependence factors for left and right [148]. Without any loads, Kip3 switched, within error margins, to the left and right with same probability. The microtubule rotations in gliding assays suggested a strongly biased left-handed rotation for single Kip3 [50]. This contradiction could be explained by the model of collectively interacting Kip3 motors in a gliding assay, where the asymmetry in the force-dependence factors caused the experimentally observed left-handed net rotation. However, experimental evidence for this model is missing so far. The ability to switch to the left and right, in contrast to exclusively stepping to the left, provides an efficient mechanism to bypass obstacle on the microtubule lattice. Stochastic simulations of kinesin stepping by Bertalan et al. [187] suggested an effective bypassing in combination with backward stepping. We did not investigate backward stepping, here. However, backward stepping of Kip3 has been observed even for small forward loads (personal communication with Anita Jannasch, concerning her measurements in [40]). Protofilament switching might be an important part of the biological role of Kip3, as the bypassing of obstacles enables it to reach the MT plus end which is crucial for its length control mechanism. A next experiment would be to observe this bypassing of artificial road blocks on a microtubule directly as it was done for kinesin-1 [52–55].

A disadvantage of the 2D assays with immobilised microtubules was the complicated geometry that ruled out a direct measurement of the actual three-dimensional trajectory of Kip3 on the microtubule. Extending the kinesin stepping assay to three dimensions however made it possible to not only directly

observe angular motion but also to detect, to our knowledge for the first time, the angular steps between neighbouring protofilaments. Although no loads were applied on kinesins in the 3D assays, the analysis of the angular motion showed angular diffusion with no preference to the left nor right in agreement with the 2D assays. A closer look into the temporal development of the angular motion revealed different intrinsic diffusion states of Kip3. The origin of these different states is not clear at the moment. The possible influence of the additional MT binding site on Kip3's tail domain could be tested by using a truncated construct in 3D assays.

My experiments showed that Kip3 makes a significant number (8–11 %) of its steps to the side and not forward. These sideward steps do not contribute to the forward motion but are presumably coupled to ATP hydrolysis. The ATP dependence of the angular motion is consistent with this hypothesis [49]. An interesting question is how Kip3 stepping would change if it cannot step to the side. This could be investigated in an assay with only one protofilament accessible for the kinesin. Such experiments were performed by Shibata et al. with kinesin-1 and dynein on so-called zinc-sheets, specially polymerised tubulin structures that have the kinesin-binding site only exposed at one edge of their sheet-like shape [188]. One could speculate that Kip3 would speed up on single protofilaments, as it would perform more forward steps instead of sideward steps.

In contrast to Kip3, the kinesin-1 rkin430 did not show significant protofilament switching in neither 2D nor 3D assays. This observation is consistent with previous studies with kinesin-1 gliding assays by Ray et al. [11] that showed protofilament tracking of the kinesin-1. The rare, equally distributed sideward stepping of kinesin-1 that was observed for quantum-dot-labelled motors in TIRF stepping assays [51] could not be confirmed but also not entirely excluded. The angular motion that was observed for rkin430 was consistent with the tracking of supertwisted protofilaments and enabled to directly measure the composition of the used microtubule preparation with respect to the supertwist pitch and protofilament number. The observed changes in the slope of rkin430's angular motion is an indirect hint on possible transitions in the protofilament number of the microtubules.

**Laser-Induced Trapping of Particles by Carbon Grids** I discovered a new trapping effect by perforated carbon films that was induced by laser light. I found that an air layer on top of the carbon film was crucial for this trapping effect. For focused laser light, the trapping had a limited range that scaled linearly with the laser power. The trapping worked for different microsphere materials and sizes and even for cells. The trapping forces were an order of magnitude below the maximum force in an optical trap for the same laser power.

While the origin of the trapping effect is unclear at the moment, we can envision several applications. Simultaneous trapping of multiple objects is of great potential use, if many objects need to be manipulated without high precision measurements of forces. The reversibility of the trapping effect enables e.g. temporary immobilisation of living cells for buffer exchange or other purposes.

Single or multiple-beam optical tweezers cannot trap that many objects simultaneously. Holographic optical tweezers [170] can trap many objects and are much more versatile. However, our trapping effect has the advantage of working with parallel laser light and thus no need for a tightly focused laser beam. Hence, expensive objectives or spatial light modulators are not required.

Still, there are several practical issues with this concept for practical applications. The air layer on top of the grid was crucial for trapping. However, this layer was difficult to achieve in a reproducible manner as described. Reliable assembly methods would have to be developed for lab-on-a-chip applications. Though the trapping was in principle reversible, some objects remained on the grid. Passivation of the carbon, e.g. by PEGylation, could reduce non-specific interactions. However, it is important that the chosen passivation method does not prevent the formation of the air layer.

**Perspective on Single-Molecule Force Spectroscopy** Our developed techniques enable new experiments in the single-molecule research. The microsphere functionalisation protocol provides an easy, reliable, and versatile method of probing a broad range of molecules that can be applied for experiments like motor protein assays or suspending cytoskeletal filaments or DNA with optical traps. The force clamp is able to apply loads and to measure displacements with high precision in three dimensions. These features can be also applied on e.g. experiments on membrane tether formation and associated proteins like dynamin [189]. Moreover, the 3D force clamp can be used in force spectroscopy experiments on various single molecules.

For example, other kinds of force-generating molecules like several DNA or RNA-associated molecular complexes like the ribosome [190], microtubule-associated proteins like XMAP2015 [191] or DAM1 [192], protein degrading enzymes like the unfoldase ClpX [193], or microtubule polymerisation and depolymerisation could be examined. The latter question could be investigated using microtubules that were suspended on topographic structures with one end free above the canyon. The dynamics of the end would be probed with functionalised microspheres and the force clamp. A similar assay could be used to investigate the behaviour of Kip3 or other kinesins an the MT end. Kip3 is known to stay at the MT plus end for minutes before dissociating [41]. Preliminary 2D-force-clamp assays have shown that Kip3 steps forward and backward at the end (unpublished data by Anita Jannasch, ZMBP, University of Tübingen, Germany). It is possible that this stepping is combined with sideward steps which could be a mechanism to "scan" the MT end for the protofilament that is to be depolymerised first. This question could be answered by 3D-force-clamp assays in the future and help to understand the biological function of kinesin-8 and related diseases such as its function in colorectal cancer [46].

# Contributions

### Chapter 3 - Implementation of a 3D Force Clamp

The used optical tweezers setup was built by Mohammed Mahamdeh. The original force-clamp routine was programmed by Volker Bormuth and was re-programmed and extended to three dimensions by Elisa Böhl and me under the supervision of Erik Schäffer. Anita Jannasch co-wrote the chapter in the book *Optical Tweezers: Methods and Protocols* [66].

Mohammad Abdousamadi helped to program the vertical video tracking routine in ImageJ.

### Chapter 4 - Kinesin Assay

Volker Bormuth established the original single Kip3 optical tweezers stepping assay. The expression of Kip3 was performed with the help of Anirhudda Mitra, Frederic Schiemann, and Anita Jannasch. The kinesin-1 rkin430 was provided by the lab of Stefan Diez (TU Dresden, Dresden, Germany). Marco Storch and Claudia Schirmer initially helped with TIRF assays in the MPI-CBG. Suman De built the used TIRF setup in the ZMBP, University of Tübingen, Tübingen, Germany. He and Mohammad Abdousamadi initially helped with TIRF assays.

The expression and purification of kinesins, used for 3D experiments (rkin430, different Kip3 constructs) were performed by or with the help of Naghmeh Azadfar.

### Chapter 5 - Functionalisation of Microspheres

The original protocol was developed by Horatiu Fontana, Anastasia Trushko and Volker Bormuth, under the supervision of Jonathon Howard and Erik Schäffer. Furthermore, H. Fontana performed basic measurements *in vivo*; A. Trushko performed assays with XMAP215. Anita Jannasch additionally varied microsphere size and PEG length for that protocol. Frederic Schiemann contributed data for the Poisson statistics and originally tested the variation of the PEG ratio.

### Chapter 6 - Topographic Surface Treatment to Suspend Microtubules

The approach to use TEM grids to suspend microtubules was originally suggested by Ernst-Ludwig Florin, University of Texas, Austin, TX, USA.

The patterned glass cover slips, used for 3D experiments, were designed, manufactured, and provided by Salvatore Girardo, BIOTEC/CRTD Microstructure Facility, TU Dresden, Dresden, Germany.

### Chapter 7 - 2D Optical Tweezers Tracking of Kinesin-1 and Kinesin-8

The Kip3 stepping simulation was programmed by and analysed with the help of Elisa Böhl.

### Chapter 8 - 3D Optical Tweezers Tracking of Kinesin-1 and Kinesin-8

Aniruddha Mitra (lab of Stefan Diez, TU Dresden, Dresden, Germany) gave useful advice concerning motility assays with PFPE structures.

### Chapter 9 - Laser-Induced Trapping of Particles by Carbon Grids

Steve Simmert built the optical tweezers setup that was used for trapping assays with flows. He also helped imaging the grid sample in IRM. Gero Hermsdorf developed and helped using the method to apply a flow inside the sample channel. Both worked in the Cellular Nanoscience lab in the ZMBP, University of Tübingen, Tübingen, Germany.

# Publications Related to this Thesis

- ***Implementation and Tuning of an Optical Tweezers Force-Clamp Feedback System***
  in "Optical Tweezers: Methods and Protocols", ed. by A. Gennerich
  M. Bugiel*, A. Jannasch* and E. Schäffer*
  Humana Press, 109–136 (2016)

- ***Versatile microsphere attachment of GFP-labeled motors and other tagged proteins with preserved functionality***
  M. Bugiel*, H. Fantana*, V. Bormuth*, A. Trushko*, F. Schiemann, J. Howard, E. Schäffer and A. Jannasch*
  *Journal of Biological Methods* **2**(4), e30 (2015)

- ***The Kinesin-8 Kip3 Switches Protofilaments in a Sideward Random Walk Asymmetrically Biased by Force***
  M. Bugiel, E. Böhl, and E. Schäffer
  *Biophysical Journal* **108**, 2019–2027 (2015)

- ***High Resolution Three-Dimensional Tracking of Kinesins Using Optical Tweezers Reveals Microtubule Supertwist***
  M. Bugiel*, A. Mitra*, S. Girardo, S. Diez and E. Schäffer
  in preparation

- ***Multiple laser-induced trapping of micro-objects by carbon grids***
  M. Bugiel, and E. Schäffer
  in preparation

* These authors contributed equally to the work.

# Bibliography

[1] J. Howard, *Motor Proteins and the Cytoskeleton*. Sunderland, MA: Sinauer Associates, 2001.

[2] B. Alberts, A. Johnson, J. Lewis, M. Raff, K. Roberts, and P. Walter, *Molecular Biology of the Cell*. Garland Science, 4 ed., 2002.

[3] E. Mandelkow and E.-M. Mandelkow, "Kinesin motors and disease," *Trends Cell Biol.*, vol. 12, no. 12, pp. 585–591, 2002.

[4] N. Hirokawa and R. Takemura, "Biochemical and molecular characterization of diseases linked to motor proteins," *Trends Biochem. Sci.*, vol. 28, no. 10, pp. 558–565, 2003.

[5] O. Rath and F. Kozielski, "Kinesins and cancer," *Nat. Reviews*, vol. 12, pp. 527–539, 2012.

[6] K. Svoboda, C. F. Schmidt, B. J. Schnapp, and S. M. Block, "Direct observation of kinesin stepping by optical trapping interferometry," *Nature*, vol. 365, pp. 721–727, 1993.

[7] K. Svoboda and S. M. Block, "Force and velocity measured for single kinesin molecules," *Cell*, vol. 77, no. 5, pp. 773–784, 1994.

[8] M. Kikkawa, T. Ishikawa, T. Nakata, T. Wakabayashi, and N. Hirokawa, "Direct visualization of the microtubule lattice seam both in vitro and in vivo," *J. Cell Biol.*, vol. 127, no. 6, pp. 1965–1971, 1994.

[9] L. G. Tilney, J. Bryan, D. J. Bush, K. Fujiwara, M. S. Mooseker, D. B. Murphy, and D. H. Snyder, "Microtubules: evidence for 13 protofilaments," *J. Cell Biol.*, vol. 59, no. 2, pp. 267–275, 1973.

[10] E. Unger, K. Böhm, and W. Vater, "Structural diversity and dynamics of microtubules and polymorphic tubulin assemblies," *Electron Microsc. Rev.*, vol. 3, pp. 355–395, 1990.

[11] S. Ray, E. Meyhöfer, R. A. Milligan, and J. Howard, "Kinesin follows the microtubule's protofilament axis," *J. Cell Biol.*, vol. 121, pp. 1083–1093, 1993.

[12] D. Chrétien, F. Metoz, F. Verde, E. Karsenti, and R. Wade, "Lattice defects in microtubules: protofilament numbers vary within individual microtubules.," *J. Cell Biol.*, vol. 117, no. 5, pp. 1031–40, 1992.

[13] D. Chrétien and R. H. Wade, "New data on the microtubule surface lattice," *Biol. Cell*, vol. 71, pp. 161–174, 1991.

[14] R. Wade and D. Chrétien, "Cryoelectron microscopy of microtubules," *J. Struct. Biol.*, vol. 110, pp. 1–27, 1993.

[15] G. J. Brouhard, J. H. Stear, T. L. Noetzel, J. Al-Bassam, K. Kinoshita, S. C. Harrison, J. Howard, and A. A. Hyman, "Xmap215 is a processive microtubule polymerase," *Cell*, vol. 132, no. 1, pp. 79–88, 2008.

[16] J. Al-Bassam, R. S. Ozer, D. Safer, S. Halpain, and R. A. Milligan, "Map2 and tau bind longitudinally along the outer ridges of microtubule protofilaments," *J. Cell Biol.*, vol. 157, no. 7, pp. 1187–1196, 2002.

[17] L. Sandblad, K. Busch, P. Tittmann, H. Gross, D. Brunner, and A. Hoenger, "The schizosaccharomyces pombe eb1 homolog mal3p binds and stabilizes the microtubule lattice seam," *Cell*, vol. 127, pp. 1415–1424, 2006.

[18] A. W. Hunter, M. Caplow, D. L. Coy, W. O. Hancock, S. Diez, L. Wordeman, and J. Howard, "The kinesin-related protein mcak is a microtubule depolymerase that forms an atp-hydrolyzing complex at microtubule ends," *Mol. Cell*, vol. 11, pp. 445–457, 2003.

[19] V. Varga, J. Helenius, K. Tanaka, A. A. Hyman, T. U. Tanaka, and J. Howard, "Yeast kinesin-8 depolymerizes microtubules in a length-dependent manner," *Nat. Cell Biol.*, vol. 8, no. 9, pp. 957–962, 2006.

[20] M. L. Gupta, P. Carvalho, D. M. Roof, and D. Pellman, "Plus end-specific depolymerase activity of kip3, a kinesin-8 protein, explains its role in positioning the yeast mitotic spindle," *Nat. Cell Biol.*, vol. 8, no. 9, pp. 913–U33, 2006.

[21] M. K. Gardner, M. Zanic, C. Gell, V. Bormuth, and J. Howard, "Depolymerizing kinesins kip3 and mcak shape cellular microtubule architecture by differential control of catastrophe," *Cell*, vol. 147, pp. 1092–1103, 2011.

[22] M. I. Mayr, S. Hümmer, J. B. T. Grüner, S. A. G. Woehlke, and T. U. Maye, "The human kinesin kif18a is a motile microtubule depolymerase essential for chromosome congression," *Curr. Biol.*, vol. 17, pp. 488–498, 2007.

[23] A. Hyman, S. Salser, D. Drechsel, N. Unwin, and T. Mitchison, "Role of gtp hydrolysis in microtubule dynamics: information from a slowly hydrolyzable analogue, gmpcpp," *Mol. Biol. Cell*, vol. 3, no. 10, pp. 1155–1167, 1992.

[24] I. Arnal and R. H. Wade, "How does taxol stabilize microtubules?," *Curr. Biol.*, vol. 5, pp. 900–908, 1995.

[25] L. A. Amos, "Microtubule structure and its stabilisation," *Org. Biomol. Chem.*, vol. 2, pp. 2153–2160, 2004.

[26] H. Xiao, P. Verdier-Pinard, N. Fernandez-Fuentes, B. Burd, R. Angeletti, A. Fiser, S. B. Horwitz, and G. A. Orr, "Insights into the mechanism of microtubule stabilization by taxol," *Proc. Natl. Acad. Sci. U. S. A.*, vol. 103, no. 27, pp. 10166–10173, 2006.

[27] A. Hyman, D. Chrétien, A. I., and R. Wade, "Structural changes accompanying gtp hydrolysis in microtubules: information from a slowly hydrolyzable analogue guanylyl-(alpha,beta)-methylene-diphosphonate," *J. Cell Biol.*, vol. 128, pp. 117–125, 1995.

[28] B. Nitzsche, F. Ruhnow, and S. Diez, "Quantum-dot-assisted characterization of microtubule rotations during cargo transport," *Nat. Nanotechnol.*, vol. 3, pp. 552–556, 2008.

[29] W. O. Hancock and J. Howard, "Kinesin's processivity results from mechanical and chemical coordination between the atp hydrolysis cycles of the two motor domains," *Proc. Natl. Acad. Sci. U. S. A.*, vol. 96, no. 23, pp. 13147–13152, 1999.

[30] C. L. Asbury, A. N. Fehr, and S. M. Block, "Kinesin moves by an asymmetric hand-over-hand mechanism," *Science*, vol. 302, pp. 2130–2134, 2003.

[31] A. Yildiz, M. Tomishige, R. D. Vale, and P. R. Selvin, "Kinesin walks hand-over-hand," *Science*, vol. 303, pp. 676–678, 2004.

[32] W. O. Hancock and J. Howard, "Processivity of the motor protein kinesin requires two heads," *J. Cell Biol.*, vol. 140, no. 6, pp. 1395–1405, 1998.

[33] W. Hua, E. C. Young, M. L. Fleming, and J. Gelles, "Coupling of kinesin steps to atp hydrolysis," *Nature*, vol. 388, pp. 393–393, 1997.

[34] M. J. Schnitzer and S. M. Block, "Kinesin hydrolyses one atp per 8-nm step," *Nature*, vol. 388, pp. 386–390, 1997.

[35] D. L. Coy, M. Wagenbach, and J. Howard, "Kinesin takes one 8-nm step for each atp that it hydrolyzes," *J. Biol. Chem.*, vol. 274, no. 6, pp. 3667–3671, 1999.

[36] R. J. Lasek and S. T. Brady, "Attachment of trasported vesicles to microtubules in axoplasm is facilitated by amp-pnp," *Nature*, vol. 316, pp. 645–647, 1985.

[37] S. M. Block, L. S. B. Goldstein, and B. J. Schnapp, "Bead movement by single kinesin molecules studied with optical tweezers," *Nature*, vol. 348, no. 6299, pp. 348–352, 1990.

[38] R. D. Vale, T. Fanutsa, D. W. Pierce, L. Romberg, Y. Harada, and T. Yanagida, "Direct observation of single kinesin molecules moving along microtubules," *Nature*, vol. 380, pp. 451–453, 1996.

[39] L. Romberg, D. W. Pierce, and R. D. Vale, "Role of the kinesin neck region in processive microtubule-based motility," *J. Cell Biol.*, vol. 140, no. 6, pp. 1407–1416, 1998.

[40] A. Jannasch, V. Bormuth, M. Storch, J. Howard, and E. Schäffer, "Kinesin-8 is a low-force motor protein with a weakly bound slip state," *Biophys. J.*, vol. 104, no. 11, pp. 2456–2464, 2013.

[41] V. Varga, C. Leduc, V. Bormuth, S. Diez, and J. Howard, "Kinesin-8 motors act cooperatively to mediate length-dependent microtubule depolymerization," *Cell*, vol. 138, pp. 1174–1183, 2009.

[42] J. Roostalu and T. Surrey, "The multiple talents of kinesin-8," *Nat. Cell Biol.*, vol. 15, no. 8, pp. 889–891, 2013.

[43] T. M. DeZwaan, E. Ellingson, D. Pellman, and D. M. Roof, "Kinesin-related kip3 of saccharomyces cerevisiae is required for a distinct step in nuclear migration," *J. Cell Biol.*, vol. 138, no. 5, pp. 1023–1040, 1997.

[44] Y. Shin, Y. N. C. S. Du, M. Ohi, M. Lang, and R. Ohi, "Biased brownian motion as a mechanism to facilitate nanometer-scale exploration of the microtubule plus end by a kinesin-8," *Proc. Natl. Acad. Sci. U. S. A.*, vol. 112, no. 29, pp. 3826–3835, 2015.

[45] M. Glunčić, N. Maghelli, A. Krull, V. Krstić, D. Ramunno-Johnson, N. Pavin, and I. M. Tolić, "Kinesin-8 motors improve nuclear centering by promoting microtubule catastrophe," *Phys. Rev. Lett.*, vol. 114, no. 7, p. 078103, 2015.

[46] M. Nagahara, N. Nishida, M. Iwatsuki, S. Ishimaru, K. Mimori, F. Tanaka, T. Nakagawa, T. Sato, K. Sugihara, D. S. Hoon, and M. Mori, "Kinesin 18a expression: clinical relevance to colorectal cancer progression," *Int. J. Cancer*, vol. 129, no. 11, pp. 2543–2552, 2011.

[47] W. Su, X.and Qiu, M. J. Gupta, J. Pereira-Leal, S. Reck-Peterson, and P. D., "Mechanisms underlying the dual-mode regulation of microtubule dynamics by kip3/kinesin-8," *Mol Cell*, vol. 43, no. 5, pp. 751–763, 2011.

[48] X. Su, H. Arellano-Santoyo, D. Portran, J. Gaillard, M. Vantard, M. Thery, and D. Pellman, "Microtubule-sliding activity of a kinesin-8 promotes spindle assembly and spindle-length control," *Nat. Cell Biol.*, vol. 15, no. 8, pp. 948–957, 2013.

[49] V. Bormuth, *Optimized optical tweezers to study the mechanics of kinesin-8: stepping, slipping, protein friction*. PhD thesis, Technische Universität Dresden, 2009.

[50] V. Bormuth, B. Nitzsche, F. Ruhnow, A. Mitra, M. Storch, B. Rammner, J. Howard, and S. Diez, "The highly processive kinesin-8, kip3, switches microtubule protofilaments with a bias toward the left," *Biophys. J.*, vol. 103, pp. L04–L06, 2012.

[51] A. Yildiz, M. Tomishige, A. Gennerich, and R. D. Vale, "Intramolecular strain coordinates kinesin stepping behavior along microtubules," *Cell*, vol. 1, pp. 1030–1041, 2008.

[52] I. A. Telley, P. Bieling, and T. Surrey, "Obstacles on the microtubule reduce the processivity of kinesin-1 in a minimal in vitro system and in cell extract," *Biophys. J.*, vol. 96, pp. 3341–3353, 2009.

[53] K. Dreblow, N. Kalchishkova, and K. J. Böhm, "Kinesin passing permanent blockages along its protofilament track," *Biochem. Biophys. Res. Commun.*, vol. 395, pp. 490–495, 2010.

[54] G. J. Hoeprich, A. R. Thompson, D. P. McVicker, and W. O. Hancock, "Kinesin's neck-linker determines its ability to navigate obstacles on the microtubule surface," *Biophys. J.*, vol. 106, pp. 1691–1700, 2014.

[55] R. Schneider, T. Korten, W. J. Walter, and S. Diez, "Kinesin-1 motors can circumvent permanent roadblocks by side-shifting to neighboring protofilaments," *Biophys. J.*, vol. 108, no. 9, pp. 1149–1157, 2015.

[56] A. Ashkin, J. M. Dziedzic, J. E. Bjorkholm, and S. Chu, "Observation of a single-beam gradient force optical trap for dielectric particles," *Opt. Lettt.*, vol. 11, no. 5, pp. 288–290, 1986.

[57] S. Chu, J. E. Bjorkholm, A. Ashkin, and A. Cable, "Experimental observation of optically trapped atoms," *Phys. Rev. Lett.*, vol. 57, no. 3, pp. 314–317, 1986.

[58] A. Ashkin and J. Dziedzic, "Optical trapping and manipulation of viruses and bacteria," *Science*, vol. 235, no. 4795, pp. 1517–1520, 1987.

[59] C. F. Bohren and D. R. Huffman, *Absorption and Scattering of Light by Small Particles*. Wiley-VCH, 2004.

[60] A. H. Compton, "A quantum theory of the scattering of x-rays by light elements," *Phys. Rev.*, vol. 21, no. 5, pp. 483–502, 1923.

[61] A. Jannasch, V. Bormuth, C. M. van Kats, A. van Blaaderen, J. Howard, and E. Schäffer, "Coated microspheres as enhanced probes for optical trapping," *Proc. SPIE*, vol. 7038, p. 70382B (8 pp.), 2008.

[62] T. Wriedt, "Mie theory: A review," in *The Mie Theory* (W. Hergert and T. Wriedt, eds.), ch. 2, pp. 53–71, Springer Press, 2012.

[63] A. Pralle, M. Prummer, E. L. Florin, E. H. K. Stelzer, and J. K. H. Hörber, "Three-dimensional high-resolution particle tracking for optical tweezers by forward scattered light," *Microsc. Res. Tech.*, vol. 44, no. 5, pp. 378–386, 1999.

[64] J. W. Shaevitz, *A Practical Guide to Optical Trapping*. University of Washington, 2006.

[65] Y. Jun, S. K. Tripathy, B. R. J. Narayanareddy, M. K. Mattson-Hoss, and S. P. Gross, "Calibration of optical tweezers for in vivo force measurements: How do different approaches compare?," *Biophys. J.*, vol. 107, pp. 1474–1484, 2014.

[66] M. Bugiel, A. Jannasch, and E. Schäffer, "Implementation and tuning of an optical tweezers force-clamp feedback system," in *Optical Tweezers: Methods and Protocols* (A. Gennerich, ed.), ch. 5, pp. 109–136, Humana Press, 2016.

[67] S. F. Tolić-Nørrelykke, E. Schäffer, J. Howard, F. S. Pavone, F. Jülicher, and H. Flyvbjerg, "Calibration of optical tweezers with positional detection in the back focal plane," *Rev. Sci. Instrum.*, vol. 77, no. 10, p. 103101, 2006.

[68] E. Schäffer, S. F. Nørrelykke, and J. Howard, "Surface forces and drag coefficients of microspheres near a plane surface measured with optical tweezers," *Langmuir*, vol. 23, no. 7, pp. 3654–3665, 2007.

[69] M. Mohamdeh, *High resolution optical tweezers optimized for biological studies*. PhD thesis, Technische Universität Dresden, 2011.

[70] M. Mahamdeh and E. Schäffer, "Optical tweezers with millikelvin precision of temperature-controlled objectives and base-pair resolution," *Opt. Express*, vol. 17, pp. 17190–17199, 2009.

[71] M. Mahamdeh, C. P. Campos, and E. Schäffer, "Under-filling trapping objectives optimizes the use of the available laser power in optical tweezers," *Opt. Express*, vol. 19, no. 12, pp. 11759–11768, 2011.

[72] V. Bormuth, J. Howard, and E. Schäffer, "Led illumination for video-enhanced dic imaging of single microtubules," *J. Microsc.*, vol. 226, no. 1, pp. 1–5, 2007.

[73] K. Visscher, M. J. Schnitzer, and S. M. Block, "Single kinesin molecules studied with a molecular force clamp," *Nature*, vol. 400, no. 6740, pp. 184–189, 1999.

[74] S. M. Block, C. L. Asbury, J. W. Shaevitz, and M. J. Lang, "Probing the kinesin reaction cycle with a 2d optical force clamp," *Proc. Natl. Acad. Sci. U. S. A.*, vol. 100, no. 5, pp. 2351–2356, 2003.

[75] J. Finer, R. M. Simmons, and J. A. Spudich, "Single myosin molecule mechanics: piconewton forces and nanometre steps," *Nature*, vol. 368, pp. 113–119, 1994.

[76] M. Rief, R. S. Rocka, A. D. Mehta, M. S. Mooseker, R. E. Cheney, and J. A. Spudich, "Myosin-v stepping kinetics: A molecular model for processivity," *Proc. Natl. Acad. Sci. U. S. A.*, vol. 97, no. 17, pp. 9482–9486, 2000.

[77] A. Gennerich, A. P. Carter, S. L. Reck-Peterson, and R. D. Vale, "Force-induced bidirectional stepping of cytoplasmic dynein," *Cell*, vol. 131, no. 5, pp. 952–965, 2007.

[78] K. J. Åström, *Control System Design*. Department of Mechanical and Environmental Engineering, University of California, 2002.

[79] J. Bechhoefer, "Feedback for physicists: A tutorial essay on control," *Rev. Mod. Phys.*, vol. 77, no. 3, pp. 783–836, 2005.

[80] K. J. Åström and T. Hägglund, *Advanced PID Control*. ISA - The Instrumentation, Systems, and Automation Society, 2006.

[81] K. J. Åström and R. M. Murray, *Feedback systems: an introduction for scientists and engineers*. Princeton University Press, 2008.

[82] G. K. McMillan, *PID Control in the Third Millennium: Lessons Learned and New Approaches*, ch. 14, pp. 415–461. Springer, 2012.

[83] T. Ota, S. Kawata, T. Sugiura, M. J. Booth, M. A. A. Neil, R. Juskaitis, and T. Wilson, "Dynamic axial-position control of a laser-trapped particle by wave-front modification," *Opt. Lett.*, vol. 28, no. 6, pp. 465–467, 2003.

[84] S. Hell, G. Reiner, C. Cremer, and E. H. K. Stelzer, "Aberrations in confocal fluorescence microscopy induced by mismatches in refractive index," *J. Microsc.*, vol. 169, no. 3, pp. 391–405, 1993.

[85] K. C. Neuman, E. A. Abbondanzieri, and S. M. Block, "Measurement of the effective focal shift in an optical trap," *Opt. Lett.*, vol. 30, no. 11, pp. 1318–1320, 2005.

[86] R. S. Dutra, P. A. M. Neto, H. M. Nussenzveig, and H. Flyvbjerg, "Theory of optical-tweezers forces near a plane interface," *Phys. Rev. A*, vol. 64, p. 053848, 2016.

[87] M. Ander, S. Subramaniam, K. Fahmy, A. F. Stewart, and E. Schäffer, "A single-strand annealing protein clamps dna to detect and secure homology," *PLOS Biology*, vol. 13, no. x8, p. e1002213, 2015.

[88] A. E. Wallin, H. Ojala, G. Ziedaite, and E. Hæggström, "Dual-trap optical tweezers with real-time force clamp control," *Rev. Sci. Instrum.*, vol. 82, no. 8, p. 083102, 2011.

[89] F. Gittes and C. F. Schmidt, "Signals and noise in micromechanical measurements," *Methods Cell Biol.*, vol. 55, pp. 129–156, 1998.

[90] F. Gittes and F. C. Schmidt, "Thermal noise limitations on micromechanical experiments," *Eur. Biophys. J.*, vol. 27, no. 1, pp. 75–81, 1998.

[91] D. J. Cooper, *Practical Process Control*. Control Station, Inc., 2005.

[92] M. Bugiel, "Protofilament switching of kinesin-8, investigated with optical tweezers," Master's thesis, Technische Universität Dresden, 2011.

[93] J. Ziegler and N. Nichols, "Optimum settings for automatic controllers," *Transactions of ASME*, vol. 64, pp. 759–768, 1942.

[94] C. Hang, K. Åström, and W. Ho, "Refinements of the ziegler-nichols tuning formula," *Control Theory and Applications, IEE Proceedings D*, vol. 138, no. 2, pp. 111–118, 1991.

[95] M. Shahrokhi and A. Zomorrodi, "Comparison of pid controller tuning methods," in *8th National Iranian Chemical Engineering Congress*, pp. 1–12, 2003.

[96] V. Bormuth, V. Varga, J. Howard, and E. Schäffer, "Protein friction limits diffusive and directed movements of kinesin motors on microtubules," *Science*, vol. 325, no. 5942, pp. 870–873, 2009.

[97] S. Jeney, E. H. K. Stelzer, H. Grubmüller, and E.-L. Florin, "Mechanical properties of single motor molecules studied by three-dimensional thermal force probing in optical tweezers," *ChemPhysChem*, vol. 5, pp. 1150–1158, 2004.

[98] A. Rose, *Vision: Human and Electronic*. Plenum Press, 1973.

[99] A. Richardson, S. Reihani, and L. Oddershede, "Non-harmonic potential of a single beam optical trap," *Opt. Express*, vol. 16, no. 20, pp. 15709–15717, 2008.

[100] M. Jahnel, M. Behrndt, A. Jannasch, E. Schäffer, and S. W. Grill, "Measuring the complete force field of an optical trap," *Opt. Lett.*, vol. 36, no. 7, pp. 1260–1262, 2011.

[101] D. Baddeley, M. B. Cannell, and C. Soeller, "Three-dimensional sub-100 nm super-resolution imaging of biological samples using a phase ramp in the objective pupil," *Nano Res.*, vol. 4, no. 6, pp. 589–598, 2011.

[102] A. Huhle, D. Klaue, H. Brutzer, P. Daldrop, S. Joo, O. Otto, U. F. Keyser, and R. Seidel, "Camera-based three-dimensional real-time particle tracking at khz rates and Ångström accuracy," *Nat. Commun.*, vol. 6, p. 5885, 2015.

[103] A. Y. Sinan Can, Mark A Dewitt, "Bidirectional helical motility of cytoplasmic dynein around microtubules," *eLIFE*, vol. 3, pp. 1–12, 2014.

[104] I. F. Sbalzarini and P. Koumoutsakos, "Feature point tracking and trajectory analysis for video imaging in cell biology," *J. Struct. Biol.*, vol. 151, no. 2, pp. 182–195, 2005.

[105] K. R. Rogers, S. Weiss, I. Crevel, P. J.Brophy, M. Geeves, and R. Cross, "Kif1d is a fast non-processive kinesin that demonstrates novel k-loop-dependent mechanochemistry," *EMBO J.*, vol. 20, pp. 5101–5113, 2001.

[106] A. Gautier, A. Juillerat, C. Heinis, I. R. C. Jr., M. Kindermann, F. Beaufils, and K. Johnsson, "An engineered protein tag for multiprotein labeling in living cells," *Chem. Biol.*, vol. 15, no. 2, pp. 128–136, 2008.

[107] Z. C. Zhu, K. K. Gupta, A. R. Slabbekoorn, B. A. Paulson, E. S. Folker, and H. V. Goodson, "Interactions between eb1 and microtubules dramatic effect of affinity tags and evidence for cooperative behavior," *J. Biol. Chem*, vol. 284, no. 47, pp. 32651–32661, 2009.

[108] M. Castoldi and A. V. Popov, "Purification of brain tubulin through two cycles of polymerization–depolymerization in a high-molarity buffer," *Protein Expr. Purif.*, vol. 32, no. 1, pp. 83–88, 2003.

[109] V. Bormuth, A. Jannasch, M. Ander, C. M. van Kats, A. van Blaaderen, J. Howard, and E. Schäffer, "Optical trapping of coated microspheres," *Opt. Express*, vol. 16, no. 18, pp. 13831–13844, 2008.

[110] J. Howard, A. Hudspeth, and R. Vale, "Movement of microtubules by single kinesin molecules," *Nature*, vol. 342, pp. 154–158, 1989.

[111] J. Kerssemakers, J. Howard, H. Hess, and S. Diez, "The distance that kinesin-1 holds its cargo from the microtubule surface measured by fluorescence interference contrast microscopy," *Proc. Natl. Acad. Sci. U. S. A.*, vol. 103, no. 43, pp. 15812–15817, 2006.

[112] M. Brunnbauer, R. Dombi, T.-H. Ho, M. Schliwa, M. Rief, and Z. Ökten, "Torque generation of kinesin motors is governed by the stability of the neck domain," *Mol. Cell*, vol. 46, pp. 147–158, 2012.

[113] Y. Oguchi, S. Uchimura, T. Ohki, S. V. Mikhailenko, and S. Ishiwata, "The bidirectional depolymerizer mcak generates force by disassembling both microtubule ends," *Nat. Cell. Biol.*, vol. 13, p. 846–852, 2011.

[114] J. A. Spudich, S. E. Rice, R. S. Rock, T. J. Purcell, and H. M. Warrick, "Attachment of anti-gfp antibodies to microspheres for optical trapping experiments," *Cold Spring Harb Protoc*, vol. 11, pp. 1370–1371, 2011.

[115] N. R. Guydosh and S. M. Block, "Direct observation of the binding state of the kinesin head to the microtubule," *Nature*, vol. 461, pp. 125–128, 2009.

[116] D. Jamison, J. Driver, A. Rogers, P. Constantinou, and M. Diehl, "Two kinesins transport cargo primarily via the action of one motor: implications for intracellular transport.," *Biophys. J.*, vol. 99, p. 2967–2977, 2010.

[117] V. Bormuth, F. Zörgiebel, E. Schäffer, and J. Howard, "Functional surface-attachment in a sandwich geometry of gfp-labeled motor proteins," in *Single Molecule Enzymology* (G. I. Mashanov and C. Batters, eds.), pp. 11–18, Humana Press, 2010.

[118] M. Bugiel, H. Fantana, V. Bormuth, A. Trushko, F. Schiemann, J. Howard, E. Schäffer, and A. Jannasch, "Versatile microsphere attachment of gfp-labeled motors and other tagged proteins with preserved functionality," *JBM*, vol. 2, no. 4, p. e30, 2015.

[119] J. Gbadamosi, A. Hunter, and S. Moghimi, "Pegylation of microspheres generates a heterogeneous population of particles with differential surface characteristics and biological performance," *FEBS Lett.*, vol. 532, no. 3, pp. 338–344, 2002.

[120] V. R. Sinha, A. Aggarwal, and A. Trehan, "Biodegradable pegylated microspheres and nanospheres," *Am. J. Drug. Deliv.*, vol. 2, no. 3, pp. 157–171, 2004.

[121] F. Madani, M. Bessodes, A. Lakrouf, C. Vauthier, D. Scherman, and J.-C. Chaumeil, "Pegylation of microspheres for therapeutic embolization: Preparation, characterization and biological performance evaluation," *Biomaterials*, vol. 28, no. 6, pp. 1198–1208, 2006.

[122] H. J. Byeon, I. Kim, J. S. Choi, E. S. Lee, B. S. Shin, and Y. S. Youn, "Pegylated apoptotic protein-loaded plga microspheres for cancer therapy," *Int. J. Nanomedicine*, vol. 10, no. 1, pp. 739–748, 2015.

[123] K. D. Caldwell, "Physical characteristics and biological use," in *Surface modifications with adsorbed poly(ethylene oxide)-based block copolymers*, ch. 25, p. 400–419, ACS Symposium Series, 1997.

[124] H. B. Lu, C. T. Campbell, and D. G. Castner, "Attachment of functionalized poly(ethylene glycol) films to gold surfaces," *Langmuir*, vol. 16, no. 4, pp. 1711–1718, 2000.

[125] M. T. Valentine, Z. E. Perlman, M. L. Gardel, J. H. Shin, P. Matsudaira, T. J. Mitchison, and D. A. Weitz, "Colloid surface chemistry critically affects multiple particle tracking measurements of biomaterials," *Biophys. J.*, vol. 86, pp. 4004–4014, 2004.

[126] S. Upadhyayula, T. Quinata, S. Bishop, S. Gupta, N. R. Johnson, B. Bahmani, K. Bozhilov, J. Stubbs, P. Jreij, P. Nallagatla, and V. I. Vullev, "Coatings of polyethylene glycol for suppressing adhesion between solid microspheres and flat surfaces," *Langmuir*, vol. 28, no. 11, pp. 5059–5069, 2012.

[127] K. Prime and G. Whitesides, "Self-assembled organic monolayers: model systems for studying adsorption of proteins at surfaces," *Science*, vol. 252, no. 5009, pp. 1164–1167, 1991.

[128] A. G. Kanaras, F. S. Kamounah, K. Schaumburg, C. J. Kiely, and M. Brust, "Thioalkylated tetraethylene glycol: a new ligand for water soluble monolayer protected gold clusters," *Chem. Comm.*, vol. 2002, pp. 2294–2295, 2002.

[129] H. T. Uyeda, I. L. Medintz, J. K. Jaiswal, Sanford, M. Simon, and H. Mattoussi, "Synthesis of compact multidentate ligands to prepare stable hydrophilic quantum dot fluorophores," *J. Am. Chem. Soc.*, vol. 127, no. 11, pp. 3870–3878, 2005.

[130] M. Müller, J. Vörös, G. Csúcs, E. Walter, G. Danuser, M. Textor, and N. D. Spencer, "Surface modification of plga microspheres.," *J. Biomed. Mater. Res. A.*, vol. 66, no. 1, pp. 55–61, 2003.

[131] D. R. Breed, R. Thibault, F. Xie, Q. Wang, C. J. Hawker, and D. J. Pine, "Functionalization of polymer microspheres using click chemistry," *Langmuir*, vol. 25, no. 8, pp. 4370–4376, 2009.

[132] G. T. Hermanson, *Bioconjugate techniques*. Academic Press, 2008.

[133] D. Chamberlin and R. Trutna, "Physics of particle size spectrophotometry," tech. rep., Agilent Technologies, 2008.

[134] G. Hermsdorf, "Single-molecule fluorescence combined with optical tweezers to study membrane mechanics," Master's thesis, Technische Universität Dresden, 2013.

[135] K. Deffar, H. Shi, L. Li, X. Wang, and X. Zhu, "Nanobodies - the new concept in antibody engineering," *Afr. J. Biotechnol.*, vol. 8, no. 12, pp. 2645–2652, 2009.

[136] M. F. Flajnik, N. Deschacht, and S. Muyldermans, "A case of convergence: Why did a simple alternative to canonical antibodies arise in sharks and camels?," *PLOS Biology*, vol. 9, no. 8, p. e1001120, 2011.

[137] H. Steins, "Interaktionsanalysen des gfp-nanobodies mit gfp zur entwicklung effizienter analysemethoden für die nanobody-target-wechselwirkung," Master's thesis, Eberhard Karls Universität Tübingen, 2015.

[138] C. Gell, M. Berndt, J. Enderlein, and S. Diez, "Tirf microscopy evanescent field calibration using tilted fluorescent microtubules," *J. Microsc.*, vol. 234, no. 1, pp. 38–46, 2009.

[139] J. N. Israelachvili, *Intermolecular & Surface Forces, Second Edition*. Academic Press, 1991.

[140] S. N. S. Reihani and L. B. Oddershede, "Optimizing immersion media refractive index improves optical trapping by compensating spherical aberrations," *Optical Letters*, vol. 32, pp. 1998–2000, 2007.

[141] J. Kerssemakers, L. Ionov, U. Queitsch, S. Luna, H. Hess, and S. Diez, "3d nanometer tracking of motile microtubules on reflective surfaces," *Small*, vol. 5, no. 15, pp. 1732–1737, 2009.

[142] W. Roos, J. Ulmer, S. Gräter, T. Surrey, and J. P. Spatz, "Microtubule gliding and cross-linked microtubule networks on micropillar interfaces," *Nano Lett.*, vol. 5, no. 12, pp. 2630–2634, 2005.

[143] Y. Sun, O. Sato, F. Ruhnow, M. E. Arsenault, M. Ikebe, and Y. E. Goldman, "Single molecule stepping and structural dynamics of myosin x," *Nat. Struct. Mol. Biol.*, vol. 17, no. 4, pp. 485–491, 2010.

[144] H. Lan and Y. Ding, "Nanoimprint litography," in *Lithography* (M. Wang, ed.), ch. 23, pp. 457–494, INTECH, 2010.

[145] H. Lan, "Soft uv nanoimprint lithography and its applications," in *Updates in Advanced Lithography* (S. Hosaka, ed.), ch. 7, pp. 1175–1177, INTECH, 2013.

[146] J. P. Rolland, E. C. Hagberg, G. M. Denison, K. R. Carter, and J. M. D. Simone, "High-resolution soft lithography: Enabling materials for nanotechnologies," *Angew. Chem. Int. Ed.*, vol. 43, pp. 5796–5799, 2004.

[147] T. T. Truong, R. Lin, S. Jeon, H. H. Lee, J. Maria, A. Gaur, F. Hu, I. Meinel, and J. A. Rogers, "Soft lithography using acryloxy perfluoropolyether composite stamps," *Langmuir*, vol. 23, pp. 2898–2905, 2007.

[148] M. Bugiel, E. Böhl, and E. Schäffer, "The kinesin-8, kip3, switches microtubule protofilaments in a sideward random walk asymmetrically biased by force," *Biophys. J.*, vol. 108, no. 8, pp. 2019–27, 2015.

[149] A. N. Lupas and M. Gruber, "The structure of $\alpha$-helical coiled coils," *Adv. Protein Chem.*, vol. 70, pp. 37–38, 2005.

[150] C. Peters, K. Brejc, L. Belmont, A. J. Bodey, Y. Lee, M. Yu, J. Guo, R. Sakowicz, J. Hartman, and C. A. Moores, "Insight into the molecular mechanism of the multitasking kinesin-8 motor," *EMBO J.*, vol. 29, pp. 3437–3447, 2010.

[151] F. Kienberger, V. P. Pastushenko, G. Kada, H. J. Gruber, C. Riener, H. Schindler, and P. Hinterdorfer, "Static and dynamical properties of single poly(ethylene glycol) molecules investigated by force spectroscopy," *Single Mol.*, vol. 2, pp. 123–128, 2000.

[152] J. Howard, "Motor proteins as nanomachines: The roles of thermal fluctuations in generating force and motion," *Séminaire Poincaré*, vol. 12, pp. 33–44, 2009.

[153] C. Leduc, F. Ruhnow, J. Howard, and S. Diez, "Detection of fractional steps in cargo movement by the collective operation of kinesin-1 motors," *Proc. Natl. Acad. Sci. U. S. A.*, vol. 104, pp. 10847–10852, 2007.

[154] R. D. Vale and Y. Y. Toyoshima, "Rotation and translocation of microtubules in vitro induced by dyneins from tetrahymena cilia," *Cell*, vol. 52, no. 3, pp. 459–469, 1988.

[155] O. Kagami and R. Kamiya, "Translocation and rotation of microtubules caused by multiple species of chlamydomonas inner-arm dynein," *J. Biol. Chem.*, vol. 103, pp. 653–664, 1992.

[156] M. A. DeWitt, A. Y. Chang, P. A. Combs, and A. Yildiz, "Cytoplasmic dynein moves through uncoordinated stepping of the aaa plus ring domains," *Science*, vol. 335, no. 6065, pp. 221–225, 2012.

[157] W. Qiu, N. D. Derr, B. S. Goodman, E. Villa, D. Wu, W. Shih, and S. L. Reck-Peterson, "Dynein achieves processive motion using both stochastic and coordinated stepping," *Nat. Struct. Mol. Biol.*, vol. 19, no. 2, pp. 193–200, 2012.

[158] R. Dixit, J. L. Ross, Y. E. Goldman, and E. L. F. Holzbaur, "Differential regulation of dynein and kinesin motor proteins by tau," *Science*, vol. 319, no. 5866, pp. 1086–1089, 2008.

[159] T. Korten and S. Diez, "Setting up roadblocks for kinesin-1: mechanism for the selective speed control of cargo carrying microtubules," *Lab Chip*, vol. 8, pp. 1441–1447, 2008.

[160] J. Yajima and R. A. Cross, "A torque component in the kinesin-1 power stroke," *Nat. Chem. Biol.*, vol. 1, no. 6, pp. 338–41, 2005.

[161] X. Pan, S. Acar, and J. M. Scholey, "Torque generation by one of the motor subunits of heterotrimeric kinesin-2," *Biochem. Biophys. Res. Commun.*, vol. 401, no. 1, pp. 53–57, 2010.

[162] J. Yajima, K. Mizutani, and T. Nishizaka, "A torque component present in mitotic kinesin eg5 revealed by three-dimensional tracking," *Nat. Struct. Mol. Biol.*, vol. 15, no. 10, pp. 1119–1121, 2008.

[163] X. Michalet, "Mean square displacement analysis of single-particle trajectories with localization error: Brownian motion in isotropic medium.," *Phys. Rev.*, vol. 82, no. 4, p. 041914, 2010.

[164] J. Helenius, G. Brouhard, Y. Kalaidzidis, S. Diez, and J. Howard, "The depolymerizing kinesin mcak uses lattice diffusion to rapidly target microtubule ends," *Nature*, vol. 441, no. 7089, pp. 115–119, 2006.

[165] T. Bickel, "A note on confined diffusion," *Physica A*, vol. 377, no. 1, pp. 24–32, 2007.

[166] K. S. Thorn, J. A. Ubersax, and R. D. Vale, "Engineering the processive run length of the kinesin motor," *J. Cell Biol.*, vol. 151, no. 4, pp. 1093–1100, 2000.

[167] P. O. Widlund, M. Podolski, S. Reber, J. Alper, M. Storch, A. A. Hyman, J. Howard, and D. N. Drechsel, "One-step purification of assembly-competent tubulin from diverse eukaryotic sources," *Mol. Biol. Cell*, vol. 23, no. 22, pp. 4393–4401, 2012.

[168] J. F. Díaz, J. M. Valpuesta, P. Chacón, G. Diakuni, and J. M. Andreu, "Changes in microtubule protofilament number induced by taxol binding to an easily accessible site," *J. Biol. Chem.*, vol. 273, no. 50, pp. 33803–33810, 1998.

[169] J. Andreu, J. Bordas, J. Diaz, J. G. de Ancos, R. Gil, F. Medrano, E. Nogales, E. Pantos, and E. Towns-Andrews, "Low resolution structure of microtubules in solution: Synchrotron x-ray scattering and electron microscopy of taxol-induced microtubules assembled from purified tubulin in comparison with glycerol and map-induced microtubules," *J. Mol. Biol.*, vol. 226, no. 1, pp. 169–184, 1992.

[170] E. R. Dufresne and D. G. Grier, "Optical tweezers arrays and optical substrates created with diffractive optics," *Rev. Sci. Instrum.*, vol. 69, no. 5, pp. 1974–1977, 1998.

[171] K. Visscher, S. P. Gross, and S. M. Block, "Construction of multiple-beam optical traps with nanometer-resolution position sensing," *Journal of Selected Topics in Quantum Electronics*, vol. 2, no. 4, pp. 1066–1076, 1996.

[172] G. Volpe, R. Quidant, G. Badenes, and D. Petrov, "Surface plasmon radiation forces," *Phys. Rev. Lett.*, vol. 96, no. 23, p. 238101, 2006.

[173] "Viscopedia: A free encyclopedia for viscosity." http://www.viscopedia.com/viscosity-tables/substances/water/ (10/31/2016).

[174] S. Kawata and T. Sugiura, "Movement of micrometer-sized particles in the evanescent field of a laser beam," *Opt. Lett.*, vol. 17, no. 11, pp. 772–774, 1992.

[175] S. Kawata and T. Tani, "Optically driven mie particles in an evanescent field along a channeled waveguide," *Opt. Lett.*, vol. 21, no. 21, pp. 1768–1770, 1996.

[176] M. Righini, A. S. Zelenina, C. Girard, and R. Quidant, "Parallel and selective trapping in a patterned plasmonic landscape," *Nat. Phys.*, vol. 3, pp. 477–480, 2007.

[177] Y. Tanaka and K. Sasaki, "Optical trapping through the localized surfaceplasmon resonance of engineered gold nanoblock pairs," *Opt. Express*, vol. 19, no. 18, pp. 17462–17468, 2011.

[178] D. Guan, Z. H. Hang, Z. Marcet, H. Liu, I. I. Kravchenko, C. T. Chan, H. B. Chan, and P. Tong, "Direct measurement of optical force induced by near-field plasmonic cavity using dynamic mode afm," *Sci. Rep.*, vol. 5, p. 16216, 2015.

[179] D. Li, Y. Xi, and H. K. Kim, "Optical trapping by a metal thin-film edge," *J. Appl. Phys.*, vol. 110, p. 103108, 2011.

[180] R. Piazza, "Thermophoresis: moving particles with thermal gradients," *Soft Matter*, vol. 4, pp. 1740–1744, 2008.

[181] S. Duhr, S. Arduini, and D. Braun, "Thermophoresis of dna determined by microfluidic fluorescence," *Eur. Phys. J. E*, vol. 15, pp. 277–286, 2004.

[182] S. Duhr and D. Braun, "Thermophoretic depletion follows boltzmann distribution," *Phys. Rev. Lett.*, vol. 96, no. 16, p. 168301, 2006.

[183] L. Helden, R. Eichhorn, and C. Bechinger, "Direct measurement of thermophoretic forces," *Soft Matter*, vol. 11, pp. 2379–2386, 2015.

[184] C. Sternling and L. Scriven, "Interfacial turbulence: Hydrodynamic instability and the marangoni effect," *AIChE J.*, vol. 5, no. 4, pp. 514–523, 1959.

[185] R. D. Deegan, O. Bakajin, T. F. Dupont, G. Huber, S. R. Nagel, and T. A. Witten, "Capillary flow as the cause of ring stains from dried liquid drops," *Nature*, vol. 389, pp. 827–829, 1997.

[186] S. Yamaguchi, K. Saito, M. Sutoh, T. Nishizaka, Y. Toyoshima, and J. Yajima, "Torque generation by axonemal outer-arm dynein," *Biophys. J.*, vol. 108, no. 4, pp. 872–879, 2015.

[187] Z. Bertalan, Z. Budrikis, C. A. M. L. Porta, and S. Zapperi, "Navigation strategies of motor proteins on decorated tracks," *PLOS ONE*, vol. 10, no. 8, p. e0136945, 2015.

[188] K. Shibata, M. Miura, Y. Watanabe, K. Saito, A. Nishimura, and K. Furuta, "A single protofilament is sufficient to support unidirectional walking of dynein and kinesin," *PLOS ONE*, vol. 7, no. 8, p. e42990, 2012.

[189] S. Morlot, V. Galli, M. Klein, N. Chiaruttini, J. Manzi, F. Humbert, L. Dinis, M. Lenz, G. Cappello, and A. Roux, "Membrane shape at the edge of the dynamin helix sets location and duration of the fission reaction," *Cell*, vol. 151, no. 3, pp. 619–629, 2012.

[190] C. Kaiser, D. Goldman, J. Chodera, o. I. J. Tinoc, and C. Bustamante, "The ribosome modulates nascent protein folding," *Science*, vol. 334, no. 6063, pp. 1723–1727, 2011.

[191] A. Trushko and J. Schäffer, E. Howard, "The growth speed of microtubules with xmap215-coated beads coupled to their ends is increased by tensile force," *Proc. Natl. Acad. Sci. U. S. A.*, vol. 110, no. 36, pp. 14670–14675, 2013.

[192] C. L. Asbury, D. R. Gestaut, A. F. Powers, A. D. Franck, and T. N. Davis, "The dam1 kinetochore complex harnesses microtubule dynamics to produce force and movement," *Proc. Natl. Acad. Sci. U. S. A.*, vol. 103, no. 26, pp. 9873–9878, 2006.

[193] R. A. Maillard, G. Chistol, M. Sen, M. Righini, J. Tan, C. M. Kaiser, C. Hodges, A. Martin, and C. Bustamante, "Clpx(p) generates mechanical force to unfold and translocate its protein substrates," *Cell*, vol. 145, no. 3, pp. 459–469, 2011.

# Acknowledgements

By the end, I want to thank first Erik Schäffer, who gave me the opportunity to work in his lab on my professional passion topic (motor proteins). He pushed me when work seemed too easy, but (almost) never demanded too much. His optimism was inspiring and his encyclopedian basically knowledge about everything helped more than once.

I also want to thank all recent and former members in the Cellular Nanoscience group (Avin, Mohammad, Suman, Mehrbod, Mayank, Christine, Basudev, Naghmeh, Marcel). A special thank goes to Anita Jannasch, whose work on Kip3 stepping assays laid the foundation for some of my work. More thanks go to Gero Hermsdorf and Steve Simmert for helping me with setup issues, to Tobias Jachowski for the patient and repetitive software explanations, and generally to all lab members for such a great time.

Another special thank goes to the former lab members Elisa Böhl, without whose help the Kip3 stepping simulation and the 3D force clamp.vi might have never worked, and Mohammed Mahamdeh, who introduced me into the lore of optical tweezers.

I thank Aniruddha Mitra from the Lab of Stefan Diez for the great collaboration and Salvatore Girardo for providing the patterned cover slips.

I also want to thank Anita Jannasch, Gero Hermsdorf, and Steve Simmert for carefully proof-reading this thesis.

I thank the Rosa Luxemburg Foundation for supporting this work! Especially, I thank Jane Angerjärv for the nice supervision and Jens Gaitzsch for helping me with the application.

Finally, I want to thank my whole family that supported me whenever necessary. All my love (the word "thank" would be an understatement beyond compare) goes to my girlfriend Danni. More thanks go to my friends and comrades Martin H. (who shares my love for Punk, physics and Sternburg beer) and Ellen T. (Nordisch by nature).

# Eidesstattliche Versicherung/Statement of Authorship

Ich versichere hiermit, dass ich

- die vorliegende Arbeit selbstständig verfasst habe,
- keine anderen als die angegebenen Quellen benutzt und alle wörtlich oder sinngemäß aus anderen Werken übernommenen Aussagen als solche gekennzeichnet habe
- und die eingereichte Arbeit weder vollständig noch in wesentlichen Teilen Gegenstand eines anderen Prüfungsverfahrens gewesen ist.

I hereby certify that

- I have composed this thesis by myself,
- all references and verbatim extracts have been quoted, and all sources of information have been specifically acknowledged,
- this thesis has not been accepted in any previous application for a degree, neither in total nor in substantial parts.

Ort, Datum/Place, Date

Unterschrift/Signature